



UNIVERSITÀ
DEGLI STUDI
DI BRESCIA

**DOTTORATO DI RICERCA IN
TECHNOLOGY FOR HEALTH**

Settore Scientifico Disciplinare
ING-INF/07 MISURE ELETTRICHE ED ELETTRONICHE
CICLO XXXIV

**PRINTED SENSORS ON
NON-CONVENTIONAL SUBSTRATES**

Dottorando
Ing. Edoardo CANTÙ

Relatore
Chiar.mo Prof. Mauro SERPELLONI

Abstract

Industry 4.0 has radically been transforming the production processes and systems with the adoption of enabling technologies, such as Internet of Things (IoT), Big Data, Additive Manufacturing (AM), and Cloud Computing. The principles of these technologies can be also translated into any aspect of everyday life thanks to the usage of printed electronics (PE), offering techniques to produce unconventional sensors and systems or to make conventional objects “smart”. With PE playing a key role in the design of next-generation objects, smart objects fulfill their original function, and they can measure physical quantities in the surrounding environment, being able to communicate with other objects or remote units. Many PE technologies could be adopted, but above all, Aerosol Jet Printing (AJP) with its characteristics can be considered for such a purpose being able to print on any kind of surface a huge variety of functional materials. In combination with Flash Lamp Annealing (FLA), a low-point temperature thermal process, it is possible to complete the production of sensors and circuits on any kind of substrate.

The aim of this thesis work is to identify innovative methods and processes allowing to directly embed sensors, circuits and electronics on the surface of objects and to analyze the metrological characteristics. To this end, compatibility studies have been carried out considering different materials, both in terms of substrates and inks for the realization of smart sensors and objects. Furthermore, design, fabrication and test of sensors and circuits has been analyzed in different fields. Chapter 1 will provide the background and the outline of this dissertation. Smart objects can be manufactured with numerous different technologies and materials depending on the performance required and on the specific application. The purpose of chapter 2 is to provide an analysis of 3D PE technologies that enable sensors printing on complex surfaces. First, an explanation of the technologies under consideration is provided. Then focusing on the used technologies, a deep analysis of AJP and FLA will be provided in chapter 3.

Examples carried out are divided into four macro-areas, wearable devices, paper-based packaging, wet laboratories applications (cells and biomolecules sensing), to demonstrate the applicability of the proposed methodologies in the realization of sensors and smart objects. Starting from chapter 4, applicative examples will be reported.

As possible wearable devices, a 3D smart orthosis with a fully integrated multi-electrodes matrix for electromyography (EMG) will be provided to improve non-invasive personalized recording during rehabilitation. Portability and comfort were enabled by customized light-weight conditioning electronics attached to the orthosis allowing wireless data transmission. Muscular activity from three subjects was then evaluated while performing the same tasks involving multiple muscles. Then, a first example of strain gauge printed directly on a PVC tube is presented, characterized by a linear relationship between mechanical deformation and electrical resistance with a gauge factor of 1.04.

Considering packaging industry, a hybrid smart device was designed and printed on cellulose substrates, testing three different substrate materials (chromatographic paper, photopaper, cardboard). The system is composed by a printed circuit and four printed capacitive sensors, a LED and a microcontroller for data exchange. Multilayer capability and SMDs (Surface Mount Devices) interconnections are possible permitting high flexibility in the fabrication process. Exploiting the hygroscopic properties of paper, carbon paper-based gas sensors for food smart packaging was analyzed, allowing to detect the presence of water-soluble gas like ammonia in an environment provided with a relative humidity above a given threshold ($> 75\%$). After being tested at different relative humidity (RH) values (75, 80, 90, 100%), and once stabilized, they were tested with different ammonia concentrations (3, 6, 9 and 12 ppm) at different temperatures (5 °C, 15 °C and 25 °C). Tests with acetone and ethanol as interferent gasses were carried out, showing a linear behavior in presence of increasing concentrations. The sensors evidenced selectivity during cross-sensitivity tests towards ammonia.

A sensing coil and a tuning capacitor to be used in a passive telemetric system for the measurement of a resistive sensor at a fixed frequency has been developed. Printed elements were validated in a telemetric system for measuring resistive loads with known commercial resistors and the maximum error between the nominal value and the measured value obtained by the telemetric system was lower than 6% in the range 2.2 k Ω and 560 k Ω .

Two examples of carbon electrodes will be presented for impedance-based measurements regarding cells growth and differentiation. This is a reliable non-destructive alternative approach for Caco-2 cells monitoring. The trends of relative impedance magnitude (RI) observed at three different frequencies were able to describe cell growth and differentiation.

The results highlighted 40 kHz as the optimal frequency to assess Caco-2 cells differentiation process. This kind of sensor were also employed to monitor the proliferation of human mesenchymal stromal cells into previously validated gelatin-chitosan hybrid hydrogel scaffolds. Results obtained showed a magnitude increase and a phase angle decrease at 4 kHz (maximum of 2.5 k Ω and -9 degrees) and an exponential increase of the modeled resistance and capacitance components due to the cell proliferation (maximum of 1.5 k Ω and 200 nF).

In addition, two custom easy-to-use electrochemical sensors platforms were developed for biomarkers detection inside liquid samples. In the first case, electrochemical tests have been performed quantifying Interleukin-8, selected as reference protein, by means of Anodic Stripping Voltammetry. Results confirmed nanostructures capability to reduce the limit of detection (from 2.1 to 0.3 ng/mL). Furthermore, AJP appeared to bring an improvement in term of relative standard deviation from 50 to 10%, if compared to screen-printed sensors. Secondly, the platform has been enriched with microfluidics to make the sample deposition (20 μ l) independent from the operator. Different glucose concentrations were considered to validate the sensors, using a standard enzyme-mediated procedure. Both mediator and enzyme were directly aerosol jet printed on working electrodes (Wes). Chronoamperometric tests show LOD = 2.4 mM and sensitivity = $2.2 \pm 0.08 \mu\text{A}/\text{mM}$ confirming the effectiveness of mediator and enzyme directly aerosol-jet-printed to provide sensing in a clinically relevant range (3 – 10 mM). The average relative standard deviation inter-platform is 10%.

The tested prototypes were involved in different working contexts, from food industry to medical rehabilitation, passing through laboratory analysis, keeping a common trait: measuring thanks to unconventional sensors. This fact underlines the applicability of the proposed methodologies to any kind of request, giving the possibility to turn everyday objects into smart ones, thus demonstrating the flexibility of the methods identified and the pervasiveness of sensors and smart objects made this way.

Estratto

L'industria 4.0 sta trasformando radicalmente i processi e i sistemi di produzione con l'adozione di tecnologie abilitanti, come l'Internet of Things (IoT), il Big Data, l'Additive Manufacturing (AM) e il Cloud Computing. I principi di queste tecnologie possono anche essere tradotti in qualsiasi aspetto della vita quotidiana grazie all'uso dell'elettronica stampata (PE), offrendo tecniche per produrre sensori e sistemi non convenzionali o per rendere "intelligenti" oggetti convenzionali. Con la PE a giocare un ruolo chiave nella progettazione di oggetti di nuova generazione, gli oggetti intelligenti adempiono alla loro funzione originale, e possono misurare quantità fisiche nell'ambiente circostante, essendo in grado di comunicare con altri oggetti o unità remote. Diverse tecnologie facenti parte della PE potrebbero essere adottate, ma soprattutto l'Aerosol Jet Printing (AJP) con le sue caratteristiche può essere considerata per tale scopo essendo in grado di stampare su qualsiasi tipo di superficie un'enorme varietà di materiali funzionali. In combinazione con il Flash Lamp Annealing (FLA), un processo termico a bassa temperatura, è possibile completare la produzione di sensori e circuiti su qualsiasi tipo di substrato.

Lo scopo di questo lavoro di tesi è quello di identificare metodi e processi innovativi che permettano di incorporare direttamente sensori, circuiti ed elettronica sulla superficie degli oggetti e di analizzarne le caratteristiche metrologiche. A tal fine, sono stati effettuati studi di compatibilità considerando diversi materiali, sia in termini di substrati che di inchiostri per la realizzazione di sensori e oggetti intelligenti. Inoltre, è stata analizzata la progettazione, la fabbricazione e il test di sensori e circuiti in diversi campi. Il capitolo 1 fornirà il background e lo schema di questa tesi. Gli oggetti intelligenti possono essere fabbricati con numerose tecnologie e materiali diversi a seconda delle prestazioni richieste e dell'applicazione specifica. Lo scopo del capitolo 2 è di fornire un'analisi delle tecnologie di elettronica stampata 3D che permettono la stampa di sensori su superfici complesse. In primo luogo, viene fornita una spiegazione delle tecnologie in esame. Poi, concentrandosi sulle tecnologie utilizzate, verrà fornita un'analisi approfondita di AJP e FLA nel capitolo 3.

Gli esempi svolti sono suddivisi in quattro macro-aree, dispositivi indossabili, packaging su carta, applicazioni di wet laboratory analysis (rilevamento di cellule e biomolecole), per dimostrare l'applicabilità delle metodologie proposte nella realizzazione di sensori e oggetti intelligenti. A partire dal capitolo 4 verranno riportati esempi applicativi.

Come possibili dispositivi indossabili, sarà mostrata un'ortesi intelligente 3D con una matrice multi-elettrodo completamente integrata per l'elettromiografia (EMG) per migliorare la registrazione personalizzata non invasiva durante la riabilitazione. La portabilità e il comfort sono stati abilitati da un'elettronica di condizionamento leggera e personalizzata attaccata all'ortesi che permette la trasmissione dei dati senza fili. L'attività muscolare di tre soggetti è stata poi valutata durante l'esecuzione degli stessi compiti che coinvolgono più muscoli. Poi, verrà presentato un primo esempio di estensimetro stampato direttamente su un tubo di PVC, caratterizzato da una relazione lineare tra deformazione meccanica e resistenza elettrica con un gauge factor di 1,04.

Considerando l'industria dell'imballaggio, un dispositivo ibrido intelligente è stato progettato e stampato su substrati di cellulosa, testando tre diversi substrati (carta cromatografica, carta fotografica, cartone). Il sistema è composto da un circuito stampato e quattro sensori capacitivi stampati, un LED e un microcontrollore per lo scambio di dati. Deposizioni selettive multistrato ed interconnessioni con SMD (Surface Mount Devices) sono possibili consentendo un'alta flessibilità nel processo di fabbricazione. Sfruttando le proprietà igroscopiche della carta, sono stati analizzati sensori cartacei di gas pensati per imballaggi alimentari intelligenti, permettendo di rilevare la presenza di gas idrosolubili come l'ammoniaca in un ambiente dotato di un'umidità relativa superiore a una determinata soglia (> 75%). Dopo essere stati testati a diversi valori di umidità relativa (75, 80, 90, 100%), e una volta stabilizzati, sono stati testati con diverse concentrazioni di ammoniaca (3, 6, 9 e 12 ppm) a diverse temperature (5 °C, 15 °C e 25 °C). Sono stati effettuati test con acetone ed etanolo come gas interferenti, mostrando un comportamento lineare in presenza di concentrazioni crescenti. I sensori hanno evidenziato una selettività durante i test di sensibilità incrociata verso l'ammoniaca.

Sono stati sviluppati un'antenna con un condensatore di regolazione dedicato da utilizzare in un sistema telemetrico passivo per la misurazione di un sensore resistivo a una frequenza fissa. Gli elementi stampati sono stati convalidati in un sistema telemetrico per la misurazione di carichi resistivi con resistenze commerciali note e l'errore massimo tra il valore nominale e il valore misurato ottenuto dal sistema telemetrico è stato inferiore al 6% nell'intervallo 2,2 kΩ e 560 kΩ.

Saranno presentati due esempi di elettrodi di carbonio per misure basate sull'impedenza riguardanti la crescita e la differenziazione delle cellule. Questo è un approccio alternativo, affidabile e non distruttivo per il monitoraggio delle cellule, come le Caco-2. L'impedenza relativa è stata osservata a tre diverse frequenze mostrandosi in grado di descrivere la crescita e la differenziazione delle cellule. I risultati hanno evidenziato 40 kHz come frequenza ottimale per valutare il processo di differenziazione delle cellule Caco-2. Questo tipo di sensore è stato anche impiegato per monitorare la proliferazione di cellule stromali mesenchimali umane in scaffold idrogel ibridi di gelatina-chitosano. I risultati ottenuti hanno mostrato un aumento dell'impedenza e una diminuzione dell'angolo di fase a 4 kHz (massimo di 2,5 k Ω e -9 gradi) e un aumento esponenziale delle componenti di resistenza e capacità modellate a causa della proliferazione cellulare (massimo di 1,5 k Ω e 200 nF).

Inoltre, sono state sviluppate due piattaforme di sensori elettrochimici personalizzate e facili da usare per la rilevazione di biomarcatori all'interno di campioni liquidi. Nel primo caso, i test elettrochimici sono stati eseguiti quantificando l'Interleuchina-8, selezionata come proteina di riferimento, per mezzo della Voltammetria Anodica. I risultati hanno confermato la capacità delle nanostrutture di ridurre il limite di rilevazione (da 2,1 a 0,3 ng/mL). Inoltre, si è ottenuto un miglioramento in termini di deviazione standard relativa dal 50 al 10%, rispetto ai sensori serigrafati. In secondo luogo, la piattaforma è stata arricchita di canali per la microfluidica per rendere la deposizione del campione (20 μ l) indipendente dall'operatore. Diverse concentrazioni di glucosio sono state considerate per convalidare i sensori, utilizzando una procedura standard mediata da un enzima. Sia il mediatore che l'enzima sono stati stampati direttamente tramite AJP sugli working electrodes. I test cronoamperometrici mostrano LOD = 2,4 mM e sensibilità = $2,2 \pm 0,08 \mu\text{A}/\text{mM}$ confermando l'efficacia del mediatore e dell'enzima stampati direttamente a getto d'aerosol per fornire un rilevamento in un intervallo clinicamente rilevante (3 - 10 mM). La deviazione standard relativa media inter-piattaforma è del 10%.

I prototipi testati sono stati coinvolti in diversi contesti lavorativi, dall'industria alimentare alla riabilitazione medica, passando per le analisi di laboratorio, mantenendo un tratto comune: misurare grazie a sensori non convenzionali. Questo fatto sottolinea l'applicabilità delle metodologie proposte a qualsiasi tipo di richiesta, dando la possibilità di trasformare gli oggetti quotidiani in oggetti intelligenti, dimostrando così la flessibilità dei metodi individuati e la pervasività dei sensori e degli oggetti intelligenti così realizzati.

Acknowledgments

Il dottorato è stato per me un percorso umano prima che di studio, ricerca e formazione. Il privilegio di lavorare coi miei colleghi mi ha permesso di progredire come persona e come professionista. Questa è stata senza dubbio l'esperienza universitaria più stimolante, per l'impatto diretto con la ricerca, e più difficile, perché non era e non è la prosecuzione esatta della mia precedente formazione, un aspetto che mi ha turbato molte volte. I momenti di difficoltà non sono mancati, vuoi per lo sconforto per esperimenti infruttuosi, vuoi per la voglia di fare sempre meglio anche quando non sai dove sbattere la testa. O molto semplicemente perché quando si è giovani si ha entusiasmo e manca invece la pazienza, nel lasciare che le azioni diano i loro frutti nel tempo a loro necessario. La pazienza per comprendere ogni situazione e per capire quale sia la scelta giusta da intraprendere, non lasciando nulla al caso. E allora ci tengo a ringraziare tutti coloro che sono al mio fianco e che mi hanno permesso di raggiungere questo prestigioso traguardo.

Grazie ai miei maestri, i Prof. Emilio Sardini e Mauro Serpelloni per le opportunità che mi avete dato, per avermi insegnato l'elettronica, per avermi stimolato ogni giorno e avermi fatto scattare la molla della competizione con me stesso per raggiungere nuovi traguardi. E qui non posso che citare il Prof. Nicola Lopomo, per i modi gentili e i consigli sempre preziosi, e l'Ing. Paolo Bellitti, collega sempre pronto a scendere in battaglia al mio fianco. Perché noi cinque insieme ci siamo posti un gran bell'obbiettivo per il nostro futuro, vi ringrazio dal profondo per la fiducia e vi prometto massimo impegno e dedizione.

Un grazie grande come una casa al mio terzo maestro, Danilo Febbrari. Sei un punto di riferimento certo, mi hai sempre aiutato nel bisogno. Se tanti lavori si sono rivelati vincenti, è stato anche merito tuo e dei tuoi insegnamenti sul campo.

Grazie all'Ing. Michela Borghetti, collega di alto profilo, competente e precisa, lavorando insieme mi hai sempre dimostrato quanto i dettagli siano essenziali per arrivare in alto.

Grazie ai miei amici Dott.ssa Sarah Tonello e Ing. Tiziano Fapanni, lavorare con voi è un privilegio perché è divertimento, è collaborazione massima, è successo. Inutile dire che l'augurio è che questo possa mantenersi per tanto tempo ancora. Assieme a voi non posso non ringraziare anche l'Ing. Ileana Armando, l'ultimo ingresso nel nostro gruppo per ordine di tempo e di grande qualità. Sei tosta e col tuo modo raggiungerai i tuoi obbiettivi. Le partite a Magic con te e Tiziano in ufficio saranno sempre un ricordo prezioso di questo periodo.

Grazie al Prof. Andrea Ponzoni e al Dott. Matteo Soprani per il percorso di lavoro fatto insieme e per il mondo che mi avete fatto conoscere, ve ne sarò sempre grato.

Un pensiero voglio dedicarlo anche a Mariaelena e Roberto, Serena e Diego, per i tanti bei momenti passati insieme e per quelli futuri, per il sincero affetto che mi avete sempre dimostrato.

Uno degli aspetti a cui sono più affezionato dei miei tre anni di dottorato è che ha coinciso con un altro percorso, quello con te Chiara. Salda e giovane roccia a cui aggrapparmi nei momenti di difficoltà, amorevole custode di sogni da realizzare insieme. Potrei perdermi in un mare di parole per ringraziarti per tutto ciò che fai per me, e ancora non basterebbe. Insieme abbiamo superato vari ostacoli, abbiamo fatto sacrifici sostenendoci a vicenda fra lauree, esami e discussioni varie. Il tuo amore è il più grande stimolo che potessi avere e il più grande dono che potessi ricevere.

Cari mamma e papà ancora una volta siete stati l'essenza e la sostanza di un traguardo prestigioso e inaspettato che mai ci saremmo sognati di raggiungere tutti e tre, in fin dei conti il mio esordio è stato "io non ho voglia di studiare". Il vostro è stato un accompagnarmi nelle scelte assecondando la mia crescente voglia di misurarmi col mondo e con me stesso, ponendomi traguardi sempre più affascinanti e aiutandomi a consolidare le mie capacità per affrontare il futuro sempre a testa alta e con entusiasmo. Siete stati fautori dell'ultimo step mentale. Non è più tempo di osservare il panorama e scorgere obiettivi, questi sono già chiari e delineati con basi solide costruite in questo periodo. Le sfide future sono affascinanti e le porteremo avanti col consueto spirito.

Insieme.

E con un innesto di assoluta qualità.

Grazie dal profondo del cuore.

Edoardo

Table of Contents

Abstract	ii
Estratto	v
Acknowledgments	viii
Table of Contents	x
List of Figures	xiii
List of Tables	xxii
1. Background	1
1.1 Motivations	1
1.2 Thesis Outline	5
2. Analysis of Printed Electronics Technologies	6
2.1 Printing Techniques and Their Characteristics	7
3. Methods	14
3.1 Aerosol Jet Printing	14
3.1.1 Introduction to AJP	14
3.1.2 Factors affecting printing quality	16
3.1.3 Process Physics	17
3.1.4 Functional inks	20
3.2 Flash Lamp Annealing	21
3.2.1 Introduction	21
3.2.2 Physics	22
3.2.3 Substrates and inks	24
4. Introduction to applicative solutions	25
5. Wearable Smart Objects	29
5.1 Printed Multi-EMG Electrodes on the 3D Surface of an Orthosis for Rehabilitation: a Feasibility Study 29	
5.1.1 Introduction	29
5.1.2 Device Fabrication and Characterization	30
5.1.3 In Vivo Acquisitions	36
5.1.4 Conclusion	48

5.1.5	Follow-on Work.....	49
5.2	Preliminary Study on a Strain Sensor Printed on 3D-plastic Surfaces for Smart Devices.....	53
5.2.1	Introduction.....	53
5.2.2	Sensor Fabrication.....	53
5.2.3	Experimental setup.....	55
5.2.4	Experimental Results.....	57
5.2.5	Conclusion.....	60
6.	<i>Smart Sensors and Objects in Packaging Sector</i>	61
6.1	Paper PCB Hybrid Circuit.....	61
6.1.1	Introduction.....	61
6.1.2	Materials and Methods.....	62
6.1.3	Results.....	68
6.1.4	Conclusion.....	77
6.2	Printed Antenna for Resistive Sensors Readout.....	79
6.2.1	Introduction.....	79
6.2.2	Design of the Sensing Coil.....	80
6.2.3	Materials and Methods.....	85
6.2.4	Results and Discussion.....	88
6.2.5	Conclusion.....	91
6.3	Paper-based ammonia gas sensors for smart food packaging.....	92
6.3.1	Introduction.....	92
6.3.2	Sensor Design.....	93
6.3.3	Experimental Setup.....	96
6.3.4	Results and Discussion.....	99
6.3.5	Conclusions.....	108
7.	<i>Cells-related Sensing.....</i>	110
7.1	Caco2.....	110
7.1.1	Introduction.....	110
7.1.2	Materials and methods.....	111
7.1.3	Results and discussion.....	115
7.1.4	Conclusion.....	127
7.2	Mesenchimal stem cells.....	128
7.2.1	Introduction.....	128
7.2.2	Materials and Methods.....	129
7.2.3	Results and Discussion.....	136

7.2.4	Discussion	145
7.2.5	Conclusion	146
8.	<i>Lab-on-chip Objects</i>	148
8.1	Protein detection	148
8.1.1	Introduction.....	148
8.1.2	Materials and Methods	149
8.1.3	Results and Discussion	155
8.1.4	Conclusion	160
8.2	Glucose sensing and microfluidics	162
8.2.1	Introduction.....	162
8.2.2	Materials and Methods	163
8.2.3	Results and discussion.....	171
8.2.4	Conclusion	176
9.	<i>General conclusions</i>	177
	<i>Courses, Seminars, Conferences, Conference Proceedings, Journal Publications, Awards</i>	179
a.	Attended Courses/Schools	179
b.	Attended Seminars	179
c.	Attended Congresses/Conferences	179
d.	Conference Proceedings.....	180
e.	Publications in Journals.....	180
f.	Awards	181
	<i>References</i>	182

List of Figures

Fig. 1 Architectures of (a) active and (b) passive smart objects. The smart object is equipped with sensors that detect changes in physical quantities like temperature, deformation, vibration, etc. In the case of active smart objects, electronics acquires, processes and exchanges data with the network, while in the case of passive objects, an external readout unit acquires the sensor output wirelessly. The power supply unit can include 1) batteries, accumulator or systems that convert other natural energies into electrical energy and 2) a power management unit that controls and distributes the power supply (orange arrow) to the other blocks.....	4
Fig. 2 Microdispensing physical functioning principle.....	8
Fig. 3 Piezojet physical functioning principle.....	9
Fig. 4 Inkjet physical functioning principle.....	11
Fig. 5 Plasmadust physical functioning principle.....	12
Fig. 6 Laser Induced Forward Transfer physical functioning principle.....	13
Fig. 7 Aerosol Jet Printing pneumatic atomization functioning principle.....	16
Fig. 8 Aerosol Jet Printing ultrasonic atomization functioning principle.....	16
Fig. 9 Schematic representation of Flash Lamp Annealing.....	22
Fig. 10 Transient surface heating and subsequent relaxation of a thin film on a comparatively thick substrate.....	24
Fig. 11 Final layout of the prototypes for inner and outer features (quotes in mm). The overall dimensions of the wearable device prototype are 100 mm in diameter and 120 mm in length [66].....	32
Fig. 12. Electrodes and tracks printed on the orthosis (quotes in cm); a tester wearing the devices with the electronics [66].....	33
Fig. 13. Profilometer results for printed traces [66].....	34
Fig. 14. Comparison of the impedances of different electrodes normalized on electrode area on subject 1. Wet commercial electrodes in blue, commercial dry electrodes with/without sweat simulation in green/black and AJ printed dry electrodes with/without sweat simulation in red/magenta [66].....	35
Fig. 15. Comparison of the impedances of same electrodes between the two subjects (1 in red, 2 in blue): a) wet commercial electrodes, b) commercial dry electrodes without sweat simulation and c)/d) AJ printed dry electrodes without/with sweat simulation [66].	35
Fig. 16. Architecture of the developed wearable device [66].....	36

Fig. 17 a) Comparison of the full protocol acquired with reference commercial electrodes (blue) and with AJ printed electrodes (red); b) Analysis of the time and frequency features of the EMG signal acquired from a single contraction respectively with commercial (blue) and AJ printed electrodes (red) [66]. 42

Fig. 18 Voltage and Root Mean Square amplitudes measured considering both commercial EMG electrodes and AJ printed electrodes. Considering the latter, from above to below channels 1 to 8 and the EMG signals recorded during a single task of sit-to-stand and stand-to-sit (from t_1 to t_7) [66]...... 43

Fig. 19 Spatial features extracted during task showing the activation of each channel during the different phases. The colorimetric scale reproduces the values of the Root Mean Square [66]. 44

Fig. 20 Maximum correlation values among the 8 channels during sit-to-stand and stand-to-sit tasks. The colorimetric scale represents the correlation at a specific time instant [66]. 45

Fig. 21 RMS features obtained with multiple acquisitions of the same task on a single device [66]. 46

Fig. 22 RMS features obtained from the acquisition of the same task performed using three different devices on the same subject [66]. 46

Fig. 23 Comparison of three subjects (blue, red and green curves) performing a single long contraction. Above: filtered rectified EMG signal and its spectrum. Below: time features and frequency features (Mean frequency solid line and median frequency dotted line) [66].... 47

Fig. 24 Comparison among the time features calculated from the EMG of the three subjects (blue, red and green curves) on channels 1 and 8 while performing a sit-to-stand and a stand-to-sit task [66]...... 48

Fig. 25 Overview of the different steps of the electrodes' fabrication process [66]. 50

Fig. 26 Printed prototype for simultaneous measurements of lactate concentration in sweat as well as electromyography [66]. 50

Fig. 27 a) Current-Concentration plot of the whole range tested (0-250 mM), with linear fitting in the two ranges 0-20 mM (red line) and 20-250 mM (blue line). b) An example of 600 s chronoamperometry recorded during following discrete injection of controlled solutions with different lactate concentrations. Red lines are associated to 0-20 mM concentration range, while blue lines are associated to 20-250 mM concentration range [66]. 52

Fig. 28 Image of two printed strain sensors on a plastic tube. In the inset, a zoom of three parallel lines is shown. The tube has an outer diameter of 20 mm and an inner diameter of 16 mm. No deformations of tube were detected after the sintering [97].	54
Fig. 29 Profile measurement of two parallel lines obtained from Profilm3D. The average width of the two lines is 160 μm , and the maximum height is 13 μm [97].	55
Fig. 30 Experimental setup and performed tests. (a) Model of the sensorized tube as cantilever, when a load of -Fe is applied at the free end along the y-axis direction. (b) Loading-unloading cycles in the first test for the calculation of the gauge factor. (c) Loading-unloading cycles in the first test for the creep analysis [97].	56
Fig. 31 (a) Resistance and (b) load curves during the six loading-unloading cycles when a weight of 500 g is applied and the sensor is on the convex side [97].	58
Fig. 32 Measured resistance change normalized on the initial resistance ($\Delta R/R_0$) as a function of strain, when the sensor is on the convex side (blue color) and on the concave side (red line) [97].	60
Fig. 33 Response of the sensor when a weight (from 50g to 1 kg) is applied and maintained constant in time [97].	60
Fig. 34 Block diagram of the circuit manufacturing steps: the first phase regards Ag ink deposition and FLA curing; the second step involves the placing of SMDs and packaged components; step three is focused on the deposition of NOA 81 to fix previously placed packaged components and as insulator on specific Ag tracks and capacitive sensors; the last phase regards the final Ag deposition in multilayer zones of the circuit and to interconnect Ag tracks with packaged components [84].	63
Fig. 35 (a) Pattern and geometrical dimensions of printed samples ($L = 22.5 \text{ mm}$, $D = 1 \text{ mm}$, $W = 1 \text{ mm}$). Image of resulting samples printed on (b) chromatographic paper, (c) cardboard and (d) photopaper [84].	64
Fig. 36 R/R_0 vs Voltage depending on impulse duration for (a) chromatographic paper, (b) cardboard and (c) photopaper [84].	66
Fig. 37 Details of encapsulated programming module and printed tracks [84].	68
Fig. 38 Microscope magnification of a multilayer zone [84].	68
Fig. 39 Cross-section magnification performed thanks to the abovementioned FE-SEM for samples printed on (a) chromatographic paper, (b) cardboard and (c) photopaper [84].	69
Fig. 40 Thickness profile for Ag on (a) chromatographic paper, (b) cardboard and (c) photographic paper [84].	71

Fig. 41 Schematic representation of the bending test [84].	73
Fig. 42 Resistance variations as a function of the bending angle on chromatographic paper (blue circle), cardboard (red square) and photographic paper (green triangle). Vertical error bars are related to standard deviation of resistance values, while horizontal ones are related to standard deviation of resistances values, while horizontal ones are related to standard deviation of angle values [84].	73
Fig. 43 SEM magnifications of (a) chromatographic paper before bending, (b) chromatographic paper after bending, (c) cardboard before bending, (d) cardboard after bending, (e) photopaper before bending, (f) photopaper after bending [84].	74
Fig. 44 Optomec AJ300 with photopaper tube during printing step [84].	76
Fig. 45 Multilayer smart-3D-device [84].	76
Fig. 46 Impedance magnitude and phase angle plots for top, right, bottom and left keys in no-finger state [84].	77
Fig. 47 (a) Schematic illustration of a smart lid for smart packaging. A resistive sensor is measured through the reading of the impedance of a readout coil, which is coupled with the sensing coil connected to the resistive sensor. (b) Lumped parameter circuit model of passive telemetric measurement system (c) Typical frequency response of the passive telemetric measurement system when the self-resonance frequency of the sensing coil is lower than of the one of the readout coil [205].	81
Fig. 48 Printed tuning capacitor and sensing coil [205].	83
Fig. 49 Manufacturing process for printing coil and capacitor through AJP [205].	86
Fig. 50 (a) Profile of NOA81 of three tuning capacitors having different numbers of deposition (from 1 to 3), indicated in the subscript. On the right the mean value of the capacitance and of the height (the error is the deviation standard calculated on ten profiles) (b) Profile of the printed lines of the coil. On the right, the mean value of the height and the mean width [205].	89
Fig. 51 (a) Characterization of a FSR by changing the applied load (by using known weight from 100 g to 1 kg) over the sensitive area [205].	90
Fig. 52 Real part of the impedance measured at the terminal of the readout coil for known resistor (R_x is indicated in the legend). The star-like symbols correspond to the real part of the impedances at the frequency f_{r2} [205].	91

Fig. 53 Validation of the telemetric system by changing the value of Rx from 2.2 kW to 560 kW (the measured values by means of a multimeter are on x axis). Rx calculated by applying (1) is on y axis [205]..... 91

Fig. 54 a) Block diagram of the manufacturing process; b) Sensor final layout on chromatographic paper and optical microscope magnification. l=12 mm, g=500 μm, w=300 μm. A-A points (12.7 mm in length) indicate where multimeter probes were placed of resistance measurements..... 96

Fig. 55 Schematic representation of the experimental setup. The colors orange, black, red, violet, and green indicate respectively the power supply to the mass flow meter (MFM) and controllers (MFC), gas flow tubing, the fixed temperature in the thermostatic chamber (25 °C), gas managing LabVIEW software, GPIB acquisition LabVIEW software..... 98

Fig. 56 Stabilization and hysteresis cycle of the sensors at different relative humidity. The blue curve represents the first study, from RH=75% to RH=100%; the orange one the comeback to lower RH values, the yellow one the comeback to higher RH values [214]. 101

Fig. 57 Ammonia behavior analysis for paper-based sensors in presence of different ammonia concentrations (blue dots). Error bars represent standard deviations calculated over eight sensors studied in this section. The red line is the straight line that best fits the measured data from 3 ppm to 12 ppm, obtained by using the method of least square ($R^2=0.9783$). 102

Fig. 58 Comparison of the three calibration curves determined at 5 °C (blue), 15 °C (orange), and 25 °C (yellow). Error bars represent standard deviations calculated over eight sensors studied in this section. 102

Fig. 59 Average percent increases for sensors tested at different ammonia concentrations. Hysteresis cycle tested: blue curve = starting cycle from 0 ppm to 12 ppm, red curve = come back cycle from 12 ppm to 0 ppm. Tests were carried out at 25 °C [214]. 103

Fig. 60 Acetone behavior analysis for paper-based sensors in presence of different acetone concentrations. Error bars represent standard deviations calculated over eight sensors studied in this section. Tests were carried out at 25 °C..... 104

Fig. 61 Ethanol behavior analysis for paper-based sensors in presence of different ethanol concentrations. Error bars represent standard deviations calculated over eight sensors studied in this section. Tests were carried out at 25 °C..... 104

Fig. 62 Dynamic stabilization curve (red) of four different sensors for cross sensitivity between ammonia (black) and acetone (blue). The light red area surrounding the red curve represents the standard deviation. 106

Fig. 63 Dynamic stabilization curve (red) four different sensors for cross sensitivity between ammonia (6 ppm) and ethanol (60 and 120 ppm), followed by cross sensitivity between ethanol (60 ppm) and ammonia (6 and 9 ppm). The light red area surrounding the red curve represents the standard deviation. 106

Fig. 64 Caco-2 to enterocyte-like cells differentiation on interdigitated carbon-based electrodes printed on a polyimide substrate. a) Printed Sensor geometry optimized with AutoCAD 2017 and b) image of the sensor acquired with microscope (magnification 1x). c) Representative pictures of Caco-2 cells evaluation at four different time-points (days 3–7–17-21) during 21 days differentiation protocol (magnification 10x and 20x for day 21) where sensor geometry is clearly visible. The 21 day picture results out of focus to better visualize the domes [233]. 117

Fig. 65 a) Caco-2 cells morphological evaluation at four different time-points (days 3-7-17-21) during 21 days differentiation protocol (magnification 4x in day 3 and 7; magnification 10x in day 17 and 21); b) Domes counting and measuring. The statistical significance was represented as follows: **p < .01; ***p < .001 versus the seventh day after seeding (no domes formation before day 7); c) ALPI assay. μg of pNP extrapolated by a standard curve at days 1-3-7-14-17 and 21 after seeding. Data are normalized for total protein amount (#p < .05, ##p < .01 versus the corresponding day 1 as control group); d) Quantitative rt-PCR time-courses of key genes CLDN4, SLC11A2, SLC15A1, SI, ALPI, and CYP3A4 during 21 days of differentiation. The values are expressed as mRNA fold increase compared to day 1 for each genes. The statistical significance was *p < .05; **p < .01; ***p < .001 versus the corresponding day 1 of each gene as control group [233]. 118

Fig. 66 Impedance-based cell monitoring vs time and relative impedance calculation. A) Impedance magnitude vs time during the differentiation process. Error bars show the standard deviation of the 5 sensors evaluated. B) Variation of the relative impedance during the 21 days of cell culture, calculated for each of the frequencies evaluated: low (400 Hz-blue) medium (4 kHz-red) and high (40 kHz-green). C) Principal component analysis. The proportion of variance (0.5843) could be represented as a percentage (about 60%) and PC1 is the first component with the largest possible variance explained; succeeding components (PC2 and PC3) are orthogonal to PC1 with the highest possible variance [233]. 121

Fig. 67 Impedance-based cell monitoring vs frequency and spectra fitting with equivalent circuit: a) Impedance magnitude and phase spectra vs frequency during the differentiation process. b) Equivalent circuit of blank and seeded sensors used to fit the spectra [233].
..... 123

Fig. 68 Evolution of Rcell and Ccell during differentiation: above, schematic of correspondence between the different parameters in the model with the circuit element; below, specific evolution of the modeling circuit parameters related to cells attached on the sensors [233]. 124

Fig. 69 a) Pearson correlation coefficients table. Significant correlations is considered for $\rho > 0.71$ (grey) and the statistical significance is obtained with correlation test and reported in bold (p-value reported for RI at 40 kHz is accepted when < 0.05); b) Bland-Altman plots represent the differences between the pairs of readings, visualizing the pattern of agreement of statistically significant measurements (RI at 40 kHz vs SLC11A2, SI, CYP3A4 and ALPI enzyme activity). Data are standardized (means=0; variance=1) to solve scale problem. The 95% of confidence interval (red line) is computed around the grand mean of the differences (green line) [233]. 126

Fig. 70 Setup for impedance-based monitoring of human mesenchymal stromal cells (hMSCs) seeded in 3D hybrid hydrogel scaffold: (a) Hybrid hydrogel scaffold and aerosol-jet printed (AJP) sensors, (b) cap for sterile measurements, (c) final measurement setup [273]. 130

Fig. 71 Preliminary impedance-based assessment for choosing the optimal cell concentration in the scaffold [273]. 137

Fig. 72 Impedance-based monitoring including controls (a. magnitude and b. phase angle versus frequency) and seeded scaffolds (c. magnitude and d. phase angle vs frequency) [273]. 138

Fig. 73 Cell index in terms of (a.) magnitude and (b.) phase angle contribution to the overall impedance value. Results concerning 4 kHz frequency are specifically highlighted for both (c.) magnitude and (d) phase angle [273]. 139

Fig. 74 Equivalent circuit modeling the (a.) blank and (b.) cell seeded conditions: measured and fitted spectra for both the (c.) module and (d.) phase are reported [273]. 140

Fig. 75 Evolution of the relevant parameters concerning the cell contribution during time (Ccells, Rcells). (a): Equivalent circuit with Rcells and Ccells highlighted (b): Evolution of Ccells during culture (c): Evolution of Rcells during culture [273]. 141

Fig. 76 CKK-8 staining in 3D culture: (a) section and (b) upper-view of CKK-8 macroscopic staining of scaffolds, control (cell-less scaffold), hMSC culture (scaffold with cells after 14 days of culture); (c) box-plot of absorbance measurements at 21 days of culture. Distribution of absorbance measurements for scaffolds exposed to 4 CKK-8 treatments ($x = \text{average} = 0.499 \pm 0.062$) and scaffolds exposed to 1 CKK-8 treatment ($x = \text{average} = 0.474 \pm 0.098$), $p = 0.64$ [273]. 142

Fig. 77 Box-plot of 3D culture proliferation detected with CKK-8 assay along the 21-day-long culture. X indicates samples average at each day [273]. 143

Fig. 78 Fluorescent images of hMSCs on hybrid gelatin-chitosan hydrogel scaffolds at several days of culture. Thinly sliced portions of the central part of the scaffolds. Nuclei staining with DAPI (blue), 10 × magnification. (a.) 3 days of culture, (b.) 7 days of culture, (c.) 14 days of culture and (d.) 21 days of culture [273]. 145

Fig. 79 Schematic representation of the final prototype [71]. 150

Fig. 80 AJP process for sensor fabrication [71]. 152

Fig. 81 (a) Final layout of the printed sensorized glass slide with sample confinement during WE functionalization; (b) Example of the sample confinement over the three electrodes during measurement; (c) Example of liquid leakage on a commercial screen-printed sensor [71]. 152

Fig. 82 Bio-functionalization protocol for the ASV measurements of IL-8 [71]. 155

Fig. 83 Fluorescence imaging, with grayscale color filter, of a bare carbon working electrode without antibodies (left) and with antibodies attached (right) [71]. 156

Fig. 84 Plots obtained during protein quantification test; each plot measures current (expressed in μA) as a function of potential (expressed in V). Dotted lines represent “blank samples” [71]. 157

Fig. 85 LSV for IL8 quantification performed using bare and nanostructured carbon-based sensors [71]. 159

Fig. 86 Calibration plot comparison between Carbon bare and nanostructured sensors [71]. 160

Fig. 87 Schematic representation of the final prototype [72]. 164

Fig. 88 A) Shear stress vs Shear rate, showing a complete linear behavior for temperature in the range 19-25 °C for AgCl ink; B) Viscosity as a function of temperature for AgCl ink [72]. 165

Fig. 89 AJP process for microfluidic sensors platform fabrication [72]. 166

Fig. 90 Process camera photo during printing of A) a chamber wall and B) a microchannel cantilevered line; representation of the critical angle (C); printing scheme and line off-set δ (D) [72].	167
Fig. 91 Final platform produced by means of AJP (a), with specific details of the two concentric limiting circles (b) and a frontal view of the triangular channel (c); a channel filled with pen ink (d) [72].	169
Fig. 92 Mechanism of enzymed mediated glucose sensing [72].	171
Fig. 93 Profiles obtained thanks to Filmetrics 3D optical profilometer for NOA 81, carbon with MWCNTs and AgCl [72].	172
Fig. 94 Electrochemical characterization of AJP sensors in presence of 5mM Ferri-ferrocyanide solution. Cyclic voltammeteries at increasing scan rates (25, 50, 100, 150 and 200 mV/s) and linear relation between peak current height and the square root of the scan rate confirming the diffusion control of the reaction [72].	173
Fig. 95 Chronoamperograms at +500 mV recorded at different glucose concentration [72].	174
Fig. 96 Current values at 60 seconds (blank corrected) at different glucose concentrations: comparison between single sensor's average value on each repetition and average of the values obtained from the sum of the currents in a single platform [72].	174

List of Tables

Table 1 Aerosol Jet Printer process parameters for employed inks.	32
Table 2 Time features selected from literature [145], [175].	39
Table 3 Printing process for Ag ink.	64
Table 4 Printing process for the photopolymer NOA 81.	67
Table 5 Samples resistance behavior in a damp environment.	75
Table 6 Electrical capacitance values at 250 kHz for the capacitive sensors in case of finger in pression and not in pression.	77
Table 7 Geometrical Characteristics of the printed Components and of the readout Coil.	84
Table 8 Inks Process Parameters.	87
Table 9 Electrical characteristics of the coils.	89
Table 10 Stabilization at different RH values.	100
Table 11 Resistance variation during cross-sensitivity tests with acetone and ethanol. .	106
Table 12 Printing process parameters.	151
Table 13 Thickness and sections of deposited inks.	155
Table 14 Current peaks heights for 10 ng/mL protein quantification on the glass-substrate sensor.	157
Table 15 LOD obtained from the different conditions, considering different WE materials and printing methods.	159
Table 16 Printing process parameters.	166
Table 17 Thickness and sections of deposited inks.	172
Table 18 Current values and standard deviation for each platform and different concentrations.	175

1. Background

1.1 *Motivations*

In recent years, Industry 4.0 (I4.0) paradigms have started a transformation process of the traditional manufacturing systems into smart factories thanks to a series of innovations and technologies able to connect objects, machines, tools and workers. Smart factories focus on flexibility, quality, efficiency and predictability of the production through the adoption of enabling technologies, such as Big Data, Internet of Things (IoT), Additive Manufacturing (AM), and Cloud Computing [1]. Big Data and Machine Learning (ML) allow to manage a large amount of real-time data generated in the smart factory and to support decisions on the industrial processes for improving productivity; this contributes to reduce costs [1] and operators workload [2], and to speed up the decision process and improve the production [3], [4].

In a smart factory, traditional machines become context-aware devices [5], and the environment is enriched with networked sensors (indoor positioning systems, cameras, etc.) to enable the interaction with operators [6]. Therefore, measuring different physical quantities (temperature, humidity, vibrations, mechanical deformations, angular velocity, etc.) that can affect the production process is essential for I4.0 to improve the quality of the final product [7] and the safety of the workers. Industrial IoT (IIoT), a network of intelligent industrial smart objects and devices, contributes to achieve a high production rate with limited operational costs and efficient control of processes, assets and operational time through real-time monitoring [8]. A new class of devices called “smart objects” contributes to control not only the smart factory but also the external environment. In this scenario, traditional tools and objects involved in the industrial processes are equipped with sensors, electronics and proper communication protocols to sense and measure, collect and exchange data with other devices or users, who can remotely supervise the industrial systems through existing networks. For example, in [9] a safety helmet for the mining industry was made smart by the integration of off-the-shelf sensors and electronics on the helmet. The smart helmet was designed to monitor climate changes and hazardous events (temperature, humidity, gas, removal helmet of the miner) and alert the room center. Besides the advantages, bulk electronics significantly affected comfort and usage.

All these concepts can also be transferred to other areas, not necessarily inherent only to the industrial production. Real-time monitoring measuring different physical quantities can be important in the industrial environment; it can cover areas such as transportation and packaging of goods, laboratory analysis, and wearable devices. Any aspect of daily life can benefit and be affected by this new concept. To pursue this kind of change, technological advances are required to make conventional objects “smart” [10]. The three key features that define an object as smart are: autonomy, intended as the ability to perform an activity or a specific task independently without the need for continuous interaction with the user; connectivity, defined as the possibility of connecting to a network of any type and size with the main purpose of exchanging information with other devices and, finally, context-awareness intended as the ability of the device to obtain information about the context to which they belong using specific sensors also to perform actions independently [10].

In light of this, a smart object is an object that preserves the function for which it was designed, and it can perceive changes in specific physical quantities (temperature, humidity, mechanical deformations, *etc.*) through its sensors and to elaborate information starting from sensor measurements. The elaborated information can be used by the smart object to make decisions autonomously or can be sent to other objects, devices, or users [3]. The shared data can be delivered to the cloud server, and data mining and machine learning algorithms can exploit this information to perform diagnosis, optimize and reconfigure intelligent product lines [11], [12]. A typical smart object can exchange data wirelessly and no cabled lines (for example main power supply) are required to supply the electronics. Therefore no cables and wires run across the factory/environment supplying or communicating with the smart object.

According to their architecture, smart objects can be classified into active or passive smart objects.

Active smart objects require an internal energy source to supply its electronics, while passive smart objects use passive elements to be interrogated wirelessly by an external readout unit.

A typical block diagram of an active smart object is shown in Fig. 1a. It contains:

- Sensor(s): one or more sensing elements react to specific changes.

- Sensor interface: analog and digital circuits read and pre-elaborate the sensor output.
- Processing unit: a microcontroller (MCU) or other programmable chip solutions transform the sensor measurement into a piece of digital information ready to be stored or shared over the network. The processing unit can make decisions according to its internal status and the sensor output, it sends or stores information autonomously as well as it can interact with other objects, devices and users if a user interface is implemented on the smart object.
- Wireless transceiver: this block includes an antenna and the protocol to communicate with the network through the gateway. The Cloud/Internet block connects smart objects, devices, users, and allows to access and store data.
- Power Unit: this block includes an internal power supply (battery, energy storage unit, *etc.*) and the power management unit to store, control and distribute the electrical power to the electronic parts. Energy harvesting is a valid alternative to batteries, reducing maintenance issues related to the battery replacement, sometimes without compromising the final weight and exploiting wasted energy present in the environment (thermal energy, kinetic energy, solar power, *etc.*) [13]. Despite the small levels of power in the nW-mW range [14], the power harvesting system can be properly designed to support smart objects, considering that low power consumption is one of the main requirements of smart objects.

Smart objects can transfer data, communicate with other devices connected to the same network through various protocols/technologies such as cellular technology (GSM/3G/4G) [15], WiFi [16], Bluetooth Low Energy (BLE) [17] and ZigBee [18].

Passive smart objects may represent a viable solution when the measurement elaboration should be demanded externally due to application constraints. The object is equipped with a passive sensor and other passive components, and it requires an external readout unit for the acquisition and the processing of the sensor measurements. The typical block diagram of a passive smart object is depicted in Fig. 1b. The smart object measures the changes in a specific physical quantity and the readout unit acquires these measurements and performs other tasks like the active smart object. This particular telemetric system uses passive wireless communication, exploiting an electric-magnetic [19], optic or acoustic link [20]. For example, in [19] the resistance of a temperature sensor was read by using two inductors, one connected to the sensor and the other to the readout unit. The resistance change of the

temperature sensor induces a change in the impedance of the inductor of the readout unit. This type of telemetric system does not require any battery or power supply for the passive smart object, which can be placed easily inside a harsh or hermetic environment, but the distance between the two inductors has to be lower than few centimeters. In the case of the telemetric device, the readout unit also acts as a bridge between the passive device and the factory network.

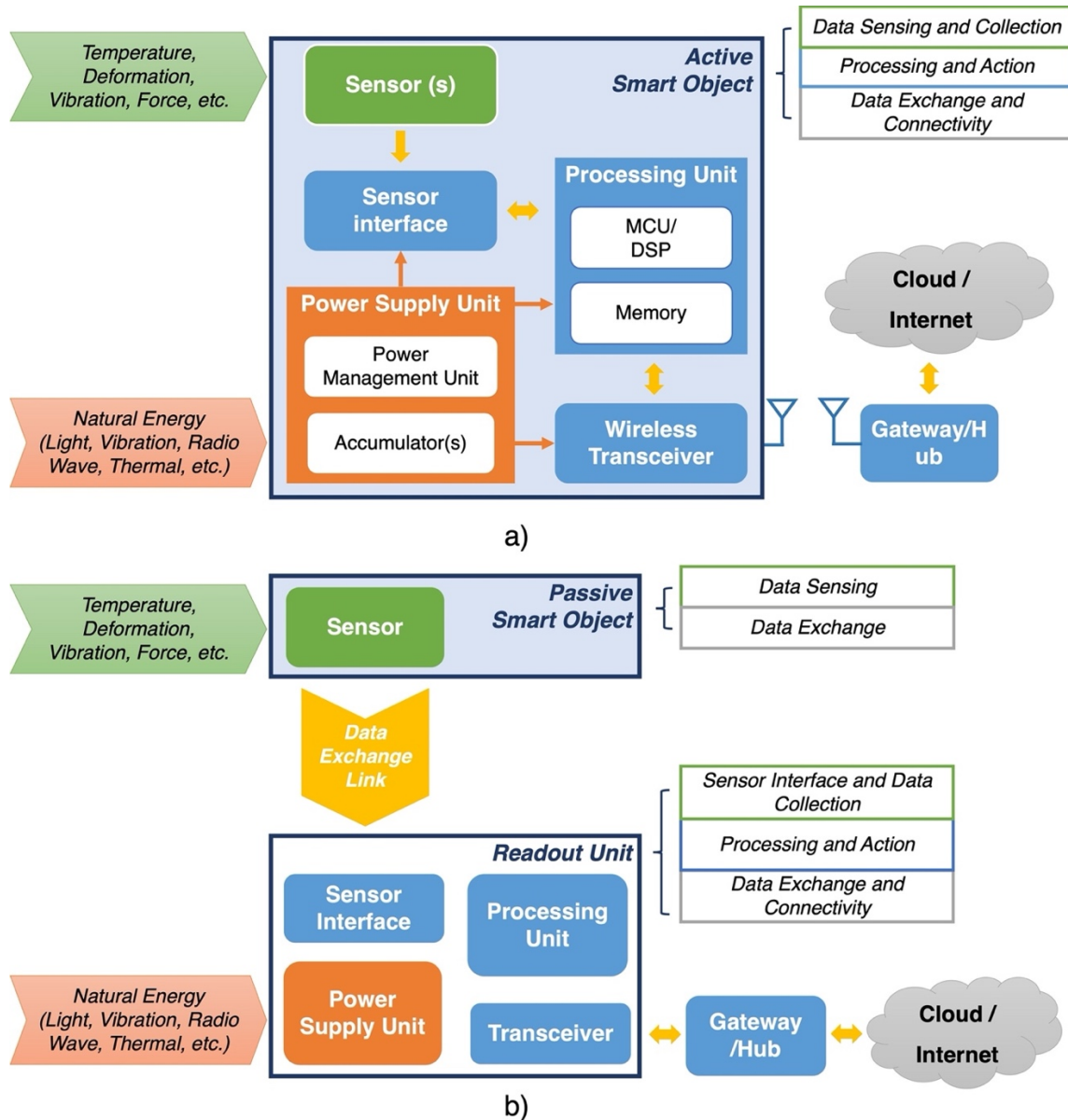


Fig. 1 Architectures of (a) active and (b) passive smart objects. The smart object is equipped with sensors that detect changes in physical quantities like temperature, deformation, vibration, etc. In the case of active smart objects, electronics acquires, processes and exchanges data with the network, while in the case of passive objects, an external readout unit acquires the sensor output wirelessly. The power supply unit can include 1) batteries, accumulator or systems that convert other natural energies into electrical energy and 2) a power management unit that controls and distributes the power supply (orange arrow) to the other blocks.

Printed electronics (PE) offers innovative technologies to make conventional objects “smart” by fabricating new sensors and electronics according to the specific context and application.

PE is also attractive for low production costs, flexibility in the design and a high variety of materials. For example, printed sensors on flexible surfaces could be intended for harsh environments (extreme temperatures, corrosive or hazardous substances, etc.) [21] or to be mounted on the challenging area due to the size of the components involved. Furthermore, PE includes technologies able to fabricate electronics directly onto objects, without installation, assembly or any surface modification (cleaning, scratching, gluing, etc.). This capability to manufacture fully-functioning sensors and circuits on 3D objects, without any kind of dimensional changing, will afford unprecedented scalability, miniaturization, and conformability (with great attention to materials compatibility), increasing the functionality of new products [22]. Finally, PE can be easily integrated into the process flow of additive manufacturing technologies to produce smart prototypes and objects [23]. Indeed, Additive Manufacturing (AM), known as 3D printing, includes promising technologies to quickly produce aids, functional prototypes and even items not available on the market [24], and PE makes these products “smart” by fabricating sensors and electronics for them.

1.2 Thesis Outline

The activities described and discussed in this work will focus on design, manufacturing and testing of smart sensors and objects realized thank to PE technologies, thus validating for their realization the proposed methodologies made up of these technologies. After defining the work context and capabilities provided by PE, an extensive analysis of PE technologies will be provided. This section will consider only printing technologies that allow the realization of custom patterns on each type of surface, deepening their functional principles, advantages and disadvantages. This part will be followed by chapter dedicated to the explanation of the technologies used in this thesis work. The demonstration of the possibilities of customization and miniaturization offered by PE will be highlighted in two major application areas. On one side, the realization of sensors and circuits for smart objects will be discussed, even with the development of a printed antenna to measure resistive sensors and to communicate the acquired information, and on the other side, the production of devices for wet laboratory applications will be considered. In details, the first macro-area will be divided into two groups: wearable smart objects and smart sensors and objects in packaging sector. The laboratory macro-area will include two subgroups: cells-related sensing and lab-on-a-chip objects.

2. Analysis of Printed Electronics Technologies

The invention of the first AM technique coincided with the filing of the patent US4575330A: “Apparatus for production of three-dimensional objects by stereolithography” [25] by Charles W. Hull in 1984. The author describes the lithographic process for the realization of objects starting from their three-dimensional model. The technique defined “additive manufacturing” involves the realization of an object by overlapping successive sections of it starting with nothing. It is defined *additive* as opposed to the classic techniques of *subtractive* manufacturing, in which starting from a solid block, the desired object is constructed by removing material. In the following decades, AM techniques have been improved and their accessibility is increased [26]. The development and study of new materials suitable or adapted for 3D deposition allows the fabrication of objects with specific mechanical and electrical properties (4d printing [27]). The availability of deposable material with known electrical properties permits to integrate sensors, electronics and conductive tracks directly during the production stage of objects. In this way, it is possible to directly fabricate “smart objects” in which electronics is not simply applied to an existing element, but it is directly embedded in it.

Some PE technologies provide different solutions in the realization of sensors, circuits, antennas, and interconnections directly on the surface of devices, thus turning any object into a smart one [28]. Low production costs, high variety of materials, flexibility are only few examples of advantages provided by PE technologies respect to conventional electronics production techniques [29]. A remarkable aspect is that different 3D-PE technologies are emerging, thus permitting to enter in a new design era in which an object can be conceptualized and realized simultaneously in all its parts in a single all-encompassing production step. The availability of data measured in the field environment will allow deeper testing phase in the application field. Consequently, it will be possible to obtain data directly from the use on the field, enabling assistance of the user and information for the design of new products. At the same time the smart object is also able to exchange data with nearby devices, and in a more complete view with specific servers, inserting itself in a collaborative scenario in which the attributed function is coordinated and improved remotely by exploiting the real-time monitoring capabilities of the object [30].

2.1 *Printing Techniques and Their Characteristics*

Here, the main printing technologies that are suitable for the fabrication of sensors, circuits, interconnections, and antennas are explained. Objects are characterized by many different shapes, and the ability to print on more or less complex 3D surfaces is essential. Respect to roll-to-roll technologies characterized by a huge production volume, by a reduced customization of the patterns, and by the usage of flexible substrates, research has shifted to technologies promising in the field of objects functionalization. These are more suitable for printing on mostly flat surfaces, covering wider spaces and with the possibility to simultaneously print multiple patterns. Furthermore, some technologies can take advantage of five-axis systems, thus being suitable for 3D applications of complex patterns. This aspect relates directly to the distance between the nozzle and substrate during the printing process that in some technologies, even if defined as contactless, show extremely small distances (micrometer scale). In light of this, the two criteria used to select the technology potentially exploitable to smart sensors and object fabrication are: the digitalization of the printed pattern, allowing to selectively print the functional material, and the possibility of material selective deposition on non-planar surfaces.

The selected printing technologies are: Microdispensing, Piezojet, Ink Jet Printing, Plasmadust, and Laser Induced Forward Transfer.

- Microdispensing is the technique of producing liquid dispensing in volumes smaller than a microliter. A droplet is formed at the exit of a nozzle and deposited by contact while the droplet is still on the nozzle. The system consists of a reservoir with a piston driven by compressed air to control the release of material to achieve the desired pattern. The flow control, through which the single drop is formed, takes place thanks to two key elements of the print head: the nozzle and the control valve. The nozzle is characterized according to the diameter and determines the geometric characteristics of the deposited drop. The amount of liquid is managed via the flow control mechanism. There are several ways to control this parameter. The two most used are by means of a solenoid valve or the control by piezoelectric elements. Solenoid valve control is normally used in cases where the volume of liquid to be deposited per drop falls within the range [100 - 1000 nL] [31]. The flow control is obtained by opening of the valve that permits the leakage of the liquid maintained under pressure. The amount of liquid coming out from the nozzle is function of the pressure and the

time for which the valve remains open. Due to the inertia of the mechanical elements, the time required to obtain the exchange of the valve position is around the 1-20 ms [32]. Flow control by piezoelectric elements allows the deposition of a volume of liquid, per single drop, in the range 0.5 - 100 nl. The minimum pressure needed to cause the leakage of the single drop is obtained deforming a thin-walled tube, a capillary wrapped by a piezoelectric element [33]. The reduced inertia of this system permits to obtain response times of approximately 100 μ s. In this way, the ejection system is not in contact with the piezoelectric elements facilitating the cleaning of the capillary in case of change of deposited material. Fig. 2 represent the schematic deposition principle of the technology. Thanks to the pneumatic system that characterizes it, microdispensing is able to process high viscosity functional materials that can be defined as pastes, being characterized by viscosity range of 50-1000000 cP. This latter aspect facilitates the deposition on 3D surfaces of various shapes, despite the fact that it is a contact printing technique [34], [35].

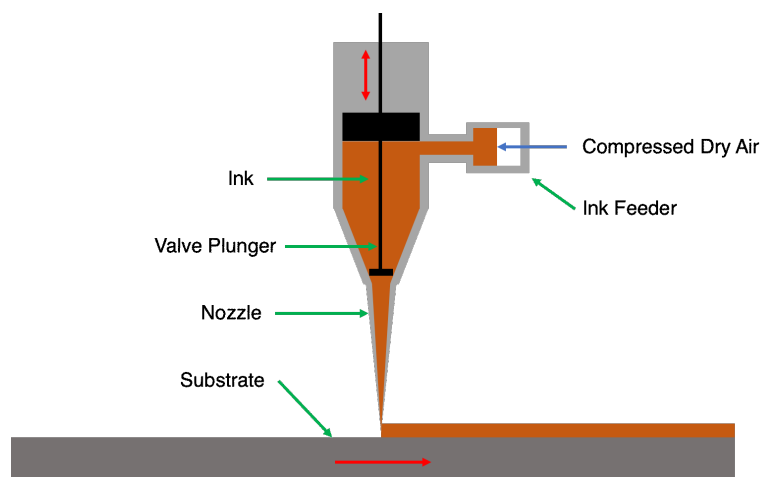


Fig. 2 Microdispensing physical functioning principle.

- Piezostack-driven jetting deposition, or Piezojet, is a printing method that allows producing patterns by the usage of conductive paste and inks from few to hundreds of thousands of cP. Belonging on the drop-on-demand printing family, the basic action is realized by a piezo-driven tappet, which generates droplets by pressing the ink through the orifice of the nozzle. In such a way, the droplets are delivered toward the substrate. The basic mechanism is based on four subsequent stages. Considering Fig. 3, at the beginning, the piezoelectric stack is powered on and the needle and the nozzle are in close contact preventing unwanted ink exit. When the signal is generated, the needle raises up and separates from the nozzle. Once the

piezoelectric stack is powered off, the needle falls in the starting position under an applied electric field and thanks to the pressure generated during such a movement, ink ejection is performed. Typically, these four phases are a 10 ms long time interval [36]–[39]. A great advantage of this technique is the possibility to work at higher nozzle-substrate distances thanks to the high level of kinetic energy of the droplets. respect to other technologies that focuses a stream of particles. The usage of a piston let Piezojet being able to process high viscous inks and pastes. This allows therefore to print on complex and 3D surfaces without incurring the risk of dispersing functional material in the printing area [40], [41]. Once more, a heater is installed in the proximity of the print head to adapt the viscosity of the functional ink by adjusting the ink’s temperature. This aspect is mandatory to enlarge the number of functional materials that can be used, like screen printing pastes [37], [42]. The working frequency and the accuracy of the jetting amount can be defined as two indices of the performance of the technology. Accuracy is mandatory to improve product quality and indicates how close the number of jetted dots is to the target amount. High frequency is necessary not only for productivity, but also to elaborate high density/surface tension inks [42].

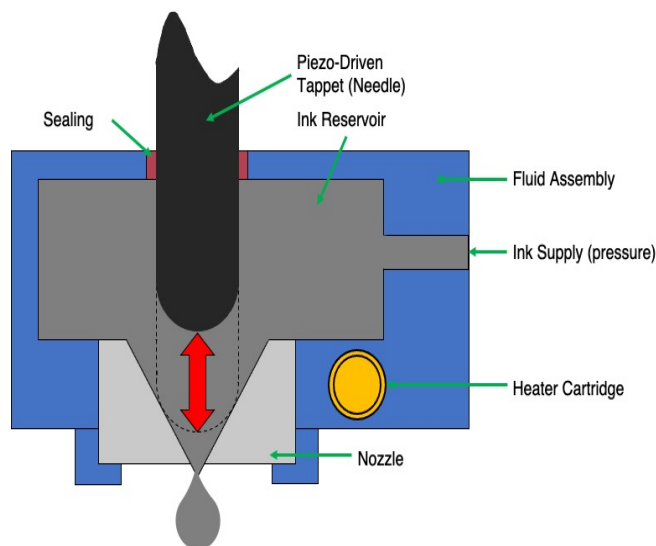


Fig. 3 Piezojet physical functioning principle.

- Inkjet printing (IJP) is a digital writing technique currently used also to fabricate printed electronics [43]. Inkjet technology, in its various forms, is one of the most widespread thanks also to its greater accessibility compared to other techniques. Despite its not recent beginnings, the scientific interest in this technology is still considerable [44]. The functional material in liquid state is transformed in small

droplets that are then deposited onto the substrate in a controlled manner, according to the Computer Aided Design (CAD) file. It guarantees reduced ink waste and prevents cross-contamination of the surface. Furthermore, the minimum variation of the droplet size ensures high reproducibility in the droplet production. Fig. 4 represents the schematic deposition principle of the technology. The inkjet printers are divided into two families: continuous inkjet (CIJ) and drop-on-demand (DOD) inkjet. In the CIJ printers, the printhead generates, electrically charges and ejects droplets continuously, while an electric field directs the charged droplet towards the substrate when it is required. The unused droplets are collected in a tank to be re-used. In DOD printers, the droplets are generated in the printhead and are forced out from the nozzles when it is required. Droplets can be generated by means of two distinct main methods: thermal or piezoelectric. In the thermal DOD the heat is produced inside the ink chamber for the vaporization of the ink, while in the piezoelectric DOD a piezoelectric actuator generates the pressure pulse in the fluid to force out the droplets from the nozzle. The piezoelectric DOD is the most used because the volume and the speed of the droplet can be better controlled [45]. In piezoelectric and thermal DOD printers, a high pressure is needed to propel the droplet through the nozzle. A further, type of inkjet technology is the electrohydrodynamic jet printing (EHD) in which a high-voltage (0.5 – 20 kV) is applied between the nozzle and the substrate [45], this generates an electric field that causes a droplets ejection when the electrostatic force overcome the solution surface tension. The two parameters that affect the volume deposited are mainly the geometry of the nozzle and the viscosity of the deposited material. In addition, in systems where the flow control is obtained by means of a solenoid valve, also intervene the pressure imposed to the material and the characteristics of the valve. The fluctuation of one or more of these parameters can lead to the deposition of an unexpected volume. To achieve good repeatability and therefore good throughput, closed-loop systems were proposed for controlling process parameters [46]–[49].

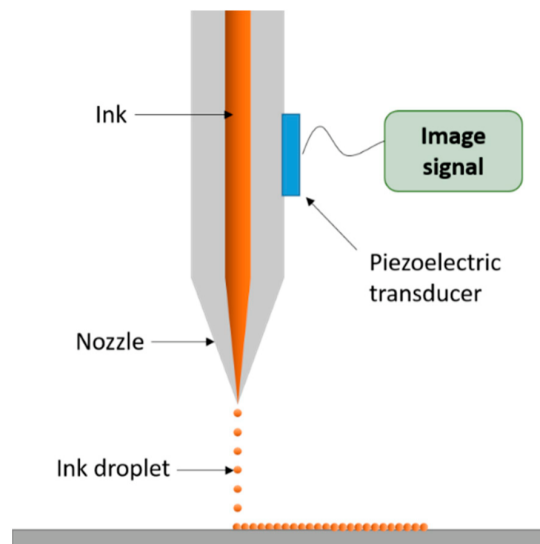


Fig. 4 Inkjet physical functioning principle.

- Plasmadust technology belongs to thermal spray family, and it also known as Cold Active Atmospheric Plasma Deposition (CAAPD). It offers the possibility to perform a direct metallization on thermoplastics thanks to a one-step process. Main components of the systems are the feeding block, responsible to carry powders (200 nm to 20 μ m in diameter) in presence of plasma; this element is typically accompanied by an exhaustion pipe dedicated to collect unused material. The second element is the plasma nozzle, composed by an internal element, the cathode in which the forming gas fluxes, and an external element, an anode. Plasmadust sees the generation of plasma thanks to the presence of a forming gas (e.g., nitrogen) in contact with electric arc. By applying a high-frequency current, a high-energy pulsed arc is generated between cathode and anode, ionizing the process gas and transforming it into a low temperature plasma. In the meanwhile, the feeding system transports functional powders close to the nozzle and part of gas energy is transferred to the particles. In such a way, the latter are melted and directed toward the substrate realizing patterns without any use of solvent to activate the functional material. Fig. 5 resumes the deposition process here described [50], [51]. Several beneficial aspects can be underlined considering this kind of PE process. First of all, respect to other thermal spray technics each step of the manufacture is realized under atmospheric pressure, avoiding any request of vacuum instrumentations and/or close chambers. Furthermore, if compared to other plasma processes, the usage of a pulsed plasma allows to work at temperature < 200 $^{\circ}$ C, with a lower power supply requested level,

implying lower wear for the nozzle. At the same time, the low process temperature permits to work in presence of low melting point substrates like plastics [51], [52].

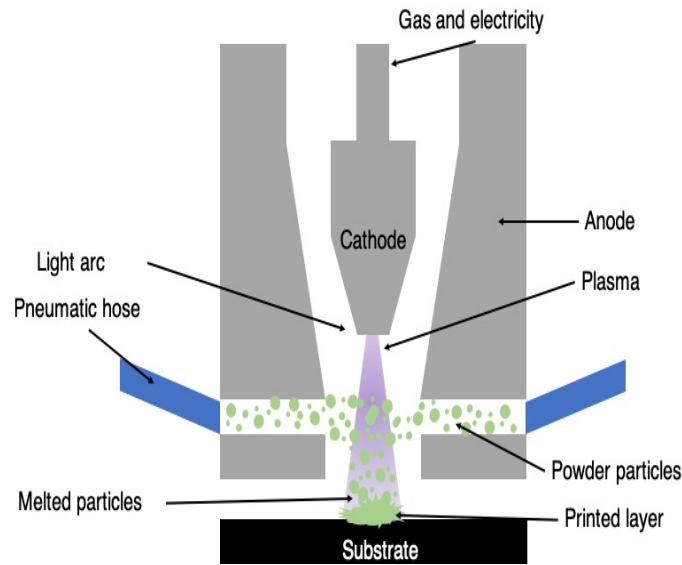


Fig. 5 Plasmadust physical functioning principle.

- Laser Induced Forward Transfer (LIFT) is a direct-write digital printing technology based on laser ablation, thus completely differing to the previously considered techniques. LIFT can be thought of as a group of printing methods that employ a pulsed laser energy source to produce specific patterns on substrates placed in close proximity to the laser [53]. Fundamental actors of the process are the laser energy source, the material that will be deposited and the substrate that will receive the latter. Before carrying out the actual deposition process, a laser-transparent substrate is prepared and coated with the selected functional material. This element is what is called the donor, in contrast the substrate on which the designed traces will be located is called the receiver. In the printing phase, a pulsed laser beam is generated and focused through specific lenses on the surface of the donor. Depending on the type of functional material deposited and its state, a threshold value is reached at which the donor film starts to deform itself. The irradiated material is accelerated towards the receiver on which it will collapse, depositing the previously heated functional material forming the desired pattern [54]. In Fig. 6 it can be found a schematic representation of LIFT deposition process. Different positive aspects distinguish LIFT from the other technologies considered in this chapter. First of all, it is solvent-free printing method that works in ambient conditions (no high temperature or vacuum chamber required), aspects that facilitates the process [55]. In addition, LIFT is a nozzle-free printing system so that any kind of clogging problem is totally

avoided. In fact, the focusing here is related to an energy source and not the functional material which is outside the “working part” of the printing machine [56]. A second key element is related to the unnecessarily post-treatments that are usually associated to other PE technologies. In LIFT, the functional material is molten and then solidifies once in contact with the receiving substrate. This aspect could be critical, especially thinking in relation to some low temperature substrates such as paper or plastic. However, the droplets that are created have a very low mass and therefore, despite the high temperature reached when hit by the laser, they do not damage the receiving substrate. Once more, LIFT printing allows the realization of 3D complex structures thanks to a layer-by-layer deposition [57]. As previously stated, this is a digital technique, thus without the need to use masks to print features because the size of the track is determined by the width of the laser spot. Another advantage is related to contactless nature of the printing principle which typically presents a gap between donor and receiving substrate from tens to hundreds of micrometers. Millimetric gaps are also possible [54], [58]. LIFT technology works with different kind of functional materials with wide viscosity range, from fractions of Pa·s to several hundreds of Pa·s. This is a key aspect when considering the final properties of printed elements, since it implies a change in dimension of particles inside the ink, thus increasing the current-carrying capacity. Printing high viscosity pastes, it is possible for the printed voxel to match congruently the illuminating laser pulse: this situation is usually defined congruent LIFT or laser decal transfer (LDT). The great advantage that comes with this approach is that voxel shape and size become controllable parameters [54], [56], [59].

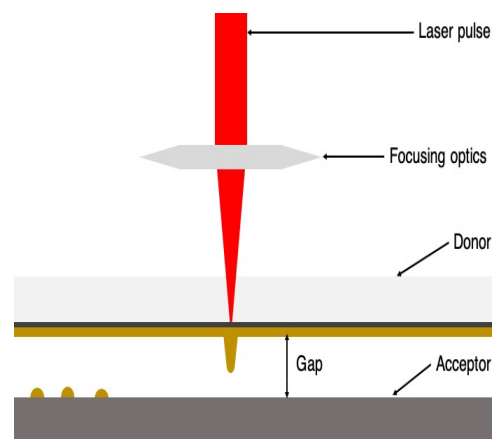


Fig. 6 Laser Induced Forward Transfer physical functioning principle.

3. Methods

Compared to the technologies that have been analyzed in the previous chapter, there is one that thanks to its characteristics can find great applicability in various areas. This is Aerosol Jet Printing (AJP), a PE technology that belongs to the family of material jetting in which small quantities of a functional material with specific viscosity are generated and sprayed on a substrate to obtain the designed pattern. After printing the pattern, PE requires heat treatment to consolidate the material and allow it to reach its final performance. To be able to process any kind of substrate, including those with low ignition point, advanced technologies are required that affect few layers of material without affecting the structure of the object undergoing the heat treatment. This is the case of Flash Lamp Annealing (FLA), a low thermal impact annealing process.

The features and mechanism of operation of the abovementioned technologies will be discussed in detail in this chapter, considering the physics behind them, influencing factors and usable materials. Applications of two technologies involved will be described from Chapter 4.

3.1 Aerosol Jet Printing

3.1.1 Introduction to AJP

AJP is a material jetting additive manufacturing technique. This technology was developed by Optomec under the Defense Advanced Research Projects Agency (DARPA) Mesoscopic Integrated Conformal Electronics (MICE) program, overcomes some of typical printing electronics defects like nozzles clogging, coffee-ring effect of droplets, limited inks viscosity. One of AJP's strongest advantages is the possibility to selectively print not only on planar substrates, but also on 3D complex surfaces. The most of printed technologies relies on techniques that allow exclusively depositing inks on planar surfaces, thus limiting the possibility to implement sensors and circuits on ready-to-use objects. On the other side, AJP lets the functionalization of complex objects with multiple nozzles, printing at the same time different materials, and 5-axis configuration. AJP consists in an aerodynamic focusing process of liquid particles that are accurately deposited onto different kind of substrates placed under the exit nozzle. The technique can also be addressed as maskless mesoscale material deposition underlining two specific advantages of this technique: the uselessness

of masks and post-treatment to obtain the designed feature, and the small dimensions of printed droplets allowing reducing material consumption [60].

To achieve the aerosol necessary to print, two possible routes can be followed: Pneumatic atomization (PA) or ultrasonic atomization (UA). In the first case, inks in the viscosity range 1 – 1000 cP can be used. Four consecutive stages compose the printing process and starts setting the pressures responsible of aerosol stream generation. A carrier gas (nitrogen or compressed dry air) is used to excite the functional ink to be deposited, which is a liquid dispersion. Thanks to a virtual impactor placed right after the atomizing block, superfluous carrier gas is removed, and droplets dimensions adjusted (smaller than 5 μm in diameter). After these two steps, the aerosol is focused inside the print head surrounded by a cylindrical sheath gas flow (one of the process parameters) which prevents possible droplets impacts. Increasing the sheath gas flow additionally, the aerosol diameter can be reduced. The whole complex is accelerated entering the printing nozzle and the droplets impact the substrate, heated in case of need, to realize a drying step during printing and/or to evaporate solvents. Fig. 7 shows this process. In case of UA, the aerosol is generated starting from a lower working volume, typically not above 2 ml, and the functional ink is characterized by a viscosity not exceeding 10 cP. A piezoelectric transducer is placed inside a medium, usually water, oscillating at high frequencies. In such a way, waves propagate reaching a glass vial inside the medium, above the transducer. The superposition of consecutive waves leads to large peaks, so that small droplets are ejected from bulk ink. A positive pressure helps driving the particles toward the substrate as seen in PA process. The big advantage in using this system compared to PA is the low dispersion of the flow, in fact no devices are required to select the particles that are part of the flow. Instead, this happens with PA, given the presence of the virtual impactor. The electrical current with which to excite the piezoelectric transducer is added in this configuration to the process parameters to be considered. In Fig. 8, it is depicted the functioning principle described above. The commercially available system prints traces from 10 μm to 3 mm in width, from 100 nm to 10 μm in thickness at translation speeds up to 10 - 12 mm/s [61]–[63]. This technology was successfully employed in applications such as high-efficiency solar and fuel cells, fully printed thin-film transistors, embedded resistors, antennas, MEMS, flexible displays and circuitry [64], photodetectors [65], wearable applications [66], [67], thermistors [68], microelectrodes arrays for biosensing applications [69], lab-on-chip devices [70], protein [71] and glucose sensing [72].

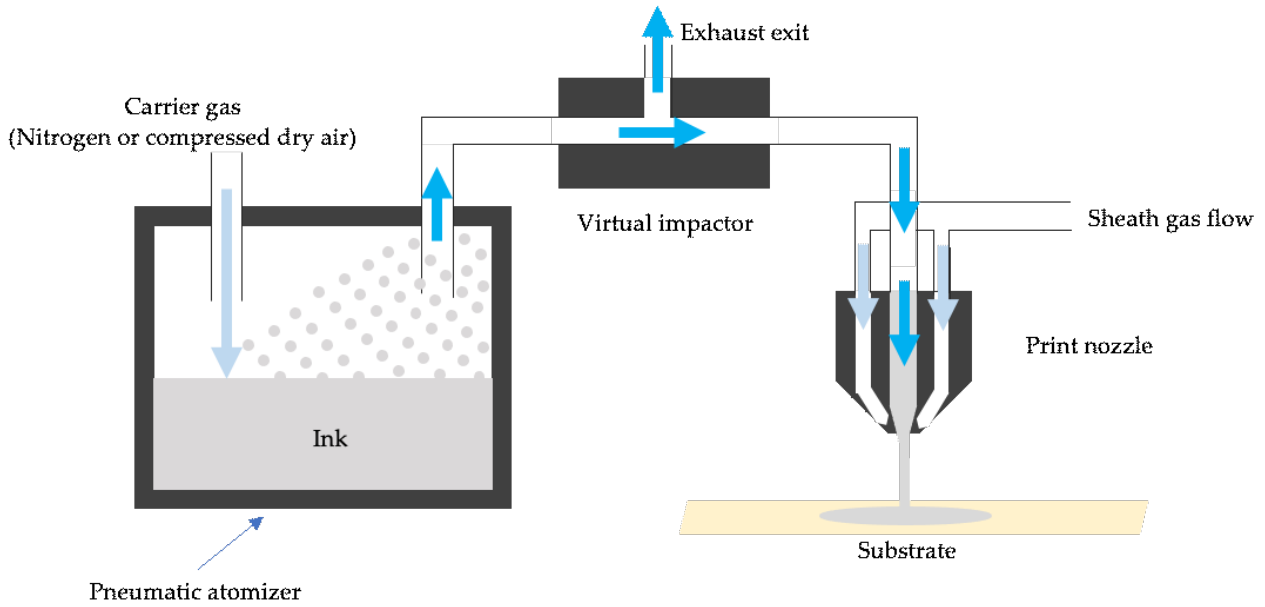


Fig. 7 Aerosol Jet Printing pneumatic atomization functioning principle.

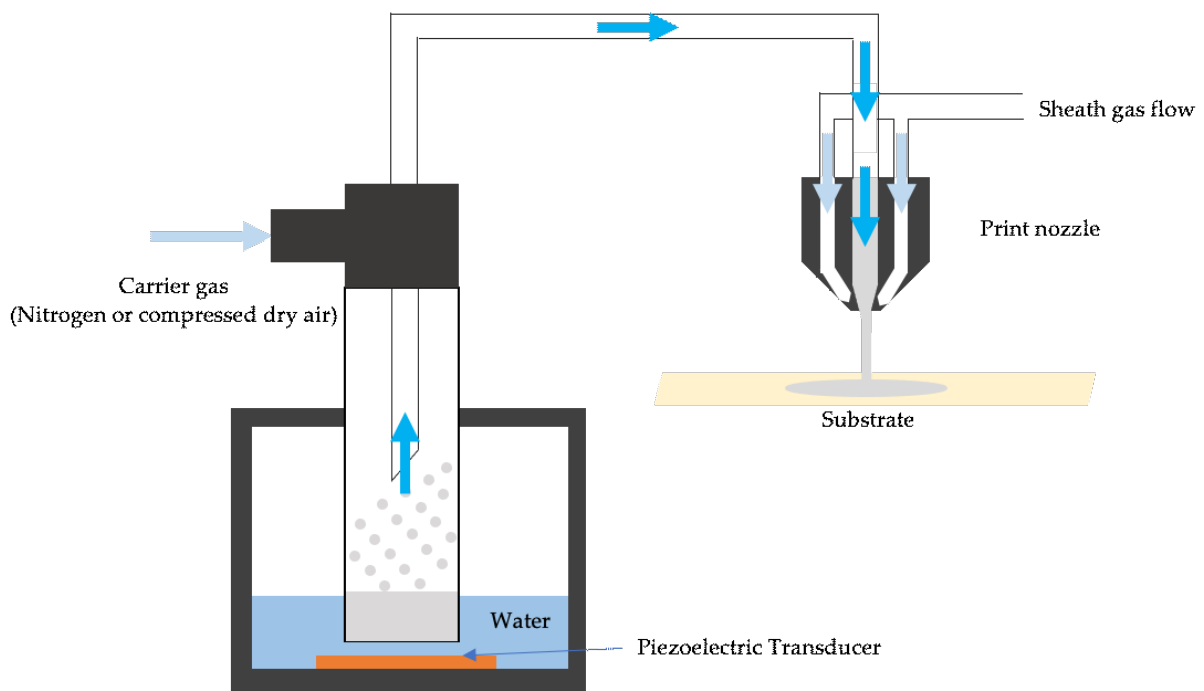


Fig. 8 Aerosol Jet Printing ultrasonic atomization functioning principle.

3.1.2 Factors affecting printing quality

In light of AJP's mechanism of operation, it can be seen that several factors affect print quality and consistency. Process parameters are clearly the primary factors responsible for determining the quality of the finish obtained during printing, and they are Sheath gas flow, Atomizer gas flow, Exhaust gas flow in case of PA, Maximum current in case of UA. With a view to having real-time information on the printing performance that is being achieved, such a control system would be necessary [73]. The viscosity of the inks clearly influences the

results that can be obtained during printing process. High viscosity materials present larger functional material particles inside, this allows the realization of higher thicknesses that lead to a higher current carrying capacity of the realized traces. At the same time, such high viscosities limit the realization of fine features that can otherwise be printed in case of low viscous materials allowing to miniaturize interconnections and circuits [74], [75]. Each ink used with a certain type of substrate requires optimization to achieve the desired dimensional values [63]. Similarly, the printing time is a determining factor in the overall quality of the process. This is the reason why time dependency was considered and studied [76]–[78]. Since one of the most troubleshooting aspect of AJP is process drift in case of long-term printing sessions, they optimized all parameters for two different Ag ink, then they started printing for a ten-hour long run. As evidenced, it is possible to find a worsening of the printing performance with a more or less widespread overspray, intended as droplets with a lack of inertia able to impact the center line of the aerosol flow. This aspect can be more critical in the presence of a large number of successive depositions and with close geometric finishes, for possible risks of short-circuiting elements that should otherwise be isolated [78]. In light of this, overspray has to be identified as an artefact of the printing process, thus its appearance can be seen as an index of print quality. This is the reason of the development of analytical models, aiming to minimize overspray and increase knowledge of the mechanism and interdependence of involved parameters [79]–[81]. Increased consistency is also due to the usage of the bubbler with the specific thinner of the ink in use. The high volatility of the solvent could be beneficial saturating the carrier gas, so that stable droplets are generated [78], [80]. Another aspect that must be analyzed is the effect of geometry to print consistency, but no significant variations can be found on the two principal geometrical features: line width and thickness. In conclusion, the machine apparatuses involved in the deposition can also have effects on the conclusive performance of the print. One example is the transport losses due to the tubes connecting the spray drying block to the printing head; these losses are related to non-linearities and tubes that are too long.

3.1.3 Process Physics

The physics of the aerosol-fluid interaction represents the fundamental step to understand, in order to improve deposition characteristics (i.e., focus, collimation, line width, reduced overspray) for all A-DW methods. In models dating back to Stokes' work in 1851, the

movement of aerosol particles can be explained by the following forces applied to Newton's 2nd law where force equals mass times acceleration as shown below [60]:

$$\frac{4}{3}\pi a^3 \rho_p \frac{d\mathbf{v}_p}{dt} = \sum \mathbf{F} \quad (1)$$

where a is the particle radius, ρ_p is the particle density, \mathbf{v}_p is the velocity vector of the particle, and $\sum \mathbf{F}$ is the sum of all forces acting on the aerosol particle. Among all the forces acting on a particle in a fluid, seven main ones are commonly used to model the fluid-particle interaction of aerosols:

$$\sum \mathbf{F} = \mathbf{F}_{St} + \mathbf{F}_{Ba} + \mathbf{F}_{Vm} + \mathbf{F}_{Ps} + \mathbf{F}_{Gr} + \mathbf{F}_{Ma} + \mathbf{F}_{Sa} \quad (2)$$

Considering the equation E.2, \mathbf{F}_{St} is Stokes force (steady viscous drag force), \mathbf{F}_{Ba} is Basset force (non-steady viscous drag force), \mathbf{F}_{Vm} is the virtual mass force (inertia of fluid surrounding particle added to particle), \mathbf{F}_{Ps} is the pressure gradient force, \mathbf{F}_{Gr} is the buoyancy force caused by gravity, \mathbf{F}_{Ma} is the Magnus lift force due to particle rotation, and \mathbf{F}_{Sa} is the Saffman lift force on a particle with local shear flow. It must be noted that other forces may act on aerosol particles in some circumstances (Brownian diffusion, thermophoresis, diffusiophoresis, photophoresis, electromagnetic radiation pressure, acoustic pressure, electrostatic, and van der Waals) [60].

Sir George Gabriel Stokes developed the first theoretical model for the forces acting on spherical aerosol particles in a viscous fluid under laminar flow conditions. Stokes solved the equations of motion (Navier-Stokes) for laminar flow around a cylinder and sphere and integrated the forces applied to the surface of the body. Stokes found the force on a particle, F_{St} :

$$\mathbf{F}_{St} = 6\pi a \mu_f (\mathbf{v} - \mathbf{v}_p) \quad (3)$$

where μ_f is the fluid viscosity and $(\mathbf{v} - \mathbf{v}_p)$ is the fluid velocity relative to the moving particle.

The Basset force is defined as:

$$\mathbf{F}_{Ba} = 6a^2 \sqrt{\pi \mu_f \rho_f} \int_0^t \left(\frac{d\mathbf{v}}{dt} - \frac{d\mathbf{v}_p}{dt} \right) \frac{d\tau}{\sqrt{t-\tau}} \quad (4)$$

where ρ_f is the density of the fluid. The virtual mass force, \mathbf{F}_{Vm} , is given by the following expression:

$$\mathbf{F}_{Vm} = -c_M \frac{\rho_f}{\rho_p} m \left(\frac{d\mathbf{v}}{dt} - \frac{d\mathbf{v}_p}{dt} \right) \quad (5)$$

where m is the mass of the particle and c_M is the added mass coefficient, which is equal to 0.5 for a sphere. The pressure gradient force, \mathbf{F}_{Ps} , due to the acceleration of the external flow past the particle, is calculated by the following equation:

$$\mathbf{F}_{Ps} = m \frac{\rho_f}{\rho_p} \frac{D\mathbf{v}}{Dt} \quad (6)$$

where D/Dt denotes the rate of change with time following a fluid particle, such that:

$$\frac{D\mathbf{v}}{Dt} = \frac{d\mathbf{v}}{dt} - [(\mathbf{v}_p - \mathbf{v}) \nabla] \mathbf{v} \quad (7)$$

The buoyancy force, \mathbf{F}_{Gr} , due to gravity is equal to:

$$\mathbf{F}_{Gr} = m \left(1 - \frac{\rho_f}{\rho_p} \right) \mathbf{g} \quad (8)$$

where \mathbf{g} is the acceleration vector due to gravity. Magnus force, \mathbf{F}_{Ma} , is present if the particle is in rotation with respect to the surrounding fluid and is given by:

$$\mathbf{F}_{Ma} = -\frac{3}{4} m \frac{\rho_f}{\rho_p} \left(\frac{1}{2} \boldsymbol{\omega} - \boldsymbol{\Omega} \right) \times (\mathbf{v}_p - \mathbf{v}) \quad (9)$$

where $\boldsymbol{\omega}$ is the vorticity of the fluid surrounding the particle and $\boldsymbol{\Omega}$ is the angular rate of rotation of the particle.

Saffman force, \mathbf{F}_{sa} , is a lift force applied to aerosol particles in a simple laminar shear flow (Poiseuille flow) and was developed by P. G. Saffman in 1965. The lift is proportional to the rate of shear and the magnitude of the relative velocity of the particle with respect to the fluid:

$$F_{Sa} = 6.46a^2(\mathbf{u} - \mathbf{u}_p) \sqrt{\rho_f \mu_f \left| \frac{\partial u}{\partial y} \right|} \text{sign} \left(\frac{\partial u}{\partial y} \right) e_y \quad (10)$$

where the value 6.46 is a constant from numerical integration determined in the addendum of Saffman, \mathbf{u} is the gas axial velocity component, and \mathbf{u}_p is the particle axial velocity component. The forces acting on the aerosol particles are important if they are appreciable as compared to Stokes force. For the analysis of aerosol particles of 0.5–5 μm , gravity force is not appreciable.

3.1.4 Functional inks

In light of the possibility to use employ two different atomizing principles, two viscosity ranges, 1-1000 cP in case of PA and 1-10 cP in case UA [62]. Generally speaking, as the viscosity increases, reaching values of a few hundred cP, the consistency becomes more and more pasty, until they become real pastes when they exceed thousands of cP. This aspect is closely related to the internal composition of inks/pastes which are made up of several components. The main parts can be summarized as:

- Nanoparticulate, the functional material that will go into making the conductive traces. This can be present in different forms (nanoparticles, nanoflakes, nanorods), in different weight percentages.
- Dispersant, which is the element that prevents agglomeration, precipitation and sedimentation of functional particles.
- Solvent, organic or water-based, takes care of distributing the various elements present in the material and evaporates immediately after the printing phase (in some cases a specific drying may be required).
- Surfactant, to adjust the surface tension and improve printability.
- Binder, to make sure that the different parts do not separate into distinct phases during the process [82].

The viscosity can then be directly associated with the versatility of the individual printing technique, thus allowing it to be used in a variety of applied fields. For example, AJP, depending on the needs, allows to work with a large number of materials such as conductive metals, semiconductors, insulators, various polymers, glues, graphene, carbon nanotubes, biological material (proteins, enzymes, glucose) [63], [64], [72], [83], [84]. It is also possible

to exploit pastes designed for other technologies and make them suitable for aerosol thanks to the use of appropriate solvents [72].

3.2 *Flash Lamp Annealing*

3.2.1 *Introduction*

In printing electronics, it is not possible to obtain a truly conductive material immediately after the printing phase, as there are several elements that do not contribute to the conduction of electrons. A similar consideration has to be done for semiconductors and insulating materials. Therefore, a pivotal role is played by the sintering process that allows to obtain two results. First, the organic additives are evaporated to leave only the functional material present in the printed traces. Secondly, the contribution of thermal energy allows the agglomeration of the particles that, once heated, collapse one on top of the other, thus going to form a network of particles thanks to a plasticization effect of the necks obtaining a unique path in which the electrons can flow [82]. The sintering process appears to be a delicate step in the realization of the desired patterns because, only with the appropriate heat input, it can achieve the elimination/minimization of voids in the printed material, necessary for the target performances. A low heat input does not allow the optimal conduction, just as an excessive heat input can lead to burns, ungluing and volumetric cracks along the selected geometries [85].

One of the most troubleshooting aspects in printing electronics relies in combining the sintering process with the usage of non-conventional materials, like plastics, fabrics, paper-based materials. It is impossible to perform a conventional heat treatment in oven which can cause irreparable damages until complete combustion [86], [87]. This technical challenge can be overcome with the usage of new kind of curing techniques, and Flash Lamp Annealing (FLA) belongs to this family (known also as Intense Pulsed Light, IPL). The samples to be annealed are placed in a closed chamber, a conveyor belt is responsible to move it where the thermal treatment takes place. Here, the principal actors are xenon flash lamps which generate the light pulse responsible of the process. Mirrors and reflectors help in reaching homogeneity of the light toward the substrate. To generate the light pulse, a dedicated circuit has to be considered and it is typically composed by a pulse forming network made of capacitors and coils which supply the flash lamps. In some cases, the capacitor bank voltage is sufficient to ignite the lamps, but in most cases a short high-voltage trigger pulse is needed. The latter must exceed the self-breakdown voltage of the lamp to

induce the ionization of the lamp gas. Once generated the voltage, lamps are crossed and the light pulse radiates energy toward the sample. Different configurations can be set before curing step, from single impulse to multiple impulse, the amount of crossing voltage basing on the materials involved and the time duration of the single impulse [88], [89]. The characteristics of the peak (shape, length, number) are determined by the time constant of the pulse forming network. A typical single pulse sees a faster rising and a slower falling edge but depending on the network more complex configurations can be achieved. The single impulse duration and energy density, thus lamp voltage, are the key factors responsible of the penetration of the light wave. The duration is approximated by the full width at half maximum, which mostly ranges between 0.1 and 20 ms, and the integral intensity of the pulse is given as the energy density of the light which hits the sample surface. The radiation spectrum ranges from the UV to IR light [89]. Fig. 9 presents a diagram explaining how FLA works. Several benefits are obtained, since the thermal process works in the sub-second range, producing minimal damage to low-temperature substrates and avoiding undesirable processes that may occur during a thermal treatment (i.e., diffusion) [88]–[90].

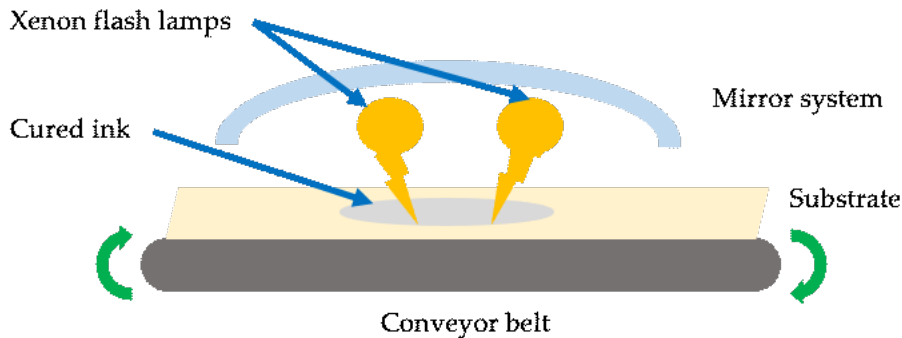


Fig. 9 Schematic representation of Flash Lamp Annealing.

3.2.2 Physics

This technology was designed following melting/sintering point depression in nanoparticles explained by Gibbs-Thompson equation:

$$T_M(d) = T_{MB} \left(1 - \frac{4\sigma_{SL}}{H_f \rho_s d} \right) \quad (11)$$

$T_M(d)$ indicates the depressed melting temperature of nanoparticles of diameter d , T_{MB} is bulk material melting temperature, σ_{SL} is the solid-liquid interface energy, H_f is the bulk heat of fusion, ρ_s is material density. In case of decreasing particles diameter (approximately below 50 nm), strong reductions in the processing temperature are observed. This aspect

provides several benefits, like thermal treating high temperature materials (metals, ceramics) on low-temperature substrates producing minimal damage since the process is in the sub-second range, avoiding undesirable processes like diffusion [90].

Considering the general conditions of PE, the basic principle of FLA relies in a thermal process performed on a film with thickness x_f with a thermal equilibration time τ_f , printed on a substrate with thickness x_s and thermal equilibration time τ_s . Each material is characterized by thermal conductivity (κ), specific heat capacity (c), and density (ρ). In light of this, it can be considered the following equation:

$$\tau_i = \frac{c_i \rho_i x_i^2}{4\kappa_i} \quad (12)$$

Looking at Fig. 10, it is worth considering that a light pulse of duration t_p heats the deposited film reaching a temperature T_{peak} , or beyond the maximum working temperature of the substrate T_{max} . Conduction allows to rapidly cool down the film, while the substrate adjacent to the film reaches a higher temperature respect to its maximum allowed one. Only for a restricted period of time this temperature is achieved, so that the substrate does not have enough time to deform and change its properties. This aspect is a key factor in let working with low-temperature point substrates and performing the whole process in few seconds. Three conditions can be identified to achieve an optimal process:

- $x_f \ll x_s$: film's thickness needs be much thinner than the substrate's one since the thermal mass of the substrate is responsible to cool down the thin film via conduction. If this does not happen, the processing temperature that can be reached without damage to the substrate is much lower.
- $t_p \ll \tau_s$: the peak temperature is reached quickly, long before the substrate mass can begin to heat up, so the thermal gradient in the substrate is not reduced thus exploiting it to achieve film cooling.
- $\tau_f \ll t_p$: a minimum amount of energy is necessary to heat the printed film, so an increasingly short pulse length dictates an increasingly high power. In case of fully dense film, this condition is always satisfied, but a printed film has a certain number of porosities. In light of this, τ_f is several orders of magnitude longer because of solvents and binders to evaporate [91].

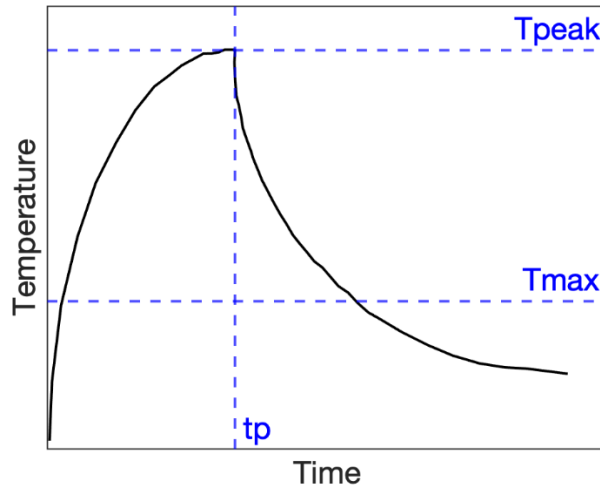


Fig. 10 Transient surface heating and subsequent relaxation of a thin film on a comparatively thick substrate.

The temperature distribution obtained during process can be determined by solving the following expression, the heat equation:

$$\frac{\partial}{\partial t}(\rho cT) = \nabla(\lambda_T \nabla T) + Q - S \quad (13)$$

Where ρ represents mass density, c is the specific heat capacity, λ_T is the thermal conductivity, Q is the inflow of energy and S is the outflow of energy due to dissipative processes. ρ , c , λ_T are location-dependent according to material's structure and time-dependent due to their temperature dependence [87], [89], [92], [93].

3.2.3 Substrates and inks

The possibilities offered by FLA in the field of the production of printed sensors allows to reach results not possible until now, starting from the materials used. The traditional thermal processes of sintering are carried out in a furnace (even vacuum) and this does not allow to process sensors, circuits and connections made on plastic substrates. Thanks to FLA, it is not only possible to involve these materials, but also to extend the range of substrates available in PE. Other than rigid substrates like glass, also polymer films like PET or Kapton were considered [94]–[96], 3D polymer substrates [97], sodium carboxymethyl cellulose [98], [99], paper-based materials like cardboard, print paper, photopaper and chromatographic paper [84], wood [99]. In addition to commonly used conductive inks (copper, silver based inks) [94], [96], functional zinc oxide inks have also been used successfully. This presents the interesting possibility of making bioresorbable conductive devices, the traces then being decomposable in water. This paved the way to a new branch of PE, transient electronics manufacturing [98], [100].

4. Introduction to applicative solutions

Nowadays one of the trend topics in sensor development is the possibility to realize them directly on 3D complex surfaces [30]. In the near future, this fact will allow manufacturing sensors and circuits embedded into objects, with the possibility to make them “smart” [101], [102]. On the other hand, the ecological aspect and the environmental impact of the materials used is of increasing importance, privileging the usage of support materials like paper-based ones or polymers [103], [104]. PE technologies have all the characteristics to be part of the ones that will change in the near future many areas of human life, thanks to the possibility to realize customized sensors and circuits on every surface and material. They can leverage on characteristics like flexibility, reduced production cost, variety of materials to be used, the capability to realize miniaturized custom sensors and circuits [21], [22].

In recent years, wearable devices have had great diffusion acquiring popularity among smart objects. Starting from the most widespread use of smart objects like smart watches and bands in fitness purposes, novel uses are emerging also in the areas of rehabilitation, patient assistance and medical practices. Real-time measure of muscular fatigue during physical exercises is highly demanded in both hospital and home-based rehabilitative and physiotherapy sessions [105]. The possibility to provide patients and medical personnel with feedback on the intensity of the muscular effort can help to improve the outcomes of each specific session, thus avoiding overload and preventing injuries [106], in particular for more fragile patients (chronic patients or elderly) [107], [108]. In addition, sensors can be implemented to not only monitor the health of the patient, but also the device itself. This could function as feedback to know if the instrument is being used correctly, remotely correct these errors, or know if in the most critical cases it is going to break down.

Together with the attention to health monitoring, also issues concerning environmental care and sustainability are becoming increasingly relevant in the design of new devices, so research is beginning to consider environmentally friendly materials as substrates materials. Among the materials that are getting more and more attention, a special mention goes to paper thanks to its ease of use, flexibility and lightweight. Paper substrates are made of multiple layers realizing an inner network of cellulose fibers, the principal component of the plant cell wall and the most abundant and widespread biopolymer. The reason of the interest

in paper materials is related to its unique combination of properties, like biodegradability, biocompatibility and renewability, thus reducing waste production, important aspects in an environmental-friendly manufacturing context [109]. Paper-based substrates show an intrinsic versatility since different kind of paper can be used as suitable materials depending on the application, from printer paper [110], [111], glossy brochure paper, newspaper, cardboard [112] to photopaper [113] and chromatographic paper [114]. Being a disposable material, paper-based sensors have proven their validity in studies of biological samples in laboratories, but they can show their usefulness in resource-limited situations thanks to low-cost, robustness and ease-of-disposal, simply burning the device in presence of biological samples avoiding sterilization [115], [116]. It is also possible to find their use in other sectors, like environmental monitoring, food and cosmetics industries [117], [118].

In chapter 5 and 6 of this dissertation, examples of devices realized on 3D surfaces will be presented, exploiting the potentialities made available by innovative technologies and methodologies. Specifically, it will be shown a prototype of orthosis for the rehabilitation of patients who need specific exercises for motor recovery. Electrodes for EMG were directly printed for a curved surface able to give more comfort to the patient. Next, the realization and characterization of a strain sensor made on a 3D plastic substrate will be explained. In chapter 6 the potential of PE in the production of electronics on paper will be investigated. The applications that will be proposed are specifically aimed at the food sector, which is increasingly moving towards this type of material to make food packaging. Three are the applications that will be discussed: a hybrid circuit made entirely of paper, an antenna to read passive sensors, then a sensor for ammonia detection inside food packaging.

The possibility to innovate biotechnological wet laboratory techniques represent an area of application in which smart objects can be interestingly exploited. Laboratory analyses in this field (e.g. cell count, analytes quantification) are usually carried out with standardized protocols, often time and cost expensive, with multiple deposition steps that can affect the repeatability of the outcome, depending on operators' experience and accuracy. In addition, most of those traditional techniques are invasive and thus prevent the possibility to perform a long-term monitoring. Finally, a limited customizability of the devices adopted for traditional assays are often limiting the possibility to improve sensitivity and specificity of the measurement using novel materials. In this light, the capabilities offered by the identified methodologies in term of cost-effectiveness, standardization, accuracy of the quantitative

results and non-invasiveness of long-term monitoring can help to improve traditional techniques exploiting smart devices and sensors.

Among the large variety of smart sensors that can find an application in wet laboratories, one of the most relevant application concern cell culture monitoring. Cell models are a useful tool for the scientific research community, and, among many others, Caco-2 cell line is being widely used as a model for different purposes, from the study of mechanisms underlying cancer development [119], toxicology [120] to the analysis of absorption and metabolism processes in food science, nutrition [121] and drug discovery [122]. Since scientific community needs an easy method to monitor the integrity and differentiation of cells in a non-invasive and non-destructive way, impedance-based monitoring appears to be a useful solution for different cell types, like Caco-2, human mesenchymal stromal cells (hMSCs) and many others. This non-invasive method can be applied to living cells and allows them to be monitored during growth and differentiation, since their morphological changes can be described by variations in impedance measurements [123]. The use of external sensors appears an acceptable compromise to integrate a suitable environment to study human cells with a minimally invasive sensing strategy. This solution can also be considered for the investigation of scaffold-based 3D cell cultures [124]–[126], a technology demonstrated to be fairly promising to monitor stem-cell proliferation and differentiation state when culturing stem-cell progeny, as in hMSC expansion [127]. Chapter 7 will focus on smart sensors made for the study of cells proliferation and differentiation, considering a flexible substrate and carbon miniaturized electrodes to perform impedance measurements.

At the same time, the sensitive quantification of specific biomolecules and analytes has a key role in medical, biotechnological and environmental research [128], [129]. Proteins, ions and biomolecules can give important information about patients' health and predict a pathology insurgence in time [130]–[132]. Similarly, the possibility to detect contaminants, specific ions or metals in drinkable water, beverages or food, when still in low concentration, might bring a significant improvement in term of food waste and of effects on human wealth [117], [133]. Several highly specific and sensitive analytical techniques have been used to detect target analytes in biological or environmental samples such as Enzyme-Linked Immunosorbent Assay (ELISA) [134], [135], Surface Plasmon Resonance (SPR) [136], Surface Enhanced Raman Scattering (SERS) [137] and high-performance liquid chromatography (HPLC) [138]. The disadvantages are the analysis high costs, the need of

expensive equipment and trained personnel [132]. In recent years, the demand for disposable biosensors with high sensitivity, low limit of detection (LOD), repeatability, miniaturization, and cost efficiency received increasing attention for early diagnosis and health monitoring [139]. Electrochemical Biosensors (EB) are good candidates for scalable production of point-of-care (PoC) disposable devices [132], [140], [141]. They are a feasible solution for analyzing the content of a biological fluid sample by directly converting a biological event into an electrical signal [142]. A promising path to overcome these issues is represented by printed electronics, allowing to manufacture totally customized sensors, with low costs and high resolution [143]. Chapter 8 will present two devices equipped with electrochemical sensors for the detection of specific analytes in liquid samples. In one case, it will be protein, in the second one glucose. The versatility offered by AJP in the second example has allowed not only the printing of functional materials for electrochemical sensors, but also to deposit the enzyme for the measurement of glucose and to microstructuring the surface of the substrate material thanks to a photopolymer to obtain a microfluidic circuit.

5. Wearable Smart Objects

5.1 *Printed Multi-EMG Electrodes on the 3D Surface of an Orthosis for Rehabilitation: a Feasibility Study*

Part of the research work reported in this section was published in IEEE Sensors Journal with the title *Printed Multi-EMG Electrodes on the 3D Surface of an Orthosis for Rehabilitation: a Feasibility Study* [66]. Part of the work reported in this section was presented in *2021 IEEE International Symposium on Medical Measurements and Applications (MeMeA)* and is part of the conference proceedings with the title *Preliminary Study of a Flexible Printed Multi-Sensing Platform for Electromyography and Lactate Measuring during Rehabilitation* [144]. Results and pictures are reported with permission of the editor.

5.1.1 *Introduction*

The countless advantages of wearable devices in terms of low cost, design flexibility, miniaturization and wide fields of applicability are pushing the research to investigate novel techniques to enable effective integration of sensors within smart and stand-alone devices that can improve the final users' life experience [145]–[148], also maintaining robustness, accuracy and repeatability required to improve the reliability of the data extracted from those devices [149].

Electromyographic (EMG) signal represents a highly investigated and discussed parameter, since the evaluation of EMG time and frequency content represents a valuable tool to provide feedback on the physio-pathological state of muscles and of its neuromuscular junction [150], to open the path to applications in the field of human-machine interfaces, but also to enable continuous monitoring of muscular progress during post-stroke recovery or rehabilitation [151], [152]. Focusing on home-based monitoring, the effective integration of EMG electrodes, of customized signal processing and transmission circuit directly onto wearable devices together is highly demanded. EMG implementation in orthoses or wearable devices could ensure effective long-term monitoring with higher repeatability and accuracy due to standardized positioning, improving rehabilitation outcomes without having to rely on bulky devices and avoiding following complex protocols, with the need of medical personnel. In such a context, exciting challenges are related to many issues to reach the diffusion of home-based wearable devices for rehabilitation: from improving user-

friendliness, ensuring accuracy, reliability and robustness as required for commercialization in non-controlled environments (e.g. hospital, homes) [147], passing through data transmission towards an external application, to detecting strategies to achieve a proper signal compression and feature classification to limit dissipated power, enabling the use of miniaturized batteries and [153]–[156]. Concluding, an essential requirement to be effective during rehabilitative tasks is the total unobtrusiveness of the equipment used to retrieve the signals, to leave the patient free to perform all the exercises without any impairment [157].

Considering this request, one of the most pressing requirements is to develop embedded customized electrodes directly on the surfaces of wearable devices, providing a ready-to-use personalized sensing device. Currently, most of the examples of electrodes integration with wearable devices show the usage of commercial EMG surface electrodes combined with an orthosis to model knee joints [158], to design a smart mechatronic orthosis [159], [160], to enable automatic recognition of terrain characteristics through an instrumented leg orthosis [161], to assess the effect of an exoskeleton [162]. None of the above examples present a fully integrated design.

In this framework, the purpose of this research was to develop a fully embedded EMG matrix with its conditioning electronics onto the 3D surface of a rehabilitation leg orthosis using AJP, aiming to pursue a totally innovative approach for making “smart” an already commercially available orthosis, with a personalized approach, depending on the specific target muscles, on patient anatomy and on rehabilitation requirements.

5.1.2 Device Fabrication and Characterization

a) Fabrication and integration of the electrodes with the wearable device

In order to set up the optimal printing and curing parameters to achieve suitable conductivity of the printed elements on the final orthosis, preliminary printing runs were performed on test samples. In detail, polypropylene (PP) samples with the same characteristics of the final orthoses in terms of material, diameter, and curvature were selected. The position of electrodes and tracks and their electrical connections were carefully designed to minimize skin-impedance and to limit invasiveness for the end-user. EMG electrodes were printed on the center of the inner (concave) surface, while tracks with pads on the outer (convex) surface of the concave samples, replicating the positioning of the EMG matrix and the electronics in the final orthosis. A proper electrical connection between each electrode and

its corresponding track was obtained by drilling 0.5 mm diameter openings on fiducial markers previously printed to evaluate the encumbrance area of the elements to be printed. Each hole was filled with conductive ink, the same material used to make the printed conductive tracks. Two consecutive depositions of silver ink were performed for tracks, pads and the first layer of each electrode, followed by two depositions of silver chloride ink only on the electrodes to ensure a better coupling with human skin.

The printed layout is shown in Fig. 11, while the positioning of the electrode matrix on the inner face and of the traces on the outer face of the device can be appreciated in Fig. 12. The position of the matrix was carefully set up to provide correct acquisitions of EMG signals of the gastrocnemius muscle, taking as reference the standard positioning of commercial pre-gelled Ag/AgCl electrodes during surface EMG recording of those muscles [163].

AJ 300 printer (Optomec, Albuquerque, New Mexico, USA) was the Aerosol Jet printer selected to realize our prototypes. Silver ink Metalon HPS 108-AE1 (Novacentrix, Austin, Texas, USA) is the selected conductive Ag ink to print tracks, pads and the first layer of each electrode. It is an aqueous suspension of silver flakes, specifically formulated for AJP, containing a polymeric additive to strengthen the adhesion to plastic substrates, thus avoiding the risk of detachment and improving long-term stability. Silver chloride ink (XA-3773) with Ag/AgCl weight proportion ratio of 8/2 was purchased by Fujikura Kasei. Co. Ltd. (Shibakouen Minato-ku, Tokyo, Japan) together with its thinner to realize the top layer of our electrodes. A dilution of the ink, with its specific thinner, was mandatory to obtain a proper viscosity for the printing stage (ink starting viscosity was 300 ± 50 dPa·s), following the equations reported in the literature regarding a two-component blend [164]. The ink was deposited at 23 °C with a viscosity of about 19.5 mPa·s [72].

Table 1 resumes the process parameters employed during the manufacturing phase. Ag deposition was followed by a one-hour-long curing step performed in an oven at 140 °C, while Ag/AgCl deposition was followed by a sintering step in the oven for 30 minutes at 125 °C. After the printing and sintering phase, corner connectors were glued to the supports in correspondence of the pads with a conductive silver epoxy (CW2400, Chemtronics) mixing the two parts in equal amounts and performing a curing step in the oven at 70°C for 20 minutes.

Table 1 Aerosol Jet Printer process parameters for employed inks.

Process parameters	Ag
Sheath gas flow (SCCM)	450
Atomizer gas flow (SCCM)	1150
Exhaust gas flow (SCCM)	1060
Plate temperature (°C)	30
Process speed (mm/s)	2

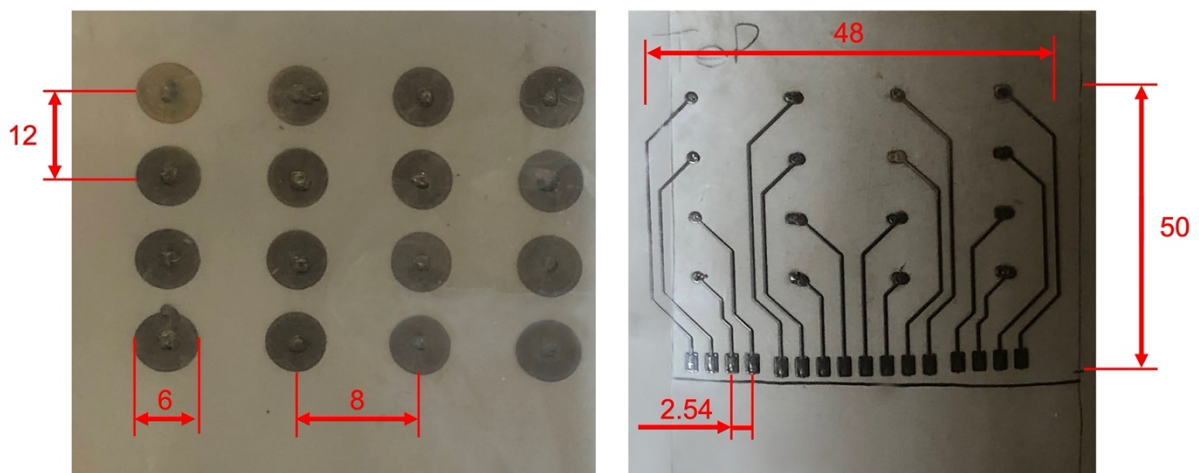


Fig. 11 Final layout of the prototypes for inner and outer features (quotes in mm). The overall dimensions of the wearable device prototype are 100 mm in diameter and 120 mm in length [66].

The board containing the conditioning electronics and the battery was attached to the outer surface of the device before the actual tests were performed. The specifications of this part will be discussed later in the following section 5.1.2 b). A total number of three prototypes were realized. The final layout of the device can be seen in Fig. 12, printed on the orthosis and worn by a tester with the complete electronics.



Fig. 12. Electrodes and tracks printed on the orthosis (quotes in cm); a tester wearing the devices with the electronics [66].

b) Morphological and electrical characterization of printed electrodes

A morphological test on the printed lines was performed thanks to Filmetrics Profilom 3D optical profilometer (Filmetrics Inc., 10655 Roselle St., San Diego, CA, USA), to evaluate the shape of the printed lines. It is based on state-of-the-art white light interferometry (WLI), a non-contact optical method for surface height measurements on 3D structures, to measure surface profiles and roughness down to $0.05\ \mu\text{m}$. The instrument works in the range of $50\ \text{nm}$ – $10\ \text{mm}$ with substrates and materials characterized by a reflectance between 0.05 – 100% . The system implements a 5MP camera, the Nikon CF IC Epi Plan 20x model (field-of-view: $1.0\ \text{mm} \times 0.85\ \text{mm}$). The samples were measured in three different areas along the total length to assess the uniformity of the thickness. The parameters evaluated in this phase are the total thickness, calculated as the difference between the maximum height and 1% of this value, and line width, calculated as the difference between two consecutive 1% values on the two sides of the maximum height. Results show an average line width of $320.85\ \mu\text{m}$ (relative standard deviation of 10%), a total thickness of $22.2\ \mu\text{m}$ (relative standard deviation of 11%) and a resistivity of $51 \cdot 10^{-8}\ \Omega\ \text{m}$ (relative standard deviation of 28%), which is in agreement with what declared by the manufacturer on the datasheet in the order of $10^{-8}\ \Omega\ \text{m}$, with values varying depending on deposition and curing parameters. Fig. 13 shows an example of the profile obtained for the printed features.

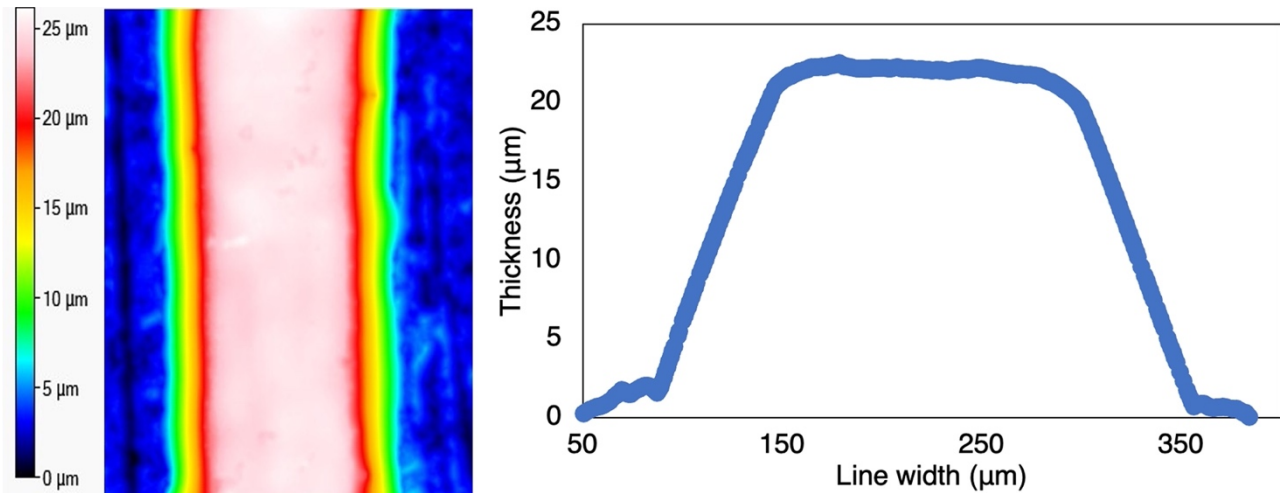


Fig. 13. Profilometer results for printed traces [66].

c) Device impedance characterization

In order to evaluate the performances of the electrodes directly embedded on the devices by means of AJP, we compared their electrode-to-skin impedance with the one of two types of commercially available surface electrodes: wet Ag/AgCl electrodes (Kendall), and dry electrodes (DRV175). For each electrode/subject combination, three measurements were acquired at rest, placing a couple of electrodes on the gastrocnemius muscle of two healthy volunteers. Only for the dry electrodes, a set of measurements with water-humid skin were acquired to simulate sweating. All the measurements were acquired with a portable impedance analyzer (PalmSens3 3EIS), configured to record impedance sweep in a range of frequencies from 10 to 1000 Hz, comprising the range of interest of EMG signal. All the measures were normalized with respect to the active area of the electrodes to provide better means of comparison. Both an intra- and an inter- subject analysis were performed. As highlighted from Fig. 14, the comparison among electrodes on the same subject showed a great similarity between our AJ printed electrodes and the commercial dry ones, with a difference around 20% for magnitude spectrum with sweat simulation and a difference of around 46% without sweat simulation. Regarding inter-subject variability, as highlighted from the average impedances for two subjects in each configuration shown in Fig. 15, comparable results could be obtained. The differences in terms of magnitude can be explained taking into consideration the variability in inter-subject device positioning, subject training and muscular anatomy.

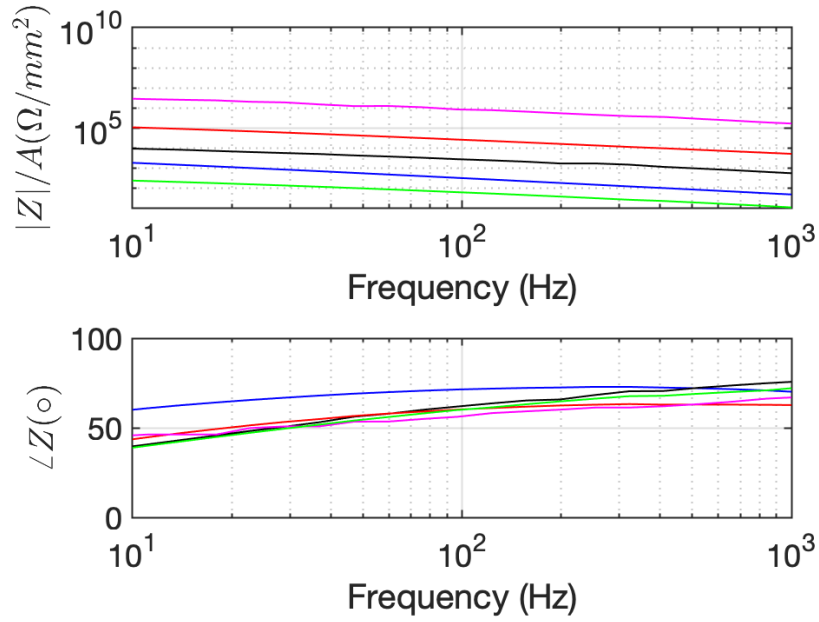


Fig. 14. Comparison of the impedances of different electrodes normalized on electrode area on subject 1. Wet commercial electrodes in blue, commercial dry electrodes with/without sweat simulation in green/black and AJ printed dry electrodes with/without sweat simulation in red/magenta [66].

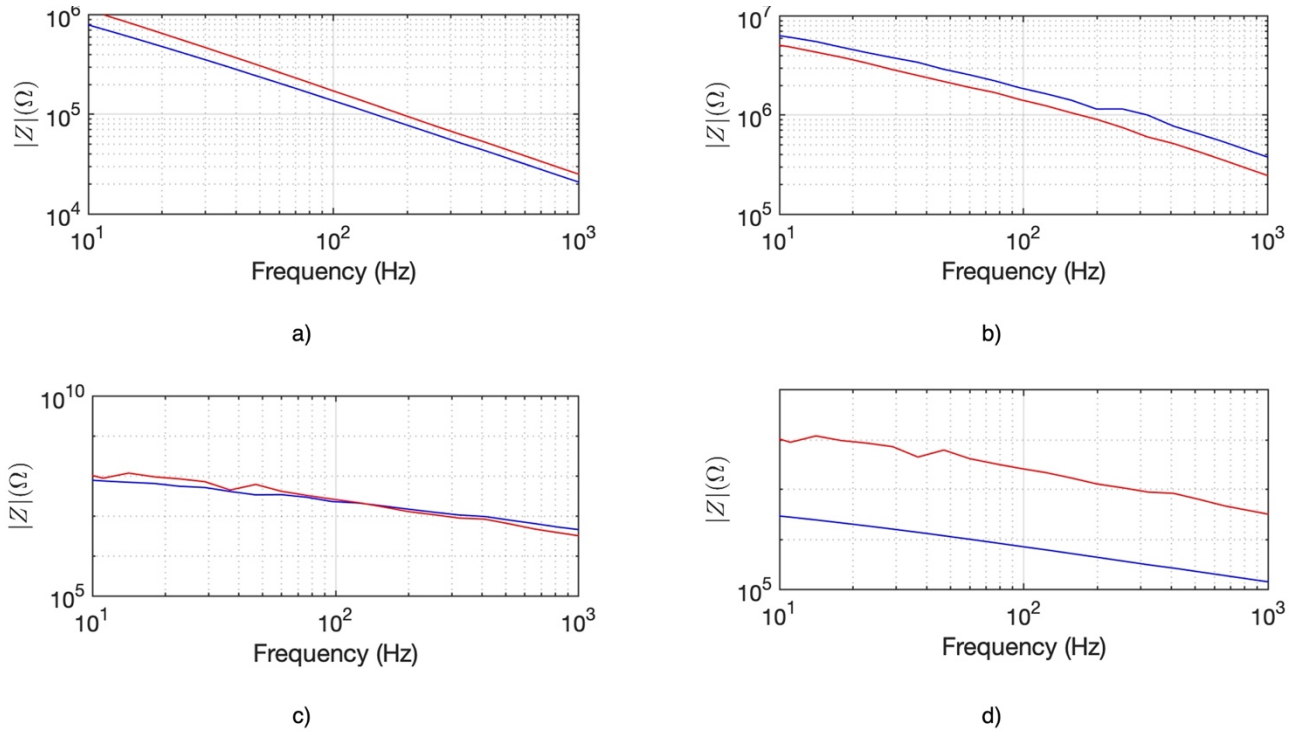


Fig. 15. Comparison of the impedances of same electrodes between the two subjects (1 in red, 2 in blue): a) wet commercial electrodes, b) commercial dry electrodes without sweat simulation and c)/d) AJ printed dry electrodes without/with sweat simulation [66].

d) Signal Acquisition section

In the present section, we briefly discuss development choices and system architecture. During electronic device development, user comfort and technical aspects were considered as key requirements. According to these considerations, the architecture depicted in Fig. 16, was developed to provide an 8-channel front-end with integrated Bluetooth Low Energy

(BLE) real-time communication using as few components as possible to reduce both the power absorption and the invasiveness of the wearable device.

We employed an ADS1298 integrated frontend for biopotential signals produced by Texas Instruments which includes an 8-channel 24-bit ADC with built-in programmable gain amplifiers and serial chip-to-chip communication. The control and communication tasks are performed by a CYBLE-222014-01 Cypress Semiconductor microcontroller whose firmware allows a configuration to perform 1 kHz signal sampling and its transmission through BLE notifications to a remote unit. The system communication was tested, and it was possible to achieve an average throughput of 27763 B/s with a percentage of correctly received packets higher than 99%. The wearable device was completed with a 1000 mAh LP603450 LiPo battery that can nominally power the system for up to 30 hours.

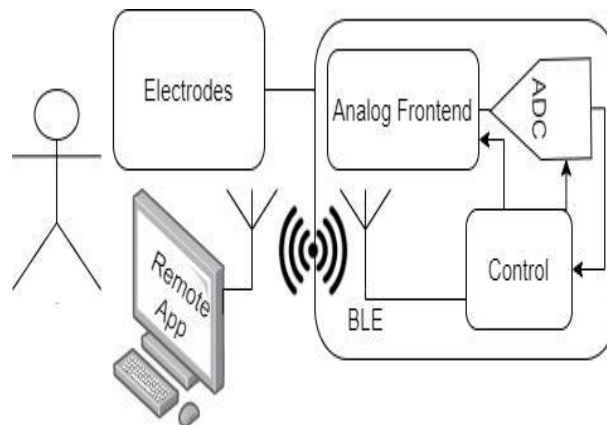


Fig. 16. Architecture of the developed wearable device [66].

5.1.3 In Vivo Acquisitions

a) Protocol for EMG in vivo acquisition

In order to assess proper functioning, the novel device was tested on three different normal abled subjects, measuring the activity of gastrocnemius while executing specific tasks, compatible with the orthosis and that are reported in the literature as useful during rehabilitation session or routine activities [165], [166]: The protocol was then composed by the following tasks:

- 1) Sitting still
- 2) Standing and sitting tasks
- 3) Standing still
- 4) Isometric contraction of the gastrocnemius muscle

5) Standing still

The acquisition of each task was repeated three times for each subject. For each subject, a complete set of measurements performing the same tasks was also executed using standard pre-gelled commercial surface EMG electrodes, to have a reference. The analysis of the signals from both commercial and AJ printed electrodes was performed exploiting well known and established features in time, frequency and spatial, to be able to compare results from our device with other studies performed in the literature.

b) Signal processing

Relying on widely accepted strategies reported in the literature, acquired data were processed and analyzed using MatLab to filter the interferences, recognize the contraction events and extract relevant frequency, time and spatial features.

i. Signal denoising and filtering

Interferences due to poor skin-electrodes contact and electromagnetic interferences are common in applications dealing with wearable electronics [167]. Raw data were then processed using a notch filter at 50Hz to remove power interferences and then using a bandpass filter between 10 and 450 Hz, to remove lower frequencies possibly due to motion artifacts or neuronal spiking, and higher frequencies due to environmental interfering signals (e.g. electromagnetic interferences). The choice of low-pass and high-pass frequencies was based on what is reported by literature, confirming that the frequency spectrum of EMG ranges from 20 to 400 Hz, with the maximum energy between 50 and 200 Hz [168], [169]. Once the raw signal was filtered, each task was isolated depending on manual timing acquired during each session. Information about both time and power of raw and filtered signals were saved as fields of a struct for each repetition.

ii. Contraction detection

The detection of each single contraction events taking place during the specific tasks was implemented relying on the use of the cumulative sum (CUSUM) of the rectified EMG signal. As reported in previous EMG analysis in the literature [170]–[172], this method was chosen here as an optimal trade-off in terms of low complexity and of robustness required in this application to discriminate between relax and contraction events [173]. In order to improve robustness against background noise, the traditional CUSUM method was improved, taking

as a reference [174], using CUSUM-slope as a measure to estimate the signal content within a noisy background statistically.

Briefly, defined x_i the EMG signal the CUSUM C_i was calculated according to the (14) reported in [174].

$$C_t = \sum_{i=1}^t x_i - \mu \quad (14)$$

The first derivative of C_i was then calculated, and a moving average applied to avoid the identification of background random fluctuation as contraction onsets or offsets. Contraction onset and end could be then identified by comparing the first derivative with a threshold to discriminate significant changes with respect to the standard deviation of the background noise. The indexes corresponding to the contractions' onset were saved depending on the moment in which the first derivative becomes higher than the threshold, and the indexes of the end of the contraction as those moments in which the first derivative becomes lower than the threshold.

iii. Time, frequency and spatial features

In order to perform intra- and inter-subject comparison, a widely accepted method in the literature is the one relying on specific time features. Among the various available, we selected here four-time features (Mean Absolute Value (MAV), Root Mean Square (RMS), Wavelength (WL) and Willison Amplitude (WAMP) since they are referenced as the most relevant in the literature using EMG for rehabilitation applications were indicated as the most useful [145], [175].

Table 2 Time features selected from literature [145], [175].

Feature	Equation
MAV	$g(j) = \frac{1}{N} \sum_{i=j-\frac{1}{2}(N-1)}^{j+\frac{1}{2}(N-1)} s(i) $
RMS	$g(j) = \sqrt{\frac{1}{N} \sum_{i=j-\frac{1}{2}(N-1)}^{j+\frac{1}{2}(N-1)} s(i)^2}$
WL	$g(j) = \sum_{i=j-\frac{1}{2}(N-1)}^{j+\frac{1}{2}(N-1)-1} s(i+1) - s(i) $
WAMP s _{lim} = 10 s _{lim} = 20	$g(j) = \sum_{i=j-\frac{1}{2}(N-1)}^{j+\frac{1}{2}(N-1)-1} [v(s(i+1) - s(i))]$ $v(s) = \begin{cases} 1, & \text{if } s \geq s_{lim} \\ 0, & \text{otherwise} \end{cases}$

Although time-features are the most frequently adopted method to characterize EMG signals and to compare different sessions, often frequency content analysis represents a useful complementary tool. During rehabilitation sessions or when evaluating the comfort of prosthesis or orthosis, one of the key aspects is to assess muscle fatigue during long or repetitive tasks. This is useful to provide feedback to the patient and to inform medical personnel about the improvement during long-term monitoring. Mean (MNF) and median (MDF) frequency (defined as detailed in (15) and (16)) were selected as frequency features since they are indicated in the literature as most related to fatigue [176].

$$\int_0^{MDF} P(t, f) df = \int_{MDF}^{\infty} P(t, f) df = \frac{1}{2} \int_0^{\infty} P(t, f) df \quad (15)$$

$$MNF = \frac{\int_0^{\infty} f P(t, f) df}{\int_0^{\infty} P(t, f) df} \quad (16)$$

After computing the frequency spectrum of the segmented EMG during the contraction using the Short-Time Fourier transform (windows length=128 ms, overlap=50 ms), MNF and MDF were calculated starting from the definitions (15) and (16) as referenced in [176].

In addition to time and frequency features, since the printed matrix represents a multichannel system, spatial features were also extracted to assess the ability of the device to evaluate signal distribution during different tasks.

The content of each of the 8 channels was evaluated at discrete time points corresponding to maximum RMS amplitude, showing how the signal was traveling along with the muscle during different tasks.

iv. Correlation analysis

Correlation analyses have been performed to characterize the device both intra- and inter-subjects, adapting protocols often adopted in the literature to evaluate EMG monitoring on single or multi-users [177]–[179]. Considering each analysis performed on a single subject, cross-correlations of each channel with the others were calculated to provide a table with the maximum correlation coefficients obtained among the different channels and the lag at which they were obtained. Considering channels activation during the same task performed by different subjects, a cross-correlation between each corresponding channel was performed, to assess how the device can collect signals from different subjects with different anatomical features.

c) Results from in vivo acquisitions

EMG signals acquired and analyzed (as described in previous sections 5.1.3 a) and b)) confirmed the functionality of the dry EMG matrix embedded in the orthosis. In particular, the possibility to detect muscle activation, muscle fatigue, contraction spatial location and to monitor muscle activity from different areas of the muscle during complex tasks were demonstrated. To extensively and organically show and discuss experimental results, they will be summarized here in three specific sections, each to highlight different investigated aspects. The first one is exclusively dedicated to the comparison between data acquired from AJ printed dry electrodes with the ones from standard pre-gelled Ag AgCl electrodes that represent the commercially available gold standard for EMG analysis. The second one will evaluate on a single subject how the different channels are correlated among them during a stand up and sit-down task and how it is possible with a color map to show contraction time and spatial evolution. The third one will show how the system work considering different subjects, in terms of time features, frequency features and correlation among the same channels.

i. Comparison between AJ printed electrode matrix and commercial electrodes

Results obtained from the comparison between the parameters of EMG signals measured with AJP and with commercial pre-gelled surface electrodes showed a comparable ability to

follow qualitatively the different time evolution of the tasks performed. Comparable qualitative trends could be obtained both in terms of RMS amplitude than of frequency features. However, quantitative differences could be observed both in terms of RMS amplitudes, of SNR and of frequency content. In detail the SNR was computed both linearly than in dB, using the average RMS values measured during a contraction event (RMS signal) and during rest (RMS rest). RMS amplitude values of the EMG recorded using printed electrodes appeared reduced with respect to the ones obtained with commercial electrodes (Fig. 17), both during rest (average reduction 40%) and during contraction (60%). The higher reduction of the RMS observed during contraction than during rest caused a reduction of the SNR associated with the printed electrodes respect to the commercial ones of nearly 5 dB (AJP electrodes showed SNR in a range between 24 to 27 dB compared to the 30 dB of the commercial surface electrodes).

Regarding frequency features, the range of mean and median frequency quantified from the spectrum of the AJP appear lower (10 Hz) than the range quantified from the spectrum of commercial electrodes during all the contraction. All those differences can be potentially explained considering the different dimensions of the electrodes and the different electrodes-to-skin impedance module (in agreement with what highlighted during the impedance characterization detailed in paragraph 5.1.2 c). However, the amplitude of all the time features recorded allowed extracting the index of start and stop of contraction needed to perform the analysis both in time and in frequency. It can be observed, from the analysis of the mean and median frequency during the contraction, that a comparable trend could be recorded during 30 seconds of contraction. A range of frequency between 80 and 140 Hz could be observed in both systems, in agreement with the maximum frequency content of the EMG signal highlighted in the literature (20 and 150 Hz [168]).

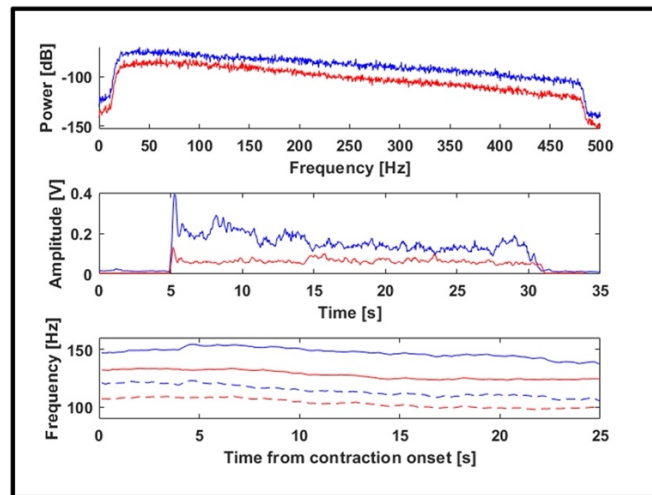
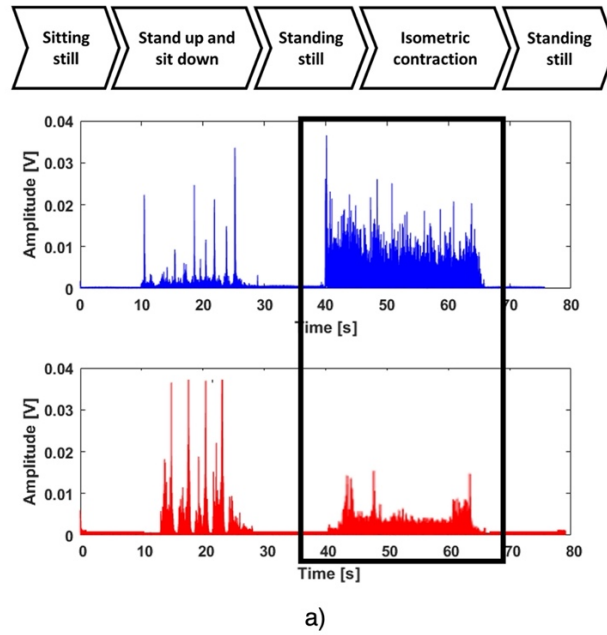


Fig. 17 a) Comparison of the full protocol acquired with reference commercial electrodes (blue) and with AJ printed electrodes (red); b) Analysis of the time and frequency features of the EMG signal acquired from a single contraction respectively with commercial (blue) and AJ printed electrodes (red) [66].

ii. Intra-subject task analysis

The intra-subject functionality of the dry EMG matrix embedded in the orthosis was exploited to investigate the amplitude of the EMG signal recorded in each subject by each channel during the sit-to-stand-to-sit task, which involves different muscles at different timings. We used [165], [166], [180] as references about standard sit-to-stand and stand-to-sit biomechanical phases and muscle activity to perform a reliable comparison of the results obtained using embedded EMG dry AJ printed electrodes. The time features extracted allowed to confirm that the device can discriminate the different events of stand up and sit down as discrete peaks (Fig. 18), in agreement what obtained with commercial electrodes and to what reported in the literature [165], [166], [181]. Further, as highlighted by the

comparison between the single graph referring to the commercial electrodes and the multiple graphs from 8 channels of the printed array, from this last it is possible to drive multiple information about the signal direction and spatial muscle activation with minimal invasiveness. Thus, a similar set of information could be obtained only by relying on 16 commercial electrodes, with a complex positioning protocol and with issues in terms of obtrusiveness for the patient. It was then possible to extract color maps that are visually showing the activation of the different muscles during the task (Fig. 19). Thinking to a future interactive tool, this visual feedback could represent an interesting opportunity for the patient to have prompt information about the correctness of the task performed.

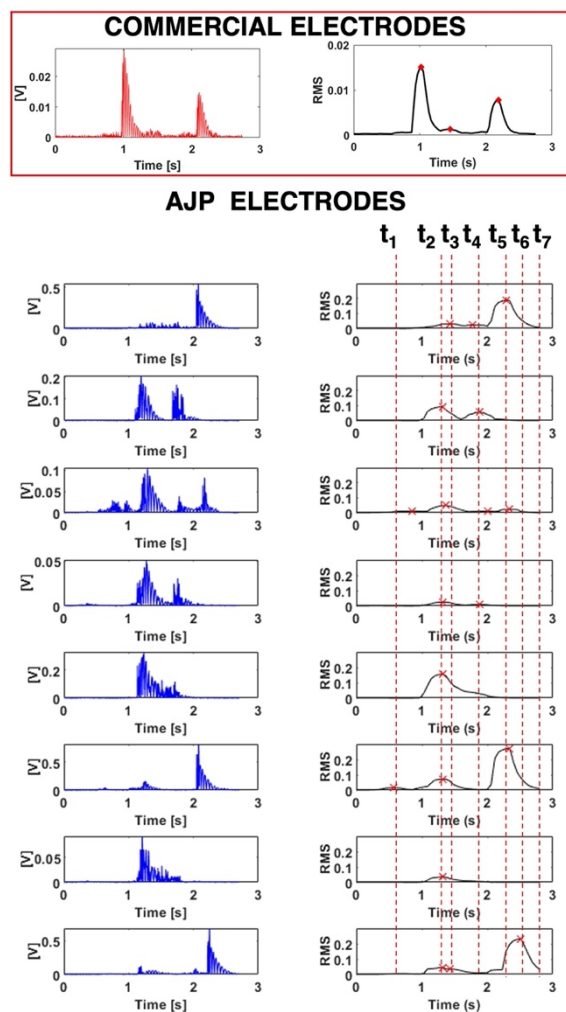


Fig. 18 Voltage and Root Mean Square amplitudes measured considering both commercial EMG electrodes and AJ printed electrodes. Considering the latter, from above to below channels 1 to 8 and the EMG signals recorded during a single task of sit-to-stand and stand -to-sit (from t_1 to t_7) [66].

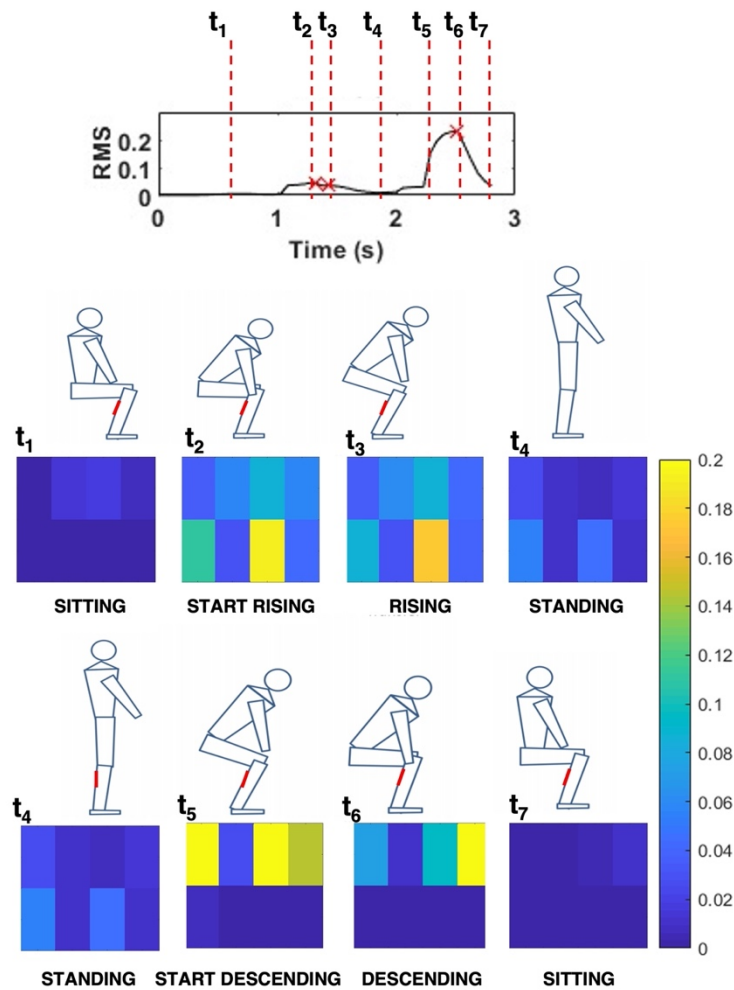


Fig. 19 Spatial features extracted during task showing the activation of each channel during the different phases. The colorimetric scale reproduces the values of the Root Mean Square [66].

The correlation among the different channels confirmed that the highest value was obtained with an average delay of 0.03 ± 0.01 s among channels 1, 8 and 6 referring to the highest part of the muscle and among channels 5, 4 and 7 referring to the lowest part in each of the three subjects, suggesting the activation of the lowest part during rising and of the upper during descending (Fig. 20).

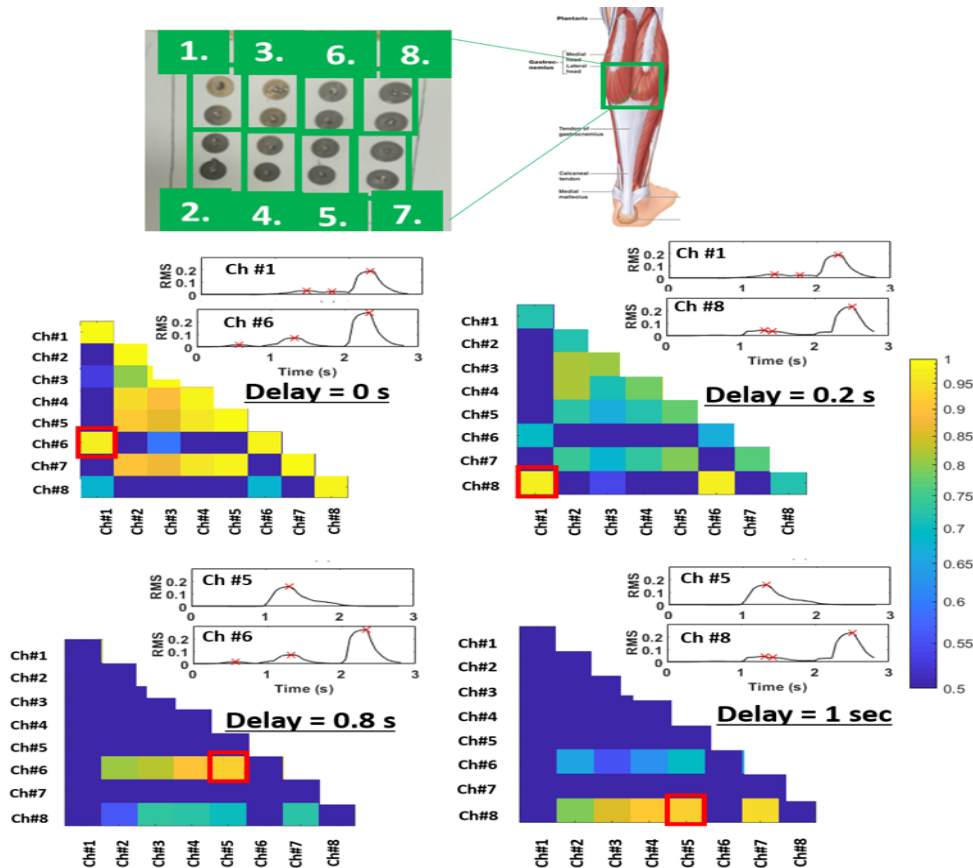


Fig. 20 Maximum correlation values among the 8 channels during sit-to-stand and stand-to-sit tasks. The colorimetric scale represents the correlation at a specific time instant [66].

Interestingly, the highest correlation values (> 0.95) could be observed at delays in agreement with the distances between the peaks of RMS recorded on the different channels. In presence of a delay 0 and 0.2, maximum values of correlation would be observed respectively between nearby channels (e.g. among upper 1,6,8 and lower 2,4,5,7). At higher delays 0.8 and 1 s, maximum levels of correlation could be observed even between upper and lower channels. This can be comparable with the interval between rising and descending tasks, suggesting that the matrix is successfully able to detect the different timings of activation of muscle with a higher resolution than classical single-channel EMG.

Recurring peaks obtained from multiple repetitions performed using the same device (Fig. 21) and from repetitions using different devices (Fig. 22) suggest the proper functioning of the device even during a long-time acquisition. This gives promising results concerning the repeatability of the results obtained.

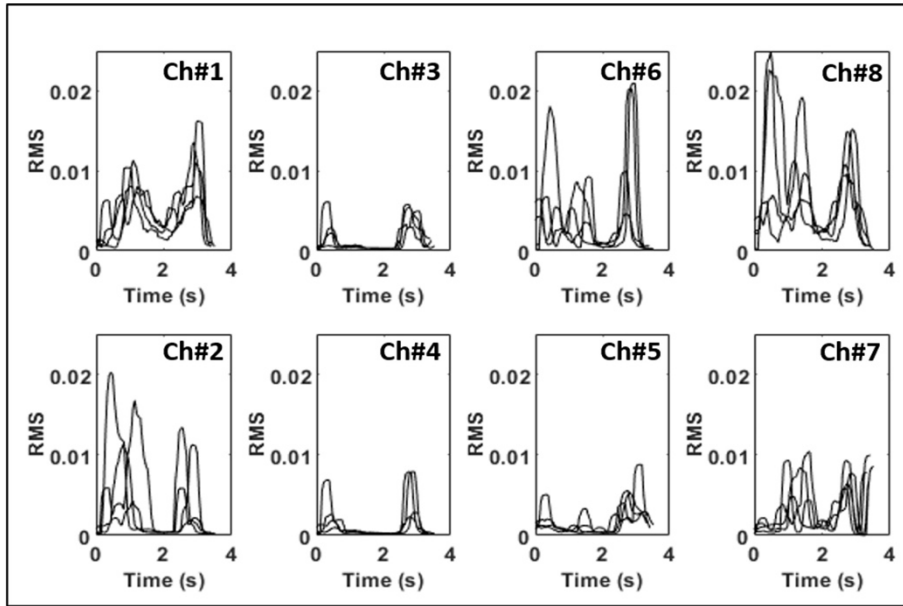


Fig. 21 RMS features obtained with multiple acquisitions of the same task on a single device [66].

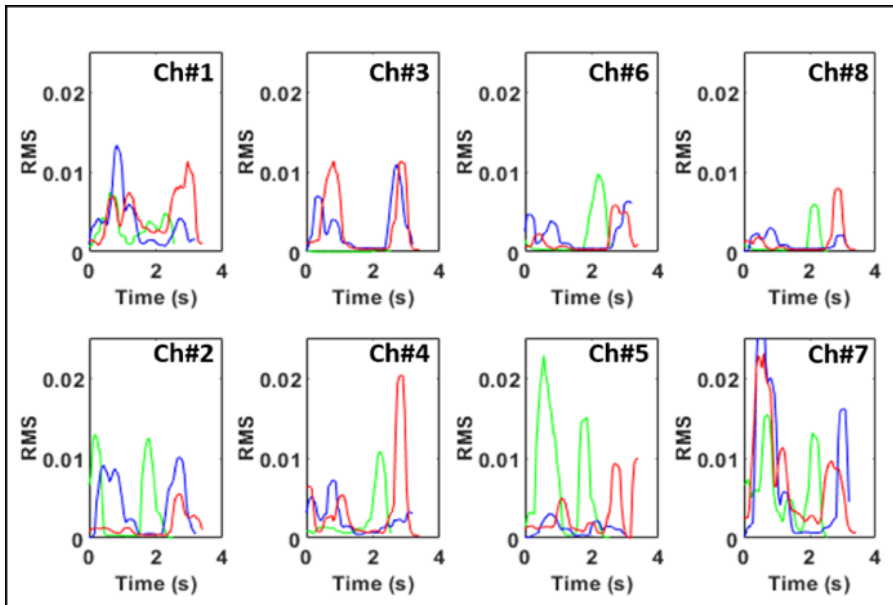


Fig. 22 RMS features obtained from the acquisition of the same task performed using three different devices on the same subject [66].

In both cases clearly, the peak of RMS EMG value due to rising and descending events could be visible. The difference in the specific shape can be explained for intra-device repetition due to imperfect contact maintained during repetition between electrodes and skin (Fig. 21), while for inter-device evaluation due to a tolerance in the correct placement of the device on the muscle (Fig. 22).

iii. Inter-subjects task analysis

Results obtained from the acquisition performed on three different subjects showed recurring time and frequency features when analyzing a single contraction and a recurring pattern with two most evident local peaks when analyzing the sit-to-stand-to-sit task, in

agreement with the phases of rising and descending confirmed by literature [165], [180], [181]. Despite clearly, these represent limited numbers that cannot allow stating strong assumption regarding the reproducibility, the agreement of those widely adopted features with the literature represents interesting preliminary data, is suggesting that the device is working properly on subjects with different calf dimensions (sb1:12.0 cm, sb2: 11.0 cm sb3:13.7), level of training and different sex.

Fig. 23 and Fig. 24 report examples of comparisons among the EMG signals from the three subjects respectively during a long contraction and during a stand-up and sit-down task. Regarding the long contraction, the differences in RMS amplitude can be explained considering the variability, detailed during impedance-based characterization, due to different subject anatomy and variability in electrodes positioning and skin-electrodes contacts. The analysis of frequency spectrum shows comparable frequency content, with a peak located at an average frequency of 67 ± 10 Hz, and most of the energy ($70 \pm 5\%$) within 20 and 250 Hz, in agreement with what was reported from the literature [168], [169]. Regarding mean and median frequency, different trends can be appreciated for the three subjects, possibly due to the different levels of training bringing to different amounts and timings of muscular fibers activated during the task. Comparable ranges of mean frequencies could be observed (100-150 Hz), in agreement with the range in which the maximum EMG energy is located (70-160 Hz according to [175]) (Fig. 23).

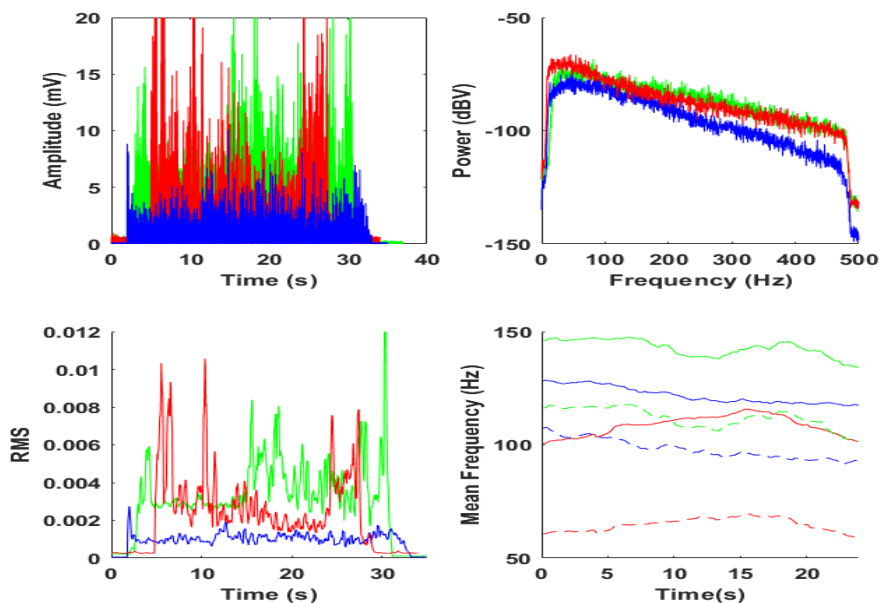


Fig. 23 Comparison of three subjects (blue, red and green curves) performing a single long contraction. Above: filtered rectified EMG signal and its spectrum. Below: time features and frequency features (Mean frequency solid line and median frequency dotted line) [66].

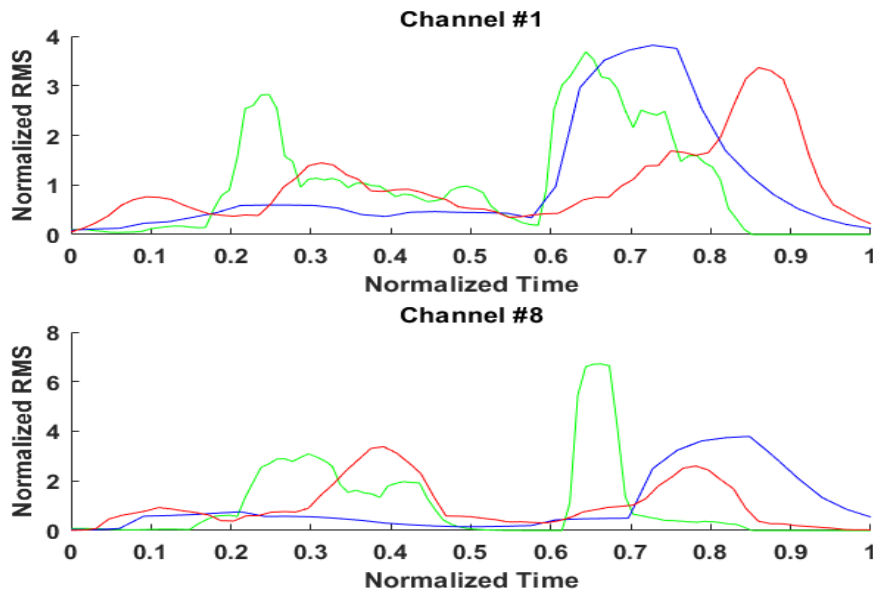


Fig. 24 Comparison among the time features calculated from the EMG of the three subjects (blue, red and green curves) on channels 1 and 8 while performing a sit-to-stand and a stand-to-sit task [66].

Similarly, median frequency (60-120 Hz) appears in complete agreement with results obtained with standard surface EMG electrodes [182]. Interestingly, a similar decreasing trend could be observed on all the three subjects in the last 5 seconds, suggesting possibly the correlation with an ending condition of fatigue.

The comparison among the EMG recorded on the three subjects during the stand-up and sit-down task interestingly allowed to recognize comparable features in all the subjects. An example can be observed in Fig. 24 where for all the three different patients tested it was possible to detect on the same channels 1 and 8 the two peaks referring to the stand-up and sit-down task. Some differences could be observed in other channels, due to the possible tolerance in the positioning of the device and in the contact impedance in the three subjects.

5.1.4 Conclusion

Thanks to the advanced physics of ink deposition and curing, electrodes and tracks of the embedded multi-EMG electrodes matrix were directly integrated into the orthosis obtaining a resistivity in agreement with what was declared by the manufacturer and an overall geometrical variation of about 10% (line width of 320.85 μm , thickness of 22.2 μm). The device was then tested acquiring muscular activity from three subjects performing the same customized circuit, evaluating both long and short contraction and complex tasks involving multiple muscles. Results obtained in terms of recurring features with both intra- and inter-subject repetitions, in agreement with the literature, are a promising starting point for deepening in future works long term acquisitions and wider statistical analyses on multiple

subjects. A comparison with the gold standard commercial electrodes for surface EMG was performed. Similar features both in frequency and time were analyzed. Due to a higher contact impedance of the electrodes, the amplitude of the time features was smaller than gelled electrodes of about 5-10 dB. Future works will try to improve this limitation by evaluating novel materials to improve the adhesion, to reduce contact impedance and to improve electrode performances. Despite this limitation, this work highlights that AJP technology could bring wearable devices to a new era, obtaining embedded sensors and conductive tracks printed directly on prostheses or orthoses. The results depicted the possibility to detect contraction events, to analyze time and frequency features and to extract useful visual feedbacks for the patient with dry multiple electrodes represent a promising result to better investigate non-invasively muscular activity on larger areas, and not in a single location as in single-channel standard acquisitions. Furthermore, the extreme customizability offered by AJP opens different opportunities in terms of integration of EMG matrix with other sensors (e.g. lactate, potassium) that could provide complementary information about the fatigue and the oxygenation during physical activity. In such a way, future rehabilitation devices would be smart, not invasive for the patient and able to bring to physiotherapists or to patient valuable feedback to improve effectiveness, consciousness and interaction during daily activities and specific exercises.

5.1.5 Follow-on Work

A smart and totally customized multi-sensing printed wearable platform was developed on a Kapton film, combining together EMG electrodes and electrochemical sensors. The aim of this device is to better investigate muscular fatigue in real-time during physical exercise with the possibility to correlate muscular activity with lactate production. This represents the key opportunity to obtain triggered feedback on electrical and biochemical profile referring to the same site [183], thus guaranteeing a perfect correlation in time and location of the acquired multi-sensor data.

Firstly, the substrate is cleaned with ethanol (a). Then, the silver tracks are printed on the top layer L1 (b). The ink is oven-dried at 140°C for 5 minutes and then the vias are drilled in place (c). The subsequent silver deposition on the bottom layer L2 deposited both the electrodes and provides electrical connection to the other layer through the vias (d). After the oven-cure (200°C for 60 minutes) of the silver ink that concludes the fabrication of the EMG electrodes, the carbon layer was deposited on the working and counter electrode of the

electrochemical sensor (layer L2) and cured at 140°C for 5 minutes (e). Fig. 25 resumes the fabrication steps of the device, while Fig. 26 presents the final prototype.

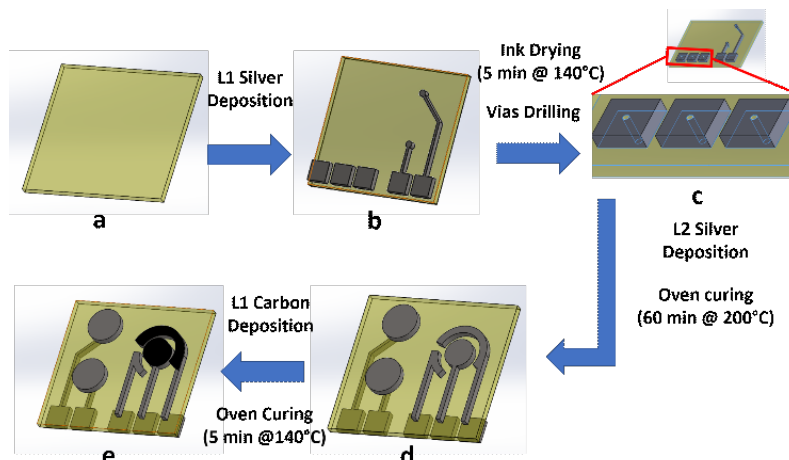


Fig. 25 Overview of the different steps of the electrodes' fabrication process [66].

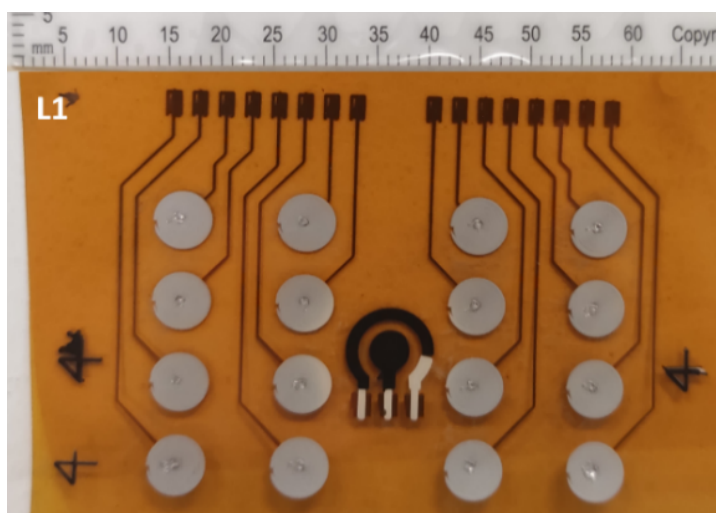
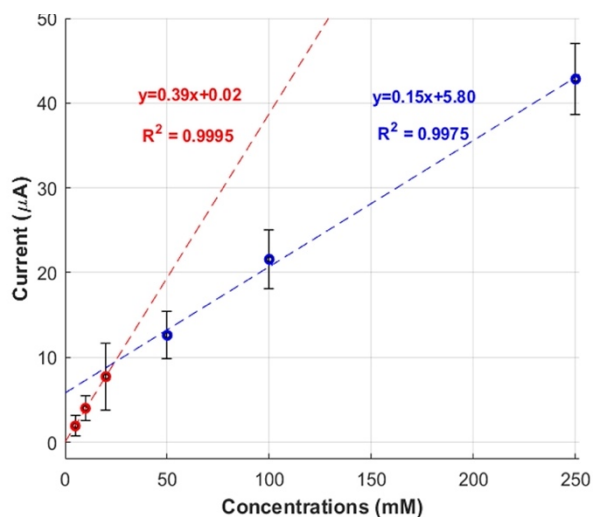


Fig. 26 Printed prototype for simultaneous measurements of lactate concentration in sweat as well as electromyography [66].

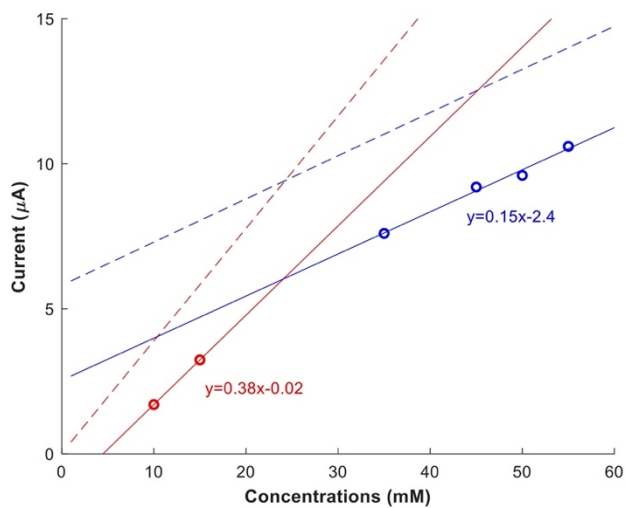
Results of the measurements performed as preliminary analysis of both the sensors printed on the patch provided consistency to pursue in the study a device able to follow changes in EMG features, adding lactate sensing in sweat during fatigue processes. As for EMG electrodes, the results are in agreement with what derived from the first part of this study printing EMG electrodes on a rigid support to realize a smart orthosis prototype. Lactate sensing measurements was divided into static and dynamic analysis. Static lactate sensing gave important information like limit of detection (LOD), linearity and sensitivity. For each test, the platforms have been previously functionalized with 5 μ l of 5 mM $[\text{Fe}(\text{CN})_6]^{3-/-4-}$ as mediator [72] and left drying at room temperature for 2 hours, protected from light. Dry L-lactate Oxidase (LOx) (Sigma Aldrich) was subsequently dissolved in PBS at a concentration of 100 U/ml and 5 μ l of the solution was cast onto the WE and left drying for 2 hours. Standard solutions of sodium-L-Lactate (Sigma Aldrich) have been prepared in

PBS with the following concentrations: 0 mM, 10 mM, 20 mM, 50 mM, 100 mM, 250 mM, 500 mM. For each concentration, 100 μ l of the solution was placed onto the three electrodes layout using a micropipette, starting a chemical reaction. In detail, LOx catalyzes the oxidation of L-lactate to pyruvate, producing hydrogen peroxide (H_2O_2) that is then oxidized to produce a current proportional to the L-lactate concentration. A ferrocene mediator is employed to shuttle the electrons between the enzyme and electrode [184]. Preliminary results suggested the possibility to study the use of the current measured from the printed electrochemical sensor to follow lactate changes continuously, within the physiologically range of interest for fatigue monitoring (10-100 mM). Indeed, Fig. 27a, obtained from the analysis of chronoamperometric measurements, suggested a high linearity ($R^2=0.9995$) of the printed sensor in the range 0-20 mM. Here a sensitivity of $0.39 \mu A/mM$ was calculated, higher than the one observed in the full range tested 0-250 mM. The curve appears however to be linear also in the range 20-250 mM, with a $R^2=0.9975$ and a sensitivity of $0.15 \mu A/mM$. Observing the plot, a higher sensibility of the overall system for lower concentrations and saturation for higher lactate concentrations is evidenced, in agreement with other work in the literature dealing with enzymatic detection on printed flexible electrodes [185].

A preliminary analysis on the ability of the sensor to detect continuous changes in the concentration of lactate was assessed by first emulating the resting condition wetting the sample pad of PBS. In those conditions, the chronoamperometry was started applying a constant +0.4 V potential to the sensor and recording the current produced. After that, at discrete well-known time points (0 s, 125 s, 250 s, 400 s, 550 s) 50 μ l of sodium-l-lactate PBS solution with different random concentrations were dropped onto the sample pad, emulating controlled increases of lactate concentration in the flux flowing onto the electrodes (Fig. 27b). The linearity ($R^2=0.9816$), the sensitivity ($0.32 \mu A/mM$) and the LOD obtained ($4.1 \text{ mM} \pm 0.6$) appear in agreement with what obtained in static condition but also from similar biosensors reported from the literature [186]. However, the lower sensitivity and absolute values of currents with respect to the static preliminary results, suggest that the main improvement need to be addressed to optimize the immobilization of the enzyme and of the mediator, in order to maximize electrons exchange, sensor stability and measurement repeatability even in presence of a flux of solution onto the sample pad.



a)



b)

Fig. 27 a) Current-Concentration plot of the whole range tested (0-250 mM), with linear fitting in the two ranges 0-20 mM (red line) and 20-250 mM (blue line). b) An example of 600 s chronoamperometry recorded during following discrete injection of controlled solutions with different lactate concentrations. Red lines are associated to 0-20 mM concentration range, while blue lines are associated to 20-250 mM concentration range [66].

5.2 Preliminary Study on a Strain Sensor Printed on 3D-plastic Surfaces for Smart Devices

The research work reported in this section was presented in *IEEE 2019 II Workshop on Metrology for Industry 4.0 and IoT (MetroInd4.0&IoT)* and is part of the conference proceedings with the title *Preliminary Study on a Strain Sensor Printed on 3D-plastic Surfaces for Smart Devices* [97]. Results and pictures are reported with permission of the editor.

5.2.1 Introduction

Industry 4.0 and Internet of Things (IoT) are two appealing topics of the recent scientific literature. They are based on the connection of smart devices, which are able to sense and communicate for controlling a process or the environment. The technologies adopted to develop new devices equipped with sensors have been changed recently, as reported in the literature [187], [188]. Indeed, new and different technologies are required to integrate electronics made of different functional materials and substrates. In this scenario, printed electronics is spreading rapidly because of its low production costs, high throughput and high variety of materials [189]. For example, screen printing [190] and inkjet printing [191] currently represent the most adopted methods for printing electronics. Both allows obtaining a resolution up to 50-100 μm , suitable for developing electrochemical sensors, antennas, planar electronics or sensors printed on plastic or paper. Despite of their low production costs and their good throughput, these printing techniques have several problems in terms of repeatability, resolution and possibility to print onto non-planar surface.

In this work, for the first time, a resistive sensor was manufactured directly integrated on a plastic and non-planar object by combining AJP and FLA. Thanks to this process, a strain gauge sensor was realized by depositing a silver ink directly onto a PVC tube, as first example of electronic device on a non-conventional and non-planar substrate.

5.2.2 Sensor Fabrication

A silver ink by Novacentrix (Metalon® HPS-108AE1) was used to print a metallic strain gauge sensor on a PVC tube (Fig. 28). The ink is based on silver nanoflakes around 400-700 nm and dispersed in a liquid vehicle. Nanosilver concentration is about 55wt%, with a viscosity of 130-180 cP.

Nitrogen was used as sheath gas and as a carrier gas because it is an inert and low-cost gas. The flow rate of the carrier gas, of the exhaust and of the sheath gas was set to 1075 SCCM, 1000 SCCM and 120 SCCM, respectively. The size of the nozzle hole was around 300 μm in order to print lines with 160 μm width. The printing speed was fixed to 1 mm/s. The tube was mechanically fixed to the motorized XY stage. A 3D CAD file containing the geometry of the sensor to be printed was used to program the 3D movement of the print head. After the printing, FLA process took place considering a single pulse with amplitude of 260 V and duration of 1 ms ensured the sintering of the silver film with an energy of density of 0.64 J/cm². No deformations of tube were detected after the sintering treatment.

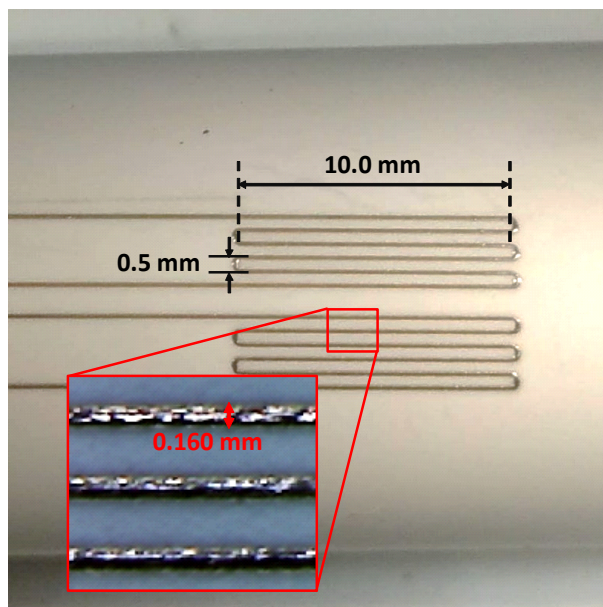


Fig. 28 Image of two printed strain sensors on a plastic tube. In the inset, a zoom of three parallel lines is shown. The tube has an outer diameter of 20 mm and an inner diameter of 16 mm. No deformations of tube were detected after the sintering [97].

The adhesion of the deposited ink was tested by means of the scotch tape method and it confirmed good adhesion and the feasibility of the fabrication method.

The terminals of the printed strain gauge (2 mm x 2 mm) were connected to the copper wires by means of Dupont 5000 silver conductor. This conductive paste is a combination of flake silver and resin technology, which is also able to paste the wire to the conductive track and thus to the tube. The paste was deposited manually on the wire and on the tube and dried in a conventional oven at 50 °C for 30 minutes. This temperature considers the maximum operating temperature of the PVC and prevents the heat distortion of the tube.

The thickness of the strain gauge sensor was measured by Profilm3D, commercialized by Filmetrics. The investigated area (1 mm x 0.841 mm) allowed to measure the thickness of two parallel lines of the sensor at the same time. Because of the 3D surface, an elaboration of the data was performed to determine the thickness of the silver film. The maximum thickness of the silver material is between 11 μm and 13 μm (8 μm in average), and the width is 160 μm , as shown in Fig. 29. Therefore, the resistivity (ρ) of material is about $35 \times 10^{-8} \Omega \cdot \text{m}$ in average, which is comparable with the value reported in the datasheet and it is obtained by the classical formula $\rho = \frac{R \cdot S}{l}$, where R , S and l are the resistance, the section and the length of the serpentine, respectively.

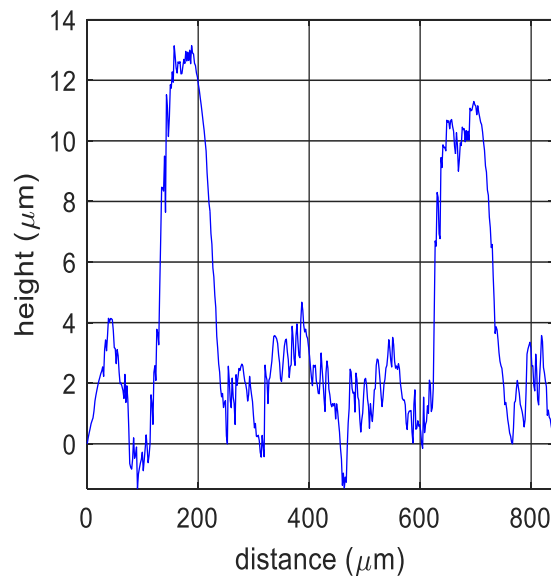


Fig. 29 Profile measurement of two parallel lines obtained from Profilm3D. The average width of the two lines is 160 μm , and the maximum height is 13 μm [97].

5.2.3 Experimental setup

The experimental activity consisted in monitoring the electrical resistance when different bending histories were applied. A PVC tube was fixed at one end (16 mm from the middle of the sensitive area of the sensor) and different loads (with value $-F_e$) were applied to the other end. In this condition, the tube can be modelled as a cantilever beam of hollow circular cross-section, and the load acts transversally to the longitudinal axis and creates pure bending; the strain sensors were printed near the joint (Fig. 30). The tested smart tubes were 386 mm long, with inner and outer diameter of 16 mm and 20 mm, respectively. The electrical resistance was measured using 4-wire connection by a 6½ digits multimeter (Agilent 34401A), which was controlled by a custom LabVIEW Virtual Instrument (VI) for collecting and storing the measurement data.

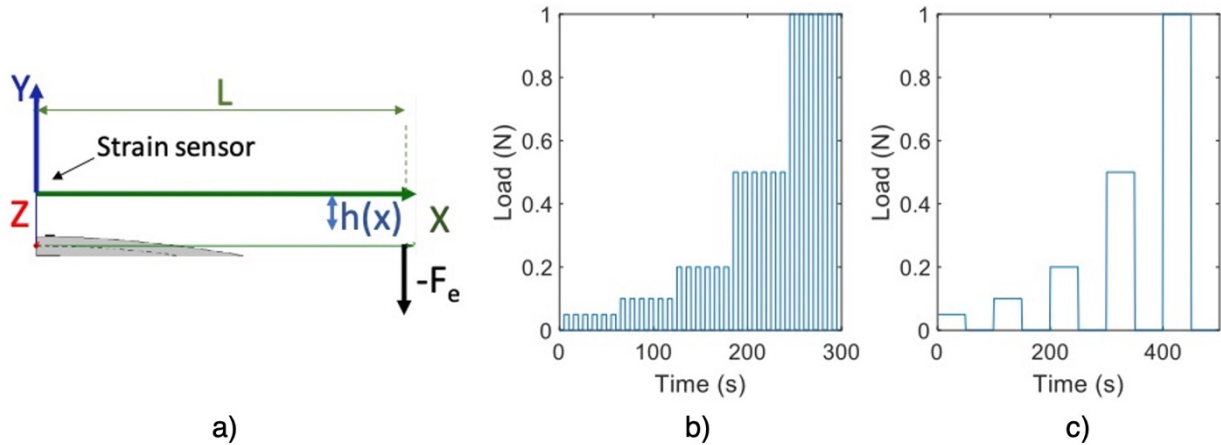


Fig. 30 Experimental setup and performed tests. (a) Model of the sensorized tube as cantilever, when a load of $-F_e$ is applied at the free end along the y -axis direction. (b) Loading-unloading cycles in the first test for the calculation of the gauge factor. (c) Loading-unloading cycles in the first test for the creep analysis [97].

As preliminary test, a test load of 1 kg was applied to estimate the Young modulus; the displacement of the free end from its original position (without the load) was measured in y -axis direction, and corresponds to the maximum deflection.

The correlation between strain and variation of the electrical resistance was investigated under two different deformation histories, schematically shown in Fig. 30b and Fig. 30c. Five precision weights (sized 50 g, 100 g, 200 g, 500 g and 1 kg) were used as loads: these values ensured that the maximum stress level was below the elastic limit of the material; indeed, the tensile yield strength of the commercial PVC is considered below 10 MPa, while the silver is higher than the 3% [192]. In the first test, called cyclic loading-unloading test, each weight was applied-unapplied 6 times every 5 s, in order to find the gauge factor of the sensor. For negative strain, the tube was turned and positioned with the sensor on the concave side. In the second test, the time interval of the loading was increased to 60 s, in order to define the resistance decay over time.

All the tests were performed at room temperature ($25\text{ }^\circ\text{C} \pm 1\text{ }^\circ\text{C}$) and two different tubes were tested. The coefficient of linear thermal expansion of PVC is typically between 50 and 100 ppm/ $^\circ\text{C}$. In this work, the temperature effects on the resistance change due to tube expansion were considered negligible because of the modest temperature fluctuations. Indeed, the temperature drift of $2\text{ }^\circ\text{C}$ could cause a strain drift of only 0.02%. For the same reason, the effects of the temperature on the resistance change due to the resistivity change were considered negligible with respect to the mechanical deformation. Indeed, the temperature coefficient of resistance (TCR) is expected lower than the TCR of the bulk silver

(0.004 /°C), while the gauge factor is expected around 2 (as for the conventional strain gauge sensor).

5.2.4 Experimental Results

a) Young Modulus

According to the elementary cantilever beam theory, when a $-F$ load is applied, the maximum deflection (h_{max}) of the beam (of length L) is

$$h_{max} = \frac{|F| \cdot L^3}{3 \cdot E \cdot I} \quad (17)$$

where I is the moment of inertia of the cross-sectional area with respect to z-axis and E the is Young modulus. In the case of a hollow circular section with inner d_{in} and outer d_{out} diameters, I is

$$I = \frac{\pi(d_{out}^4 - d_{in}^4)}{64} \quad (18)$$

Combining (1) and (2), the Young modulus can be calculated as

$$E = \frac{64 \cdot |F| \cdot L^3}{3\pi(d_{out}^4 - d_{in}^4) \cdot I} \quad (19)$$

By applying a weight of 1 kg, the measured maximum displacement was 23 mm. According to (3), the Young modulus is 1.7 GPa.

According to the flexure formula, the bending stress σ_x at the surface (convex side) and next to the fixed end is

$$\sigma_x = -\frac{-F \cdot L \cdot \frac{d_{out}}{2}}{I} = \frac{-m \cdot g \cdot L \cdot \frac{d_{out}}{2}}{I} \quad (20)$$

where m is the mass of the applied weight.

The strain (ε) below the elastic limit is

$$\varepsilon_x = \frac{\sigma_x}{E} \quad (21)$$

According to (20) and (21), the maximum stress and the maximum strain were 8.17 MPa and 0.47%, respectively.

b) Electrical response

The experimental results shown in Fig. 31 and Fig. 32 were obtained on one tube during the test shown in Fig. 30b, but they are comparable with the results obtained on the other tube, confirming good repeatability of the fabrication process.

In Fig. 31a, an example of the waveform of resistance measured during the six loading-unloading cycles (weight = 500 g) is shown. The initial resistance is 34.51 Ω and the variation change 0.175%. The corresponding waveform of the applied load is shown in Fig. 31b.

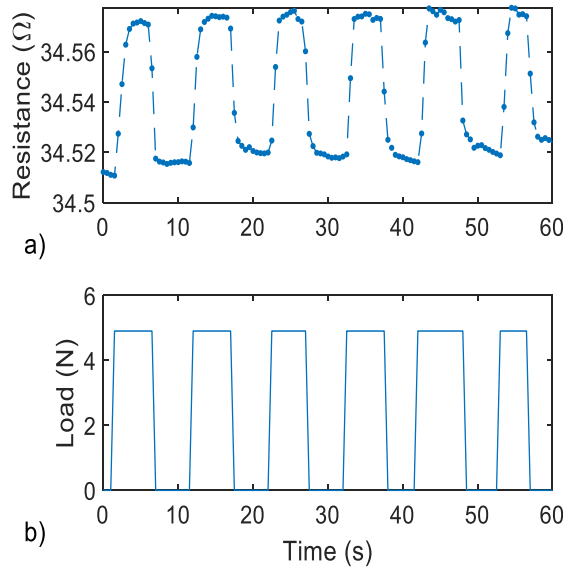


Fig. 31 (a) Resistance and (b) load curves during the six loading-unloading cycles when a weight of 500 g is applied and the sensor is on the convex side [97].

The relationship between sensor's resistance change and strain, calculated according (20) and (21), was found through loading-unloading tests. Since σ_x and ε_x depend linearly on the distance between the x -point and the application of the weight, we considered $L = 367$ mm, which corresponds to the distance between the middle of sensor's sensitive area (x -point) and the application of the weight. According to the state of art, electrical resistance (R) and strain (ε) are linearly dependent below the elastic limit, and the ratio is called gauge factor (GF),

$$GF = \frac{\frac{R - R_0}{R_0}}{\varepsilon} = \frac{\frac{\Delta R - R_0}{R_0}}{\varepsilon} \quad (22)$$

where R_0 is the electrical resistance of the unstressed sensor. For both tubes, the initial resistance is $(35 \pm 1) \Omega$, and this suggests good reproducibility of the printing method.

The experimental results of the test shown in Fig. 30b are summarized in Fig. 32.

The sensor behavior on concave side (red color) and the one on convex side (blue color) were investigated separately. For each weight, the average value of the resistance measured during each loading cycle was calculated and the error bars define the range of its variation in the six cycles. The asterisk markers are the resulting average. The R_0 value is the resistance measured at the beginning of the first cycle. The gauge factor GF is the slope of the best-fit line using the least square method. The GF for positive and negative strain is equal to 1.0417 and 1.0758, respectively; the Pearson correlation coefficient (r) is higher than 0.99. The average resistance decreases of about 0.026% when the weight is 1 kg (worst case), which it suggests a good repeatability of the measurements.

The experimental results referred to the test of Fig. 30c are shown in Fig. 33. By applying a constant weight for 50 seconds, the relative change of the resistance with respect to the nominal value decreases from 0.001% (weight = 0.05 kg) to 0.0594% (weight = 1 kg). The resistance change is still maintained linearly dependent on the strain. Considering the average value over 50 s, the gauge factor decreases to 0.99. The printed strain gauge sensor could show nonlinear response due to certain physical parameters, such temperature, especially on polymer surface as reported in [193], [194]. A mechanically stabilizing encapsulation could reduce the nonlinear effects on the sensor response, however it causes a lower sensitivity of the sensor, as proved in [195].

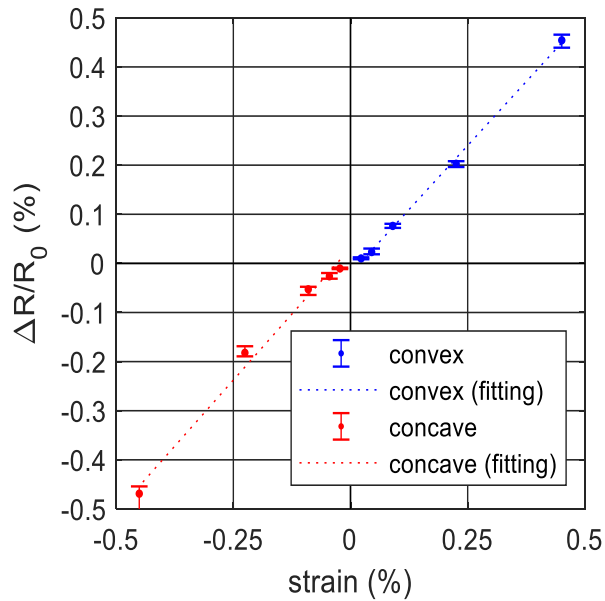


Fig. 32 Measured resistance change normalized on the initial resistance ($\Delta R/R_0$) as a function of strain, when the sensor is on the convex side (blue color) and on the concave side (red line) [97].

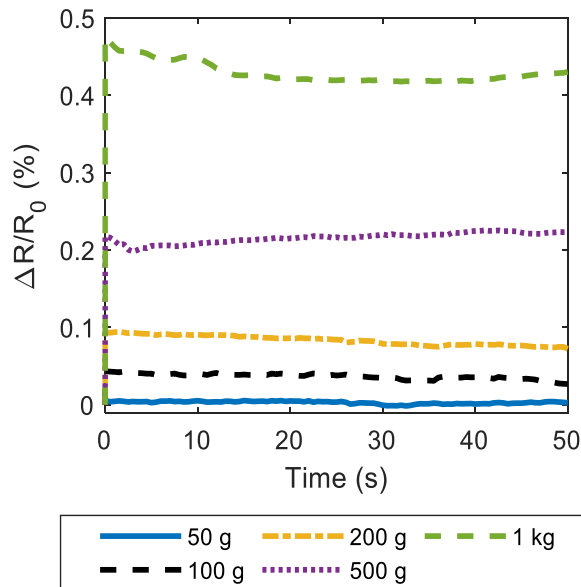


Fig. 33 Response of the sensor when a weight (from 50g to 1 kg) is applied and maintained constant in time [97].

5.2.5 Conclusion

A metallic strain gauge was printed on a 3D plastic surface by using AJP and FLA, highlighting the possibility to deposit inks on complex surfaces. Strain sensors directly embedded on the surface ensure the maximum adhesion avoiding gluing issues. Experimental results proved the possibility to measure a strain of 0.5%, unlike the classical strain gauge sensors. As expected, the electrical resistance depends linearly on the strain, in accordance with the silver properties of the deposited material. The calculated gauge factor is around 1, with a low number of parallel lines. On the other hand, FLA ensured a proper sintering process, without changing the mechanical properties of the plastic surface.

6. Smart Sensors and Objects in Packaging Sector

6.1 Paper PCB Hybrid Circuit

The research work reported in this section was published in the MDPI journal *Sensors* with the title *Printed Smart Devices on Cellulose-Based Materials by means of Aerosol-Jet Printing and Photonic Curing* [84]. Results and pictures are reported with permission of the editor.

6.1.1 Introduction

Driven by greater attention to the environmental impact of the materials used, research is increasingly favoring the study and use of substrate materials such as paper. This choice is due to paper's unique capabilities and properties (high Young's modulus, biodegradability, biocompatibility, renewability, low-cost, lightweight). In light of this, paper electronics is emerging thanks to the possibility to realize circuits and electrical components avoiding conventional techniques [196]–[199] but presenting limitations in the realization of complex devices which can be produced only considering multilayer steps, thus lengthening the manufacturing process [109]. Thanks to paper ease of functionalization, different techniques have been proposed, like the so-called 3D-origami technique, consisting in a specific paper folding to develop a final electro-device [200], [201]. The advantage of this technique is at the same time a drawback and a limitation, since origami electronics devices are simple to use and develop, but they need human presence to follow the specific folding procedure, otherwise the device will be useless. Another possible fabrication method is transfer printing, consisting in the use of an intermediate stamp for the transfer of a geometry on the substrate, obtaining flexible and stretchable complex structures. The main challenge is the ink transfer from the stamp to the final substrate, especially for soft and flexible substrates such as paper [202]. Also laser-assisted techniques have been proposed, but the heat source must be controlled to avoid defects and damages [203], [204].

Considering the abovementioned limitations, the innovative methodologies proposed in this dissertation can outgo these factors. The possibility to realize smart devices (also on 3D surfaces and with 3D interconnections and multilayer features) by means of AJP and FLA on cellulose-based substrates was investigated, providing a step-by-step guide to fabricate a complete device. The manufacturing method is tested on three different cellulose substrates (chromatographic paper, photographic paper and cardboard), in order ensure the

compatibility between employed materials and their functionality in different working conditions. Printed samples were initially tested to evaluate curing parameters and mechanical behavior in bending situations, together with electrical resistance in presence of a damp environment. Finally, the manufacturing method was used for the fabrication of a multilayer smart-3d-device equipped with printed capacitive touch sensors, electronic components and 3D interconnections. The proposed method could develop in the future 3D-functionalized objects with low-cost and environmental-friendly materials like cellulose based one, i.e. objects able to interact with human beings and the environment and measure physical quantities.

6.1.2 Materials and Methods

a) Materials

HPS 108-AE1 (Novacentrix, Austin, Texas, USA) is the selected conductive ink for printing tracks and interconnections in this work. It is an aqueous suspension of silver flakes, specifically formulated for AJP, containing a polymeric additive to strengthen the adhesion to substrates. For bonding and insulating, a UV-curable polymer is selected, its commercial name is NOA 81 (Norland Products, Cranbury, New Jersey, USA); it is a fast UV-curing adhesive, which produces, after curing, a hard, resilient bond. This ink is characterized by a viscosity of 300 cP at 25 °C, showing an excellent adhesion on glass, paper and metal, and a fair adhesion on plastics; it is known to be biocompatible. In this work, it was used as insulating layer to realize a multilayer structure, as gluing medium to place SMDs and as insulator for the capacitive touch sensors developed in the final prototype.

As cellulose substrates, three different types were selected: chromatographic paper, photographic paper and packaging cardboard. Whatman chromatographic paper grade 1 (GE Healthcare, Little Chalfont, Buckinghamshire, U.K.), was purchased from Carlo Erba, selected because of its characteristics of purity without additives of any kind that guarantees the total absence of contamination, high quality and homogeneity. It is used for biosensors, chemical sensors, point of care systems and is characterized by a thickness of about 180 µm. Photographic paper Hp Everyday A4 Photo Paper (Hp, Palo Alto, California, USA) was purchased from a local shop, selected because of its ease of handling and usage in relationship with inks. Photopaper presents a thickness of about 400 µm. It is widespread and used for low-cost applications. Packaging cardboard (thickness of about 250 µm) was sourced from internal stock and was selected since it is a recycle material, used for

packaging thus with a higher mechanical stiffness respect to the other two selected substrates.

b) Manufacturing of conductive tracks and insulating coatings

The block diagram in Fig. 34 depicts the proposed manufacturing process. In (b), Ag tracks are realized by using AJP and cured by FLA. In (c), SMDs (surface mount devices) are placed on the substrate. Flat no-leads packages such as quad-flat no-leads (QFN) and dual-flat no-leads (DFN) are placed in a lateral chip configuration, so as to have the pads positioned up. In (d), NOA 81 was selectively deposited by using AJP and exposed to UV light during printing to fix SMDs on cellulose and to make an insulating coating on tracks for multilayer purposes. Phase (e) consists in printing Ag track by AJP and curing by FLA to interconnect components. To manufacture multilayer circuits with more than two layers, phase (d) and (e) could be repeated.

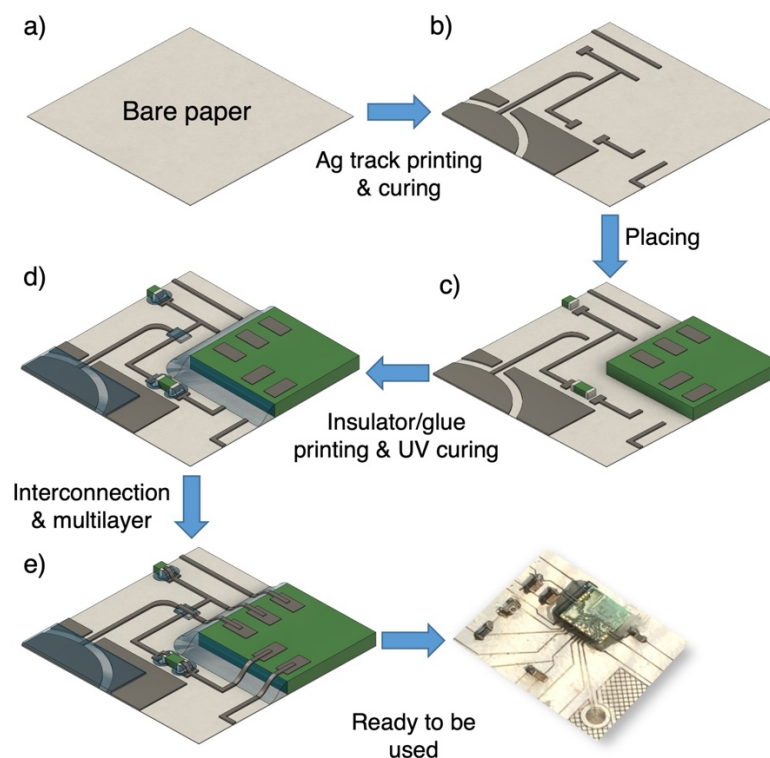


Fig. 34 Block diagram of the circuit manufacturing steps: the first phase regards Ag ink deposition and FLA curing; the second step involves the placing of SMDs and packaged components; step three is focused on the deposition of NOA 81 to fix previously placed packaged components and as insulator on specific Ag tracks and capacitive sensors; the last phase regards the final Ag deposition in multilayer zones of the circuit and to interconnect Ag tracks with packaged components [84].

c) Ag ink deposition and Photonic Curing

The process parameters considered during the steps regarding Ag ink printing are reported in Table 3. To reach the desired conductivity values, Ag ink was deposited ten times on chromatographic paper and cardboard, five times on photographic paper before curing. Fig.

35 shows the printed samples that were used for experimental tests on the different substrates. These consist of a U-shaped trace of about 44.55 mm long. After printing Ag ink, the samples were oven-dried at 140 °C as suggested by the ink manufacturer.

Table 3 Printing process for Ag ink.

Process parameters	HPS 108-AE1
Sheath gas flow (SCCM)	500
Atomizer gas flow (SCCM)	1350
Exhaust gas flow (SCCM)	1000
Plate temperature (°C)	35
Process speed (mm/s)	1

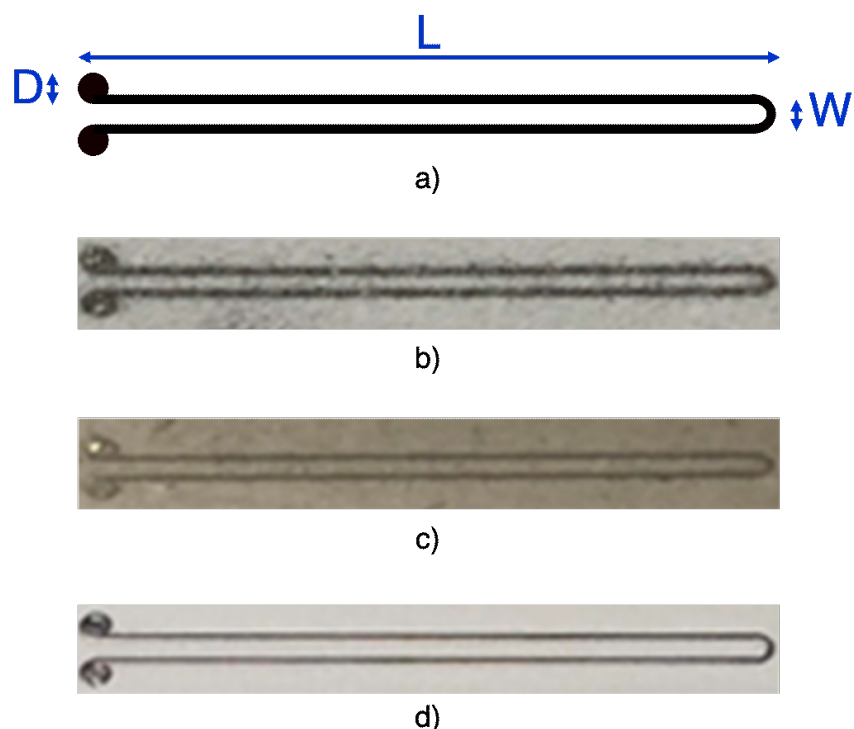


Fig. 35 (a) Pattern and geometrical dimensions of printed samples ($L = 22.5$ mm, $D = 1$ mm, $W = 1$ mm). Image of resulting samples printed on (b) chromatographic paper, (c) cardboard and (d) photopaper [84].

Being the voltage of the lamp and time duration of single impulse the two main process parameters, these two were studied during the experiments. To better understand the influence of these two aspects and define the best photonic curing parameters for each substrate, the printed samples were cured with a single lamp flash at four different time durations (1200, 1400, 1600 and 1800 μ s) and for each of these, the voltage was varied, increasing this factor of 20 V per flash irradiation. A total amount of 285 samples was tested.

Fig. 36 summarizes electrical resistance analysis, performed right before and after curing through the digital bench-top multimeter Hewlett-Packard HP34401a. Testing probes to the pads at the extremities of each sample in 4-wire resistance measurements were applied using a probe station with 4 probe holders. Resistance measurements were performed in laboratory under controlled environmental conditions. For each point of the plots in Fig. 36, three samples were tested. The results of these measurements are reported in terms of ratio between the final resistance (R) of the sample after curing versus its own resistance before curing (R_0).

On chromatographic paper, a mean resistance before curing of 11.9Ω was found, with a relative standard deviation (RSD) of 38%. In Fig. 36, each one of the four series shows a significant decrease of the resistance after curing near 460 V, which then deviates in a sort of plateau. The results show a minimum resistance in correspondence of 580 V & 1200 μ s, 560 V & 1400 μ s, 520 V & 1600 μ s and 500 V & 1800 μ s with values of 2.62Ω (RSD = 9 %), 1.7Ω (RSD = 1 %), 1.75Ω (RSD = 2 %) and 1.52Ω (RSD = 3 %), respectively. The last combination (520 V & 1800 μ s) appears to be the most efficient, achieving the lowest resistance (1.52Ω , RSD = 3 %), with a resistance reduction of 83 %.

Ag samples on cardboard have a resistance before curing of 13.02Ω (RSD = 19 %). The procedure was similar to the one for chromatographic paper substrate, the samples presented a plateau which is common to all sintering durations. More specifically, 1200, 1400, 1600 and 1800 μ s, showed their minimum in resistance in correspondence of 580, 560, 520 and 500 V with a value of 1.98Ω (RSD = 1 %), 1.92Ω (RSD = 19 %), 2.085Ω (RSD = 2 %) and 2.085Ω (RSD = 1 %), respectively. The curing process allowed to reach a resistance reduction of about 85 %. In order to limit R.S.D., 1200 μ s and 580 V can be proposed as best sintering parameters.

Ag samples printed on photographic paper presented a mean resistance before curing of 6.9Ω (RSD = 39 %). Thanks to the sintering process, it is possible to achieve a resistance reduction of about 73 % showing the best compromise in presence of 1400 μ s impulse duration at 540 V (mean resistance = 1.26Ω , RSD = 6 %). 1200, 1600 and 1800 μ s show their best in correspondence of 540, 500 and 480 V and the specific resistance values are 1.5Ω (RSD = 10 %), 1.78Ω (RSD = 8 %) and 2.035Ω (RSD = 11 %), respectively. In fact, in case of 1600 and 1800 μ s, resistance values are higher, and this fact can be connected

to a higher thermal stress which can cause fracture along the length of the sample. This event happened in all situations when the tracks reached a thermal state in which some cracks take place, as witnessed by the ascents shown from each curve at high voltage levels.

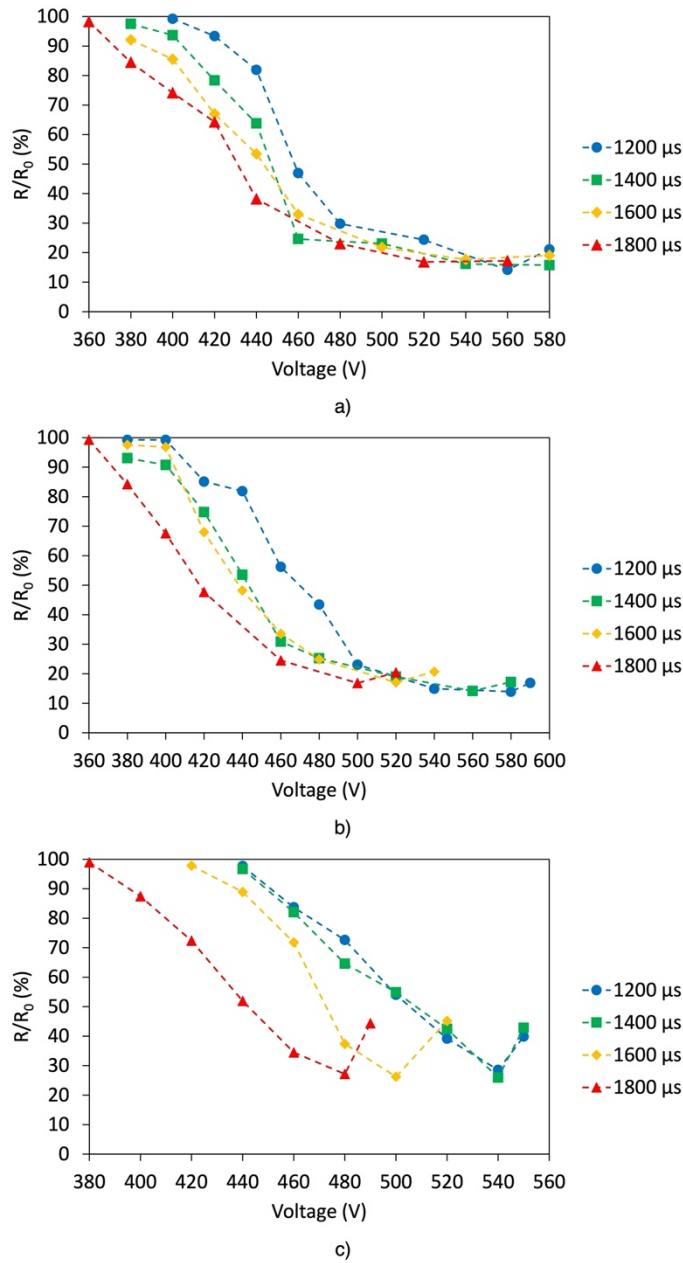


Fig. 36 R/R_0 vs Voltage depending on impulse duration for (a) chromatographic paper, (b) cardboard and (c) photopaper [84].

d) *Insulator printing and UV polymerization*

The capability of AJP to selectively print different inks was investigated printing insulating or adhesive inks for insulating tracks or fixing SMDs. NOA 81 is a liquid adhesive photopolymer that can be easily printed by AJP. The ink has been UV-cured during deposition by using the LED Spot type Panasonic ANUJ6180 (Panasonic, Osaka, Japan) and the lens

ANUJ6423 as UV Curing System, characterized by a spot diameter of 3 mm, a peak UV intensity of 17200 mWcm⁻² at an irradiation distance of 8 mm. In our tests, the selected power was 5 % of the maximum peak intensity. NOA 81's specific printing process parameters are reported in Table 4. Specifically, NOA 81 was used as insulating layer for capacitive sensors, to glue SMDs on cellulose-based substrates during placing step and to create the intermediate layer in multilayer zones of the circuit. The SMDs and IC were placed and fixed on the substrates thanks to NOA 81, realizing an oblique wall on which connections between component pads and silver tracks on paper were printed. Correct placing was ensured by pads and fiducials, specifically designed for each kind of SMDs to place (Fig. 37).

Table 4 Printing process for the photopolymer NOA 81.

Process parameters	NOA 81
Sheath gas flow (SCCM)	600
Atomizer gas flow (SCCM)	1350
Exhaust gas flow (SCCM)	1000
Plate temperature (°C)	/
Process speed (mm/s)	1
Number of depositions	4

e) Multilayer and Interconnections

Ag ink was selectively printed to interconnects SMDs and previously printed tracks (Fig. 37), or multilayer zones (Fig. 38), permitting the manufacturing of two or more circuit layers. The optical microscope by Orma Scientific NB50T (trinocular zoom 0.8x–5x–LED), with its devoted HDMI MDH5 camera model, was used to acquire the images (Orma Scientific, Sesto San Giovanni, Milan, Italy).

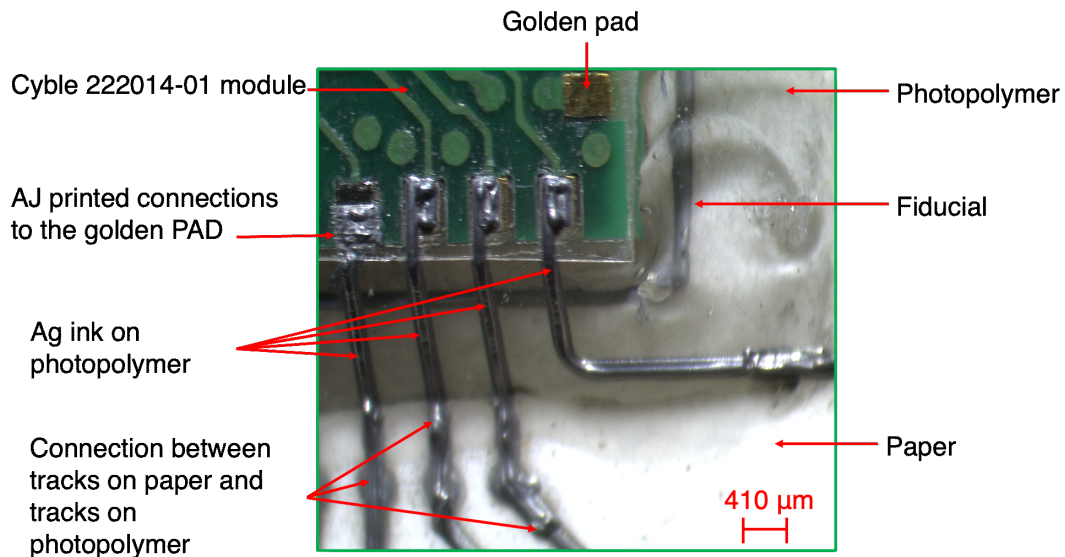


Fig. 37 Details of encapsulated programming module and printed tracks [84].

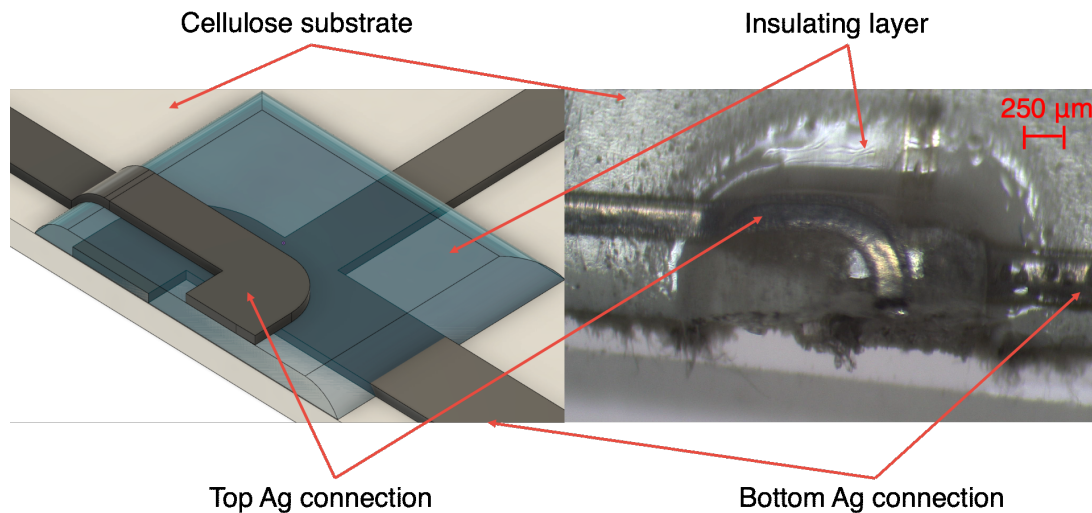


Fig. 38 Microscope magnification of a multilayer zone [84].

6.1.3 Results

a) Resistivity Analysis

In order to calculate the resistivity of the printed samples, geometrical analysis of the tracks was necessary. The morphology of the sample cross-sections was investigated by using a field emission scanning electron microscope (FE-SEM model LEO 1525, ZEISS) operated at 2–10 keV energy beam (Fig. 39). The microscope was coupled with an Oxford energy dispersive x-ray analysis (EDX). Samples were attached with carbon glue to metallic stubs to reduce charging effects due to the electron beam. Among the substrate employed in this study, chromatographic paper is the most hygroscopic one with great absorption capacity. This behavior is supported by SEM analysis, Fig. 39a shows the cross-section of the track analyzed by the EDX of the SEM system, evidencing the chemical composition of the sample and confirming the depth penetration of Ag ink in chromatographic paper. Thus,

considering what stated in the previous chapter, a longer impulse duration to fully penetrate in paper thickness is mandatory.

The need not to involve the entire thickness of the cardboard in the sintering process can be explained observing Fig. 39b: the silver ink does not penetrate completely thanks to its more compact structure, compared to the chromatographic paper that makes porosity its strength. Looking at the photopaper magnification in Fig. 39c, one can note that, unlike what happened in presence of chromatographic paper, Ag ink did not reach the total depth involving only a portion of the substrate thickness, so that high values of impulse duration are not mandatory.

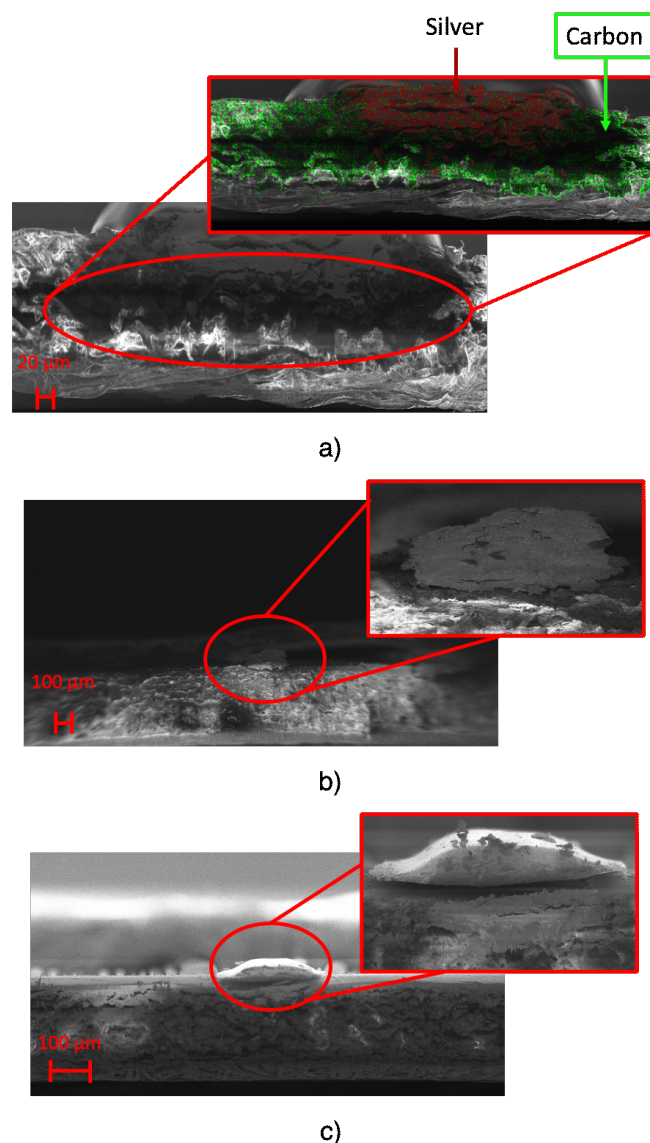


Fig. 39 Cross-section magnification performed thanks to the abovementioned FE-SEM for samples printed on (a) chromatographic paper, (b) cardboard and (c) photopaper [84].

The geometrical analysis was then performed on cellulose samples thanks to Filmetrics Profilm 3D optical profilometer (Filmetrics Inc., 10655 Roselle St., San Diego, CA United

States of America), to evaluate the shape of the printed lines. It is based on state-of-the-art white light interferometry (WLI), a non-contact optical method for surface height measurements on 3-D structures, to measure surface profiles and roughness down to 0.05 μm . The instrument works in the range of 50 nm – 10 mm with substrates and materials characterized by a reflectance between 0.05 – 100 %. The system implements a 5MP camera, the Nikon CF IC Epi Plan 20x model (field-of-view: 1.0 mm x 0.85 mm). The samples were measured in three different areas along the total length in order to state the stability of the thickness. The parameters evaluated in this phase are the total thickness, calculated as the difference between the maximum height and 1 % of this value, and line width, calculated as difference between two consecutive 1 % values on the two sides of the maximum height.

Fig. 40 shows profilometer data obtained for the three different substrates, with a visual representation of lines geometry and a heat map regarding the thickness of a single line. The mean thickness and line width of the chromatographic samples are, respectively, 24.9 μm and 274 μm with RSD = 15 %. The result achieved is due to the intrinsic nature of chromatographic paper, which is a 3D network of fibers with hydrophilic properties which tends to absorb a liquid. Silver deposition on cardboard shows a peak height which is higher respect to chromatographic paper, about 51 μm with a total width about 258.05 μm (relative standard deviation of 18 % and 10 %, respectively). As for photopaper, the mean thickness for Ag lines printed on this substrate is 28.5 μm with a relative standard deviation of 12 %. On the other side, mean line width is 255.5 μm with a relative standard deviation of 4 %. It must be kept in mind that the number of depositions on photopaper are the half of the other substrates.

Once defined the geometrical profiles, samples volume resistivity was evaluated and compared with the one reported in the manufacturer data sheet. Volume resistivity was calculated considering the definition of resistance:

$$R = \rho \cdot \frac{l}{S} \quad (23)$$

where R is the total resistance of the sample, l is the total length of the sample and S represents the section of printed track. The calculated resistivity is about $26.3 \cdot 10^{-8} \Omega \cdot \text{m}$,

22.3·10⁻⁸ Ω·m and 13.1·10⁻⁸ Ω·m respectively for chromatographic paper, photopaper and cardboard. These values agree with what Novacentrix declared on the data sheet, which are in the range from 14·10⁻⁸ Ω·m to 44·10⁻⁸ Ω·m, depending on deposition and curing parameters.

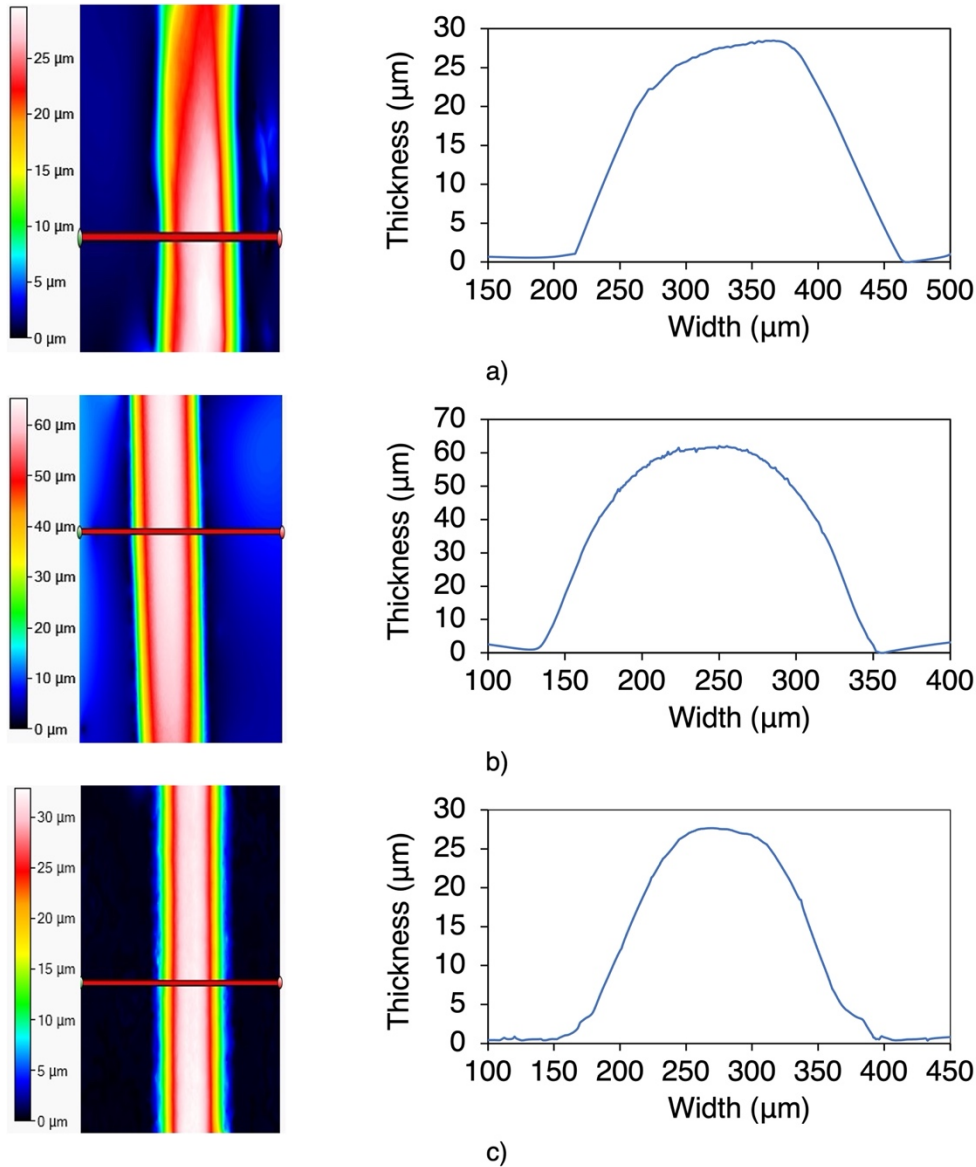


Fig. 40 Thickness profile for Ag on (a) chromatographic paper, (b) cardboard and (c) photographic paper [84].

b) Electrical and Mechanical Stability under Bending Conditions

A bending test was performed using a custom support fabricated via additive manufacturing, consisting in a beam with a rotating part. Thus, it was possible to perform complete 0-90° manually operated movements. Resistance changings were recorded using the digital bench-top multimeter Hewlett-Packard 34401a connected thanks to a GPIB-USB cable to a personal computer and monitored thanks to a program written in LabVIEW. The bending angle measurement was simultaneously performed via the STEVAL-MKI005V1 MEMS

(STMicroelectronics, Plan-les-Ouates, Geneve, Swiss). Fig. 41 shows a schematic representation of the experimental set-up employed during bending test.

Fig. 42 shows how Ag ink samples paper behave under a bending load, also depending on the type of paper substrate. The results of these measurements are reported in terms of ratio between the resistance measured at a specific bending angle (R) versus its own resting resistance (R_0). Considering chromatographic paper, in the range 0-90° only restricted variations take place with a quasi-stationary value, thus aiming that during the bending cycle the sample did not break up. Focusing the attention on cardboard, Fig. 41 underlines that a substrate with a higher mechanical stiffness (with respect to chromatographic paper) shows limited variations until 70°, while reaching 80° the resistance value is about five times the starting value. Then possible cracks appear along the track and this fact led to an increase of orders of magnitude of resistance reaching a complete break up approaching to a bending angle of 90°. If compared to the other two substrates, photographic paper behaves in a third different way: the samples presented a quasi-constant value of resistance until 60°, during this first load time interval some cracks developed so that the samples undergo breaking before reaching the maximum degree of bending. To give evidence of these behaviors, SEM analysis was performed in order to state the microscopic aspect of the printed tracks before and after bending test (Fig. 43). Considering the samples on photopaper (Fig. 43e and Fig. 43f) and cardboard (Fig. 43c and Fig. 43d), SEM magnifications evidenced the presence of severe cracks (Fig. 43d and Fig. 43f) that caused variations in the section of the tracks until a total break up. SEM showed the presence of small cracks also on the surface of Ag tracks printed on chromatographic paper (Fig. 43b). Since we do not encounter any critical rupture in chromatographic samples, we assume that the influence of these cracks is superficial. Future studies that require more samples and a different configuration of the setup will further analyze deeply this behavior.

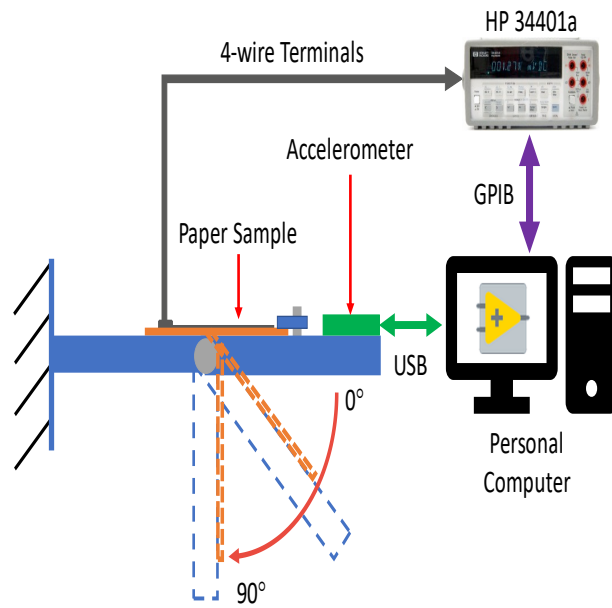


Fig. 41 Schematic representation of the bending test [84].

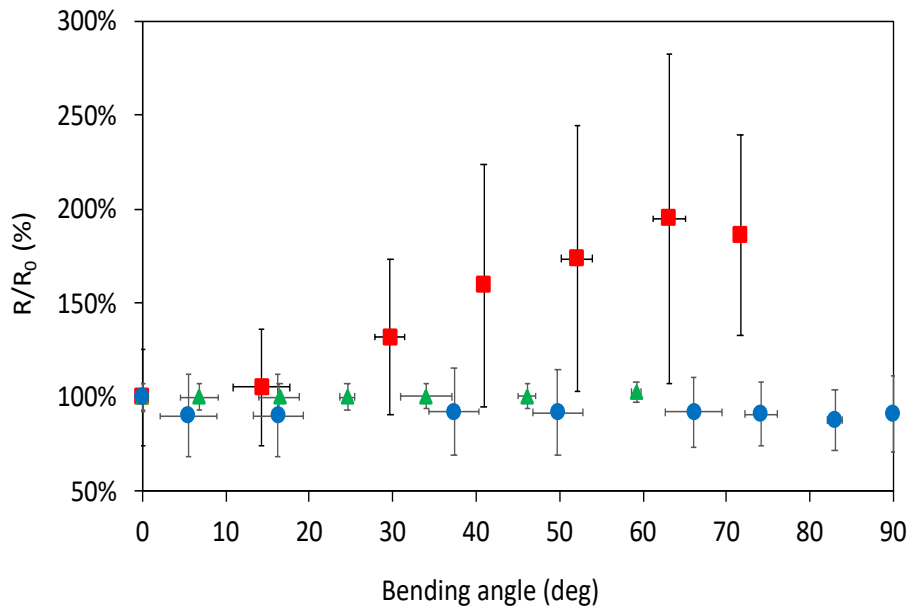


Fig. 42 Resistance variations as a function of the bending angle on chromatographic paper (blue circle), cardboard (red square) and photographic paper (green triangle). Vertical error bars are related to standard deviation of resistance values, while horizontal ones are related to standard deviation of resistances values, while horizontal ones are related to standard deviation of angle values [84].

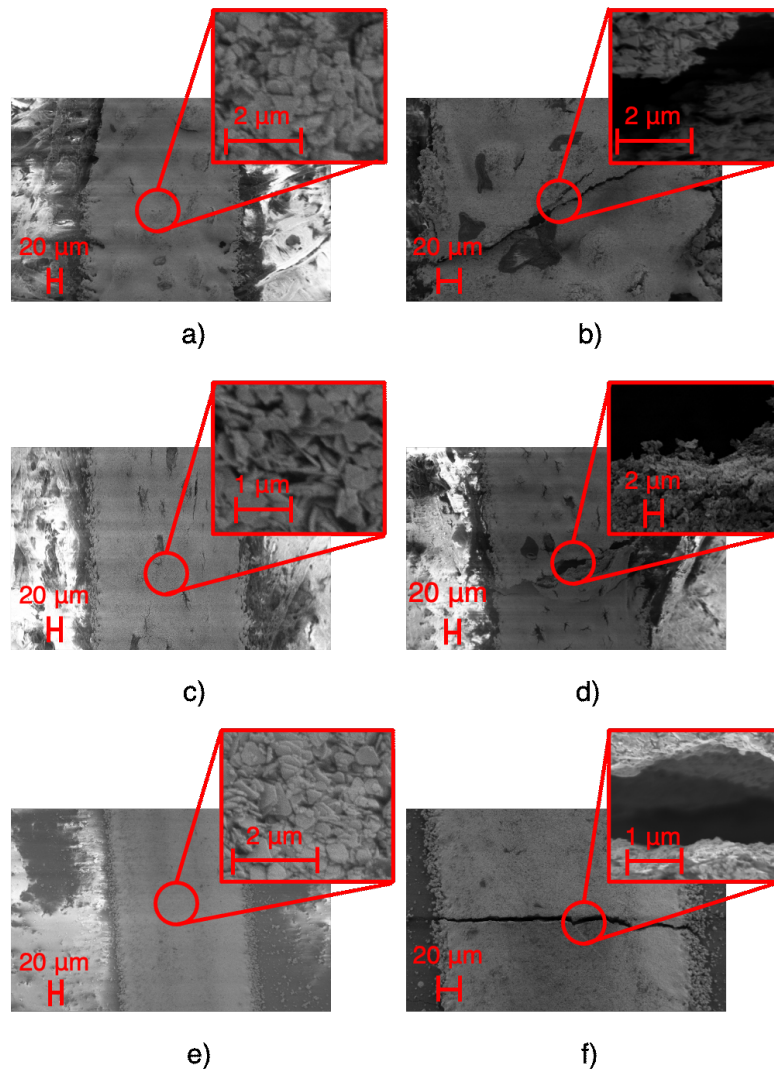


Fig. 43 SEM magnifications of (a) chromatographic paper before bending, (b) chromatographic paper after bending, (c) cardboard before bending, (d) cardboard after bending, (e) photopaper before bending, (f) photopaper after bending [84].

c) Electrical Stability in Damp Environment

Ag samples printed on cellulose-based materials were also tested in a damp environment in order to check possible resistance variations due to an increased relative humidity (RH). Six samples, for each kind of substrate, were placed inside the incubator MCO-170M (PHC Panasonic Healthcare Holdings Co., Tokyo, Japan) in order to keep the temperature stable during the tests at around 27 °C (± 0.2 °C). The damp atmosphere was generated thanks to an ultrasonic mist maker, temperature and relative humidity parameters were monitored thanks to the evaluation board HDC 1080 EVM (Texas Instruments, Dallas, Texas USA). Resistance changings were recorded for 13 minutes using the digital bench-top multimeter Hewlett-Packard 34401a controlled through a GPIB-USB cable by a custom-made LabVIEW Virtual Instruments interface.

Table 5 shows these measurements in terms of ratio between the sample resistance (R) measured at 35, 45, 55, 65 and 80 % RH versus the sample resistance at the starting relative humidity point (R_{35}). As expected, no significant resistance variation was registered during this test. These combinations of substrate and Ag ink can carefully work in presence of high relative humidity.

Table 5 Samples resistance behavior in a damp environment.

%RH	R/R ₃₅ (%)		
	Chromatographic Paper	Cardboard	Photopaper
35	100 ± 6	100 ± 4	100 ± 9
45	101 ± 9	95.3 ± 6	99.3 ± 8
55	102 ± 8	102 ± 6	99.7 ± 9
65	103 ± 6	95.7 ± 3	98.6 ± 8
80	96 ± 7	94.4 ± 8	97.3 ± 8

d) Multilayer Smart-3D-Device

The proposed manufacturing method was used for the fabrication of a multilayer smart-3D-device. We fabricated the circuit through the proposed method on a photopaper tube (Fig. 44). The device basically consists in a touchpad made of four capacitive touch sensors, a LED and a microcontroller, which perform a simple function: while one capacitive touch sensors is pressed by the finger, the LED is kept turned off (Fig. 45) and touchpad data are transmitted via the integrated Bluetooth module. The microcontroller is Cypress CYBLE-222014-01 module; PSoC Creator was the selected software to configure the firmware of the microcontroller. A flexible battery of 3.7 V and 12 mAh was used to give power to the device (Lionrock Batteries, Kowloon, Hong Kong). Resistances (5.1 and 1.1 kΩ), capacitors (150 and 3.3 pF), a ferrite chip (330 Ω at 100 MHz), Cypress CYBLE-222014-01 module and a red LED were placed on the substrate, glued by means of NOA 81 and connected to the tracks. The abovementioned components are characterized by 0603 package.

The tests on the printed capacitive touch sensors were realized both in case of pressing and not pressing the finger for 10 times, by means of the impedance analyzer HP 4194A. Impedance/phase measurements between ground and each one of the four tracks of the

capacitive sensors were performed from 1 kHz to 2 MHz using a compensated claw probe connected to analyzer HP4194A. Furthermore, electrical capacitance measurements were performed at 250 kHz, which is the working frequency of Cypress CYBLE-222014-01 module, by HP 4194A in fixed frequency configuration. Fig. 46 shows impedance magnitude and phase angle of the four capacitive touch sensors, evidencing that in the analyzed range they have a purely capacitive behavior. Table 6 shows the capacitance values (average and standard deviation) of the four capacitive touch sensors in the two analyzed conditions. The data show an increase in electrical capacity of about 42 % from no-finger to finger situation.

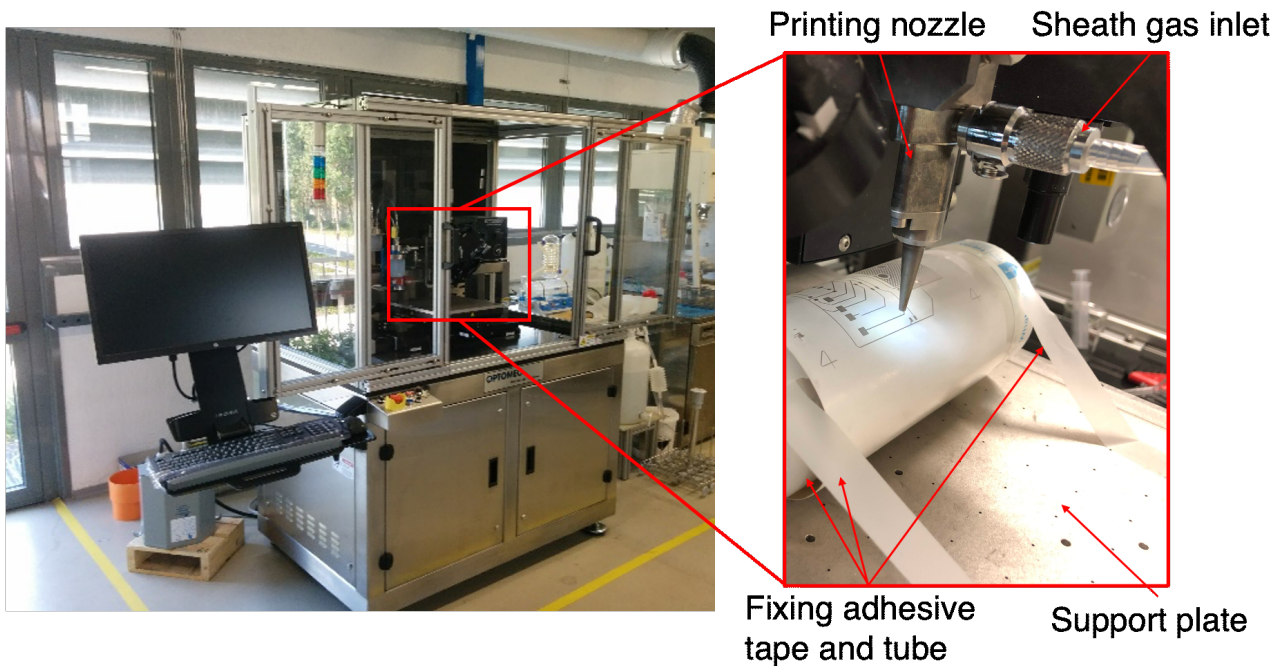


Fig. 44 Optomec AJ300 with photopaper tube during printing step [84].

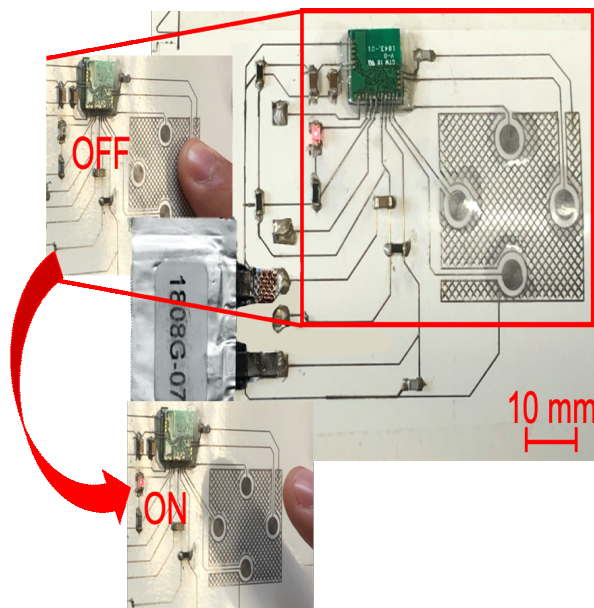


Fig. 45 Multilayer smart-3D-device [84].

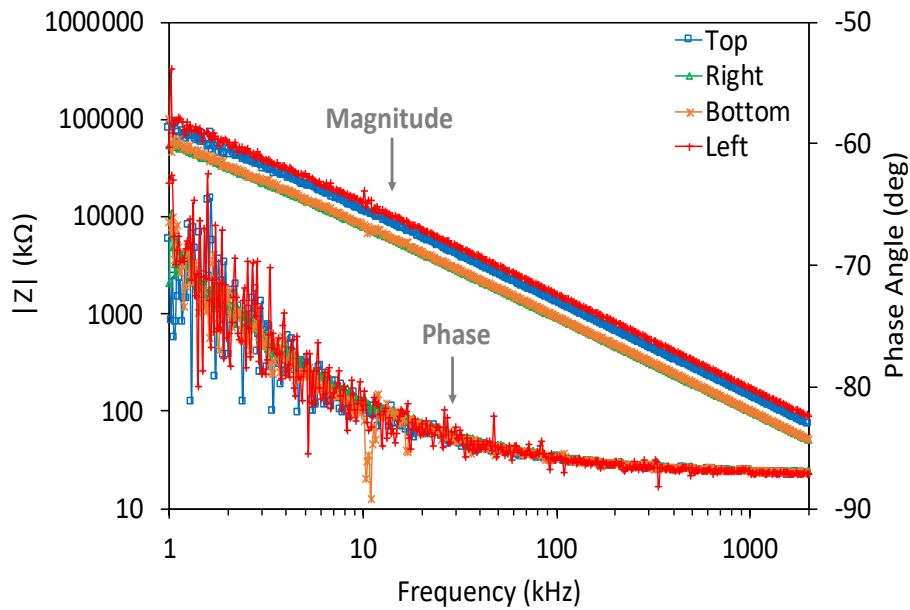


Fig. 46 Impedance magnitude and phase angle plots for top, right, bottom and left keys in no-finger state [84].

Table 6 Electrical capacitance values at 250 kHz for the capacitive sensors in case of finger in pression and not in pression.

Key position	Capacitance (pF)	
	No Finger	Finger in touch
Top	1.32± 0.08	1.86± 0.19
Right	1.92± 0.08	2.85± 0.35
Bottom	1.87± 0.09	2.72± 0.21
Left	1.13± 0.09	1.55± 0.15

6.1.4 Conclusion

A methodology to realize multilayer smart-3D-devices by means of AJP and FLA on cellulose-based substrates, specifically on chromatographic paper, photopaper and cardboard was reported. Curing parameters were optimized for each substrate, 1800 μ s and 500 V for chromatographic paper, 1400 μ s and 540 V for photopaper, 1200 μ s and 560 V for cardboard. Optical microscope, profilometer and SEM investigations have shown three different behaviors for the substrates in terms of line width and thickness. Under bending loads, chromatographic paper samples did not show any significant resistance variation suggesting they can still work properly, unlike sample printed on the other substrates which increase their resistance reaching a final break up. In presence of high relative humidity, silver tracks maintain their resistance values without any significant increase or decrease. The final circuit developed on photopaper tube is characterized by four capacitive touch

sensors that if pressed, they switch off a LED. Electrical capacity measurements evidenced an increase of about 42 % from non-pressed to pressed situation. The obtained results allow to demonstrate the applicability of the proposed method for the manufacture of smart electronic devices also on 3D cellulose substrates.

6.2 Printed Antenna for Resistive Sensors Readout

The research work reported in this section was presented in *IEEE 2021 II Workshop on Metrology for Industry 4.0 and IoT (MetroInd4.0&IoT)* and is part of the conference proceedings with the title *Preliminary Study on Wireless Passive Resistive Sensor Applied for Smart Objects* [205]. Results and pictures are reported with permission of the editor.

6.2.1 Introduction

Internet of Things (IoT) is one of the most appealing topics in many sectors. For example, it can be adopted to provide information about industrial production processes and to improve safety [206], to monitor the health and to support the early detection of medical issues [207], or to collect data for smart homes and smart cities [208]. IoT is a network of different smart devices that can collect and analyze data, and share information with other devices [10]. Among IoT devices, smart objects represent an interesting category of objects, because they are everyday objects with a specific function, but they are equipped with “intelligence” (sensors, computational ability, storage, *etc.*) [30]. Smart objects can be adopted in industrial background to improve efficiency, maintenance, and traceability. The object becomes “smart” when sensors or electronic devices are implemented on the object, but sometimes the installation of commercial devices is challenging due to geometrical constraints or materials compatibility. Furthermore, in some applications, specific requirements need the design of custom solutions, and they can include the fabrication of the electronic components directly onto the object [9].

An autonomous device that communicates wirelessly is preferred, when cables and wires could not reach the measurement device, or the installation and the replacement of batteries are challenging. For example, in smart packaging applications, only sensors capable of measuring temperature, humidity, and the presence of volatile amine compounds, to estimate food freshness should be installed on the package and should be interrogated wirelessly [209]. Passive telemetric systems based on a passive sensor (resistive or capacitive) and a coil coupled with a readout coil could represent a valid solution to read in real-time passive sensors [19]. In several cases, a sweep in frequency is required to read the output of the sensor [199], [210]. In [19], a telemetric method based on the impedance reading at a specific frequency is proposed to a resistive temperature sensor, but this method required a tuning capacitor to adjust the impedance. In this work, a coil and a tuning capacitor were manufactured in order to develop a passive telemetric system working at a

fixed frequency for Industry 4.0 and smart packaging applications. Investigations on the properties of the ink were carried out, then specific attention was put on the design and on the manufacturing process. The printed coil and the capacitor were tested from electrical and geometrical viewpoints, and they were used in a passive telemetric system to measure resistive components.

6.2.2 Design of the Sensing Coil

a) Theoretical Background

According to [19], the resistive sensor to be measured is connected to a tuning capacitor and a sensing coil, which is magnetically coupled with an external readout coil (Fig. 47a). In this application, all the components of the sensing part are printed directly onto a lid, and the resistance R_x of the resistive sensor could be calculated through the measurement of the impedance Z at the readout terminals. The sensor could be a resistive humidity sensor, a temperature sensor, or a piezoresistive sensor (for the pressure or force measurement). As discussed previously in [19], the electronic components could be modeled with lumped elements (L_1, C_1, R_1 for the readout inductor, L_2, R_2, C_2 for the sensing inductor, C_x for the tuning capacitor, R_x for the resistive sensor,), as depicted in Fig. 47b. The resistive sensor and the tuning capacitor are considered as ideal components. Fig. 47c is an example of Z real part depending upon R_x in the case of the resonance frequency of the sensing part (f_{r2}) lower than the one of the readout part (f_{r1}). The distance between the two coils affects the amplitude of $Re(Z)$: the greater is the distance, the lower is the sensitivity of the wireless system. To simplify the $Re(Z)$ formula, the following assumptions were considered:

R_x is greater than one kilo Ω ;

R_2 is negligible because R_2 is usually lower than some tens of Ω ;

the distance between the two coils is kept constant;

f_{r1} is greater than f_{r2} , to ensure good sensitivity of the measurement system for the R_x estimation.

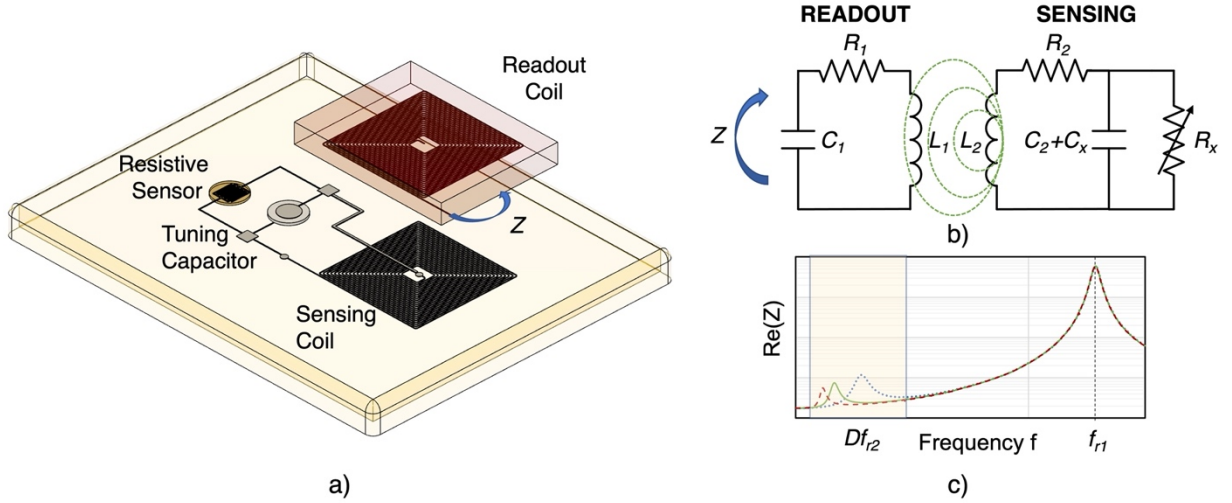


Fig. 47 (a) Schematic illustration of a smart lid for smart packaging. A resistive sensor is measured through the reading of the impedance of a readout coil, which is coupled with the sensing coil connected to the resistive sensor. (b) Lumped parameter circuit model of passive telemetric measurement system (c) Typical frequency response of the passive telemetric measurement system when the self-resonance frequency of the sensing coil is lower than of the one of the readout coil [205].

These assumptions allow calculating R_x by using (24), which is obtained from the simplified expression of $Re(Z)$ in (2) at the fixed frequency f_w expressed in (26), which corresponds to the self-resonant frequency of the sensing part:

$$R_x = \frac{L_2(Re(Z(f_w)) - R_1)}{\beta - C_0 \cdot R_2 \cdot (Re(Z(f_w)) - R_1)} \quad (24)$$

$$Re(Z(f_w)) = \frac{\beta \cdot R_x}{L_2 + R_x \cdot C_0 \cdot R_2} + R_1 \quad (25)$$

$$f_w = f_{r2} = \frac{1}{2\pi\sqrt{L_2 \cdot C_0}} \quad (26)$$

With

$$C_0 = C_x + C_2 \quad (27)$$

$$\beta = \frac{L_M^2}{L_2 \cdot n^2} = (Re(Z(f_w)) - R_1) \left(\frac{L_2}{R_x} + C_0 \cdot R_2 \right) \quad (28)$$

where the inductance L_M models the coupling flux between the two coils and n is the ratio between the equivalent number of windings of L_1 and L_2 . β can be calculated through a calibration procedure adopting resistors with a known value. This method allows simplifying

and optimizing the design of the impedance measurement circuit for the readout coil since the impedance measurement is performed at only one frequency.

b) Coil Design

According to the previous section, the estimation of R_x can be obtained by measuring $Re(Z)$ of the wireless system at f_w . In order to optimize the design of the equipment for impedance measurements, f_w is preferred to be lower than f_{r1} [19]. For example, the most common impedance/gain-phase analyzers are capable of measuring impedance up to 20/110 MHz. Furthermore, the proposed lumped parameter circuit model could not be valid for greater self-resonance frequencies. According to (26), in order to reduce the value of f_w , the coil should be designed with the greatest inductance L_2 .

A flat coil in the shape of a spiral is preferred for printed devices because it allows an easier optimizing of its geometry and aspect ratio [211]. Among the most typical geometries (circular, square, hexagonal, and octagonal) for spiral coils, the square spiral coil (an example is shown in Fig. 48) has the highest inductance for the same occupied area, as demonstrated in [212]. For inductance calculation, the modified Wheeler formula could be used for square spiral coil

$$L = 2.34 \frac{n^2 d_{avg}}{1 + 2.75\rho} \quad (29)$$

where n is number of turns, $d_{avg}=0.5(d_{out} + d_{in})$ and $\rho=(d_{out} - d_{in})/ (d_{out} + d_{in})$. d_{out} (the outer side of the coil) is usually defined by the constraints final application because it defines the encumbrance of the coil: even if a large area allows increasing L , it could be not compatible with the available printing area of the object. Since the coil will be printed by means of AJP, which is an additive technique, the corners will be smoothed to ensure smooth motion control of the printer and a uniform deposition along the printed path.

The optimization of L implies an increase of the coil resistance according to Ohm's law

$$R = \rho_{coil} \frac{l}{wt} \quad (30)$$

where ρ_{coil} is the resistivity of the conductive material of tracks, w is the width of the tracks, t is the thickness and l is the total length of the spiral track and could be expressed as

$$l \cong 4n(d_{out} - (s + w)(n - 1)) \quad (31)$$

where s the spacing of the tracks.

As assumed in the previous section, R should be kept low (up to some tens of ohms): a good practice is the increase of the thickness t or the use of conductive material with low resistivity.

The design of the coil (Fig. 48) started from the definition of d_{out} equal to 27 mm, because it defined a reasonable printing area for smart packaging applications. d_{in} was fixed to 4.5 mm due to the need to manually attached the wire to the internal pad of the coil. n was set to 23, because in [19] the self-resonant frequency on a coil with these same characteristics resulted lower than 40 MHz. The final dimensions are listed in Table 7.

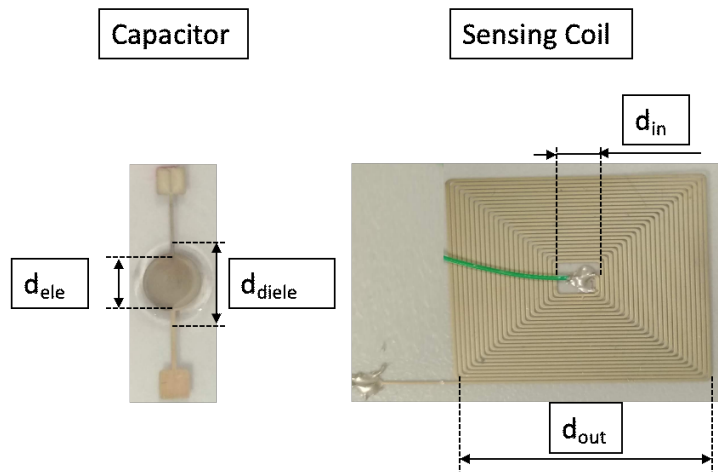


Fig. 48 Printed tuning capacitor and sensing coil [205].

Since AJP is capable of depositing layer with a thickness in the range 0.1-2 μm , the printing of the pattern would be repeated several times to increase the thickness t and thus to reduce R . The number of overlapped deposition (n_{dep}) was limited to four to ensure thickness uniformity of the printed track.

Table 7 Geometrical Characteristics of the printed Components and of the readout Coil.

Property	Sensing	Readout
Coils Characteristics		
d_{out} , outer side (mm)	27.25	27
d_{in} , inner side (mm)	4.5	4
n, number of windings	23	23
w, Winding width (μm)	250	300
s, Winding spacing (μm)	250	200
n_{dep} , Number of depositions	4	
Capacitor characteristics		
d_{el} , Electrode diameter (mm)	6	
d_{diel} , NOA 81 diameter (mm)	8	
n_{dep} , number of dielectric depositions	3	

c) Capacitor Design

According to (26)-(27), adding a capacitor in parallel to the coil is required to tune the self-resonant frequency of the printed coil. The self-resonant frequency of the printed coil could be tuned at a frequency around 12.5 MHz by printing an external capacitor. Therefore, since the capacitance of C_2 was expected to be lower than 5 pF, a tuning capacitor (the final device is shown in Fig. 48) was designed to reduce the self-resonant frequency of the sensing coil. As depicted in Fig. 48, the tuning capacitor is a parallel plate capacitor with round electrodes. The circle shape of the electrode ensures good uniform deposition by

means of AJP. The classical formula of a parallel plate capacitor with round electrodes of diameter d_{el} is

$$C = \varepsilon_0 \varepsilon_r \frac{\pi d_{el}^2}{4t_{diel}} \quad (32)$$

where ε_0 is the vacuum permittivity, ε_r is the relative permittivity of the dielectric layer and t_{diel} is the thickness of the dielectric layer between the two electrodes. Some overlapped depositions (n_{dep}) of dielectric ink for a uniform dielectric layer were considered. By combining (26) and (27), the tuning capacitor was designed to have a capacitance C_x equal to 20 pF when f_{r2} is set to 12.45 MHz. Defined the value of t_{diel} and ε_r (Section IVA) and by applying the inverse formula of (32), the resulting d_{el} was fixed to 6 mm (Table 7).

6.2.3 Materials and Methods

a) Materials

Smart Aerosol Conductive Ink (S-CS61308, Genesink, France), based on silver nanoparticles, was selected because it is suitable for applications requiring high conductivity and high resolution at very low curing temperatures (such as in the case of plastic or paper substrates). The ink was developed to design antennas, conductive tracks, and electrodes even on conformable or flexible substrates. The ink has a viscosity in the range 500-700 mPas and it requires to be atomized together with ethanol during the printing process to obtain a better printability and adhesion to the substrate. The expected resistivity is $4.5 \cdot 10^{-8} \Omega \text{ cm}$. NOA 81 (Norland Products Inc., Cranbury, New Jersey, USA), a UV-curable polymer, was selected to obtain the dielectric and insulating layer, as NOA 81 has already been resulted suitable for this type of application in [84]. The viscosity of the ink is 300 mPas at 25 °C. A polyester (PET) based substrate (Novele IJ-220) was selected as a substrate for the passive smart antenna because it is widely used for everyday objects. Furthermore, it is compatible with the selected ink and is thermally stable at the curing conditions recommended by the proposed fabrication process. For the prototype, 32 AWG wires were attached to the pads of the inductor and the capacitor by means of a conductive glue (CircuitWorks Conductive Epoxy CW2400) for electrical tests.

b) Manufacturing process

The AJ-300 Aerosol Jet Printer (Optomec, Albuquerque, NM, USA) was adopted in the pneumatic atomizer mode to deposit both the silver-based ink and the insulator ink. In the proposed method, the temperature of the platen that translates the substrate in the X-Y direction was fixed at 50 °C to dry the ink during the printing, and the printed speed was fixed at 2 mm/s. Printing process parameters tuned to obtain the desired track width are listed in Table 8. Process flows are expressed in the unit standard centimeter cube per minute (SCCM).

We drew the layout of the coil and the capacitor by using AutoCAD software, which can provide an output file to control the printer movements during the manufacturing process. The dimensions of each component, already discussed in Section II, are listed in Table 7. The two plates of the capacitor have the same layout, but they are symmetrical. The dielectric layer has a larger diameter to prevent shortcuts between the two plates.

As depicted in Fig. 49, while the inductor was printed in one single step, the capacitor and the track that electrically connect the inner pad of the inductor to one pad of the capacitor required three steps: at first, the silver-based bottom electrode was printed and thermally sintered, then the dielectric layer of the capacitor and the insulating track were printed and UV cured, and finally, the upper electrode and the conductive track were printed and thermally sintered.

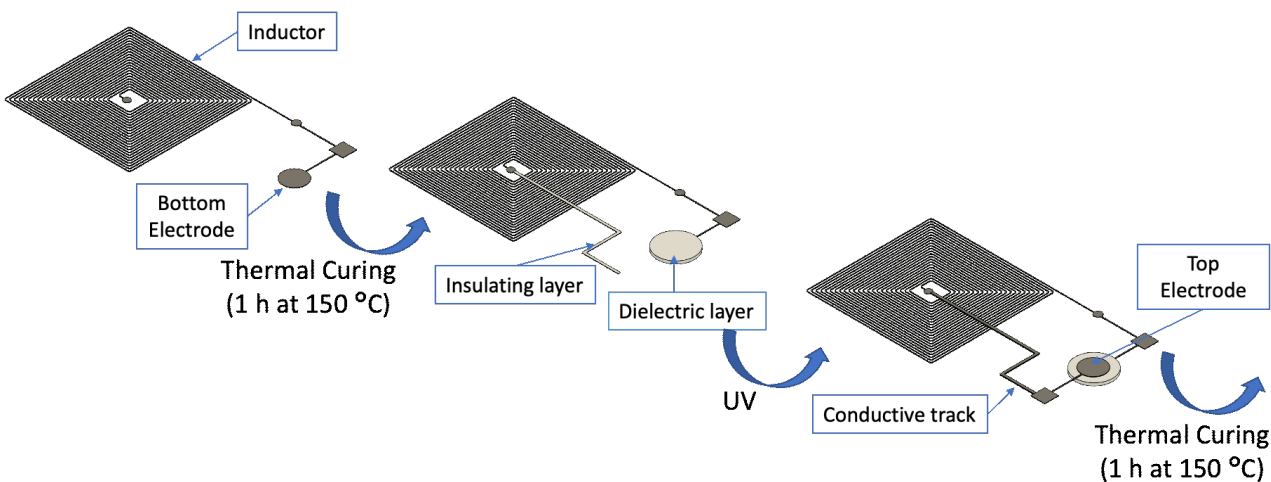


Fig. 49 Manufacturing process for printing coil and capacitor through AJP [205].

Several consecutive overlapped depositions n_{dep} of silver allowed reducing the resistance of the conductive parts (inductor, tracks, and electrodes) and the capacitance of the resulting capacitor. The deposition of the silver ink was repeated four times for all the conductive parts.

Once the coil, the conductive tracks, and the bottom electrode was printed, the printed prototype was thermally treated at 150 °C for 1 h (as recommended by the manufacturer) in an oven to sinter the ink and to reach the highest conductivity. The next step was the printing of the dielectric/insulating layers by using NOA 81. NOA 81 was cured in-flight during the printing process of the insulator layer by exposing it to a UV light, whose source is optional of the AJ-300 printer.

After the n_{dep} deposition of NOA 81, the upper electrode and the last conductive track were obtained by following the same manufacturing process adopted in the first step. Finally, the wires were attached to the pads of the inductor and the capacitor.

Table 8 Inks Process Parameters.

Parameter	S-CS61308	NOA81
Sheath gas flow (SCCM)	400	750
Atomizer gas flow (SCCM)	612	1350
Exhaust gas flow (SCCM)	610	1100

c) Characterization

Preliminary tests were performed for determining the geometrical characteristics (profile and width) of the printed layers and the impedance of the final device. The thickness and the width of the printed tracks, as well as the thickness of the dielectric layer of the capacitor, were measured by means of Profilm3D (Filmetrics, San Diego, CA, US). The measurements of the impedance from 100 Hz to 40 MHz were performed by means of an impedance analyzer HP4194A, while the resistance of the resistive device was measured by means of a multimeter HP34401A. The setting and the data acquisition were performed through a Virtual Instrument developed in LabVIEW and a GPIB USB module.

Finally, the printed device was validated with a readout coil fabricated with a Printed Circuit Board (PCB) technique. The telemetric system consists of:

- A square planar coil with copper tracks on a substrate of FR4 glass-reinforced epoxy (geometrical characteristics are listed in Table 7).

- The printed coil used as sensing inductor.
- The printed capacitor, connect in parallel to the sensing coil, for tuning the resonance frequency of the sensing device.
- A resistor connected in parallel to the sensing coil and the capacitor. The resistor represents the resistive sensor to be measured.

The two coils were kept in parallel and coaxial position, at a distance of 4 mm. We considered the measurement of a force resistive sensor (FSR) with a telemetric system as a real application because FSRs can be printed together with the sensing coil and the capacitor on the same substrate by easily modifying the manufacturing process. To know the resistance range of the FSR (Tekscan, MA, US) and thus R_x range, different and known weights (100 g, 200g, 500g, and 1 kg) were applied over the sensitive area of FSR and the resistance was measured by mean of a multimeter. The applied force is the product of applied weight and 9.81 N/m^2 . For the calibration of the telemetric system, three commercial resistors of known resistance were adopted to find β according to Section IA. The validation of the system was obtained by comparing the resistance obtained through the proposed techniques of Section IA and the one measured by means of the multimeter. For the validation, other commercial resistors of known resistance (ranging from 2.2 k Ω and 560 k Ω) were used.

6.2.4 Results and Discussion

a) Geometrical and Electrical Characterization

The optimization of the printed coil and the tuning capacitor required some preliminary tests to estimate 1) the resistivity, the thickness and the width of the silver tracks and 2) the thickness of the printed dielectric layer.

Nine capacitors (3 samples for each n_{dep} , ranging from one to three) were manufactured according to the manufacturing process described in Section IIIC and their profile was measured. An example of their profile is shown in Fig. 50a. The relative permittivity of NOA-81 resulted in 3.62 by applying the inverse formula of (32) ($d_{el} = 6 \text{ mm}$, $t_{die} = h_{1/2/3}$, $C = C_{1/2/3}$). The error is calculated as the maximum difference between the measured capacitances with the same characteristics and the mean value. The profile of the printed coil (the geometrical characteristics are listed in Table 8) was also measured on ten lines 1-mm long (Fig. 50b). The mean thickness (3.15 μm) was the mean value. The profile of the printed coil (the

geometrical characteristics are listed in Table 8) was also measured on ten lines 1-mm long (Fig. 50b). The mean thickness ($3.15 \mu\text{m}$) was calculated averaging the ratio between the area of the acquired profiles and the mean width ($259.44 \mu\text{m}$). The resistivity ρ_{coil} matches the value declared by the manufacturer. It resulted in $4.6 \cdot 10^{-8} \Omega\text{m}$ by considering the resistance R measured on 10 lines 10-mm long and by applying the inverse formula of (30). A printed coil and one capacitor of 14.14 pF ($n_{dep} = 3$) were connected in parallel and the impedance of the resulting system acquired in the range of $100 - 40 \text{ MHz}$ to find the equivalent lumped parameter circuit model. Also the impedance of the readout inductor was acquired.

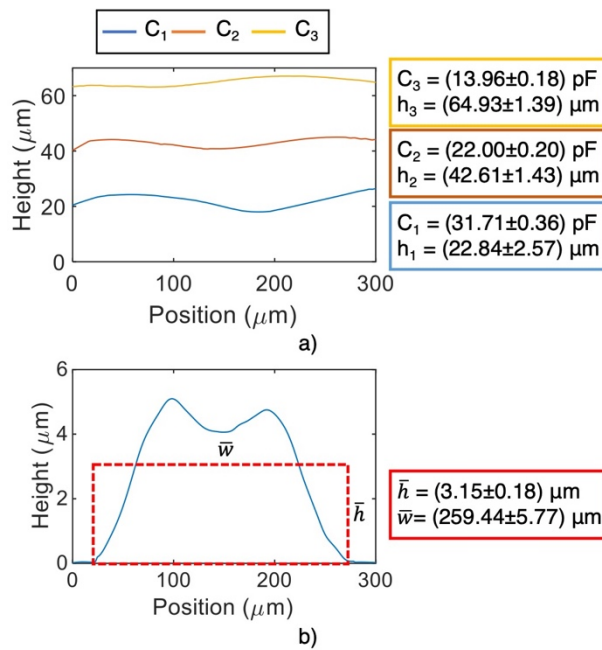


Fig. 50 (a) Profile of NOA81 of three tuning capacitors having different numbers of deposition (from 1 to 3), indicated in the subscript. On the right the mean value of the capacitance and of the height (the error is the deviation standard calculated on ten profiles) (b) Profile of the printed lines of the coil. On the right, the mean value of the height and the mean width [205].

Table 9 Electrical characteristics of the coils.

Property	Sensing	readout
L , Equivalent inductance (μH)	8.24	7.44
R , Equivalent resistance (Ω)	87	24.16
C , Equivalent capacitance (pF)	19.23	2.79
f_r , Self-resonance frequency (MHz)	12.45	35

b) Calibration of the Telemetric System

The final range of R_x was determined from the results of the FSR characterization. The correlation between the applied force and the measured resistance is shown in Fig. 51, and it was found experimentally according to the procedure described in the previous section. The resistance of FSR is infinite when no load is applied, and it drops to 460 k Ω for applied weight greater than 100 g. For 1 kg the resistance drops to 20 k Ω . For the calibration procedure of the telemetric system, three commercial resistors of values 5606 Ω , 46123 Ω , 269300 Ω were connected to the sensing part of the system for the calculation of β . The acquired real part of the impedance read at the terminals of the readout coil is shown in Fig. 51. The measurements were repeated three times, with good repeatability (the maximum difference between the measurement taken at the same frequency was lower than 5 Ω). By reading $\text{Re}(Z)$ at $f_w = 12.45$ MHz and by applying (28), β resulted 6.36 μH , 6.29 μH , and 6.32 μH when R_x is 5606 Ω , 46123 Ω , 269300 Ω , respectively.

c) Validation of the Telemetric System

For the validation test, other commercial resistors were connected to the sensing part to validate the system. As shown in Fig. 52, the frequency where the real part of the impedance is maximum (f_2) shifted and for this reason $\beta = 6.36$ μH was used for $\text{Re}(Z(f_w))$ lower than 1500 Ω , $\beta = 6.29$ μH was used for $\text{Re}(Z(f_w))$ between 1500-1700 Ω , $\beta = 6.32$ μH was used for $\text{Re}(Z(f_w))$ greater than 1700 Ω . The results are shown in Fig. 53: the value of the commercial resistors calculated by implementing the proposed technique (y-axis) was correlated with the value measured by means of the multimeters before the experiment (x-axis). The maximum deviation of R_x from the reference curve is lower than 6%, despite the large range of the resistances, which causes a shift of f_2 with respect to f_{r2} .

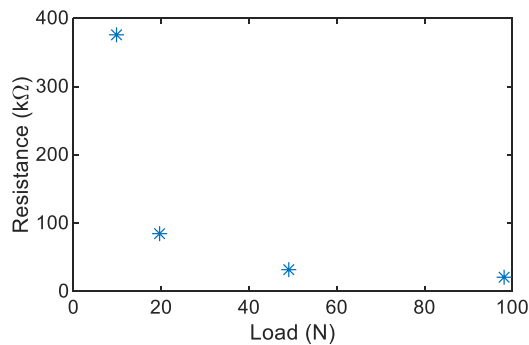


Fig. 51 (a) Characterization of a FSR by changing the applied load (by using known weight from 100 g to 1 kg) over the sensitive area [205].

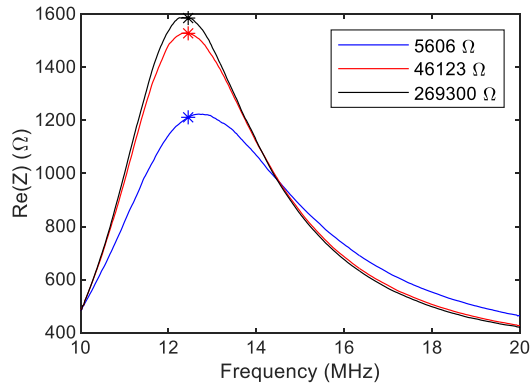


Fig. 52 Real part of the impedance measured at the terminal of the readout coil for known resistor (R_x is indicated in the legend). The star-like symbols correspond to the real part of the impedances at the frequency fr_2 [205].

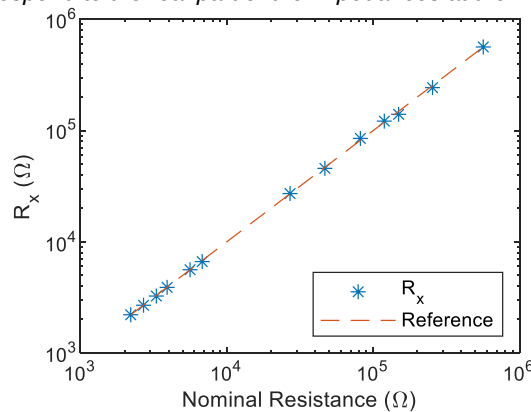


Fig. 53 Validation of the telemetric system by changing the value of R_x from 2.2 kW to 560 kW (the measured values by means of a multimeter are on x axis). R_x calculated by applying (1) is on y axis [205].

6.2.5 Conclusion

The fabrication of sensors and electronic devices directly onto the surface of the objects represents a new frontier to fabricate smart objects, which can be used in different scenarios (industry, agriculture, healthcare, smart city management, etc.). The passive telemetric method is a valid solution to interrogate the passive sensors without the integration of complex electronic circuits and batteries on the objects. The only components on the object are the sensor, the sensing coil, and an optional capacitor. This is a viable solution for smart packaging, to reduce costs, encumbrance, and complexity.

A manufacturing process to fabricate the coil and the tuning capacitor was proposed. A preliminary study of the components was described in order to fabricate a sensing device with the self-resonant frequency of 12.45 MHz, compatible with the most typical impedance analyzers. The resistivity and the permittivity of the involved ink were evaluated as well as the thickness of the deposited materials, in order to support the design of the coil and of the capacitor. Finally, the printed devices were adopted in a telemetric system to validate the proposed solution. The measurement of the resistance deviates from its nominal value of 6% at maximum, when the resistive sensor ranges from 2.2 k Ω and 560 k Ω .

6.3 Paper-based ammonia gas sensors for smart food packaging

Part of the research work reported in this section was presented in the conference *BIOSTEC 2020* and is part of the conference proceedings *Proceedings of the 13th International Joint Conference on Biomedical Engineering Systems and Technologies* with the title *Preliminary Analysis on Cellulose-based Gas Sensor by Means of Aerosol Jet Printing and Photonic Sintering* [213]. Part of the research work reported in this section was presented in *IEEE 2021 II Workshop on Metrology for Industry 4.0 and IoT (MetroInd4.0&IoT)* and is part of the conference proceedings with the title *Preliminary Analysis on a Paper-based Ammonia Sensor for Future Food Smart Packaging* [214]. Results and pictures are reported with permission of the editor. Part of the work presented in this section is currently undergoing the review process at *IEEE Transaction on Instrumentation and Measurements Journal*.

6.3.1 Introduction

In recent years, the use of unconventional substrates like paper has been one of the turning points in the development of new sensors. There are many reasons for this, but on all of them should be pointed out the greater environmental and ecological awareness, the desire to reduce waste and pollution, as well as being able to exploit the peculiar properties of paper. For these reasons, people have begun to exploit paper for various measurement applications, such as strain, pressure, microfluidics, or electrochemistry [103], [215], [216]. The combination of the abovementioned methodologies opens the way to the application of sensors and circuits in application fields with current issues that require urgent responses. Food freshness monitoring application is a possible example. Because of the economic, social, and moral repercussions, one of the great challenges of this time is food waste [217]. Technological and economic efforts can provide improvement in food control and safety by preventing food waste throughout the supply chain, from the producer through the distribution network to the final consumer. A significant advancement could be represented by food smart packaging with embedded measuring devices to assess food integrity [218].

Ammonia is fundamental to the aforementioned application since it is the simplest compound among the so-called total volatile basic nitrogen compounds (T-VBN), whose concentration is a marker of the food-spoilage status [219]. None of the technological solutions already developed have the advantages of paper-based gas sensors, such as the use of low-cost fabrication processes and eco-compatibility materials [219], [220] [221]

[222], [223]. These characteristics are mandatory requirements to make the sensing technology appealing for integration into food smart packaging.

The aim of this work is the development of a paper-based ammonia gas sensor. The sensing mechanism relies in the intrinsic hygroscopic properties of cellulose paper fibers, containing moisture as a consequence of absorption from the surrounding environment. This allows the electrical detection of water-soluble gases like ammonia due to food degradation, thanks to carbon electrodes realized on the surface of the paper sheet [213], [224]. Considering the complexity of food off-flavors and off-odors, which comprise a large variety of gaseous compounds [225], [226], cross-sensitivity to possible interferents is a fundamental issue. More specifically, alcohols and ketones are expected to be among the most meaningful interferents owing to their relevance in the volatiloma and to their high solubility in water, which is comparable to the one of ammonia [227]. To gain better knowledge about ammonia measurement with paper-based gas sensors, the possible interfering effects arising from ethanol and acetone were investigated, chosen as key representatives of their respective classes of compounds, testing these compounds both individually and in mixtures with ammonia.

6.3.2 Sensor Design

In this section, a focus on the physical principle of the sensors is presented (paragraph a)). The sensors manufacturing process (paragraph d)) is explained considering materials involved and sensors layout (paragraph b) and c)). Geometrical and electrical evaluation is considered in paragraph e).

a) Physical measuring principle

The measuring method proposed in this work exploits the intrinsic hygroscopic properties of cellulose paper. Cellulose fibers present a certain amount of moisture absorbed by the surrounding environment, even if the paper looks and feels dry. For example, at a relative humidity (RH) of 50%, the paper contains ~5% water by weight. When a water-soluble gas is in the proximity of the paper, it increases the ionic conductance of paper. Being an electrolytic solution, what is measured is the result of the dissociation reaction of a species in presence of specific conditions, water-soluble gases in the surface-bound thin film of water. Starting with Ohm's law, we know that resistance can be expressed as:

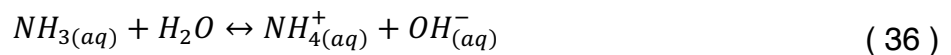
$$1/R = 1/\rho \cdot S/l \quad (33)$$

where R is the electrical resistance expressed in ohm $[\Omega]$, ρ is the electrical resistivity expressed in $[\Omega\text{m}]$, S is the cross-section $[\text{m}^2]$ and l is the length of the current path $[\text{m}]$. S/l can be defined as the cell constant. Electrical resistivity ρ can be expressed as follows:

$$1/\rho = n \cdot \alpha \cdot z \cdot F \cdot (u_+ + u_-) \quad (34)$$

where n indicates the number of moles in the volume unit expressed in $[\text{mol}/\text{cm}^3]$, α is the degree of dissociation of ionic species, z is the ion charge, F is Faraday's constant, which represents the total amount of electric charge of a mole of elementary charges ($e \cdot N_A = 96485,336521 \text{ C/mol}$), $(u_+ + u_-)$ represents ion velocities at unit electric field $[\text{cm}^2/(\Omega\text{C})]$ or ion mobility. Ionic mobility in a solution and gas solubility are affected by temperature. However, it is assumed that in the application temperature range the effect is small and lies in the error bars [224]. According to (35), considering a solution with only one electrolyte and z , F , and u constant, the electrical resistivity is a function of the number of ions n present in the unit volume and the degree of dissociation α . The electrical resistivity of an electrolytic solution also depends on the electrolyte concentration. Indeed, by increasing the concentration, the number of ions in the unit volume increases, while the degree of dissociation decreases [224], [228]–[230]. For this reason, the characterization of an ammonia sensor should keep the working volume of the system under control.

Considering the food application field, ammonia is released during the degradation of foods such as meat and fish. This gas is largely soluble in water (H_2O). Hence, if ammonia (NH_3) is present in the atmosphere, an appreciable amount is released from the gas phase to the water film covering the cellulose fibers, where it dissociates according to the following reaction:



According to (37), with fixed RH and temperature, water quantity adsorbed is constant, so any impedance change is due to ammonia presence in a specific amount in the surrounding environment. Considering (38), an elevated amount of ammonium (NH_4^+) and hydroxide (OH^-) ions generated by ammonia dissociation in water increases ionic conductivity, and thus

changes the impedance of paper, which can be measured thanks to carbon electrodes printed on the paper surface.

b) Materials

Whatman™ chromatography 1 (Whatman, Maidstone, UK) cellulose paper was the selected substrate to avoid influences related to chemical additives, thanks to its higher degree of purity than that of commercial papers. The chromatographic paper has high hygroscopic properties so that cellulose fibers contain a substantial amount of moisture. The carbon ink EXP 2652-28 (Creative Materials Inc., 12 Willow Road, Ayer, MA, USA) was used to manufacture the electrodes through which conductance changes can be measured. The ink (starting viscosity of 15-20 mPa·s) was properly atomized together with its thinner during the printing process to obtain better printability and adhesion to the substrate.

c) Sensor layout design

AutoCAD was the software used for electrodes design. An interdigitated layout with two comb electrodes was selected to capture water-soluble ions which lie between two consecutive fingers. As can be seen in Fig. 54, each comb electrode consists of 8 fingers with length (l) 12 mm, and it was designed with finger width (w) of 300 μm and a gap (g) between two consecutive fingers of 500 μm .

d) Manufacturing process

The aerosol jet printer AJ300 model (Optomec, Albuquerque, NM, USA) was the printing machine used in this work. Carbon interdigitated electrodes (IDE) were printed designing a specific toolpath consisting in two consecutive overlapped depositions per run. Process parameters were defined to obtain the geometrical finishes described above. In detail, sheath, atomizer, and exhaust gas flows were set at 650 SCCM, 1140 SCCM, and 1075 SCCM, respectively. The printing plate was heated up to 50 °C, a total number of 3 runs was performed each one at a printing speed of 4 mm/s. A total number of fifty sensors was manufactured, in five batches of ten sensors each one. Photonic sintering (Pulseforge 1300 - Novacentrix, Austin, TX, USA) was used as an optimal sintering method avoiding burning the paper substrate. Considering the previous study performed on finding the best sintering parameters, a single pulse was applied at a voltage of 250 V with a duration of 1750 μs [213]. Fig. 54a presents the manufacturing process, while Fig. 54b the final layout and a magnification of the fingers.

e) Geometrical and electrical evaluation

The geometrical and electrical properties of the carbon IDEs, once printed, were evaluated. Resistance measurements were performed by the digital benchtop multimeter Hewlett-Packard 34401a, placing the multimeter probes in A-A points (Fig. 54b). Mean resistance values for left and right electrodes were respectively equal to (231 ± 20) k Ω and (249 ± 28) k Ω . The geometrical analysis was then performed on cellulose samples thanks to the optical microscope by Orma Scientific NB50T (trinocular zoom 0.8x–5x–LED), with its devoted HDMI MDH5 camera model used to acquire the images (Orma Scientific, Sesto San Giovanni, Milan, Italy). Optical measurements confirmed what was designed before printing: mean value of tracks widths and gaps was respectively of 340 ± 44 μm and 460 ± 36 μm (relative standard deviation respectively of 13% and 8%), as can be seen in Fig. 54b.

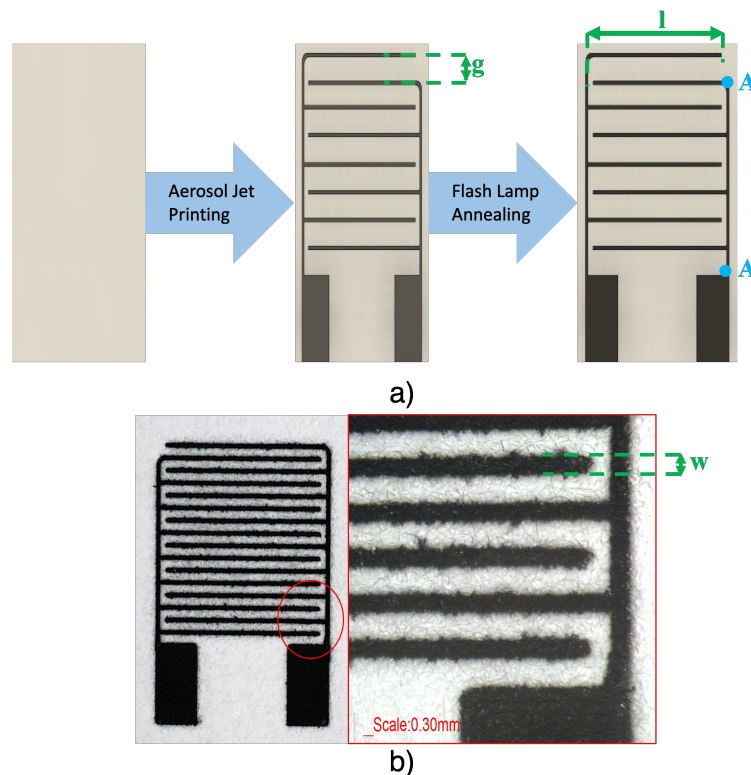


Fig. 54 a) Block diagram of the manufacturing process; b) Sensor final layout on chromatographic paper and optical microscope magnification. $l=12$ mm, $g=500$ μm , $w=300$ μm . A-A points (12.7 mm in length) indicate where multimeter probes were placed of resistance measurements.

6.3.3 Experimental Setup

To test the behavior of the paper sensors in the presence of different gases, a dedicated pneumatic circuit was implemented. Fig. 55 shows the schematic of the realized system: four sensors were simultaneously placed inside a vial together with a humidity sensor during experiments. The latter was a resistive humidity sensor (Model IH-3610-1, Honeywell Inc., 24B Concord Street, El Paso, TX, USA), a full-scale RH sensor characterized by 2% RH

accuracy at 25 °C. It was used as feedback to check if the system was leaking along its path and to have evidence of the humidity present in the test chamber. The circuit was designed to force the flux being pumped inside a vial, which worked as the test chamber. The circuit has been developed to manage the simultaneous presence of four gaseous components: dry air, humidity-saturated air, ammonia as basic analyte gas, and a varying interferent gas like acetone or ethanol (Interferent in Fig. 55). Four mass flow controllers (MFCs) tuned and controlled the fluxes during tests, while a mass flow meter (MFM) was used as feedback to verify the possible presence of leaks in the system. MF-1 model (Andover, Massachusetts, USA) were the selected devices withstanding a maximum flow of 200 SCCM, while the constant flux of our experiment was 100 SCCM. As shown in Fig. 55, the MFCs were connected downstream to the different gases used, specifically two of them to the dry air cylinder, one to the ammonia, and one to the interfering gas (ethanol or acetone). The saturated humidity line consisted of one of the two MFCs connected to the compressed air connected in series to a vial partially filled with water, which served as a bubbler, in order to obtain the percentage of moisture needed in the sensor chamber at the various times of the tests performed. The above-mentioned elements were placed inside a thermostatic chamber to keep fixed the temperature during tests. MFCs and the MFM were connected to an ISO-TECH power supplier (DC voltage set to 24 V) and via USB communication to a personal computer. Here, a devoted LabVIEW software was properly designed to manage the flowing mix of gases coming from certified bottles (SOL SpA, Italy) and thus the atmospheric composition inside the test chamber, and to acquire data from paper-based sensors connected each one to a benchtop multimeter thanks to a GPIB interface at the same time.

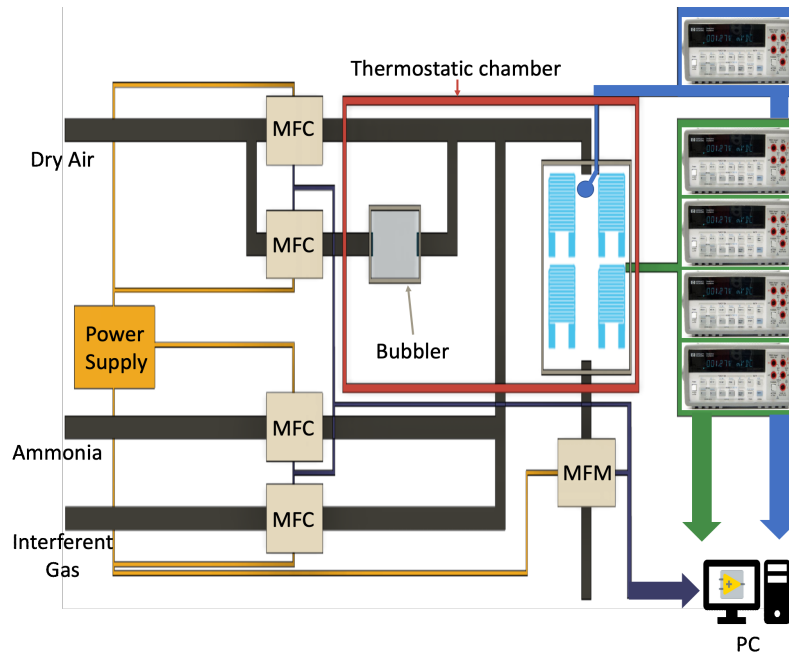


Fig. 55 Schematic representation of the experimental setup. The colors orange, black, red, violet, and green indicate respectively the power supply to the mass flow meter (MFM) and controllers (MFC), gas flow tubing, the fixed temperature in the thermostatic chamber (25 °C), gas managing LabVIEW software, GPIB acquisition LabVIEW software.

The tests carried out were divided into four phases:

- i. Humid environment stabilization: considering the application case, the presence of food inside packaging ensures a moisture saturated environment. During humid environment analysis, the behavior of the sensors was investigated as a function of the humidity level and with no additional gases. So, the first part of the experimental tests was related to state at different values of RH the electrical resistance presented by the sensors under test, and the time required by them to reach a complete stabilization, considering fourteen sensors. This is necessary for the following part of the tests in which we introduced ammonia and interferent gases like acetone and ethanol. According to RH food-packaging typical values, we considered as possible RH values 75%, 80%, 90%, and 100%. Analysis chamber temperature was kept fixed at 25 °C.
- ii. Ammonia behavior analysis: it consisted in determining the characterization curve of the sensors for measurement of ammonia concentrations (3, 6, 9, and 12 ppm). This study was repeated in the analysis chamber considering three temperatures, (25 ± 2) °C, (15 ± 2) °C, (5 ± 2) °C to check the effect of this environmental parameter on the sensor properties.
- iii. Interferent gas behavior analysis: it was focused on investigating the influence of interfering gases typically present during the degradation processes of foods like meat

and fish. In particular, we selected acetone and ethanol, respectively part of the family of ketones and alcohols, owing to their relevance in the food volatiloma and their high-water solubility. The sensors were exposed separately to acetone and ethanol. Once reached the stabilization at RH=75%, acetone tests were carried out considering as target concentrations 12, 24, 36, and 48 ppm, while during ethanol testing the concentrations were 60, 120, 180, and 240 ppm. These concentrations were selected to overexcite the sensors with respect to ammonia [231]. Each concentration was kept fixed for two hours. Analysis chamber temperature was kept fixed at 25 °C.

iv. Cross-sensitivity tests: different concentrations of ammonia were injected into the testing chamber simultaneously with the two interfering gases, one at a time. Considering the lack of knowledge about such possible interfering effects, measurements have been carried out both exposing sensors to ammonia and then adding the interferent vapors and vice versa, i.e. exposing the sensors to the interferent compound and then adding ammonia. In detail, the sensors were exposed to an atmosphere that included the co-presence of two gases, ammonia and one of the two interfering gases. The sensors were fed with the specific humidity background determined during humid environment analysis. In the following 8 hours ammonia was kept fixed at 6 ppm, while an interferent gas was fed in the 4 central hours. For acetone, the two selected concentrations were 12 and 24 ppm, while for ethanol 60 and 120 ppm. Later, the role of the gases was inverted: the interfering gas was kept fixed (12 ppm for acetone concentration, 60 ppm for ethanol concentration), while ammonia could vary between 6 ppm and 9 ppm. Analysis chamber temperature was kept fixed at 25 °C.

6.3.4 Results and Discussion

i. Humid environment stabilization

The sensors were tested starting from RH=75% to 100%. Humidity was increased at the next value only after the sensors output stabilization. In Table 10 the obtained results are listed. In this stage of the tests, we noticed that a period of 8 h can be considered sufficient to reach stabilization for RH=75 and 80%, while for RH=90% and 100% the mandatory time interval for a complete stabilization decreases to 3 h. In Fig. 56, the blue line represents the mean resistance mean of the four sensors after the sensors output stabilization. The mean absolute deviation around the mean was considered negligible (5% in the worst case) for all the calculated points, also with respect to the resistance change due to the RH change. To

evaluate the possible hysteresis phenomenon, once stabilized in the humidity saturated environment, the same sensors were exposed to the same set of humidity values as before but in decreasing order. In this way, the first RH cycle was completed. As can be seen in Fig. 56, the mean resistance at the end of the first entire RH cycle (6.43 MΩ) is about two orders of magnitude smaller than the value measured at the beginning (102.59 MΩ). Furthermore, in the second part of the RH cycle, the minimum time interval required to stabilize the sensors was respectively 3 h at RH= 90% and 4 h at RH=80, 75%. Fig. 56 also shows the results of the humidity test repeated a further time. Compared to the first cycle results, the hysteresis between the values of the second part of the first cycle and of the last RH ramp is lower (21% at RH=80% calculated on the span 3.63 MΩ-6.42 MΩ). These results stated that paper-based sensors need a long period to desorb moisture. Furthermore, they needed to be stabilized in a totally humidity saturated environment (RH=100%) before working at a lower value of RH stably, assessing the importance of a high RH pre-treatment (blue curve in Fig. 56) for achieving stable (with no hysteresis) properties.

Table 10 Stabilization at different RH values.

RH (%)	Measured Quantities		
	Testing Time (h)	Mean Resistance (MΩ)	Relative Standard Deviation (%)
75	24	102.6	7
80	12	46.2	10
90	12	5.9	8
100	10	3.8	2
90	14	4.3	4
80	24	5.2	5
75	29	6.4	5
75	8	5.9	5
80	8	4.7	3
90	4	4.2	2
100	4	3.6	2

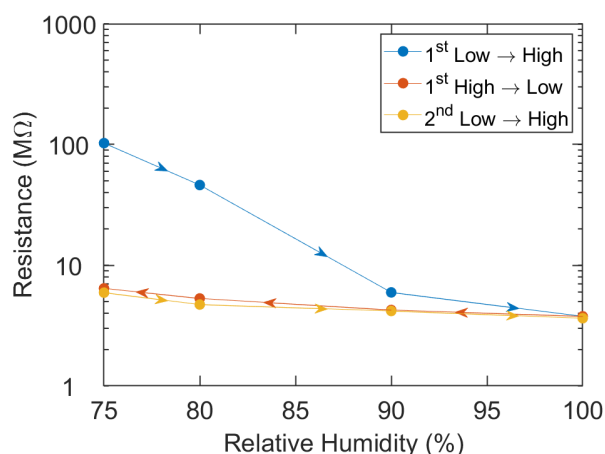


Fig. 56 Stabilization and hysteresis cycle of the sensors at different relative humidity. The blue curve represents the first study, from RH=75% to RH=100%; the orange one the comeback to lower RH values, the yellow one the comeback to higher RH values [214].

ii. Ammonia Behavior Analysis

The sensors were first stabilized at RH=100% for 4 h, then RH=75% was set for 8 h. Once achieved, RH was maintained at 75% and varying concentrations of ammonia were pumped in the testing chamber, starting from a concentration of 3 ppm to 12 ppm. The ammonia concentration was step by step increased by the same amount of 3 ppm every 4 h because according to the results, after this time interval the output of the sensor is stable.

The results of this test can be found in Fig. 57. The graph shows the sensor response as $\Delta R/R_0$, where R_0 indicates the average resistance value of the eight sensors calculated at the end of the stabilization interval (0 ppm of ammonia) and ΔR represents the difference between R_0 and the average resistance value of the eight sensors, extrapolated for each given concentration during the last 2 hours of exposure to ammonia ($\Delta R = R_0 - R$). The standard deviation calculated considering the last two hours of each step in presence of ammonia (12 sensors) is lower than 2%. No linear dependence of the sensor response towards different ammonia concentrations can be found. Excluding $\Delta R/R_0$ change from 0 ppm to 3 ppm, mean plotted points always show the same change in presence of a 3 ppm increase of ammonia from 3 ppm to 12 ppm. Specifically, the average $\Delta R/R_0$ change between the various concentrations is 2.6%, according to the slope of the best fit line calculated in the range 3 ppm - 12 ppm. Finally, it can be seen that the various points of the curve, each with its error bars, do not overlap each other.

The calibration curve was also repeated at 15 °C and 5 °C in order to verify whether the thermal factor can affect the response during ammonia absorption on the paper sensor surface. Fig. 58 reports the results obtained at the three different mentioned temperatures.

As expected, the temperature does not appreciably influence the sensor behavior. The calculated midpoints (on 8 sensors) for each concentration show the same type of trend, regardless of the temperature at which the sensors were held during the test.

Hysteresis was evaluated at 25 °C and RH=75% in the cyclic test by increasing and decreasing ammonia concentrations: after reaching 12 ppm with steps of 3 ppm, lower concentrations were restored in the same order (12, 9, 6, 3 ppm). A new air flux, without ammonia gas and with RH=75%, was restored at the end of the cycle. Considering Fig. 59, a strong decrease of the resistance was detected in the interval 0-3 ppm, evidencing the capability of such sensors to trace ammonia presence inside the working environment. From cyclic tests, no relevant difference between the curve representing the growth of ammonia concentration (blue curve) and the decreasing curve (red curve) was evidenced. The most interesting aspect to point out concerns the last point of the decreasing curve, which is the return to a zero concentration of ammonia.

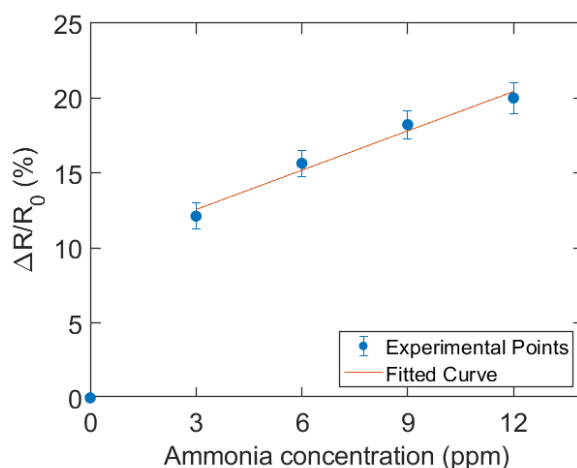


Fig. 57 Ammonia behavior analysis for paper-based sensors in presence of different ammonia concentrations (blue dots). Error bars represent standard deviations calculated over eight sensors studied in this section. The red line is the straight line that best fits the measured data from 3 ppm to 12 ppm, obtained by using the method of least square ($R^2=0.9783$).

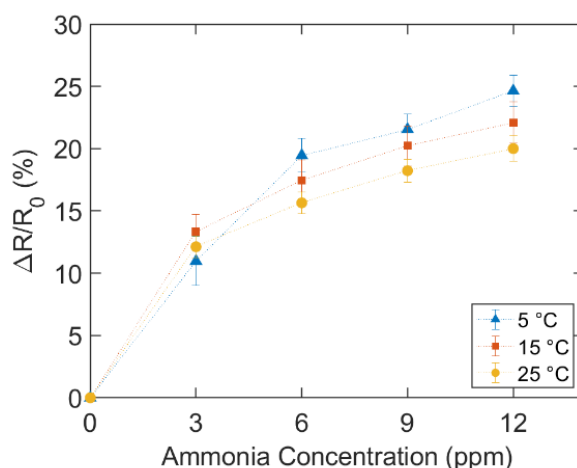


Fig. 58 Comparison of the three calibration curves determined at 5 °C (blue), 15 °C (orange), and 25 °C (yellow). Error bars represent standard deviations calculated over eight sensors studied in this section.

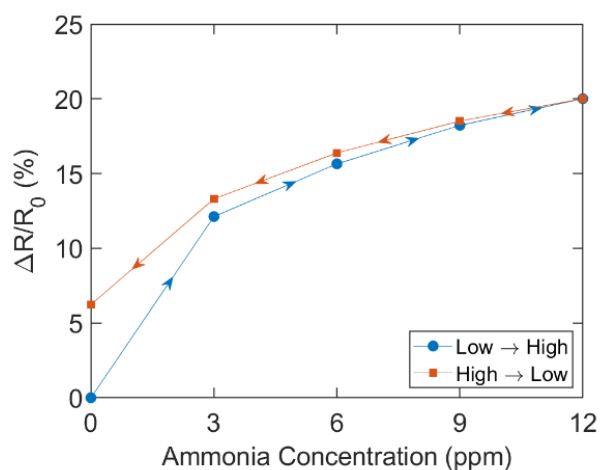


Fig. 59 Average percent increases for sensors tested at different ammonia concentrations. Hysteresis cycle tested: blue curve = starting cycle from 0 ppm to 12 ppm, red curve = come back cycle from 12 ppm to 0 ppm. Tests were carried out at 25 °C [214].

The sensors need much longer times during the removal of the analyte to re-establish the starting condition (only RH=75%). In this regard, it should be noted that these paper sensors are designed to be disposable. Moreover, considering their possible integration into smart packaging allowing to monitor in situ the food spoilage process, food samples are expected to develop a single, monotonically increasing, ammonia concentration ramp [232].

iii. Interferent Gases Behavior Analysis

The results of the third part of our experiments consisting in performing two concentration scales in presence of acetone and ethanol, separately, are shown in Fig. 60 and Fig. 61. The points represent the averages calculated on the eight output sensors used in this phase of the study at a specific concentration considering the stable period for each concentration. They are therefore average points calculated over a period of the last one hour (on a total of 2 hours), for having a stable sensor output. The data are reported as $\Delta R/R_0$, where $\Delta R = R_0 - R$, R is the resistance for each analyte concentration, and R_0 is the resistance before fluxing the analyte. The temperature was kept at 25 °C and RH at 75%.

Regarding the acetone results, the first evidence regards the behavior of the sensors in presence of the highest acetone concentration of 48 ppm. Here, resistance change was not exceeding 8%, while in presence of ammonia it was sufficient a concentration of 3 ppm to reach a resistance variation of 12%. Once more, the curve exhibits good linearity, as evidenced by the R^2 value in Fig. 60. Regarding the ethanol, the concentrations are different, and 240 ppm is the maximum concentration allowed by the setup. As for the acetone test, an approximately linear trend can be found for ethanol, with a more pronounced tendency

than shown by the acetone calibration curve. The absolute relative change of resistance from one concentration to the next (60, 120, 180, 240 ppm) is equal to 5%, and $\Delta R/R_0$ is maximum (20%) at 240 ppm of ethanol. Similar to the acetone case, the devices revealed much less sensitive to ethanol than to ammonia. $\Delta R/R_0$ is 12% when ethanol concentration is 120 ppm, while the sensor has the same response for 3 ppm of ammonia. Comparing this curve with the previous one for acetone, one can see larger error bars. Considering the weak responses induced by ethanol, drift and hysteresis phenomena cause larger effects on the average response, thus contributing to the widening of error bars. In addition, this may be due to the nature of ethanol itself, which does not separate as easily as ammonia does into ions participating in the electrical conduction, instead of forming more complex compounds that may contribute less to resistance variation. In the future it could be appropriate to enlarge the concentrations to be investigated, both at the bottom and at the top, to verify if the trend of the curve is maintained, or if, on the contrary, a change of the power-law should occur losing linearity.

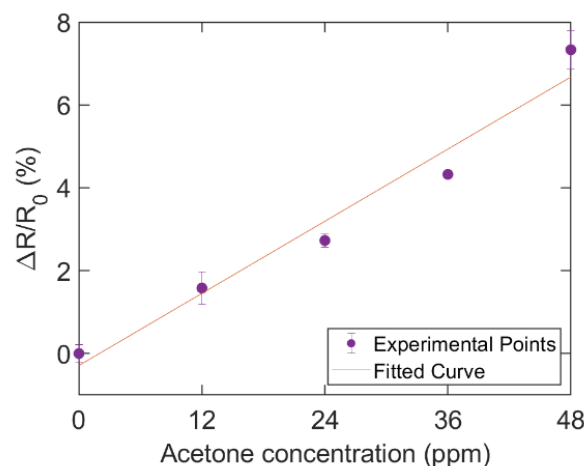


Fig. 60 Acetone behavior analysis for paper-based sensors in presence of different acetone concentrations. Error bars represent standard deviations calculated over eight sensors studied in this section. Tests were carried out at 25 °C.

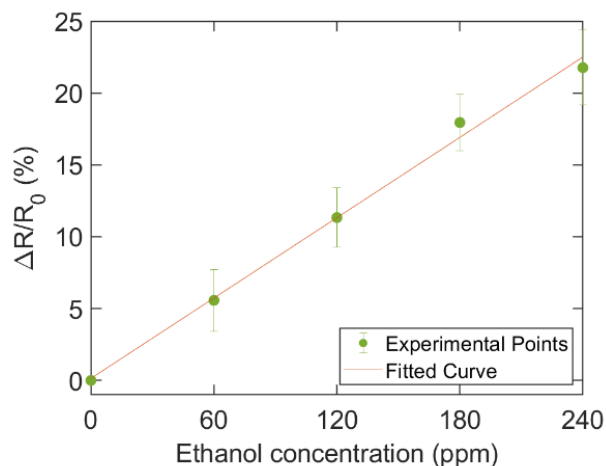


Fig. 61 Ethanol behavior analysis for paper-based sensors in presence of different ethanol concentrations. Error bars represent standard deviations calculated over eight sensors studied in this section. Tests were carried out at 25 °C.

iv. Cross Sensitivity Tests

These tests were focused on investigating the selectivity of paper sensors towards ammonia in the presence of interfering gases, as it may happen in real scenarios. The cross sensitivity procedure was divided into two parts: in the first, ammonia was kept fixed at 6 ppm for 8 h consecutively, while two concentrations of the interfering gas (acetone or ethanol) were fed at different times. The operation was then repeated inverting the role between ammonia and the interfering gases. Acetone (or ethanol) was fed one at a time, while ammonia concentration was changed. Fig. 62 represents the dynamic curve of ammonia-acetone tests, while Fig. 63 depicted the dynamic curve of ammonia-ethanol tests. Table 11 summarizes the relative resistance change ($\Delta R/R_0$) in presence of ammonia and ethanol, respectively. Here, $\Delta R/R_0$ was calculated considering R_0 as the average resistance of the baseline. ΔR was calculated as $R_0 - R$, where R was the average resistance in presence of a specific mixture of ammonia and acetone/ethanol. The baseline (RH=75%, 0 ppm of ammonia, 0 ppm of interferent gases) of each sensor was determined by considering the two sections at RH=75% before and after pumping interfering gases concentrations. An exponential law was employed for complete curve fitting (red curve) as described in (39).

$$y = a \cdot \exp(bx) \quad (40)$$

The coefficients a and b were calculated using a Matlab embedded function. In both tests, the dominant role of ammonia can be evidenced as responsible for the resistance change of the paper sensors. The changes of $\Delta R/R_0$ induced by the air composition are in accordance with the results reported in Section IVb for ammonia, and Section IVc and Section IVd for interfering compounds. As shown in Fig. 62 and Table 11, the two concentrations of acetone (12 and 24 ppm) do not significantly influence the detection of ammonia molecules in the study atmosphere. Indeed, if $\Delta R/R_0$ is 21.3% when the concentration of ammonia is 6 ppm without acetone, with the same concentration of ammonia $\Delta R/R_0$ is only 22.3% and 23.1% and 12 ppm and 24 ppm of acetone, respectively. This finding is more evident in the second part of the test. For 12 ppm of acetone and no ammonia gas, $\Delta R/R_0$ is only 1.5%, while $\Delta R/R_0$ is 25.2% and 27.2%, after introducing 6 ppm and 9 ppm of ammonia, respectively. It should be noted that the change in resistance relative to 6 ppm is greater than in the case of only ammonia.

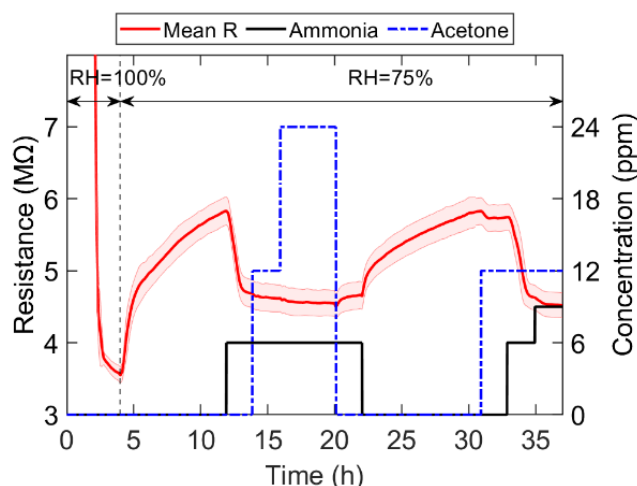


Fig. 62 Dynamic stabilization curve (red) of four different sensors for cross sensitivity between ammonia (black) and acetone (blue). The light red area surrounding the red curve represents the standard deviation.

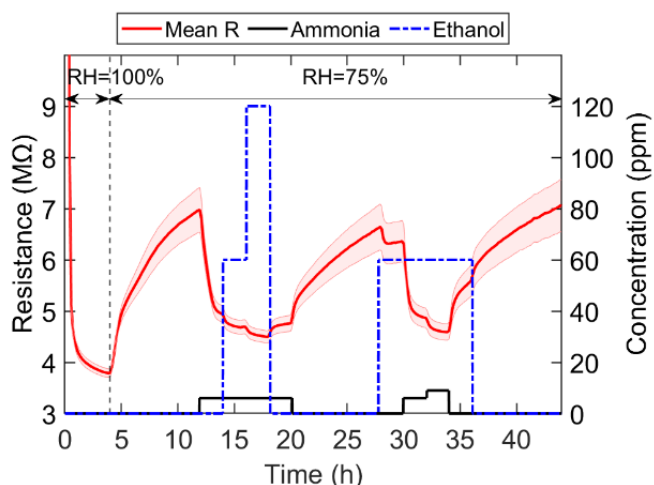


Fig. 63 Dynamic stabilization curve (red) four different sensors for cross sensitivity between ammonia (6 ppm) and ethanol (60 and 120 ppm), followed by cross sensitivity between ethanol (60 ppm) and ammonia (6 and 9 ppm). The light red area surrounding the red curve represents the standard deviation.

Table 11 Resistance variation during cross-sensitivity tests with acetone and ethanol.

Ammonia concentration (ppm)	Acetone concentration (ppm)	Ethanol concentration (ppm)	$\Delta R/R_0$ (%)
	0		21.3
6	12		22.3
	24		23.1
0		0	1.5
6	12		25.2
9			27.2
6	0	0	30.9

	60	35.2
	120	37.9
0		3.5
6	60	26
9		30.4

Also, in the ethanol cross-sensitivity test, the significant change in resistance measured by the sensors is mainly associated with the detection of ammonia. In the first part of Fig. 63 where ammonia concentration is 6 ppm, 60 ppm and 120 ppm of ethanol induce a resistance change $\Delta R/R_0$ of 35.2% and 37.9%, respectively. These relevant changes are mainly induced by the concentration of ammonia. Indeed, before introducing ethanol in the vial and with 6 ppm of ammonia, $\Delta R/R_0$ is 30.9%. Moreover, in the second part of the cross-sensitivity test, before introducing ammonia, $\Delta R/R_0$ was only 3.5% for 60 ppm of ethanol. Similarly, the next feeding of 6 ppm of ammonia produced a resistance variation of 26% while 9 ppm generated a change of 30.4%.

According to the results of cross-sensitivity tests, it can be concluded that the response provided by the sensors can be traced to the presence of ammonia, also when ammonia is in smaller quantities than the other two gases. This evidence occurs more prominently during the acetone cross-sensitivity test. During cross-sensitivity tests, the resistance change ($\Delta R/R_0$) related to 6 ppm ammonia was found greater than obtained in paragraph IVb, mainly in presence of ethanol. Even in the case of commercial sensors, ethanol should be considered with care. For example, for metal oxide-based ammonia sensors, ethanol induces a response similar to those of the target compound [226]. Here, the concentrations of ethanol, as well as those of acetone, are deliberately placed together in the test chamber to verify both their individual and combined effects on the sensor response. Though the two interferent compounds can dissolve in water and damp environments, they are not able to dissociate into simple ionic species as it happens to ammonia. Therefore, while they generate ionic forms that can contribute to conduction, they do so in a much smaller way than ammonia can do, hence explaining the much lower individual response. When the target and the interfering compound are present at the same time in the environment, our results indicate that the paper-based sensors exhibit an almost additive response, the

response of the mixture being almost the sum of the individual responses of the two compounds, reflecting the good selectivity in favor of ammonia.

In addition, Fig. 62 and Fig. 63 show the repeatability of the sensors against ammonia, the target gas to be tracked. In the cross-sensitivity steps, they always stabilized at the same resistance values (approximately 4.8 M Ω) and consistently with respect to the administered concentrations. This further demonstrates the independence of the proposed sensor from the presence of acetone and ethanol, which does not suffer interference, also when interfering gas concentrations are one or two orders of magnitude higher than those used with ammonia.

6.3.5 Conclusions

Paper-based gas sensors were manufactured through AJP and FLA showing the reproducibility of 8% and 13% in terms of geometrical features (gaps and line widths, respectively), despite a porous and extremely cheap sensing material such as chromatographic paper. The hygroscopic properties of paper allow the measurement of a water-soluble gas such as ammonia within a moisture environment. This condition occurs inside food packaging if food goes through a degradation process releasing ammonia. Firstly, the sensors were studied in a damp environment considering different RH values from 75% to 100% to determine the stabilization time. Taking advantage of a custom setup to manage gaseous samples, the sensors were first doped with an RH=100%, then a background of RH=75% was set, and only at the end of this step ammonia concentrations were introduced, ranging from 0 ppm to 12 ppm in steps of 3 ppm. The capability of the sensors to correctly detect the presence of ammonia was evidenced, starting from the lowest concentration showing a resistance change of 12% with respect to the humidity background, and no significant hysteresis phenomenon was highlighted. Temperature dependence was investigated, and no specific influence was discovered linked to this parameter. The influence of interfering gases such as acetone and ethanol was studied. Different increasing concentrations were considered for each of the two gases, maintaining the background of RH=75%. The sensors showed a linear behavior, both in presence of acetone and ethanol. A maximum resistance variation of 7.5% was registered in the case of acetone with 48 ppm, while a maximum of 20% was registered with ethanol at 240 ppm. These two gases carried responses comparable to those of ammonia only at the highest concentrations (48 ppm, 240 ppm, and 12 ppm, respectively). Cross-sensitivity tests confirmed that the response to gas

mixtures is nearly given by the sum of individual responses, with the response contribution from the target compound (ammonia), dominating the contribution from the interferents, despite their larger concentration in the gas phase. In detail, resistance differences due to acetone and ethanol are respectively of 1.5% and 3.5%. The response offered by the sensor depends only on the ammonia administered they stabilize at the same resistance values in the cross-sensitivity phases, regardless of the interfering gas. Ammonia is the major contributor in resistance drop, responsible for a variation exceeding 20% with acetone and 30% with ethanol.

7. Cells-related Sensing

7.1 Caco2

The research work reported in this section was published in the Elsevier journal *Biochimica et Biophysica Acta - General Subjects* with the title *Monitoring Caco-2 to enterocyte-like cells differentiation by means of electric impedance analysis on printed sensors* [233]. Results and pictures are reported with permission of the editor.

7.1.1 Introduction

Caco-2 cell line has been proposed as a model to investigate absorption mechanism at intestinal level, and many efforts have been performed to improve and standardize this line as a suitable alternative to more expensive and complex models such as the in vivo ones [234], [235]. While deriving from colorectal cells, one of the best advantages in using this line is its ability to spontaneously differentiate into a monolayer when placed in culture, expressing several morphological and biochemical characteristics typically showed by mature small intestinal enterocytes [236], [237].

The development of a methodology able to monitor the monolayer integrity and assess the differentiation of cells, in an easy, non-invasive and non-destructive way, is a mandatory objective of the scientific community, because the presence of an intact and differentiated barrier is crucial for in vitro experiments. In this perspective, electrochemical sensors - able to detect specific variations in current, potential, capacitance, conductivity and, primarily, impedance signals - have been already demonstrated to be a non-invasive reliable method capable to provide useful and accurate information, concerning not only on cell adhesion [238], but also cell growth [239] and differentiation [240] processes. In particular, impedance-based sensors - used as convenient and highly customizable technology - can provide real-time quantitative feedback on physiological processes [241], [242]. In general, this technique requires the application of an alternating field voltage - with a constant amplitude (usually between 5 and 10 mV) and a defined range of frequency - to the measuring electrodes, and the measurement of the resulting alternating current. The overall impedance (Z) can be thence determined by applying Ohm's law [243], [244]. Without cells the current flows freely from the surface to the electrodes; conversely, cells adherent on the electrode act as an insulator and impede the current flow, thus increasing the overall impedance of the system.

In this perspective, the aim of this work was to perform impedance measurements to specifically monitor growth and differentiation of Caco-2 cells by using dedicated sensors. More in detail, carbon-based interdigitated electrodes were outlined on polyimide substrate by means of AJP. Final sensors were seeded with cells, and impedance measurements were performed at different time intervals during the differentiation process (1-3-7-10-14-17-21 days after seeding). In addition, the relevance of such measurements in monitoring Caco-2 differentiation to enterocyteslike cells was evaluated comparing impedance measurements at different frequencies with the morphological, biochemical and molecular data.

7.1.2 Materials and methods

a) Cell culture

Commercial Caco-2 cell line (Sigma Aldrich, Merck KGaA) were routinely cultured in 100mm dishes at 37 °C in humidified 5% CO₂ atmosphere. Dulbecco modified Eagle's medium was supplemented with 10% heat-inactivated fetal bovine serum, 2mM glutamine, 50µg/ml penicillin and 100µg/ml streptomycin. For the differentiation experiments, cells were seeded at a density of 6×10^4 cells/cm² [245], cultured at 80% of confluence density and maintained for 21 days in complete medium, changing the medium three times a week [246]. All cell culture reagents were acquired from Sigma-Aldrich (Merck KGaA, Darmstadt, Germany).

b) Morphological assessment

In order to have a first feedback of the status of cell differentiation, initial morphological differences at different passages were evaluated by simply observing cell morphology changes with the microscope (Olympus, Italy) and counting domes, a characteristic feature used to evaluate Caco-2 to enterocyte-like differentiation [247]. Furthermore, the number and the dimension of domes evaluated with Fiji software (ImageJ Software).

c) Real-time PCR

Real-time PCR (rtPCR) was performed to quantify the expression of the following gene: sucrase-isomaltase (SI), intestinal alkaline phosphatase (ALPI), cytochrome P450 intestinal isoform (CYP3A4), claudin-4 (CLDN4), solute carrier family 15 member 1 (SLC15A1) and solute carrier family 11 member 2 (SLC11A2). After different days of differentiation (1-3-7-10-14-17-21), cells were harvested through trypsinization and the pellets were kept at -20 °C until RNA extraction. RNA was extract using TRIzol, chloroform and isopropanol

(Sigma-Aldrich, Merck KGaA, Darmstadt, Germany). RNA (2 µg) was retro-transcribed using M-MLV reverse transcriptase (Promega, Madison, Wisconsin, USA), using random hexamers and the cDNA was then subjected to realtime PCR analysis with ViiA 7 Real-time PCR system (Applied Biosystems), using the iTaq™ Universal SYBR® Green Supermix (BIORAD, USA). The following specific primers (6 pmol) were used:

SI (s: AATCCTTTTGGCATCCAGATT, as: GCAGCCAAGAATCCCAAAT),

ALPI (s: CATACTGGCTCTGTCCAAGA, as: GTCTGGAAGTTGGCCTTGAC),

CYP3A4 (s: GATGGCTCTCATCCCAGACTT, as: AGTCCATGTGAATGGGTTCC),

CLDN4 (s: TCCGCCAAGTATTCTGCTG, as: CGTGGCACCTTACACGTAGTT),

SLC15A1 (s: TCTCTGTACGGGATTGGA, as: CTGCCTGAAGCACCGACT),

SLC11A2 (s: CACCGTCAGTATCCCAAGGT, as: CCGATGATAGCCAACTCCAC),

TBP (s: GAACATCATGGATCAGAACAACA, as: ATAGGGATTCCGGGAGTCAT).

The PCR program was initiated by 10 min at 95 °C before 40 cycles, each one of 1 s at 95 °C and 30 s at 60 °C. Experiments were done in biological and technical triplicate and expression data were normalized using the Ct of the internal control TBP [246], [248].

d) Alkaline phosphatase assay

ALPI activity was assayed using the substrate p-Nitrophenyl phosphate (p-NPP) and evaluating the yellow product p-Nitrophenol (p-NP) formation (Sigma-Aldrich, Merck KGaA, Darmstadt, Germany) detected spectrophotometrically at 405 nm. ALPI was measured during differentiation (1-3-7-14-17-21 days after seeding), by applying a standardized method on cell homogenates adapted from [249]. Briefly, after washing the cells at 4 °C with PBS with 1mM CaCl₂ and 1mM MgCl₂, Caco-2 cells were harvested with scraper into 500 µl of ALPI collection buffer (10mM Tris-HCl, 150mM NaCl pH 8.0) on ice. Then, cells were sonicated 5 times for 5 s, quantified with Bradford's method (BIO-RAD, USA) and kept at -20 °C until the enzymatic assay. The activity was measured transferring cell homogenate in pNPP solution (2.5 mg/ml pNPP dissolved in Tris 0.2M pH 9.5) in a reaction tube and then incubating at 37 °C. At various time intervals (2-4-6-8 min) 100 µl of reaction were transferred from the reaction tube to the 96-well plate containing 25 µl of 0.5M NaOH.

Enzyme activity was calculated by means of a standard curve prepared with different concentration of pNP (0-50-100-200-300-400-500-600 μM). Data were expressed as μg of pNP normalized over the amount of μg of total protein and experiments have been performed in triplicate.

e) Sensors production

For the production of the sensors, Kapton® MT polyimide film with a thickness of 25 μm was purchased from DuPont (USA) whereas an electrically conductive carbon-based ink (EXP 2652–28, sheet resistivity 100 $\Omega/\text{sq.}/\text{mil}$) was acquired from Creative Materials (USA). Since the final aim of this work was to monitor the adhesion, growth and differentiation of a large population of cells, an interdigitated geometry was designed by a commercial CAD (AutoCAD 2017) [250], taking into account the necessity to realize a sensor compatible with 24 multiwells plates for cell cultures. The developed sensors have a diameter of 13mm including 2 interdigitated electrodes (Fig. 64a). In order to fit the plate, printed polyimide substrate was cut into circles (diameter 14 mm) with a mechanical puncher. Particular care was put in the design and printing of the interdigitated electrodes thus to obtain tracks 50 μm wide. AJP accuracy ensured to reach dimensions of each electrode fingers in the order of magnitude of cells (around 10 μm). Thus, the number of cells sensed by each finger could be reduced and the overall sensitivity to evaluate their number and reciprocal position increased, in comparison with screen printed or inkjet-printed sensors, where best resolution is around 50–100 μm . In order to reduce the overall resistance of each interdigitated electrodes ($< 1 \text{ k}\Omega$), two subsequent layers of carbon-based ink were deposited. After the deposition, sensors were cured for 15 min at 150 $^{\circ}\text{C}$. The sensors were then sterilized and fixed to the bottom of wells with a biocompatible high vacuum grease that prevented their floating in the culture medium.

f) Impedance measurements

Impedance measurements in term of magnitude and phase angle were carried out by considering a standardized protocol and using a commercial portable potentiostat (PalmSens PS Trace, PalmSens BV, Netherlands) applying a sinusoidal voltage to the sample and measuring the current response in the range of frequencies from 400 Hz and 50 kHz. Measurements were performed before and after cell seeding, in order to correlate variations in the electrical properties with cell adhesion, growth and differentiation. All the pre-seeding tests were carried out with the medium after performing poly-L-lysine (Sigma-

Aldrich, Merck KGaA, Darmstadt, Germany) coating, thus to obtain a value of reference, to be compared with after-seeding measurements. The measurements realized after cell seeding (6×10^4 cells/cm²) were performed at different time points (1-3-7-10-14-17-21 days after seeding), in order to follow the variation of impedance characteristic spectra (i.e. impedance magnitude and phase angle with respect to frequency) during the differentiation process. Experiments were performed in quadruplicate. Data were analyzed by evaluating the impedance magnitude at low, medium and high frequencies (400 Hz, 4 kHz and 40 kHz), in order to assess the most sensitive ones for cells growth and differentiation monitoring. Results have been then expressed as relative impedance magnitude (RI), calculated as $RI = ((|Z|_{\text{with cells}} - |Z|_{\text{without cells}}) / |Z|_{\text{without cells}}) * 100$ [251].

g) Equivalent circuit modeling

For further analysis of impedance spectra alterations, phase angle and magnitude spectra were fitted on an electronic equivalent circuit model, used to describe tissue-electrode interface [244], [252]. Parameters of the equivalent circuit were determined by means of a two-step optimization procedure considering the measurements performed by sweeping all the frequencies from 400 Hz to 50 kHz. First, the contribute of the not-seeded sensors was modeled considering a reduced equivalent circuit, i.e. including electrodes and solution electrical contributes (resistance R_{Cell} , capacitance C_{Cell} of the electrode, and resistance R_{medium} of the solution), but without considering the cell-specific contribution. Subsequently, the cell-covered electrodes were analyzed by applying the entire equivalent circuit, thus including cell membrane/intercellular capacitance (C_{Cell}) and resistance (R_{Cell}), including both the contributes of cell membrane and of the extracellular resistance, determined by the fitting procedure. The fitting procedure and the corresponding analysis was performed with PS PalmSens Trace dedicated software.

h) Statistical analysis

Statistical analyses were performed using Graph Pad Prism version 5.0 (Graph Pad Software Inc., San Diego, CA, USA). All values are presented as mean \pm standard error of mean (SEM) unless otherwise designated. Statistical significance of differences was determined by one-way ANOVA, followed by the Bonferroni test. Student's t-test was also used to compare values in different groups. Further, in order to extract a component score which is a linear combination of the different impedance measured at three selected frequencies, the Principal Component Analysis (PCA) [253] was also included. In addition,

correlation coefficients of multiple method data progression were determined applying two-tailed Pearson correlation test ($\rho > 10.71$) and the statistical significance is considered when $p\text{value} < .05$ [242]. The concordance between two measure was also analyzed by using the Bland-Altman plots [254], [255], after standardizing the data (means=0; variance=1) in order to solve scale problem related to measures extremely different in magnitude. In details, it displays the mean (x-axis) and the differences (y-axis) of the two measures in a scatterplot. The 95% of confidence interval (red line) is computed around the grand mean of the differences (green line). Two measures are concordant when dots are randomly distributed around the grand mean. PCA, Person test and Bland-Altman plot were performed by using R version 3.5.1.

7.1.3 Results and discussion

a) Morphological, biological and biochemical characterization of cell differentiation

Cells seeded at a density of 6×10^4 cells/cm² reached the confluence after few days from the seeding and started to create domes at the seventh day after seeding (Fig. 65a) and both domes number and to further evaluate Caco2-cells spontaneously differentiated into mature enterocytes, we followed the mRNA expression levels of some intestinal markers during the 21 days of differentiation. In particular, we specifically evaluated some small intestinal enzymes such as SI, ALPI and CYP3A4. In addition, we evaluated the gene expression of CLDN4 which encodes an integral membrane protein that is component of the epithelial cell tight junctions. Finally, for brush border transporters, we analyzed SLC15A1 which encodes an intestinal hydrogen peptide cotransporter protein that plays an important role in the uptake and digestion of dietary proteins and SLC11A2 that encodes a member of the solute carrier family 11 protein family involved in the transport of divalent metals and in iron absorption. SI and CYP3A4 showed a progressive increase during differentiation that became statistically significant starting from day 10 for SI and from day 17 for CYP3A4 (Fig. 65d). SI is commonly expressed in the adult small intestine where, as a brush border hydrolase, it is involved in the final steps of digestion of sucrose, starch, and glycogen. Its expression is limited to the villous enterocyte. CYP3A4 the principal cytochrome P450 present in human liver and small intestinal epithelial cells (enterocytes) has been implicated in several transport functions, including the transport of some drugs [256]. Together with the intestinal alkaline phosphatase, it is often used as a marker of terminal differentiation of enterocytes [248], [257]. In our experiments, ALPI mRNA expression substantially showed

a peak when the domes appeared at day 7. From day 10, its expression decreased but remained anyway higher if compared with the day 1 and 3, when the culture was not yet at confluence. This trend for ALPI is confirmed also by other authors [248], [249]. RNA expression of CLDN4, significantly enhanced at day 21 after seeding. Similarly, the two genes SLC15A1 and SLC11A2, whose encoded products, are members of solute carrier families, showed higher mRNA expression when enterocytes are completely differentiated. These results confirmed not only the structural maturation (i.e., CLDN4) but also the functional differentiation with an increase of enzyme expression typical of mature enterocytes (SI, ALPI and CYP3A4), and small intestine transporters (SLC15A1 and SLC11A2). These data are consistent with results already reported in the literature [246], [248]. In addition, data regarding the ALPI enzymatic activity in cell homogenates corroborated the effective complete functional differentiation of Caco-2 cells to enterocytes. In fact, ALPI enzymatic activity, measured as μg of pNP product over total protein, significant increased starting from day 14 (Fig. 65c). That ALPI activity linearly increases during differentiation of enterocytes is well recognized, and it is therefore considered another marker of Caco-2 cell differentiation *in vitro* [258]. All this information initially confirmed the proper occurrence of the differentiation process.

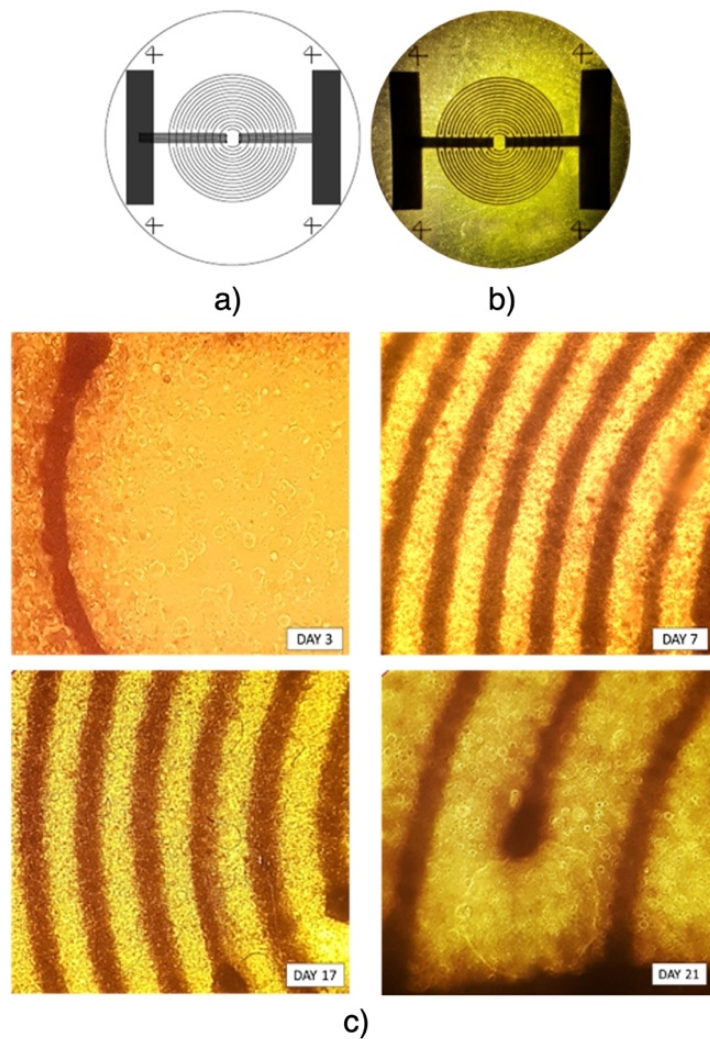
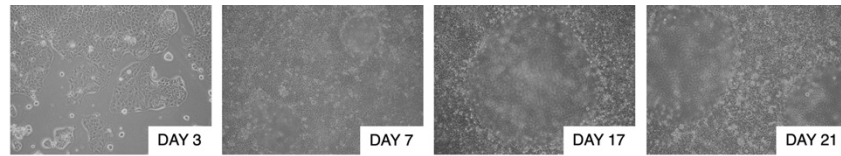
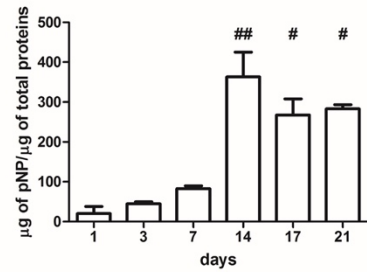
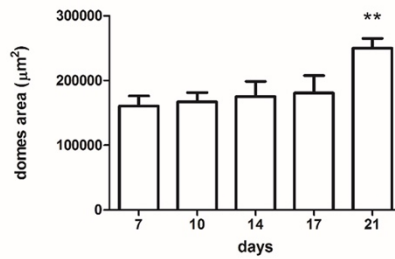
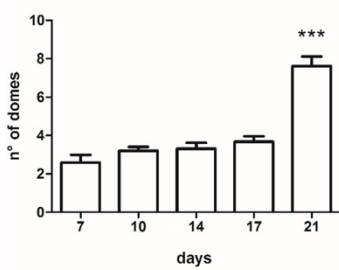


Fig. 64 Caco-2 to enterocyte-like cells differentiation on interdigitated carbon-based electrodes printed on a polyimide substrate. a) Printed Sensor geometry optimized with AutoCAD 2017 and b) image of the sensor acquired with microscope (magnification 1x). c) Representative pictures of Caco-2 cells evaluation at four different time-points (days 3–7–17–21) during 21 days differentiation protocol (magnification 10x and 20x for day 21) where sensor geometry is clearly visible. The 21 day picture results out of focus to better visualize the domes [233].

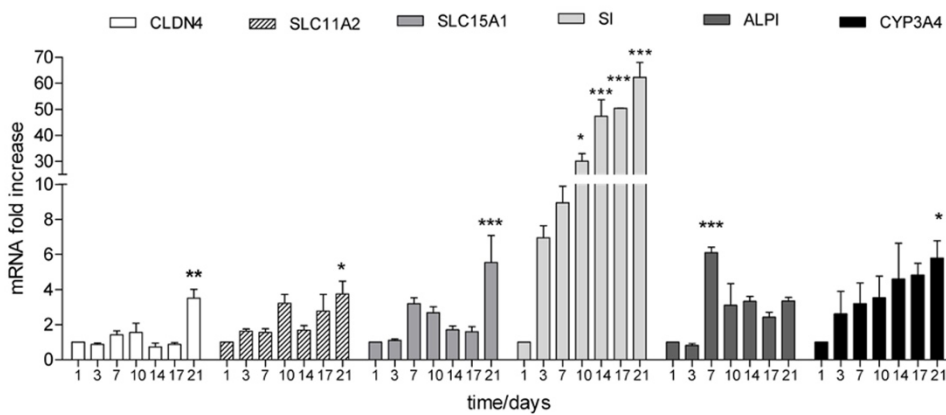


a)



b)

c)



d)

Fig. 65 a) Caco-2 cells morphological evaluation at four different time-points (days 3-7-17-21) during 21 days differentiation protocol (magnification 4x in day 3 and 7; magnification 10x in day 17 and 21); b) Domes counting and measuring. The statistical significance was represented as follows: ** $p < .01$; *** $p < .001$ versus the seventh day after seeding (no domes formation before day 7); c) ALPI assay. μg of pNP extrapolated by a standard curve at days 1-3-7-14-17 and 21 after seeding. Data are normalized for total protein amount (# $p < .05$, ## $p < .01$ versus the corresponding day 1 as control group); d) Quantitative rt-PCR time-courses of key genes CLDN4, SLC11A2, SLC15A1, SI, ALPI, and CYP3A4 during 21 days of differentiation. The values are expressed as mRNA fold increase compared to day 1 for each genes. The statistical significance was * $p < .05$; ** $p < .01$; *** $p < .001$ versus the corresponding day 1 of each gene as control group [233].

b) Impedance measurements during Caco-2 cell differentiation

One of the main hurdles regarding Caco-2 cell enterocyte-like differentiation is the lack of non-invasive and non-destructive method for quantitatively monitoring the integrity of the monolayer and assess the differentiation process. Common biological and biochemical methods such as rtPCR and enzymatic assays are in fact expensive, invasive, and destructive. To overcome these limits, we investigated the possibility to apply the electrical impedance analysis to monitor the differentiation process and verify the monolayer integrity. In order to achieve this goal, an impedance-based measurement setup was designed and realized, including dedicated sensors, specifically customized and realized by means of AJP (Fig. 64). First, the choice of carbon-ink and polyimide substrate was specifically performed after a deep analysis, assessment and comparison of several inks and materials [143],

taking into account the necessity to realize a sensor cytocompatible and resistant to common sterilization processes (e.g., autoclave). The interdigitated geometry of the sensors was demonstrated to be more suitable for cell population monitoring, if compared to the monopolar one [259], [260]. Indeed, this specific configuration has been gaining more and more popularity and it is extensively used for different application in biological sensing [261], [262]. Here, we designed circular interdigitated sensors of 14mm diameter that fitted with 24 multi-well plates (Fig. 64). When cells were seeded on the biosensors and cultured for 21 days, they grew well and differentiated at a mature enterocyte monolayer, as showed by the characteristic dome formation (Fig. 64). These results were in line with data reported in literature on the biocompatibility of the interdigitated carbon ink printed on polyimide substrate [143]. The production by means of printed flexible electronics represents a real promising tool able to combine cost and time effectiveness, with the maximum possibility of customization and optimal geometric and electronic performances. It ensures the possibility to easily tune the electrical resistance of the electrodes, by changing the number of printed layers and the duration of the curing, but also the geometrical parameters of the sensor, by tuning ink viscosity, and printer parameter [80]. Furthermore, compared with more traditional printing techniques such as ink jet or screen printing, AJP allows to achieve resolution in the order of 10 μm with a very high repeatability, features that are particularly valuable for application in biological assays [263]. Comparing the impedance magnitude and phase angle variation after cell seeding at different frequencies, a significant initial increase of the impedance magnitude, with the maximum value of 1 $\text{k}\Omega$ recorded at low frequency (400 Hz) and a decrease of the phase angle toward a capacitive-like behavior [264], [265], with the maximum decrease recorded at lower frequencies (-30 degrees), could be observed suggesting an effective cell adhesion (Fig. 66a). This suggests that the seeded cells effectively adhered on the sensors acting as an insulating layer on the electrodes, forcing the low frequency current to flow around the cellular bodies on paracellular pathways, thus strongly increasing the ohmic resistance of the total system compared with the pre-seeding condition. The decrease in impedance recorded at 400 Hz and 40 kHz during day 3 can be presumably due to cells crowd resulting in more regions of cell-cell contact and a slight drop in resistance. This factor appears to be essentially highly reduced at high frequencies, in agreement with the literature [266], [267]. Thus, at low frequencies the majority of the current tends to flow below or in between cells while at high frequencies the current goes through the cells. Consequently, the high frequency impedance, more affected by cell-coverage, is

more influenced from the formation of domes, whereas the low frequency, responding more strongly to changes in the spaces either under or between the cells, better follows the adhesion process at day 1 and the tight junction formation at day 21. Fig. 66b reported the relative impedance magnitude (RI), normalized over the background, at the three different frequencies, 400 Hz, 4 kHz and 40 kHz. Interestingly, a significant increase of RI during the 21 culturing days was observed at 40 kHz, and a similar but weaker trend was found at 4 kHz, suggesting that the monitoring of RI at these two frequencies might be useful to follow the Caco-2 cell growth and differentiation. More in detail, the trend of RI observed at these frequencies allowed to recognize three interesting moments of cell growth and differentiation (Fig. 66). As previously discussed, the first increase observed at day 1, maximum at low frequencies, could be correlated with the initial capacitive coupling of the current directly through the insulating cell membranes of the initially attached cells. After that, the following monotone increase recorded between day 3 and day 10 can be associated with cells growth on the sensors. Due to cell proliferation and spreading, the percentage of sensor's surface covered by cells increases and the current has to flow through them, affecting the overall measured impedance. Finally, the increase recorded between day 15 and day 21, concluding with a sort of plateau suggesting the effective formation of a confluent and tight layer of cells, supporting our hypothesis of correlation with cell differentiation. At this regard, to better evaluate which frequencies could better highlight Caco-2 to enterocytes-like cells differentiation we combine the multiple measures of impedance by using the Principal Component Analysis (PCA), an exploratory statistical method that converts a set of observations of possibly correlated variables into a set of values linearly uncorrelated called Principal Components (PCs). Thus, it is possible to extract the loadings that represents the weight of each standardized variable (RI at 400 Hz, 40 kHz and 4 kHz) within the PC1 component score. In details, as reported in Fig. 66c, the first component PC1, where RI 4 kHz and RI 40 kHz have a greater weight, was able to describe nearly the 60% of explained variance. All these data are supported from literature, since the specific frequencies 40 kHz and 4 kHz have been previously highlighted as two of the most sensitive for recognizing cells coverage during electric impedance measurements [268]. In particular, the highest sensitivity that can be observed at 40 kHz from the trendline of the RI during the 21 days, appears to be coherent with findings observed by Wegener et al. [123], where this specific frequency has been indicated as the most sensitive ones for monitoring Caco-2 cells using an impedance-based technique. Respect to widely used TEER where a pair of chopstick

electrodes are used to measure the resistance between the apical and the basolateral compartment [269], our impedance-based sensors represent a different approach, less expensive and with a more uniform and coherent monitoring of the impedance both in terms of magnitude and phase angle, with a complete analysis over a range of defined frequencies.

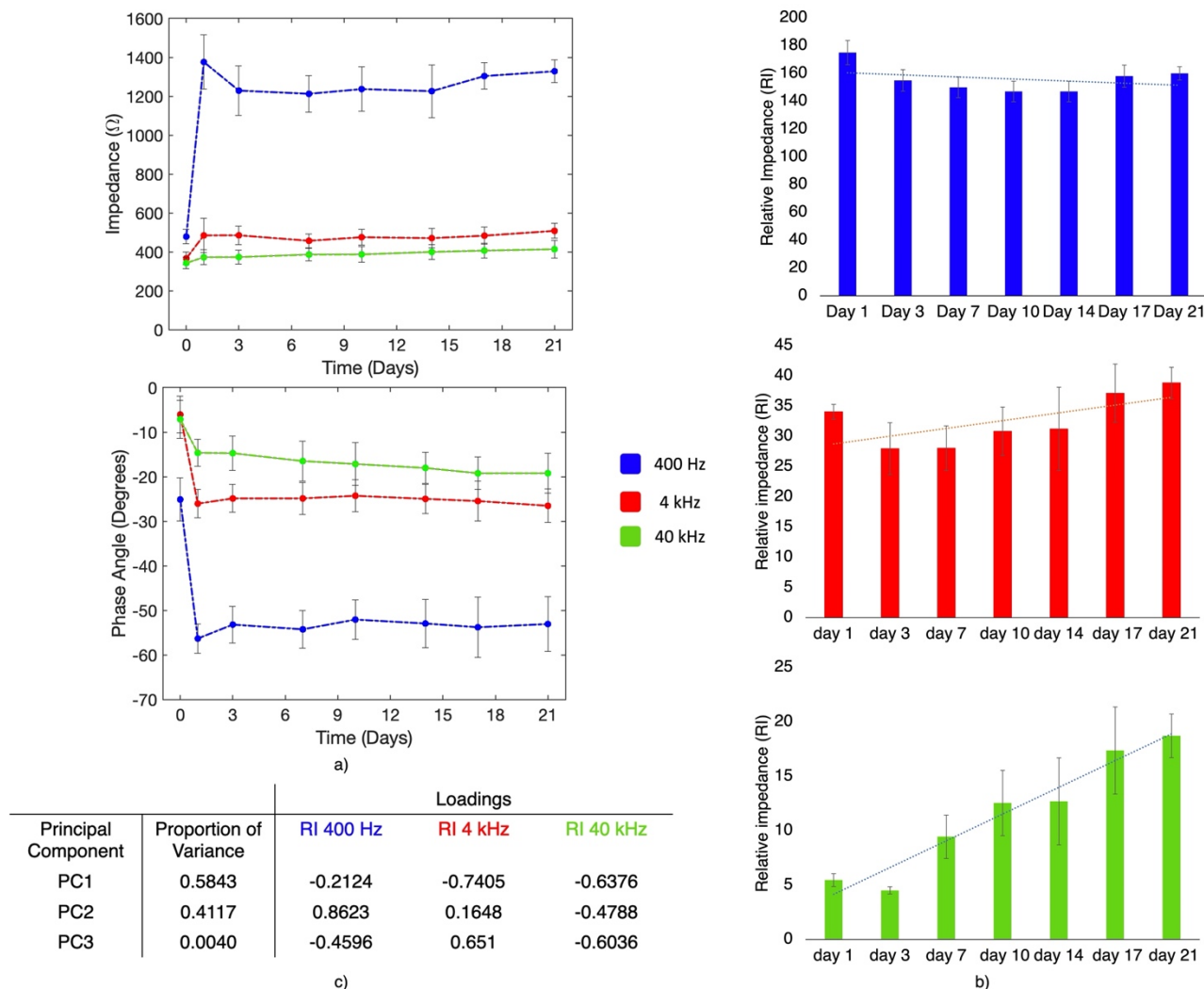


Fig. 66 Impedance-based cell monitoring vs time and relative impedance calculation. A) Impedance magnitude vs time during the differentiation process. Error bars show the standard deviation of the 5 sensors evaluated. B) Variation of the relative impedance during the 21 days of cell culture, calculated for each of the frequencies evaluated: low (400 Hz-blue) medium (4 kHz-red) and high (40 kHz-green). C) Principal component analysis. The proportion of variance (0.5843) could be represented as a percentage (about 60%) and PC1 is the first component with the largest possible variance explained; succeeding components (PC2 and PC3) are orthogonal to PC1 with the highest possible variance [233].

c) Equivalent circuit modeling

Electric circuit model of adherent cells on conductive electrodes has been widely investigated by several groups, including different levels of circuit complexity depending on the specific features that the impedance-based measurement aimed to highlight. Literature reports models ranging from the simplest circuit – which considers just the overall resistive and capacitive contribute of cells [270] to the more complex ones which analyze the

contribute of each specific cell components (attached membrane and superior membrane, cytoplasm, organelles and protein across the membrane) [265]. In our model we choose a specific circuit including only the components required to model the predominant behavior of all the elements involved (cells, electrodes and medium). More in detail, the electrolytic solution was modeled as a constant resistance (R_{medium}), the electrodes as a parallel RC (R_{cell} and C_{cell}) and cell coverage as well as an additional parallel RC (R_{cell} and C_{cell}). While R_{cell} , C_{cell} and R_{medium} could be considered constant in all the fitting, R_{cell} provided useful information about the effective adhesion of the cells, on their proximity and on the tight junction presence. C_{cell} instead, more sensitive to the number of the cells and on the multiple layers, provided feedback on the increase of cell number and on domes formation. Using the described circuit, the impedance spectra obtained from measurements without and with cells seeded on the sensor at the different timepoints (Fig. 67a) could be analyzed with the circuit described above, as presented in Fig. 67b, where measured and fitted spectra are graphed together in order to better highlight the approximation performed with the circuit considered. The analysis performed with the modeling approach is able to provide us with information on the gap left between the cells and to highlight the contribution of adhering cells on the electrode surface. Both the resistive and the capacitive components can be integrated in the circuit and compared to the cell-free model (Fig. 68). Regarding R_{cell} , the highest increase (around 600 Ω) could be measured during the first 24 h, due to the reduction of the paracellular pathways available for low frequency current paths, suggesting an effective adhesion of cells. After the first day, the resistance kept on increasing, until day 21, showing a plateau after the day 17, suggesting a complete differentiation of the monolayer. Regarding C_{cell} , it increases during the first 15 days of differentiation, due to the double layer capacitive contribute of the cell membranes on the electrodes. Then, after a maximum reached around day 15, it decreases in the last two time points. Results obtained both for R_{cell} and for C_{cell} appear in agreement with what found by using different cell types. In detail, as referred also in [269], [271], where endothelial cells were involved, the R_{cell} appears to show a high increase due to the adhesion and then a slow increase due to proliferation, with a sort of plateau corresponding to the monolayer formation. Differently, C_{cell} evolution can be correlated with the number of cells and in particular with their morphological changes due to differentiation process. It appears to increase until confluence is reached and then is reduced when domes, the typical structure of enterocyte-like cells, are created. This decrease in the overall capacitance can be explained taking into

consideration the domes structure, which can be modeled as a series of capacitors [272]. In addition to the pure impedance analysis, the proposed modeling approach allowed to analyze both resistance and capacitance giving additional information about the barrier properties and cell processes such as adhesion, growth and differentiation [264].

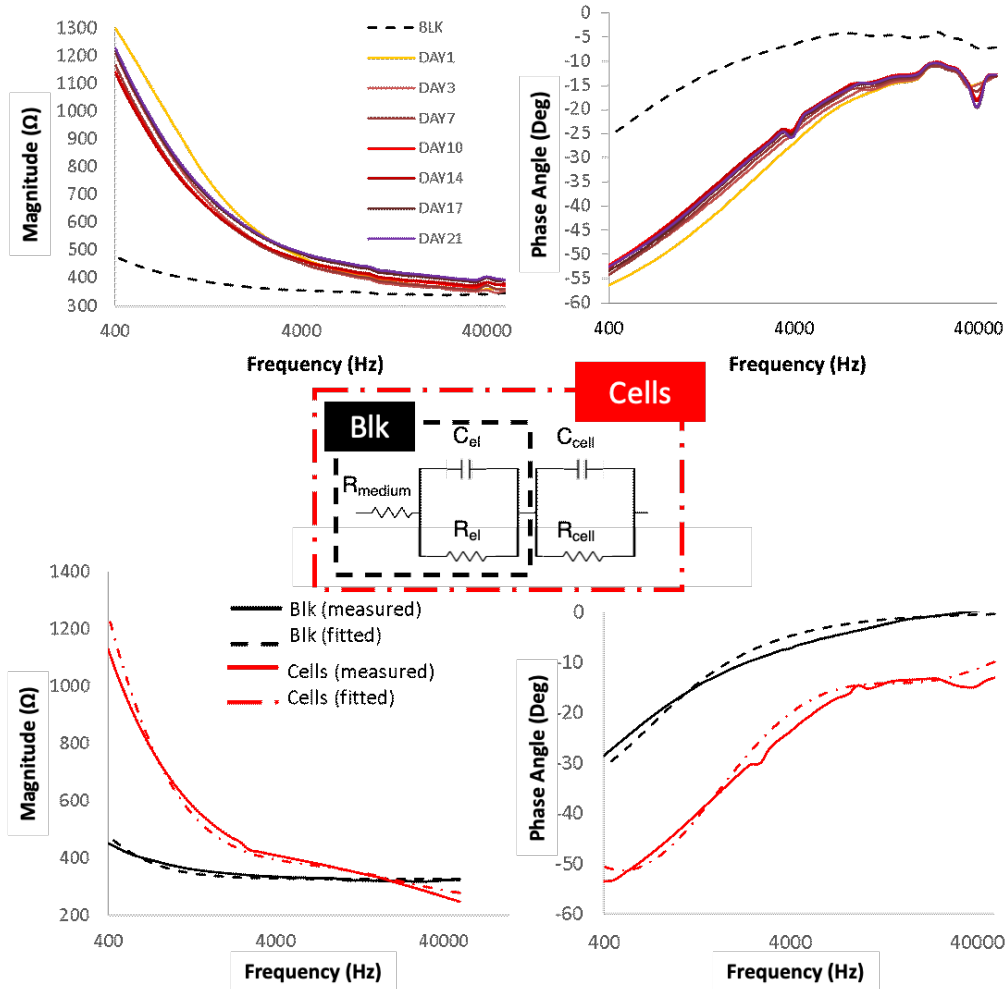


Fig. 67 Impedance-based cell monitoring vs frequency and spectra fitting with equivalent circuit: a) Impedance magnitude and phase spectra vs frequency during the differentiation process. b) Equivalent circuit of blank and seeded sensors used to fit the spectra [233].

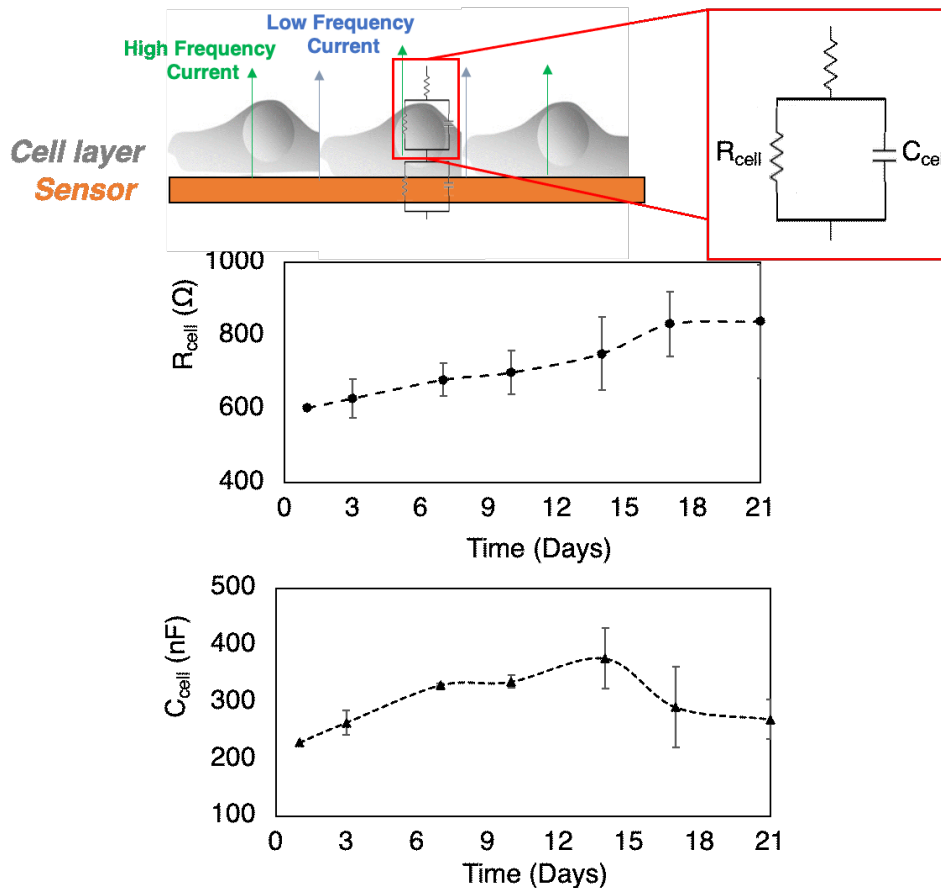


Fig. 68 Evolution of R_{cell} and C_{cell} during differentiation: above, schematic of correspondence between the different parameters in the model with the circuit element; below, specific evolution of the modeling circuit parameters related to cells attached on the sensors [233].

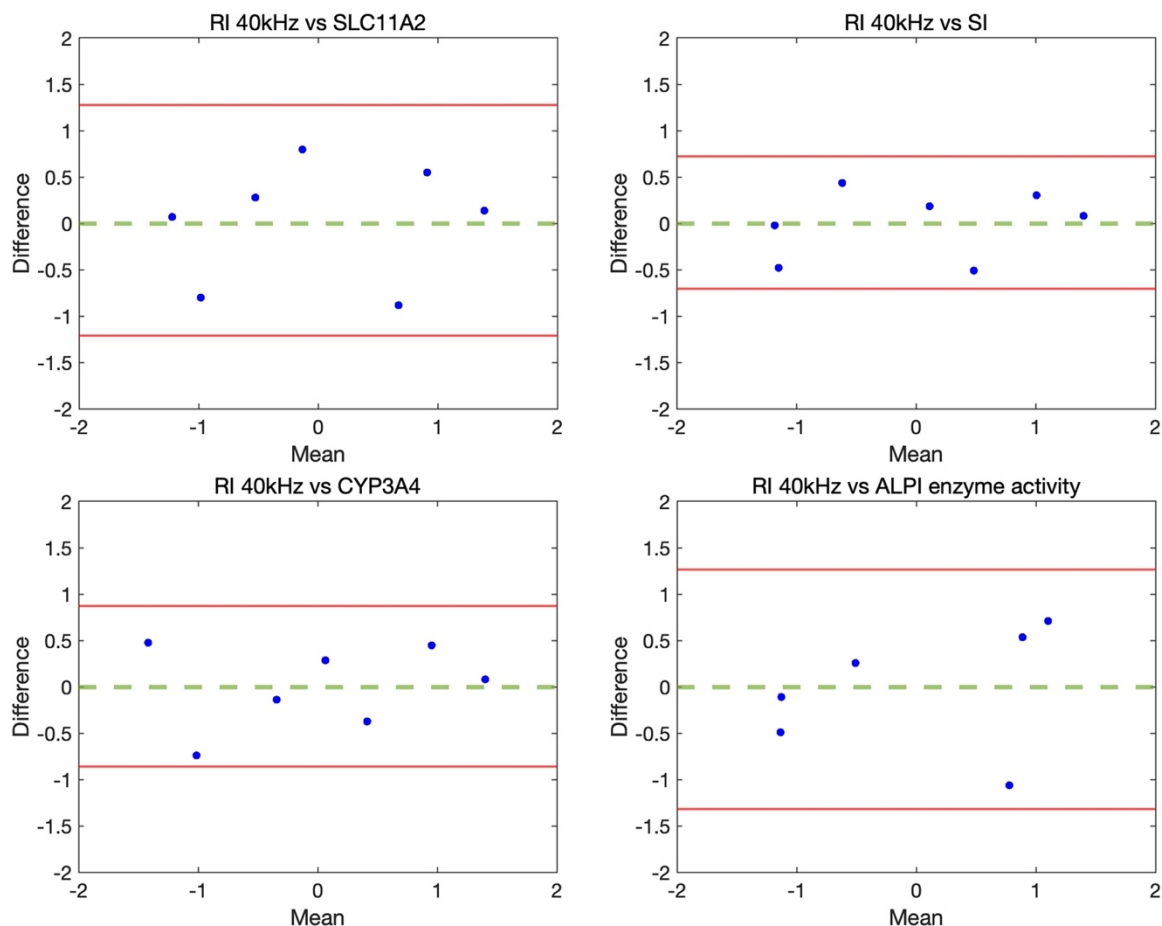
d) Concordance between relative impedance magnitude and morphological, biochemical and molecular data

To highlight possible concordance between changes in impedance magnitude and other parameters related to cell differentiation, a Pearson correlation analysis was performed, specifically considering RI at the two frequencies (4 kHz and 40 kHz) and the PC1 obtained excluding 400 Hz. In fact, the re-computed PC1 described nearly the 86% of explained variance and the two frequencies (40 kHz and 4 kHz) had the same weight (-0.7071). In particular, the Pearson analysis reported in Table in Fig. 69a, described the linear relationship between the behavior of RI with that of the biological, morphological and biochemical parameters during the differentiation process. Interestingly to note, among different frequencies, RI measured at 40 kHz better correlate with the other variables. We specifically found a good statistically significant correlation during the 21 days of differentiation between the increase of RI at 40 kHz and SLC11A2 ($\rho=0.8199$ and $p=.0239$); SI ($\rho=0.9427$ and $p=.0015$), and CYP3A4 ($\rho=0.9134$ and $p=.0040$) genes mRNA expression (Table in Fig. 69a). On the contrary, no correlation was found for CLDN4, SLC15A1 and

ALPI genes, despite for this latter a good correlation was at least found for its enzyme activity ($\rho=0.8300$ and $p=.0409$). Although a good correlation between RI at 4 kHz and 40 kHz with morphology (domes numbers and area) was found, it was not statistically significant, probably due to the small sample size tested. Interestingly, when Pearson test is performed using PC1 the correlation coefficients are reduced, confirming the relevance of 40 kHz respect to 4 kHz. Moreover, the strong and significative correlation between RI 40 kHz and SLC11A2, SI, CYP3A4 and ALPI enzyme activity has been also confirmed by the Bland-Altman plots, where the dots (blue) are randomly distributed closely around the grand mean (green).

	RI 4 kHz	RI 40 kHz	p-value (RI 40 kHz)
RI 4 kHz	1		
RI 40 kHz	0.7255	1	
CLDN4	0.4969	0.5577	0.1933
SLC11A2	0.5410	0.8199	0.0239
SLC15A1	0.3680	0.6318	0.1279
SI	0.6902	0.9427	0.0015
ALPI	-0.1764	0.3556	0.4338
CYP3A4	0.5081	0.9134	0.0040
Domes Numbers	0.8038	0.7933	0.1093
Domes Area	0.8137	0.8008	0.1035
ALPI Enzyme Activity	0.4898	0.8300	0.0409

a)



b)

Fig. 69 a) Pearson correlation coefficients table. Significant correlations is considered for $p > 10.71$ (grey) and the statistical significance is obtained with correlation test and reported in bold (p -value reported for RI at 40 kHz is accepted when < 0.05); b) Bland-Altman plots represent the differences between the pairs of readings, visualizing the pattern of agreement of statistically significant measurements (RI at 40 kHz vs SLC11A2, SI, CYP3A4 and ALPI enzyme activity). Data are standardized (means=0; variance=1) to solve scale problem. The 95% of confidence interval (red line) is computed around the grand mean of the differences (green line) [233].

7.1.4 Conclusion

The feasibility and reliability of an additional method for monitoring cell differentiation of Caco-2 to enterocyte-like cells, based on impedance measurements, was reported. Using AJP as powerful technique to achieve high resolution printed electronics, customized interdigitated sensors were designed and realized depositing a carbon-based ink on flexible polyimide, obtaining low-cost sensors easy to sterilize and integrate with cell culture routine. Results derived from the statistical analysis, performed to evaluate the concordance between morphological, biochemical and molecular data and impedance outputs, allowed to highlight 40 kHz as the optimal frequency to assess Caco-2 to enterocyte-like cells differentiation process. Overall, these results support the here-presented non-invasive and nondestructive approach not only to assess the barrier integrity, but also for cell differentiation monitoring during in vitro experiments.

7.2 *Mesenchymal stem cells*

The research work reported in this section was published in the MDPI journal *Materials* with the title *Impedance-Based Monitoring of Mesenchymal Stromal Cell Three-Dimensional Proliferation Using Aerosol Jet Printed Sensors: A Tissue Engineering Application* [273]. Results and pictures are reported with permission of the editor.

7.2.1 *Introduction*

Nowadays, three-dimensional (3D) cell cultures represent a widespread approach adopted in several fields, ranging from pharmaceuticals to regenerative medicine. The possibility of reproducing the conditions undergone by cells in living tissues plays a fundamental role in improving the effectiveness of drug testing and tissue engineering [274]. From this perspective, regenerative medicine strategies can be focused on the restoration of damaged tissue by using human mesenchymal stromal cells (hMSCs) in combination with 3D scaffolds [275]. hMSCs were reported to promote tissue repair thanks to several key characteristics, such as their ability to migrate towards injured tissues, their immunomodulatory action and their trophic effect [276]. The combination of bioengineered scaffolds with hMSCs represents one of the most attractive strategies, since it combines the structural, biological and chemical properties of the scaffolds with the possibility of modulating hMSC activities [277]. In recent years, among the multitude of biomaterials used to support hMSCs, hydrogels, both synthetic and natural ones, have been back in the limelight due to their inherently tunable characteristics and their ability to mimic native extracellular matrix (ECM) [278].

From the perspective of optimizing the scaffold-culture system, the need for non-invasive methods able to monitor cell proliferation and differentiation within 3D environments still remains one of the main hurdles to improve scaffold design and better understand cell-material interaction [279], [280]. Nowadays, traditional methods adopted for those analytical evaluations (e.g., dyes, DNA sequencing, immune-based assays, fluorescence tags) interfere, in most cases, with the cellular cycle. Therefore, most of these approaches make it fairly impossible to perform a continuous monitoring of cell culture health, requiring either the sacrifice of the tested samples or the introduction of an unaffordable toxic effect. The possibility of non-invasively obtaining information on cell activities within the scaffolds—strictly avoiding affecting their vitality and proliferation—would allow a step forward to be made in terms of understanding complex pathophysiological processes.

Among the available electrical-based cell monitoring techniques, impedance-based solutions represent one of the most adopted approaches, easily integrable with labware and microfluidic devices [281]. This approach is based on the hypothesis that cellular membranes act as insulating elements when seeded on conductive electrodes. Thus, by measuring the impedance changes between two electrodes, information related to cell number, shape and their motility can be obtained [282]. In the last decades a huge interest has been addressed to the possibility of translating the planar approach towards 3D settings [283]. Two possible approaches can be highlighted from the literature: (1) making the scaffold conductive or (2) monitoring cell and scaffold dielectric properties by introducing external conductive elements in contact with the scaffold itself. The first option represents the most convenient in terms of electronic performances. However, as reported by Kahn et al. [284], further research is still required to achieve solutions that are able to offer the very same positive effect that non-conductive scaffolds can provide to cell development.

Due to these reasons, the main goal of this study was to design, develop and validate a reliable impedance-based solution, easily integrable with a traditional multi-well culture system and easily scalable in terms of processing cost and time effectiveness. In more detail, AJP sensors specifically designed to adapt to 96-well plates were produced, folded to create 3D parallel electrodes structures and tested to monitor the adhesion and growth of hMSCs seeded into gelatin-chitosan hybrid hydrogel scaffolds. Reliability of the methodology was assessed in terms of impedance-based results in conjunction with enzymatic outputs and proliferation assays.

7.2.2 Materials and Methods

a) Setup Design and Production

The proposed measuring setup was designed in order to fit into a standard plastic 96-well non-treated plate, usually adopted in cells suspension culture and bio-assay experiments. Hybrid gelatin-chitosan hydrogel scaffold were prepared following the procedure described in [285], cut, sterilized using gamma irradiation with Cobalt 60 gamma rays using 27–33 kGy following UNI EN ISO 11137 (Sterilization of Health Care Products) and stored in sealed bags until use. Before sterilization, scaffolds were cut into standard cylinders of 4 mm in diameter and 2 mm in height, in order to ensure the correct fitting within the wells, considering their volumetric expansion when wet. Sensors were realized by means of a commercial Aerosol Jet® 300. On the same 20 μm thick polyimide substrate (Kapton® MT

from DuPont, Wilmington, Delaware, USA), two monopolar structures were printed by depositing 3 layers of an electrically conductive carbon-based ink (EXP 2652–28, sheet resistivity 100 Ω /sq./mil) from Creative Materials (Creative Materials Inc., Ayer, MA, USA), in order to achieve a proper electrode conductivity (<1 k Ω). After printing, electrodes were cured in oven for 30 min at 140 °C. After that, interfacing pads for electrical contacts were realized, in order to limit measurement uncertainty due to possible variability in reproducing the same tips positioning. Square silver pads of 8 × 8 mm were printed on one side of the structure by depositing three layers of silver-based ink (Novacentrix, Austin, TX, USA) and then cured in an oven at 140 °C for 30 min. The final sensors are reported in Fig. 70a. Cured sensors were then sterilized in autoclave and stored in sealed bags until use. Sterility during scaffold impedance monitoring was ensured by performing all the measurements under a class A laminar flow hood and using a customized sterile cap. In detail, a cover of a standard 96-well plate was modified, creating 4 measuring sites by drilling 2 holes to access the silver pads from outside. The modified cap was sterilized by means of UV rays for 24 h before each measuring session and stored under the sterile hood when not in use. Thus, the measuring cap was employed only during measurement sessions in order to avoid altering the sterility of the scaffold-sensor systems during culture in the incubator, for which the standard sterile cap of the multi-well was used. The overall setup is highlighted in Fig. 70.

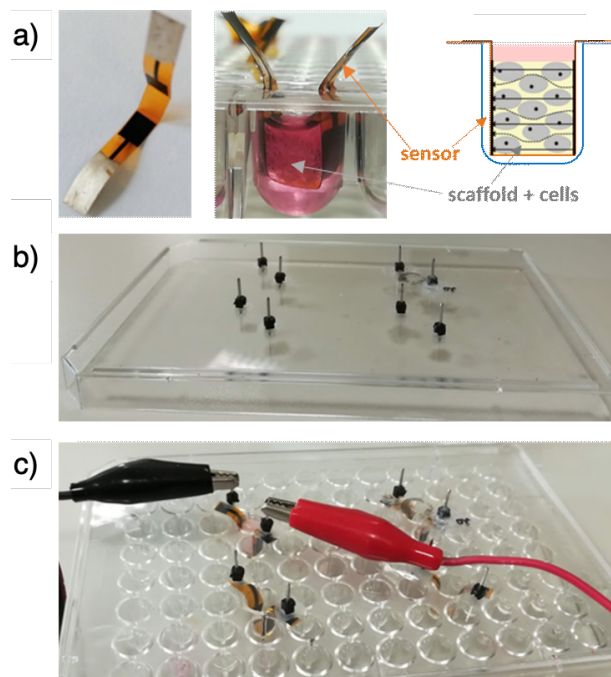


Fig. 70 Setup for impedance-based monitoring of human mesenchymal stromal cells (hMSCs) seeded in 3D hybrid hydrogel scaffold: (a) Hybrid hydrogel scaffold and aerosol-jet printed (AJP) sensors, (b) cap for sterile measurements, (c) final measurement setup [273].

b) Experimental Design

Three-dimensional cell cultures—including scaffolds—were set up in 96-well sterile suspension culture U-bottom plates (Cellstar Greiner bio-one, Kremsmünster, Austria), in order to prevent the adhesion of hMSCs to the plastic substrate. In each plate only four wells in correspondence of the lid measurement sites were used. As hereinafter reported, in a preliminary study we established the optimal number of hMSCs to sow in each well (i.e., 200,000 cells/scaffolds). Therefore, we set up ten 96-well plates by assigning to each of the four available measuring sites a scaffold with its relative sensor, which remained associated to it until the end of the culture session. In order to determine the basal electrical signals of each system (i.e., scaffold/sensor) before seeding, we hydrated the scaffolds with complete culture medium (Iscove's culture medium (σ) with 200 mM L-glutamine, penicillin 100 U/mL/streptomycin 100 μ g/mL, 25 μ g/mL fungizone, 0.6 U/mL sodium heparin and 5% human platelet lysate) and then repositioned them back in the well including the sensor and in the presence of medium. Basal electrical signals were recorded after incubating the plates (5 h in a humidified incubator, 37 °C, 5% CO₂). After the measurements, scaffolds and sensors were dried and exposed to air flow under the class A hood for 3 h and to UV rays for 12 h. Dry-seeding was thence realized the day after. Impedance measurements were performed on culture on days 3, 7, 10, 14, 17 and 21. Viability and cell proliferation were instead assessed on days 3, 7, 14 and 21 using a colorimetric enzymatic test. Control scaffolds for colorimetric testing and scaffolds for microscopy analysis were provided at all time points.

c) Impedance Measurements

Impedance measurements (magnitude and phase angle) were performed in a laminar flow hood (class A) to maintain sterility, using a commercial portable potentiostat (Palmsens PS Trace, PalmSens BV, Netherlands), with the protocol as previously optimized in [143], [233]. A sinusoidal voltage with frequency linearly sweeping from 100 Hz to 10 kHz was applied to samples through the printed parallel carbon electrodes, and the current response was measured in that frequency range. In order to correlate changes in the measured impedance with the adhesion and growth of cells within the scaffold, we performed impedance measurements before and after cell seeding. All the pre-seeding tests were carried out using the very same type and quantity of medium that was used for cell culture, after leaving the scaffold in immersion for 1 h to allow the material to swell and to come in contact with the

parallel electrodes, due to its volumetric expansion. The same measurements were repeated for all the sensors in order to obtain for each of them a reference value to be compared with the corresponding after-seeding measurement and also to assess the variability among the different scaffold/sensors systems.

Measurements after cell seeding were realized at specific time points (3, 7, 10, 14, 17 and 21 days), monitoring the variation of both impedance magnitude and phase angle during cell adhesion and growth with respect to frequency. Measured spectra were analyzed over all the range of frequencies considered, in order to identify the most suitable to enhance cell adhesion and growth monitoring. The same protocol was performed for a preliminary experiment with different cell numbers (50,000, 100,000, 200,000, 500,000 and 1,000,000 cells/scaffold) in order to assess the optimal amount, and then, the same measurements were repeated in parallel with biochemical viability assays using the optimized number of cells (i.e., 200,000 cells/scaffold).

d) Equivalent Circuit Modeling

Cell contribution to the overall acquired impedance spectra was extracted by fitting magnitude and phase angle spectra with an electronic equivalent circuit model; this approach was used to describe sensor-scaffold-cells system, adapting to the presented set up the models adopted in recent literature to model scaffold-based 3D cell cultures [286]. Parameters related to the contribution of scaffold and sensors were defined by modeling the pre-seeding acquisition performed in a range of frequencies from 100 Hz to 10 kHz considering only the culture medium and with culture medium and swelled cell-free scaffold. The parameters therefore included in the cell-free model were C_{scaffold} , $C_{\text{electrodes}}$, $R_{\text{electrodes}}$, R_{solution} , modeling respectively scaffold and electrodes electrical capacitances and electrodes and solution electrical resistances. After that, impedance spectra from cell-seeded scaffolds were modeled by integrating in the previous model the contribution of seeded hMSCs. The parameters added in the cell-seeded model were thus C_{Cell} , modelling cell membrane/intercellular capacitance, and R_{Cell} , modelling cell resistance both in terms of cell membranes and intracellular cytoplasms. PS Palmsens Trace dedicated software was adopted for fitting the spectra and evaluating the variation of the extracted parameters at each time point.

e) hMSC Culture and Seeding

Bone-marrow-derived MSC from a single healthy donor were obtained, cultured, expanded and characterized, as previously described in [287]. All experiments were conducted with cells between passage 3 and 4. Cultures were trypsinized, washed and resuspended as single cells in a phosphate-buffered saline solution (PBS) with 5% of fetal bovine serum (5% FBS). Cell count and viability were performed in TRUCOUNT tubes (BD Biosciences, San Jose, CA, USA), by addition of 7-amino-actinomycin D (7-AAD) (BD Biosciences, San Jose, CA, USA), and analyzed using flowcytometry (FACS Canto Diva software byBD Bioscience, San Jose, CA, USA). After centrifugation, hMSCs were collected and resuspended at high cell density (5000 cells/ μL) in complete culture medium (Iscove's culture medium (σ) with 200 mM L-glutamine, penicillin 100 U/mL/streptomycin 100 $\mu\text{g}/\text{mL}$, 25 $\mu\text{g}/\text{mL}$ fungizone, 0.6 UI/mL sodium heparin and 5% human platelet lysate). In the preliminary experiments, the cell concentration was adapted to have the required number of cells in a volume of 40 μL as needed. Dry scaffolds were placed in wells of 96-well sterile suspension culture F-bottom plates (Cellstar Greiner bio-one) for cell seeding. We adapted two static seeding methods for our experiment, namely "cold " and "dry", to increase the efficiency of cell penetration and distribution within the scaffold, by exploiting their characteristics; this approach was necessary since by using static seeding methods, most of the cells often adhered to the surface of the scaffold [288], [289]. A small drop (40 μL — 2×10^5 viable hMSCs) was slowly deposited on top of dry cylindrical scaffold, waiting for the complete absorption of the drop. Any unabsorbed cell suspension was re-seeded on the scaffold. The plates were then covered and incubated for 1 h at 4 °C in the refrigerator and then for 2 h at 37 °C with 5% humidified CO₂. The two incubations were performed without adding culture medium to improve cell adhesion. Every 30 min the plates were opened in sterile conditions, to re-seed any cell suspension present on the bottom of the well. The seeded scaffolds were then transferred with sterile forceps to the wells of the U-bottom culture plates previously set up with the corresponding sensors and conditioned in a humidified incubator (37 °C, 5% CO₂). Only at this point, 150 μL of culture medium was added to each well with half fresh medium replacement every two days. Seeding wells were examined under an inverted microscope to check cell adhesion to the plastic.

On the days of the enzymatic test (days 3, 7, 14), the 96-well culture plates were replaced with new sterile plates to prevent the risk of contamination and get rid of any cellular debris

adhered to the wells. In addition, the complete culture medium was completely replaced. To ensure correct humidity inside the plate, 12 peripheral wells were each filled with 200 μL of sterile water, restored if necessary.

f) hMSCs Enzymatic Proliferation Assay

To monitor hMSC proliferation during 3D culture, we used the Cell Counting Kit-8 colorimetric assay (CKK-8—Sigma-Aldrich, Merck Life Science S.r.l., 20149 Milano, Italy) based on the dehydrogenase activity detection in viable cells. Preliminary experiments with 2D culture in 96-well plates (2000 cells/cm²) were performed to test hMSCs' response to CKK-8. In detail, 4-times treated hMSCs showed an average absorbance value of $15 \pm 5\%$ lower than cells at first-time treatment. Flow-cytometry counts confirmed a lower cell average ($18 \pm 5\%$) in cultures after 4-times treatments. Difference could be partially explained by the greater number of washes related to the 4 treatments, and however, it is in any case comparable to the variability range ($16 \pm 5\%$) observed between replicates with the same number of CKK-8 treatments (data not shown).

Moreover, we tested CKK-8 efficiency to detect a large number of cells in 3D culture, measuring the absorbance of 200,000 hMSCs/scaffold at the time of seeding (time 0) and after 14 and 21 days of culture (data not shown). Scaffolds were positioned in a new 96-well sterile suspension culture plate without sensors, covered with 200 μL of CKK-8 solution diluted (1-part CKK-8 + 10 parts of culture medium) and filtered (0.2 μm) to ensure sterility. The plates were then incubated (for 2 h 30') in a humidified incubator (37 °C, 5% CO₂). A cell-free control scaffold was incubated to determine the background measurement. 100 μL of solution was transferred into a 96-well F-bottom plate, and the absorbance at 450 nm was measured for each well using a microplate reader (ELX800, Bio Tek Instrument Inc, Winooski, VT 05404, USA). Cell proliferation was assessed on days 3, 7, 14 and 21 from sowing, and triple exposures of each sample were made under the same conditions. Before being put back into culture on the corresponding sensors, scaffolds were washed in new wells twice with 300 μL PBS 0.2% human albumin solution and once with 300 μL of culture medium (30', humidified incubator 37 °C, 5% CO₂).

Although CKK-8 product information reported “a very low cytotoxicity”, no standard indications were given about possible interferences during repeated exposures in the presence of 3D porous scaffold material. Therefore, the possible effect of the dye on cultures

subjected to repeated CKK-8 treatments (up to 4) was also verified. We compared absorbance measurements in relation to the number of applications and culture days, to assess if any residues potentially trapped in the pores even after scaffold washes could exert any detrimental effects on cell viability and proliferation. For each measurement time point, we provided control scaffolds to be treated for the first time.

g) Immunostaining and Microscopy

This specific assessment required three different phases: fixation, permeabilization and blocking and imaging using fluorescence microscopy.

After removing culture medium, the scaffold was gently washed with PBS (Sigma-Aldrich, Merck Life Science S.r.l., 20149 Milano, Italy) and placed on a glass slide. The cylinder was then sectioned vertically in two parts and cut into thin slices (about 1 mm thick) starting from the side of the central cut. Each slice of scaffold positioned on a slide was then incubated (22 ± 2 °C, 10') with 100 μ L of 3.7% formaldehyde solution preheated to 37 ± 2 °C. Once the fixing solution was removed, the slices were washed with 100 μ L of PBS and immediately removed.

Washed slices were permeabilized by adding 100 μ L of 0.1% Triton X-100 solution (Sigma-Aldrich, Merck Life Science S.r.l., 20149 Milano, Italy) to 22 ± 2 °C for 5 min. Once the permeabilizing solution was removed, 2 rapid washes were carried out with 100 μ L of PBS for each slice. The slices were subsequently incubated (22 ± 2 °C, 30') with 3% FBS (fetal bovine serum—Sigma-Aldrich, Merck Life Science S.r.l., 20149 Milano, Italy) PBS solution.

Cell presence and distribution in the scaffold was visualized at 3, 7, 10, 14 and 21 days of culture by sacrificing the scaffolds and analyzing the thin slices with an inverted fluorescence microscope (Olympus IX70, OLYMPUS, 20034 Hamburg, Germany). The cell nuclei were stained with DAPI (4',6-diamidino-2-phenylindole—Resnova). Thin slices were photographed at a magnification of 10 \times .

h) Statistical Analysis

To verify if the use of multiple KK-8 treatments influences hMSC proliferation, we used analysis of variance (ANOVA) techniques and the two-sample Student's *t*-test. Whenever applicable, the Tukey HSD (honestly significant difference) procedure was used to test differences among two sample means, controlling the probability of making one or more

type I errors. To investigate the trajectory of hMSC proliferation over time we fit a linear trend time series regression. To investigate the association between mean hMSC CKK-8 absorbance levels and mean impedance measurements at 3, 7, 14 and 21 days, we employed simple regression analysis techniques. The association between absorbance and impedance was further summarized using the Pearson's correlation coefficient. We employed the Student's t-test to evaluate the statistical significance of regression coefficients' estimates. Statistical significance was set as $p < 0.05$ for the regression analyses.

7.2.3 Results and Discussion

a) hMSC Culture in 3D Hydrogel Scaffold

Results of the relationship between impedance measurements and number of cultured cells obtained from the preliminary pilot study comparing different cell concentrations (50,000, 100,000, 200,000, 500,000, 1,000,000) are summarized in Fig. 71.

Regarding the impedance-based assay, results from the preliminary evaluation allowed 200,000 cells/scaffold to be selected as the optimal concentration to perform the comparison between this novel assay with the standardized cell proliferation enzymatic assay and the optical imaging. As highlighted in Fig. 71, the higher concentrations (500,000 and 1,000,000 cells/scaffold), despite showing rapid growth during the first week, appeared to reach saturation after 14 days. This finding appeared to be in agreement with an acidification of the medium pH that could be observed during culture medium change after day 10, suggesting a condition of cell sufferance that is not ideal for a long-term healthy culture. On the other side, the lowest concentrations (50,000 and 100,000 cells/scaffold), despite showing a proliferation trend, reported a high variability indeed, probably due to the difficulty of seeding such a low cell number with high reproducibility in the different scaffolds. The condition with 200,000 cells/scaffold instead showed a better linearity ($R^2 = 0.9932$), suggesting that this concentration is the best one to perform complete proliferation assays over a 21-day culture period.

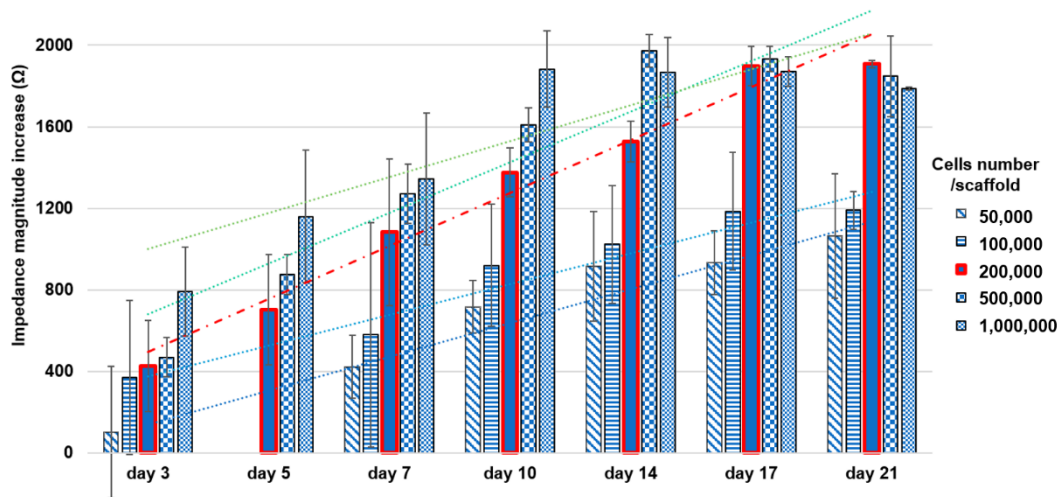


Fig. 71 Preliminary impedance-based assessment for choosing the optimal cell concentration in the scaffold [273].

b) Impedance-Based Cell Proliferation Monitoring

Results from the preliminary experiments performed monitoring 200,000 cells/scaffold for 21 days using an impedance-based assay highlighted the possibility to adopt this approach to correlate a change in the electrical impedance parameters with the number of cells inside the scaffold. Comparing blank scaffolds to the hMSC-seeded ones, a decrease in the overall impedance can be highlighted in both conditions; this was probably due to the presence of the electrolytic medium, which was hydrating the hydrogel scaffold, enhancing the conductivity of the overall system. However, this conductivity increase appeared to be more enhanced in the blank scaffolds rather than in the cell seeded ones, due to the presence of the cells themselves that, spreading inside the pores of the scaffold, acted as insulating elements against the current flow within the culture medium (Fig. 72).

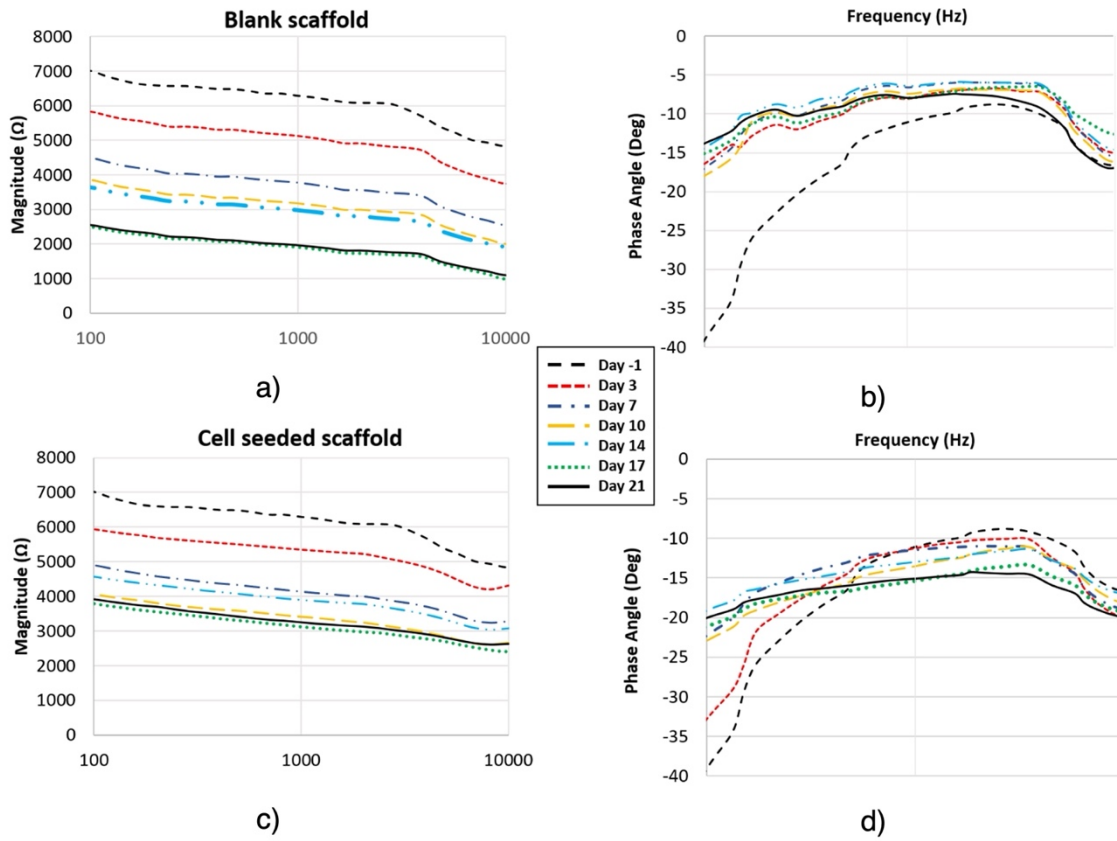


Fig. 72 Impedance-based monitoring including controls (a. magnitude and b. phase angle versus frequency) and seeded scaffolds (c. magnitude and d. phase angle vs frequency) [273].

The contribution of cells within the scaffold/electrolyte/cell system can be obtained by calculating the corresponding cell index (CI) in terms of both magnitude and phase angle, by subtracting the effect of the scaffold/electrolyte system at each specific time point, n , as detailed in the equation in Fig. 73.

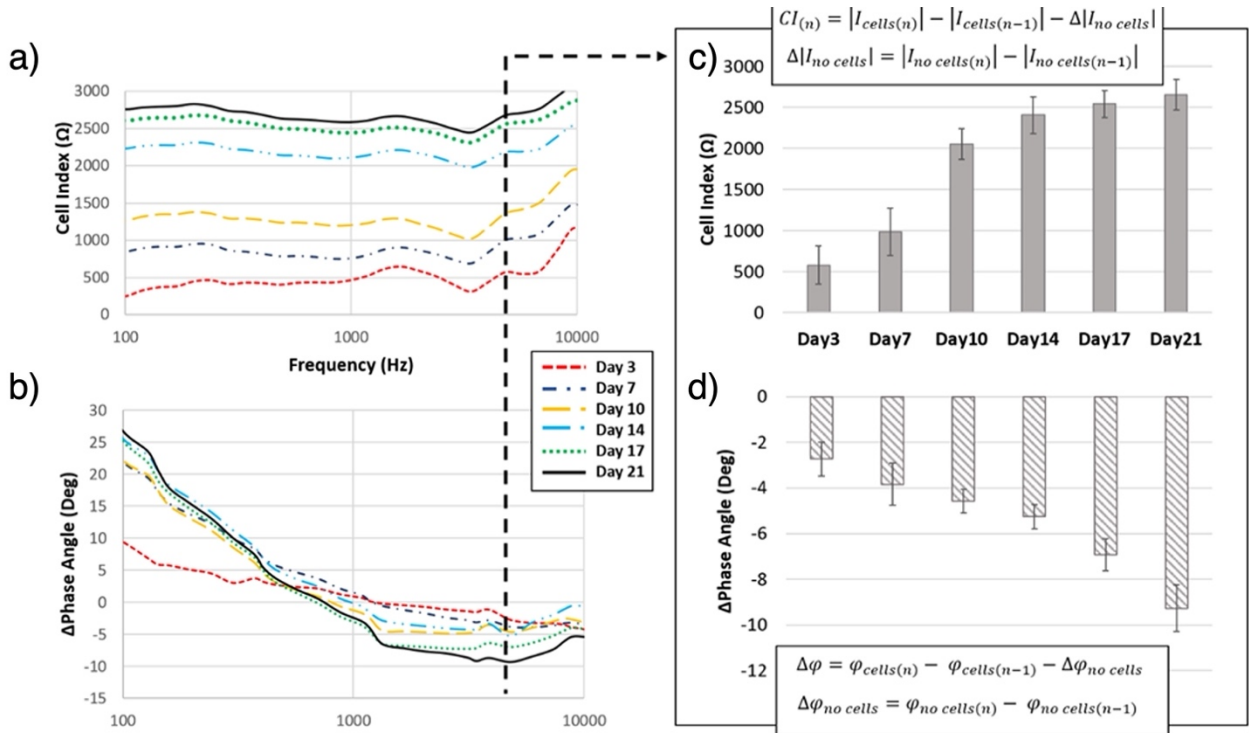


Fig. 73 Cell index in terms of (a.) magnitude and (b.) phase angle contribution to the overall impedance value. Results concerning 4 kHz frequency are specifically highlighted for both (c.) magnitude and (d) phase angle [273].

Due to the capacitive like behavior of cells—which act as insulators for lower frequencies and as conductors for higher frequencies—the CI was represented by an increase of magnitude, proportional to the amount of cells effectively attached to the scaffold, and by a decrease of the phase angle, particularly evident around 4 kHz. This specific value is perfectly in agreement with several works reported in the literature which highlighted this frequency as the optimal one for discriminating the contribution of cells with respect to the other elements that form the system [268].

c) Equivalent Circuit Modeling

The equivalent model adopted to fit the impedance spectra allowed the resistive and capacitive contribution of the cells to be highlighted, extracting the specific value of each parameter during the evolution of the cell culture. The best fitting was achieved with the equivalent model reported in Fig. 74. By using this model, both the capacitive and the resistive behavior of the electrode and of the cells were enhanced.

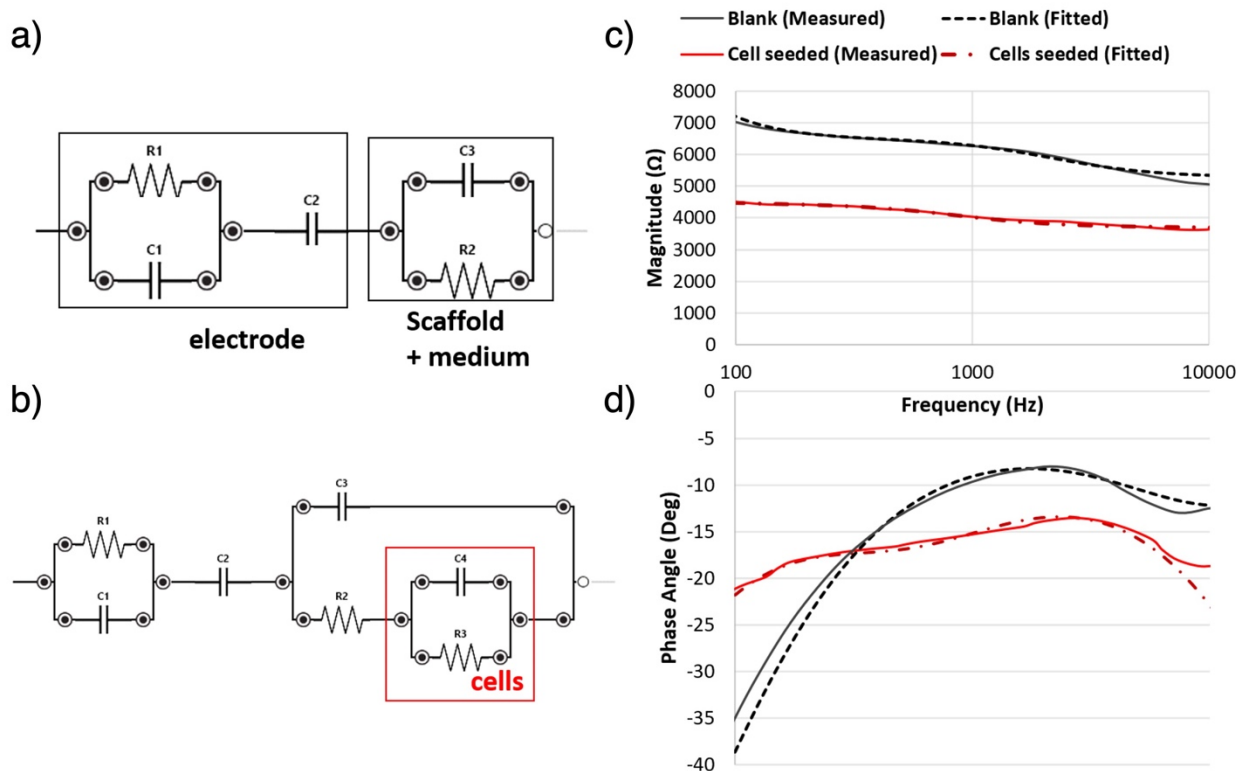


Fig. 74 Equivalent circuit modeling the (a.) blank and (b.) cell seeded conditions: measured and fitted spectra for both the (c.) module and (d.) phase are reported [273].

Regarding the modeling circuit fitting the system without cells, we can highlight both a resistive and a capacitive behavior of the carbon-based electrode itself, as well as the typical double layer capacitance due to the interaction between the electrolyte/scaffold and the sensor itself. Additionally, most of the contribution in the impedance was given by the scaffold itself (i.e., a non-conductive material, so mainly expressing a capacitive behavior) and the medium (i.e., an electrolytic solution, which can be modeled as a resistor).

Comparing the conditions with and without cells, we observed that the presence of cells can be reliably modeled by adding parallel between a resistor and a capacitor (RC parallel) in series to the culture medium and in parallel to the scaffold. The cells attaching within the pores of the scaffold acted as series resistance with respect to the culture medium and in parallel to the scaffold material.

As shown in Fig. 75, an exponential increase of both R_{cells} and C_{cells} can be observed throughout the 21 days of culture, suggesting a proliferation of cells within the scaffold and thus an increase of both the resistive and the capacitive contribution to the overall impedance. This result appears to be in agreement with that reported by scientific literature [290]; in particular, the capacitance and resistance extracted from the equivalent circuit

models are highlighted as useful parameters to describe cell proliferation in a 3D cell culture, since they closely relate to the overall cell number and volume.

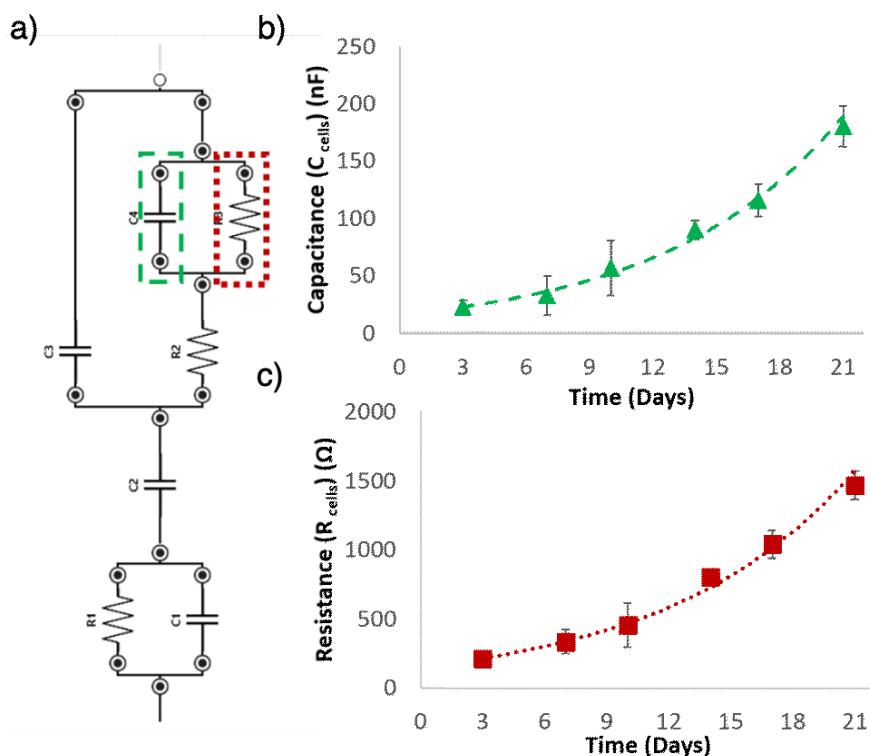


Fig. 75 Evolution of the relevant parameters concerning the cell contribution during time (C_{cells} , R_{cells}). (a): Equivalent circuit with R_{cells} and C_{cells} highlighted (b): Evolution of C_{cells} during culture (c): Evolution of R_{cells} during culture [273].

d) Enzymatic Activity-Based Cell Proliferation Monitoring

Preliminary experiments performed to test the growth of different hMSC concentrations on hybrid gelatin-chitosan hydrogel scaffolds, indicated that the seeding concentration of 200,000 hMSCs/scaffold was the most suited to monitor cell proliferation in 21-day culture, both in terms of electrical impedance measurements and absorbance measurements.

Macroscopic evaluation of CCK-8-stained scaffolds after 14 days of culture showed a uniform distribution of formazan dye, as evidenced by the vertical sections performed on the cylinders. This indicated that the CCK-8 solution had reached all parts of the scaffolds and that the cells were uniformly distributed along and inside the scaffold. Furthermore, the cell-free scaffold (control) shows that CCK-8 treatment did not cause any non-specific staining of the scaffold (Fig. 76a, b).

Results obtained by testing if repeated treatments (up to 4) over time with CCK-8 could affect cell viability showed no significant differences. This suggested that potentially trapped residues of the dye in the scaffold pores did not interfere with cell proliferation.

In detail, at 7 days of culture, absorbance measurements of scaffolds never treated with CKK-8 were compared with those that already had been at 3 days of culture. The statistical test did not reveal any differences between the two groups of scaffolds (*t*-test, $p = 0.49$). Similarly, the comparisons between scaffolds (1 vs. 2 vs. 3 CKK-8 treatments) at 14 days of culture did not show significant differences (ANOVA, $p = 0.8$; *t*-test 3 vs. 2, $p = 0.78$; *t*-test 3 vs. 1, $p = 0.88$). Similarly, 21-day culture comparisons, between 4-times treated scaffolds (3, 7, 14, 21 days) and the scaffolds that received less treatments did not show significant differences in the absorbance values (ANOVA, $p = 0.54$; *t*-test 4 vs less than 4, $p = 0.84$). Fig. 76c shows the distribution of the absorbance measurements at 21 days of culture, for 4th CKK-8 exposure scaffolds and those at the first treatment. The statistical comparison, also in this case, showed no significant differences (*t*-test, $p = 0.64$); therefore, we considered all the scaffolds comparable regardless of the number of CKK-8 staining performed.

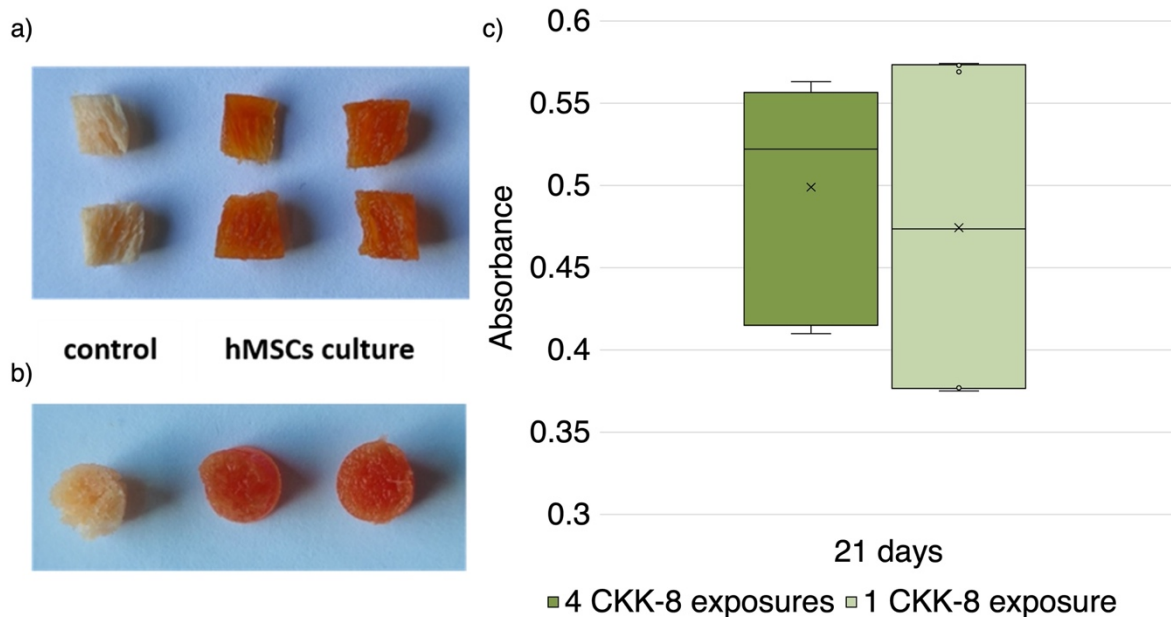


Fig. 76 CKK-8 staining in 3D culture: (a) section and (b) upper-view of CKK-8 macroscopic staining of scaffolds, control (cell-less scaffold), hMSC culture (scaffold with cells after 14 days of culture); (c) box-plot of absorbance measurements at 21 days of culture. Distribution of absorbance measurements for scaffolds exposed to 4 CKK-8 treatments (\bar{x} = average = 0.499 ± 0.062) and scaffolds exposed to 1 CKK-8 treatment (\bar{x} = average = 0.474 ± 0.098), $p = 0.64$ [273].

Absorbance measurements obtained from CKK-8 at days 3, 7, 14, and 21 showed a progressive increase over time. In more detail, the mean absorbance values were 0.247 ± 0.015 (median value = 0.244), 0.338 ± 0.045 (median value = 0.341), 0.366 ± 0.044 (median value = 0.368) and 0.474 ± 0.075 (median value = 0.466) at 3, 7, 14 and 21 days of culture, respectively (Fig. 77).

We performed a linear regression analysis of the absorbance measurements of the cultures over time to obtain the estimated daily growth rate in the first 21 days. The results suggested that the absorbance value increases by approximately 0.013 for every day in the scaffold ($p < 0.001$).

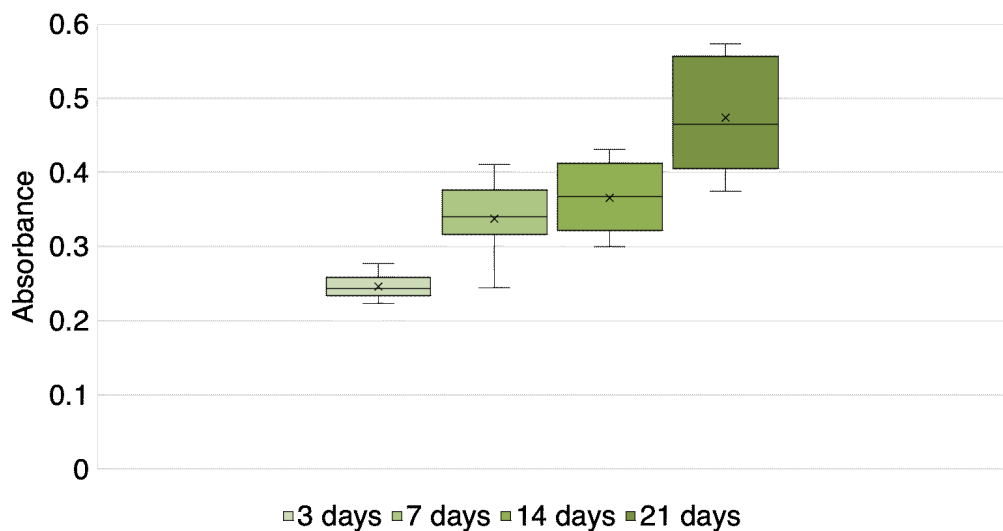


Fig. 77 Box-plot of 3D culture proliferation detected with CKK-8 assay along the 21-day-long culture. X indicates samples average at each day [273].

e) Association Between Impedance Measurements and Biochemical Analysis

Results obtained from the regression analysis confirmed a valid relationship between the electrical impedance outcomes and the corresponding absorbance values of the proliferation assay. On the other hand, no significant relationship could be observed between the magnitude CI increase and the absorbance due to cell proliferation ($p = 0.125$). This result is expected since the estimation of the CI may be affected by additional variables related to cell adhesion and not directly linked to cell proliferation. Indeed, it is pointed out in [287] that CI is not directly related to the total cell number in the culture—like the absorbance value recorded from the enzymatic assay—but to newly attached cells, as they contribute to the overall magnitude because of the insulating composition of their membrane. In comparison, the results obtained by evaluating the relationship between phase angle measurements and the absorbance measurement indicated a significant negative association. More specifically, an increase of 0.01 in the cell proliferation resulted in a negative change of phase angle of -0.3 degrees ($p = 0.019$). The corresponding Pearson's correlation coefficient was -0.981 ($p = 0.019$). These results can be supported by considering that phase angle decrease is positively associated with capacitance and negatively associated with resistance, and for these reasons, it is often taken as a key indicator for cell proliferation [291]. Thus, the higher phase angle suggests an increased

quantity of intact cell membranes and an increase of the contribution of the cells to the overall impedance of the scaffold-cell system [292].

Considering the parameters modeling the contribution of the cells within the culture system, the results of the regression analysis indicated a significant association between both capacitance and resistance values with the extinction outcomes obtained with the enzymatic proliferation assay. More specifically, regarding the capacitance an increase of 0.01 in the cell proliferation resulted in a positive change of 6.5 nF ($p = 0.044$). The corresponding Pearson's correlation coefficient was 0.956 ($p = 0.044$). Regarding the resistance, an increase of 0.01 in the cell proliferation resulted in a positive change of 51.6 Ω ($p = 0.038$). The corresponding Pearson's correlation coefficient was 0.962 ($p = 0.038$). This relationship is well supported from related literature investigating 3D hMSC impedance-based monitoring with a very similar setup [290]. Thus, the capacitance and resistance extracted from equivalent circuit models appears to be closely related to the number/volume of live cells during proliferation, thus explaining the association with the extinction values obtained from the enzymatic proliferation assay.

f) Immunostaining and Microscopy

In addition to the data obtained from CKK-8 colorimetric assay, the results achieved from the fluorescence microscopy analysis performed on scaffolds thin sections (at 3, 7, 14 and 21 day of culture) also confirmed the findings highlighted from the impedance measurements. In more detail, the images reported in Fig. 78 show the presence of intact cell nuclei stained with DAPI; the number of identified nuclei specifically increased with increasing days of culture. These findings prove that scaffolds support hMSC growth over time. The microscopic data also confirms homogeneous cell distribution within the scaffold, as already highlighted by the sections macroscopic stained with CKK-8 (Fig. 76a, b).

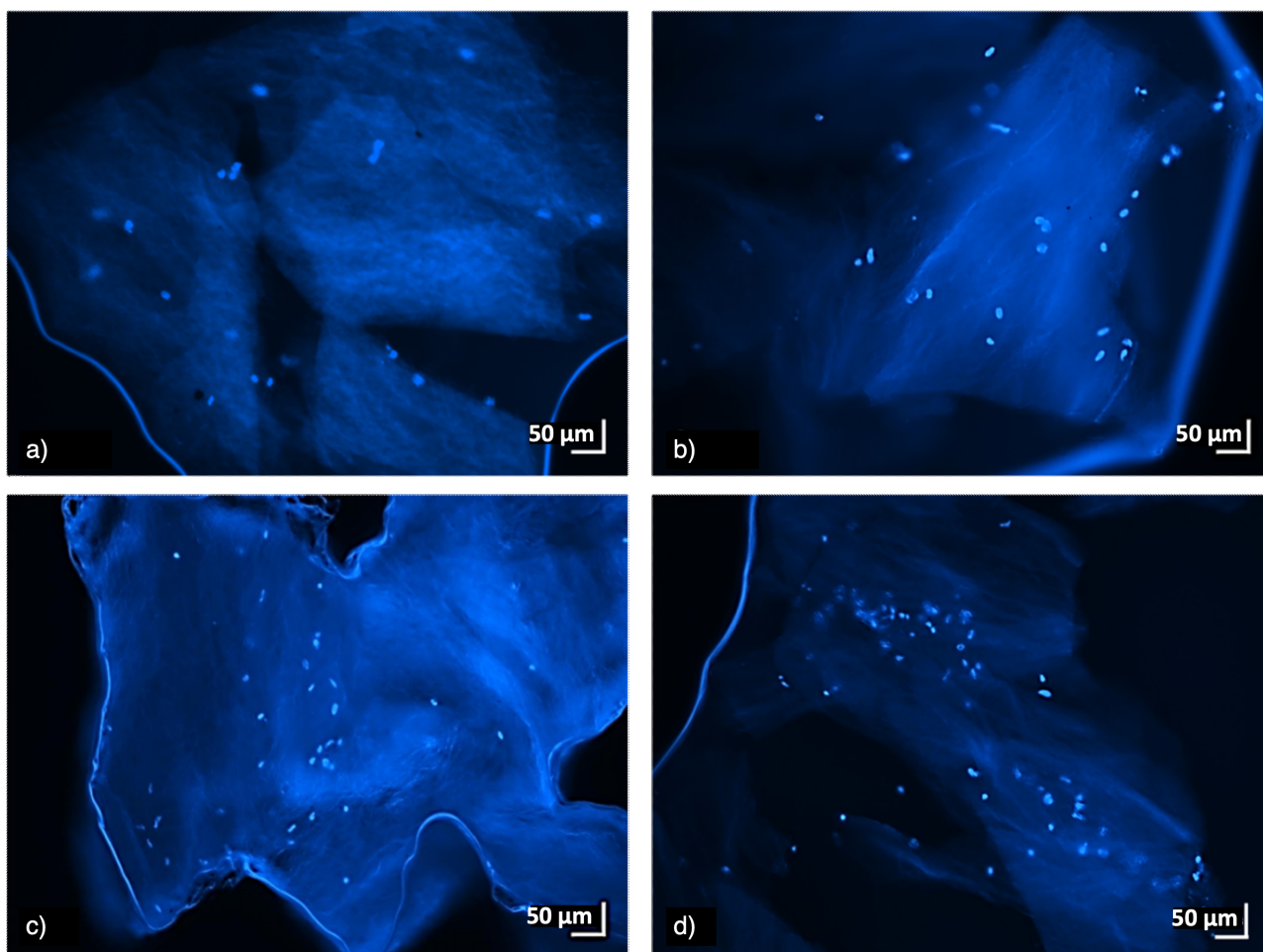


Fig. 78 Fluorescent images of hMSCs on hybrid gelatin-chitosan hydrogel scaffolds at several days of culture. Thinly sliced portions of the central part of the scaffolds. Nuclei staining with DAPI (blue), 10 × magnification. (a.) 3 days of culture, (b.) 7 days of culture, (c.) 14 days of culture and (d.) 21 days of culture [273].

7.2.4 Discussion

Overall, results obtained in terms of impedances appeared well supported by enzymatic assay outputs and by microscopy. Enzymatic tests, in fact, showed a continuous increase in average absorbance over the 21 days of culture, indicating that gelatin-chitosan hybrid hydrogel scaffolds well support hMSC cultures. Macroscopic staining and microscopic preparations of scaffolds confirmed a homogeneous distribution of cells within the volume of the scaffold starting from the first days of culture. Furthermore, the results of the regression analysis indicated a significant relationship between the extinction values of the enzymatic proliferation assay and respectively the phase angle ($p = 0.019$), C_{cells} ($p = 0.044$) and R_{cells} ($p = 0.038$). These findings support the possibility of associating the variation of those impedance-related parameters with the contribution of cells adhering onto the scaffold pores, thus affecting the overall impedance of the systems composed by seeded scaffold/medium/sensors. The results highlight the presented work as an interesting starting point for future investigation. As in any pilot study, there are—however—several limitations

to be pointed out. Concerning the impedance-based measurements, a wide range of variability could be observed among the different independent systems evaluated (sensors/scaffold/culture medium). Most of them are due to the variability in samples geometry and the non-intrinsic conductivity of the adopted scaffold. Thus, the starting impedance of the non-seeded sensor-scaffold systems around 7 k Ω could represent a limiting factor for the overall sensitivity of the method. Only from a measuring perspective, the reproducibility and sensitivity could be improved through an enhanced standardization of the scaffold characteristics (e.g., porosity and dimensions) and of the conductivity of the overall system. On the other hand, results obtained from these scaffolds, non-conductive but already validated for regenerative medicine purposes in terms of cytocompatibility and porosity [285], [293], are really promising and may lead to the direct adoption of this monitoring strategy for the optimization of 3D seeded scaffold ready for in vivo implantation.

Concerning the enzymatic reference method adopted, limitations are mainly related to the intrinsic additional complexities introduced while translating the reference methods from the 2D to the 3D environment, as highlighted in [294], [295]. The commercial enzyme test used in this study was chosen for its low toxicity and ease of use, but obviously, it is not able to describe cell cultures in their complexity and in their interaction with the scaffold.

Considering the results and limitations, future developments will deal primarily with increasing the sensitivity and reducing the variability of the method presented. From a setup perspective, alternative designs and materials will be investigated to lower the overall impedance, to go beyond the monitoring of cell viability and proliferation, exploiting the potential of the presented method for also monitoring other events (e.g., differentiation or adhesion) which induce smaller signal variations. Gold standard methodologies, both invasive (e.g., DNA extraction, SEM analysis) or non-invasive (i.e., optical), will be adopted to confirm the possibility of associating those variations with cell morphological or phenotypical changes. From the signal processing perspective, additional strategies of denoising and feature extraction will be implemented to strengthen data analysis.

7.2.5 Conclusion

In conclusion, a non-invasive disposable modular system for monitoring cell proliferation in 3D scaffold-based cell cultures by means of impedance-based measurements was presented. Flexible sensors were realized using AJP technology, depositing carbon-based

ink on polyimide substrates specifically designed to fit into 96-well plates. After that, they were folded, sterilized and inserted in each well, together with the scaffold, to be monitored. Preliminary experiments confirmed the possibility to use this approach to monitor the proliferation of hMSCs seeded at different initial concentrations, highlighting the saturation of the growth curve, in agreement with optical and pH acidification of culture medium. Considering all this information and the maximum sensitivity achieved (200 Ω /day), 200,000 cells/scaffold was selected as the most suitable concentration for evaluating the repeatability of the methodology and to validate the output of the impedance-based assay with an enzymatic proliferation assay. Using this concentration, results obtained comparing impedances at 4 kHz throughout 21 days of culture showed a steady increase in the magnitude (total increase of 2.5 k Ω at day 21) and a decrease of the phase angle (total shift of -9 degrees at 21 days). The use of an equivalent circuit to model the scaffold-based culture allowed to highlight the specific contribution of cells in terms of capacitance and resistance at each time point to be extracted, highlighting an exponential increase of the resistance and capacitance during the 21 days of culture (with maximum values of 1.5 k Ω and 200 nF). Overall, the statistical association between outputs from the impedance-based method with the standard enzymatic assays supports the potential of the non-invasive approach proposed to perform a continuous monitoring of scaffold-based 3D cell cultures. Additionally, the intrinsic modularity and ease of customization of the approach proposed suggest the possibility to translate it in more complex 3D perfusion-based bioreactors. This would represent a promising scenario for obtaining useful feedback from environments mimicking physiological conditions, with interesting possible applications for regenerative medicine purposes, also from the perspective of optimizing the scaffold-culture system.

8. Lab-on-chip Objects

8.1 Protein detection

Part of the work reported in this section was presented in *2018 IEEE Sensors Applications Symposium, SAS 2018* and is part of the conference proceedings with the title *Design and implementation of a microsensor platform for protein detection realized via 3-D printing* [296]. Part of the research work reported in this section was published in the MDPI Journal *Sensors* with the title *Aerosol Jet Printed 3D Electrochemical Sensors for Protein Detection* [71]. Part of the work reported in this section is part of the book *Lecture Notes in Electrical Engineering* published in 2019 and presented during *Convegno Nazionale Sensori* with the title *Aerosol jet printed sensors for protein detection: A preliminary study* [297]. Results and pictures are reported with permission of the editor.

8.1.1 Introduction

Recently, printed electronics have been increasingly investigated as convenient and promising for providing reliable feedbacks on biological samples or physiological processes, in applications ranging from diagnostics, pharmaceuticals to tissue engineering. Moreover, the recent attention for disposable, low-cost and reliable biomolecule-to-chip interface systems for high-throughput in-vitro assays is becoming an urgent need due to novel international regulatory guidelines [298].

Regarding the area of biotechnological applications, the most used and accepted design is the one commercially available produced by companies such as Ddropsens or Metrohm, which provide a very wide variety of different materials or designs, easily manageable and applicable to different areas of biotechnological research [299]. IJP and screen-printing are the most adopted techniques for these applications, providing proper geometrical properties electrochemical sensors for a wide range of biotechnological applications such as chemicals detection, DNA or protein recognition [2,3]. Despite the cost and time effectiveness of both these techniques, they present some issues in term of reproducibility, resolution, and difficulty to realize 3D structures useful for a proper management of liquid samples. Several articles have been dedicated to evaluate and compare the performances of different material and sensors producers and electrochemical techniques [299]. Focusing on the current trends of electrochemical sensors applied in medicine, biotechnology, and pharmacology where high levels of standardization, repeatability, sensitivity, and miniaturization are

demanded [302], the potential of AJP in term of reproducibility, resolution and 3D customization represents a valuable source [11,25].

In this picture, AJP is here investigated as promising tool for improving the requirements of electrochemical sensors, in term of both repeatability and limit of detection (LOD), thanks to an optimization of the biofunctionalization process of the working electrode (WE), achieved ensuring a proper liquid confinement by a customized 3D environment, which avoids possible leakages while managing liquid samples. Microscopy glass slides with a sample holding concavity were chosen as substrates, in order to realize a device easily integrable with the laboratory routine. The ability of AJP to print also on these curve non-porous substrates makes possible from one side to combine electrical measurements with optical or biochemical assays and from the other side makes simpler to manage liquid samples in the concavity. Liquid confinement has been also ensured depositing a photopolymer to realize a 3D structure similar to a real well. The validation of the customized measuring device with electrochemical sensors is presented using Interleukin-8 (IL-8) chosen as reference protein, due to its multiple applications in diagnostics and biotechnological research. The high number of replicates performed for each concentration, allowed to perform critical considerations from the metrological point of view, comparing AJP results with the ones obtained from screen-printed electrodes (SPEs).

8.1.2 Materials and Methods

a) Sensors Design and Material Choice

After evaluating available designs on the market and in the literature [304], a 3-electrodes system (working (WE), counter (CE) and reference (RE) electrodes), usually employed for electrochemical measurements, was selected as layout (Fig. 79).

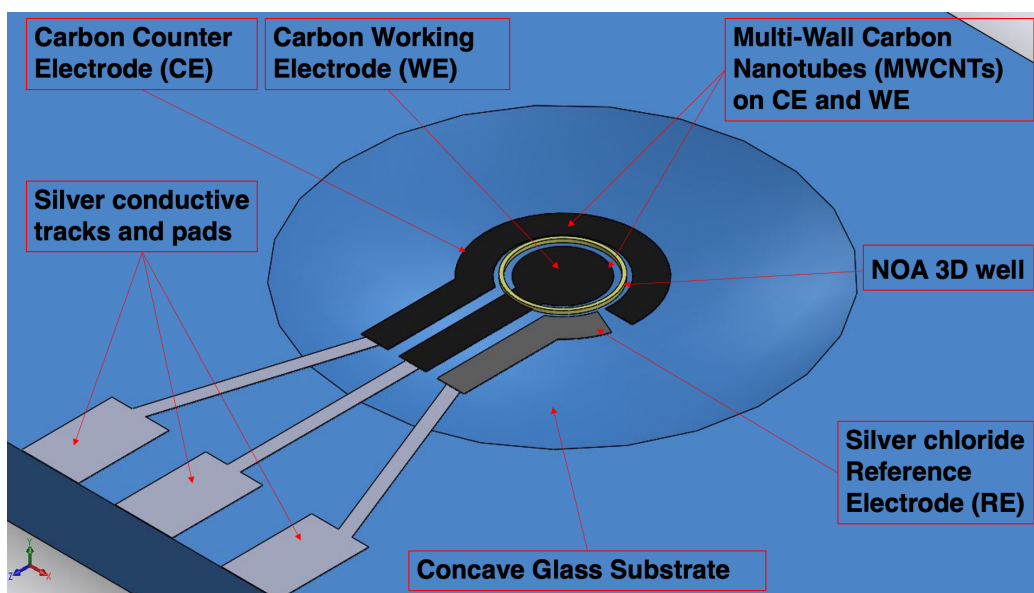


Fig. 79 Schematic representation of the final prototype [71].

In order to realize proper sensing devices suitable for microscopy and for easy managing during biological sample modifications, concave glass slides were selected as substrates. In addition to a proper rigidity, glass provides an optimal transparency and suitable dimensions standardized for most of the instrumentation used for biochemical and optical assays. Fig. 79 shows an example of all the layers corresponding to the different employed inks: (i) silver for the conductive tracks, (ii) carbon for WE and CE, (iii) silver chloride for RE and (iv) NOA 81 for creating a sort of delimiting hedge for liquid samples. Further, an electronic performances improvement and an increase of the surface to volume ratio for biofunctionalization have been achieved by printing an additional layer of MWCNTs (multiwall carbon nanotubes) over carbon electrodes. Silver ink is produced by UTDots Inc. (Champaign, IL, United States of America), with its own thinner, UTDAg ink is based on silver nanoparticles with an average size around 10 nm and dispersed in a liquid vehicle. Nanosilver concentration is about 25–60 wt.%, with a viscosity of 1–30 cP. Since they are surface stabilized, UTDAg inks are highly soluble in nonpolar organic solvents and stable under atmospheric conditions at room temperature. Silver chloride ink (XA-3773) was purchased from Fujikura Kasei. Co. Ltd. (Shibakouen Minato-ku, Tokyo, Japan) together with its own thinner. The ink was chosen with Ag/AgCl weight proportion ratio of 8/2. Since the ink starting viscosity was 300 ± 50 dPas, it was necessary to dilute the ink with its thinner before printing, following the equations present in the literature regarding a two-component blend [164]. Carbon ink (EXP 2652-28) characterized by a starting viscosity of 15–20 Pas was purchased from Creative Materials Inc. (Ayer, MA, United States of America). The layer of MWCNTs was obtained printing Nink 1000, commercialized by NANOLAB (Waltham, MA,

United States of America). It is a carbon nanotube ink for direct printing techniques containing carboxyl (-COOH) functionalized carbon nanotubes in an aqueous suspension (the viscosity is proximal to the one of water) with the minimum concentration of additives to impart long-term stability and printability to the ink. Finally, the UV-curable polymer NOA 81 exploits the ability of the AJ printer to realize a 3D structure able to confine the liquid sample only on WE, as needed during specific steps of sensors functionalization. NOA 81 was purchased from Norland Products (Cranbury, NJ, United States of America). It is a fast UV-curing adhesive, which produces, after curing, a hard, resilient bond. The material is characterized by a viscosity of 300 cP at 25 °C, showing an excellent adhesion on glass and metal, and a fair adhesion on plastics. The different process parameters are summarized in Table 12. Each ink was printed with two consecutive depositions, followed by its own specific heat treatment, using a 200 μm nozzle tip. Pneumatic atomization was selected. The final line width was about 60 μm .

Table 12 Printing process parameters.

Process Parameters	Ag	AgCl	C	NOA 81	Nink 1000
Sheath gas flow (SCCM)	20	30	110	80	65
Exhaust flow (SCCM)	570	570	1000	1400	800
Atomizer flow (SCCM)	550	530	900	1360	750
Process speed (mm s ⁻¹)	2	2	2	0.75	3.5
Plate temperature (°C)	60	65	70	/	45

b) Sensor Fabrication

The aerosol jet printer AJ300 was used in order to fabricate all the electrochemical sensors. Each conductive layer has been printed and cured following the sequence and the curing parameters reported in Fig. 80. In the last step, a hollow cylinder of around 30 μm height was obtained by depositing a 3D spiral composed by 5 circles, to achieve a structure able to contain samples up to 20 μL but not limiting the possibility to perform the measurements using the three electrodes structure. In order to control precisely the height of the 3D customized walls, NOA 81 has been UV-cured right after deposition using as UV curing system the LED Spot type Panasonic ANUJ6180 series, model 6423 (Panasonic, Kadoma, Osaka, Japan) characterized by a spot diameter of 3 mm, a peak UV intensity of 17,200

$mWcm^{-2}$ at an irradiation distance of 8 mm. In our experimentation, the select power was 5% of the peak intensity.

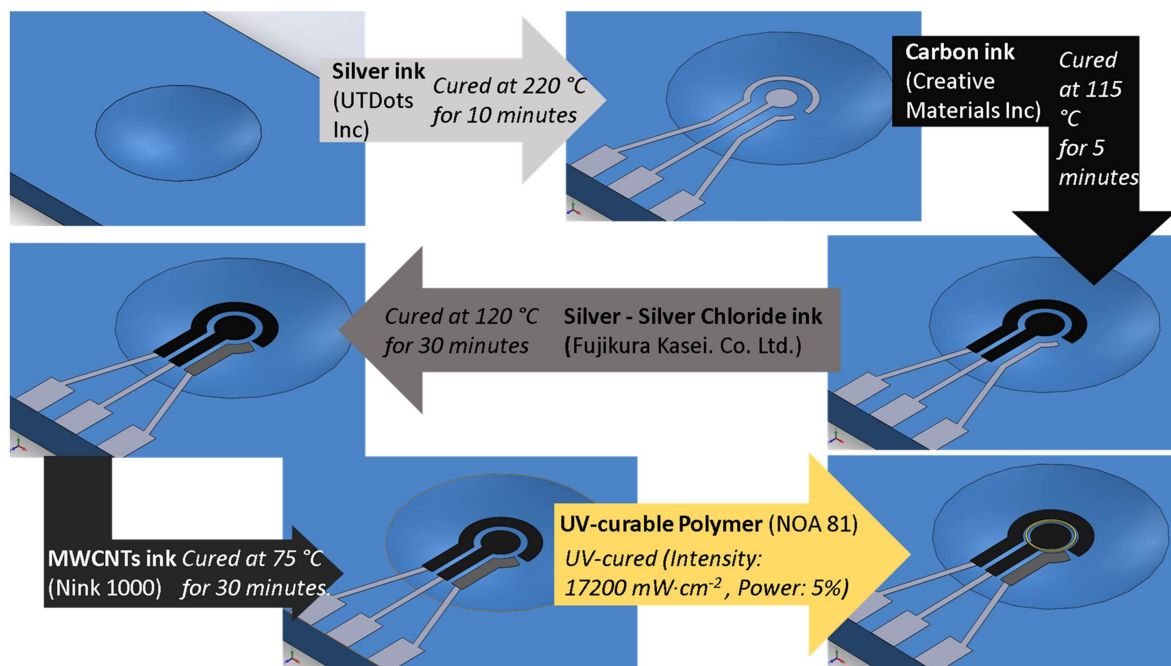


Fig. 80 AJP process for sensor fabrication [71].

These sensors were fabricated in different sizes, in order to evaluate the correlation between the miniaturization of electrochemical sensors and their performances in term of repeatability, sensitivity, and LOD. The initial comparison among the different geometries has been performed fabricating 10 sensors for each geometry. The selected geometry has been then replicated fabricating other 10 sensors with the same geometry. In Fig. 81a, a drop of a buffer solution has been deposited on the WE electrode highlighting the ability of the NOA ring to efficiently contain liquid sample during functionalization, avoiding any leakage often experienced with SPEs (Fig. 81b).

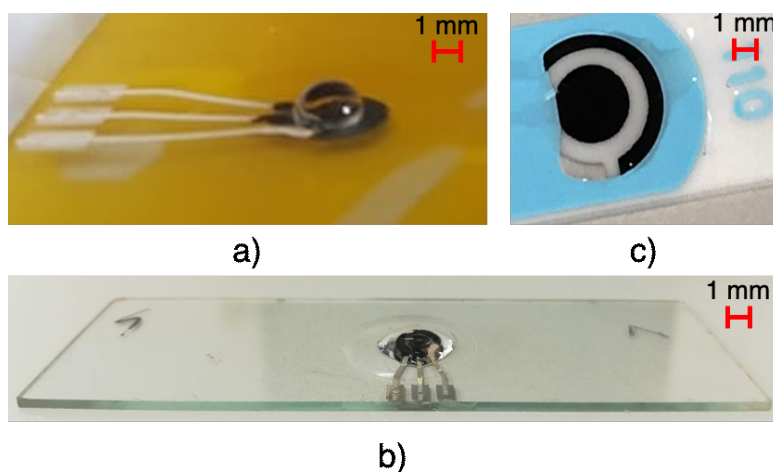


Fig. 81 (a) Final layout of the printed sensorized glass slide with sample confinement during WE functionalization; (b) Example of the sample confinement over the three electrodes during measurement; (c) Example of liquid leakage on a commercial screen-printed sensor [71].

c) Geometrical Analysis and Electrical Resistances

To assess the suitability of substrate-ink combination to test liquid biological samples, different aspects of the sensors were investigated. After analyzing geometrical and electrical parameters of the printed tracks, the effective coating of a layer of antibodies on the surface of AJP sensors was assessed using fluorescence imaging.

Regarding geometrical analysis, a diamond stylus-based system for step height measurements, (Alpha-Step IQ Kla Tencor profilometer, Kla-Tencor, Milpitas, CA, United States of America), has been used to measure printed layers thickness, with a range 8 nm–2 mm and an uncertainty of 0.1%.

Electrical resistance was then evaluated using a Hewlett-Packard 34401a digital bench-top multimeter (HP, Palo Alto, CA, United States of America), applying testing probes to the extremities of each path, in standardized and repeatable points, thus measuring the resistance offered by all its length. Each measure has been repeated ten times, in order to ensure the proper calculation of the mean values and of the standard deviations.

Resistivity was then calculated from the classical equation $R = \rho S^{-1}$ where R is resistance, ρ is resistivity, l is the length of the considered path and S its section.

After evaluating geometrical and electrical features, the possibility to functionalize WE with an effective protein coating has been assessed using fluorescence imaging with a near infrared imaging system. More specifically, the binding between carbon WE and the primary antibody anti-human IL-8 (8 $\mu\text{g/mL}$), produced in mouse (Duo Set kit), was evaluated recording the emitted light deriving from a secondary antibody specie-specific (anti-mouse), labelled with a fluorescent tag and its signal was acquired with Odyssey[®] Fc Dual-Mode Imaging System from LI-COR Biosciences (Lincoln, NE, United States of America). Thus, sensors were washed and excited with a 685 nm light source to study coating deposition, keeping two electrodes as control blank samples (i.e., covered with a buffer solution of phosphate buffered saline).

d) Voltammetry-Based Protein Quantification

The protocol adopted for testing sensors' ability to quantify proteins involved IL-8 as reference protein for the assay. IL-8 quantification was characterized by a specific functionalization of the sensor using immunocomplexes formed by a capture and a detection

antibody (DuoSet ELISA kit, Human CXCL8/IL-8, R&D System, Minneapolis, MN, USA), and by an Anodic Stripping Voltammetry (ASV) based measurement technique, optimized in [32,33].

In detail, each WE was exposed to the following bio-functionalization steps (Fig. 82): (i) overnight immobilization of anti-IL-8 antibody to sensor surfaces via drop-casting; (ii) 2-h incubation with recombinant human IL-8, at different concentrations; (iii) 2 h incubation with biotin-labelled detection antibody; (iv) addition of streptavidin-tagged alkaline phosphatase (AP) enzyme that catalyzes the oxidation of ionic Ag (AgNO_3) to metallic Ag, thanks to the reaction happening in presence of ascorbic acid (AA-p), as described in [305]. Once completing the bio-functionalization, sensors were covered with PBS in order to perform the final measurement. A constant potential of -0.12 V was applied for 10 s and then a Linear Sweep Voltammetry (LSV) was performed at a scan rate of 40 mV/s up to +0.4 V, measuring Ag oxidation current. Since the measurement technique allows only one repetition for each sensor, the reproducibility has been tested by testing the same protocol for each selected concentration on ten different sensors for each geometry. All measurements were performed using a potentiostat (Palmsens, Compact Electrochemical Interfaces, Houten, Utrecht, The Netherlands) controlled using a dedicated software (PS Trace 5.3), used to quantify the current peaks corresponding to each concentration and to derive the calibration curve. The LOD has been then calculated using the 3-sigma rule [35,36].

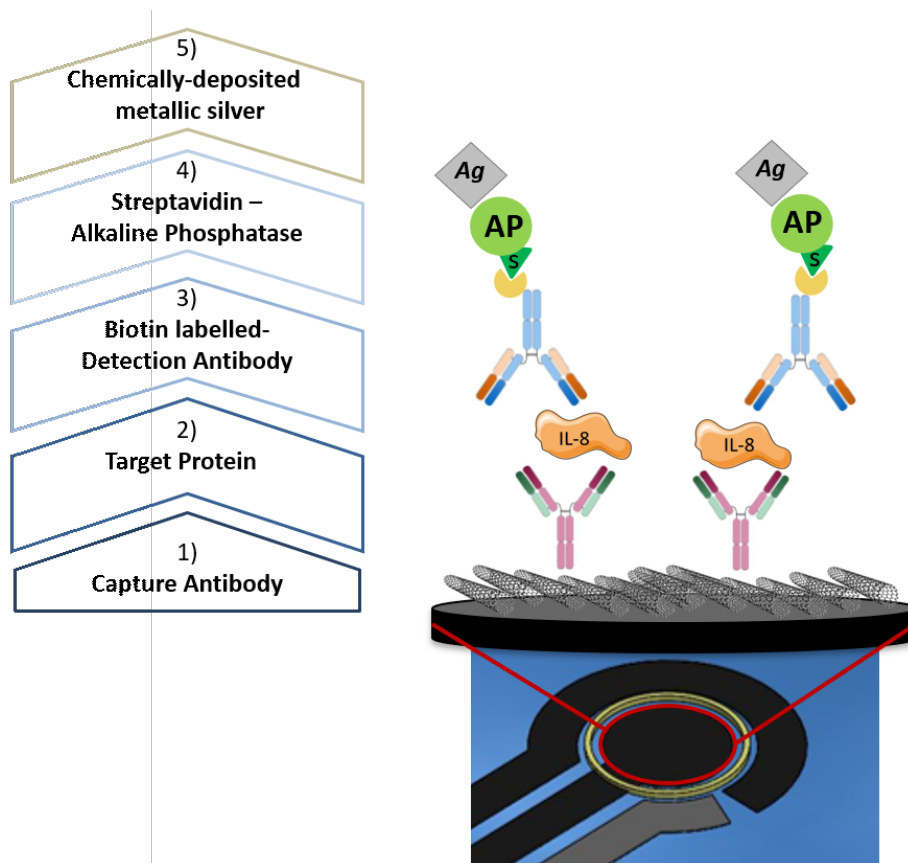


Fig. 82 Bio-functionalization protocol for the ASV measurements of IL-8 [71].

8.1.3 Results and Discussion

a) Sensors Testing

Results obtained from the geometrical analysis (Table 13) shows a different thickness for each layer. The different values can be addressed to the different process parameters, number of printed layers and viscosity (higher thicknesses were obtained for inks with higher viscosity) adopted for each ink. The standard deviation is always less than 20% demonstrating an acceptable process variability in the thicknesses for all the printed sensors.

Table 13 Thickness and sections of deposited inks.

Material	Thickness (μm)	Standard Deviation (μm)	Section (μm^2)
Ag	6.8	± 1	854.2
AgCl	4	± 0.8	392.3
C + MWCNTs	6.5	± 0.2	365.3
NOA 81	25	± 3	1400

Results from electrical tests show resistance and resistivity data in agreement with the nominal values of the manufacturers, considering the specific process parameters for each ink. Ag experimental resistivity ($12.2 \times 10^{-8} \Omega\text{m}$) is comparable with the nominal one ($3 \times 10^{-8} \Omega\text{m}$). The use of the thinner in order to achieve the proper final viscosity may have affected AgCl experimental resistivity value ($71.3 \times 10^{-8} \Omega\text{m}$), but it can be compared with the nominal one reported by Fujikura Kasei. Co. Ltd. ($56 \times 10^{-8} \Omega\text{m}$). Finally, C experimental resistivity ($10.3 \times 10^{-4} \Omega\text{m}$) was slightly decreased compared to the one given by Creative Materials ($25 \times 10^{-4} \Omega\text{m}$), due to the choice performed during the heat treatment in term of duration and temperature.

Results obtained from fluorescence imaging shows a clear difference between blank and antibodies coated electrodes (Fig. 83). The red arrows indicate the surfaces successfully covered by immunocomplexes, which appear as the only ones emitting in the near infra-red region. Differently, the blank sample, treated with the same protocol, but incubated with PBS instead of IL-8 recombinant protein, do not emit any light, confirming the specificity of the binding between protein and immunocomplexes.

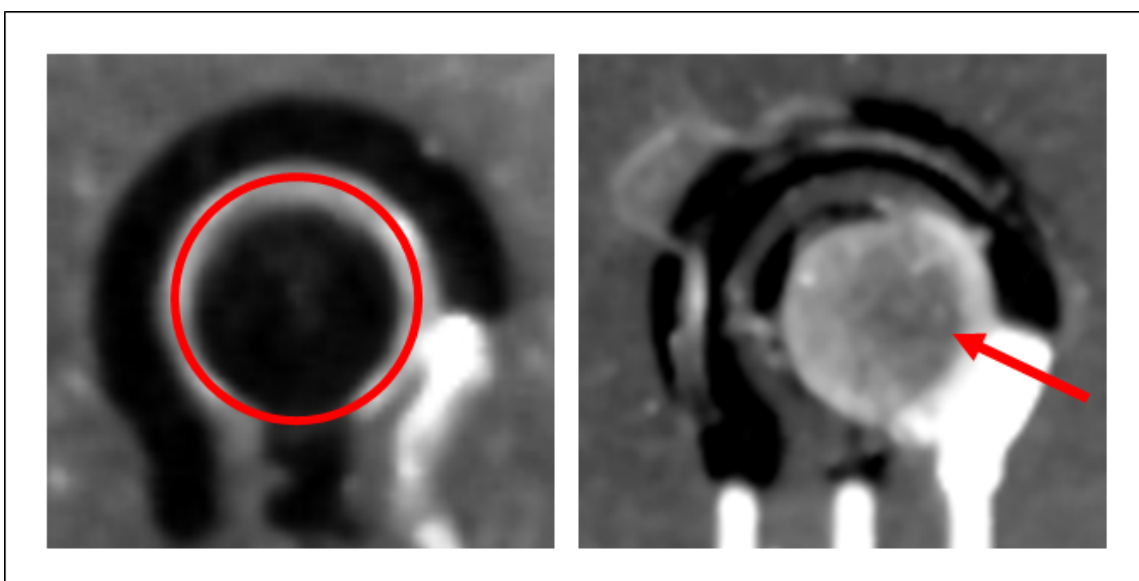


Fig. 83 Fluorescence imaging, with grayscale color filter, of a bare carbon working electrode without antibodies (left) and with antibodies attached (right) [71].

Thanks to these confirmations, it is possible to state that these materials and AJP technique can be employed to produce electrodes allowing a homogeneous adhesion of antibodies, essential to perform a complete functionalization to perform immune-sensing of proteins.

b) Voltammetry-Based Protein Quantification

IL-8 was selected as the protein to be tested to evaluate the possibility of using the sensor designed for voltammetric based protein quantification. This member of the CXC chemokine subfamily is considered as universal biomarkers—from cancer and inflammation to neurodegeneration [131]—thus making the present PoC platform available for various applications in the clinical field. Furthermore, IL-8 strong interaction with its capture antibody allows reducing the variability to the functionalization phase. Results in Fig. 84 report the comparison performed among the three different geometries in quantifying 10 ng/mL of IL-8 sample using ASV.

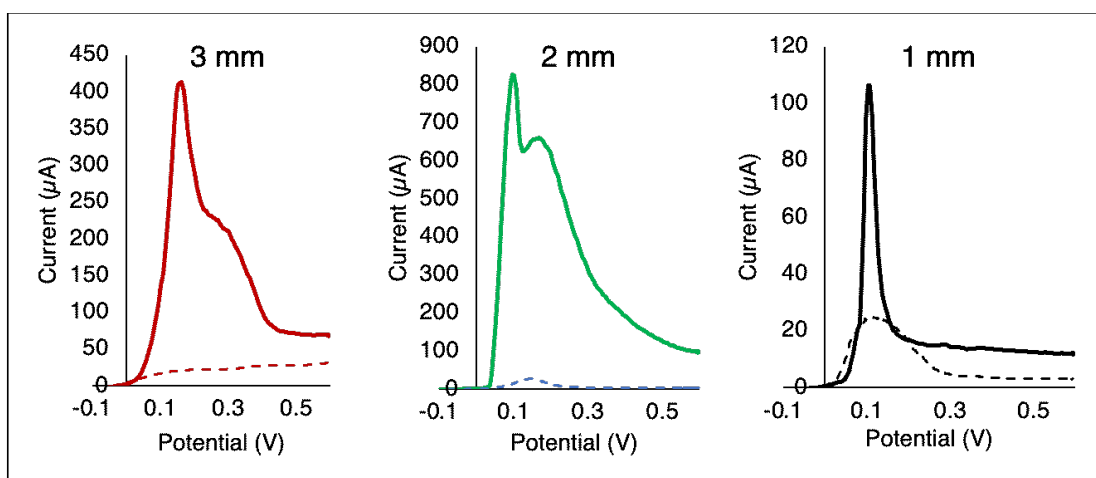


Fig. 84 Plots obtained during protein quantification test; each plot measures current (expressed in μA) as a function of potential (expressed in V). Dotted lines represent “blank samples” [71].

All the peaks obtained in the ASV has been quantified and summarized in Table 14, both in term of current and of current density, normalized for the WE area, averaged among ten replicates. For all the evaluated geometries, a clear difference in peaks heights could be appreciated between blank and samples (Fig. 84), confirming the possibility to successfully apply the described ASV protocol for protein quantification on all the AJP sensors.

Table 14 Current peaks heights for 10 ng/mL protein quantification on the glass-substrate sensor.

WE Diameter	Current Peaks (μA)	Standard Deviation (μA)	Current Density ($\mu\text{A}/\text{mm}^2$)
3 mm	280.8	118.8	39.7
2 mm	632.0	142.0	201.3
1 mm	82.0	27.9	104.5

To better discuss these results, it is fundamental to take into account both electrical and biological point of view. 3 mm sensors, with a geometry similar to the commercial SPEs produced by Dropsens, despite presenting a quite high absolute current peak of 281 μA , does not appear as the most performing one in term of current density ($39.7 \mu\text{A}/\text{mm}^2$) (Table 14). 1 mm sensors, instead, despite a clearly reduced height of the absolute current peak due to the limited area for electrodes exchange, present a higher current density of about $104.5 \mu\text{A}/\text{mm}^2$ compared with 3 mm sensors, and showed really sharp peaks with a very low background noise.

Interestingly, the results obtained for the 2 mm WE appeared as the most performing one, especially in term of current density, $201.3 \mu\text{A}/\text{mm}^2$. This result can be explained with the closeness between WE and CE obtained shrinking electrochemical cell dimensions, which appear to be significative to enhance the current peak height and reduce the current loss and the background noise. These features, combined with the compatibility of the dimensions with a manual functionalization, make this geometry the most suitable to reduce sample volume, without sacrificing performances and sensitivity. These results allowed selecting the 2 mm geometry as the most suitable ones for a complete test analysis selected in a range of concentration from 1.25 to 10 ng/mL of IL-8 solution.

Fig. 85 and Table 15 summarize the results obtained performing the analysis with the ASV protocol on two types of printed sensors, on bare C electrodes and on MWCNTs functionalized WE. Considering the curves in both the plots in Fig. 85, referring to AJP sensors, clear oxidative peaks could be observed around a potential of 0.1 V, corresponding to the Ag stripping from WE. A slight potential shift (around 10 mV) could be observed in the MWCNTs WE compared to the bare C ones, suggesting an improved electron transfer due to the nanostructures, making easier the oxidation of the Ag. Furthermore, comparing the curves of bare C with MWCNTs in Fig. 85 and LOD of Table 15, it can be highlighted how the nanostructures decrease the LOD of 7 folds, in agreement with what could be observed in previous works performed with SPEs [308].

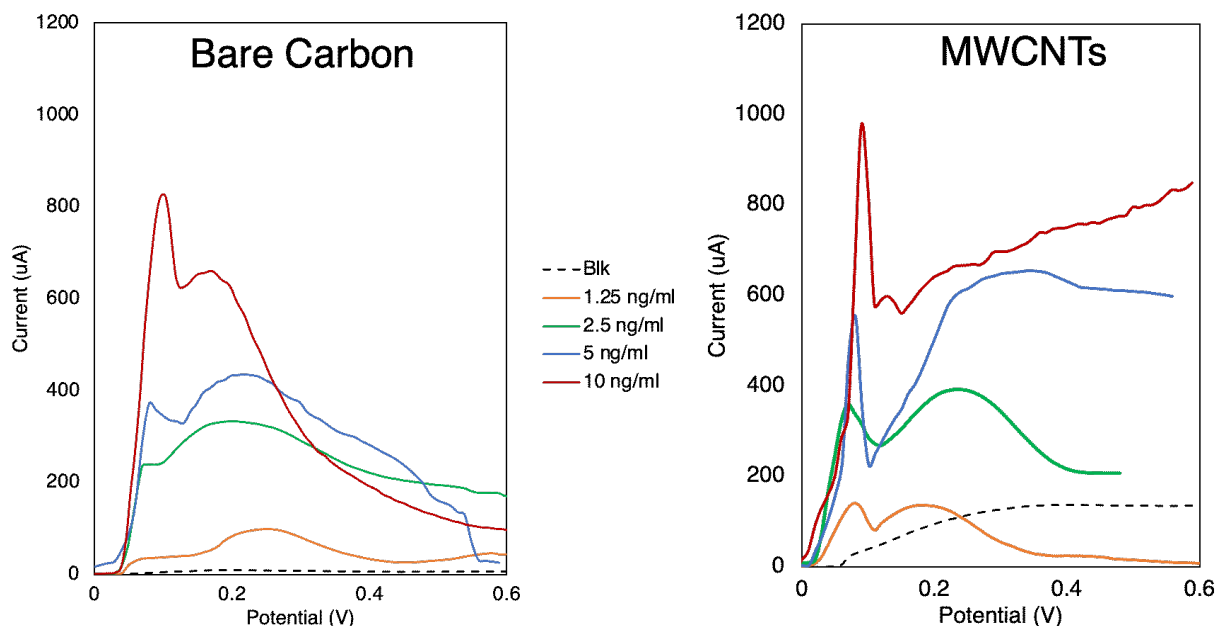


Fig. 85 LSV for IL8 quantification performed using bare and nanostructured carbon-based sensors [71].

Additionally, the performance of AJPEs (Fig. 85) has been compared to the one of commercially available C SPEs, both bare and nanostructured, performing ASV with the same protocol (Table 15).

Table 15 LOD obtained from the different conditions, considering different WE materials and printing methods.

	SPEs	AJPEs
Bare C	3.4 ± 0.5 ng/mL	2.1 ± 0.2 ng/mL
MWCNTs	0.5 ± 0.4 ng/mL	0.3 ± 0.2 ng/mL

All the results were obtained from ten replicates for each concentration, in order to perform a critical evaluation of the variability. Due to the different dimensions of the WE, results were compared in term of current density peaks and in term of relative standard deviation (RSD), as the ratio between the standard deviation of ten repetitions and the average value of the current density of each peak. An improvement in term of measurements repeatability, which in turn resulted in a reduced LOD, can be highlighted both from the results in Table 15 than discussing the plots of Fig. 86. Interestingly, the high geometrical resolution and the possibility to control precisely the parameters using AJP appeared to decrease the LOD from 3.4 to 2.1 ng/mL, even when using the same material than in the SP (carbon), with a reduction of the RSD of almost 2 times. The higher control on deposition of the nanostructures appears to have a strong influence as well, considering the decrease of the LOD of almost 2 folds, confirmed by the high reduction of the RSD obtained (from 60% to

15%) comparing drop-casted MWCNTs with AJP ones. Additionally, a significant role that needs to be considered and that might have an influence in reducing variability can be addressed to the presence of the 3D well in the AJPEs, and not in the SPEs, which ensured a proper coating, avoiding unspecific protein deposition on CE or RE.

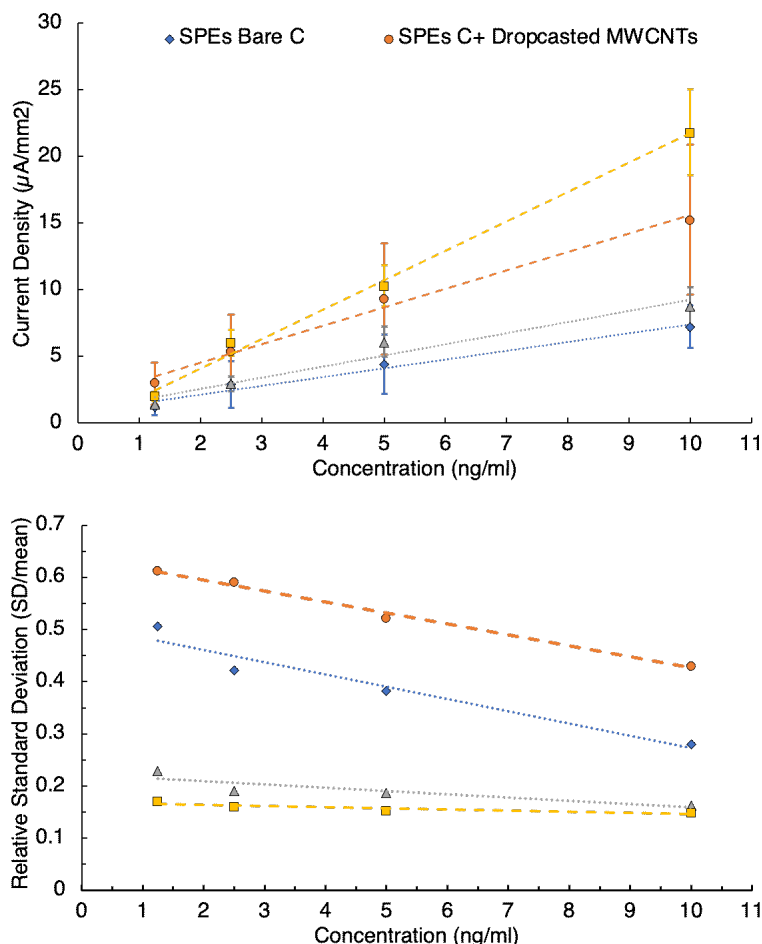


Fig. 86 Calibration plot comparison between Carbon bare and nanostructured sensors [71].

8.1.4 Conclusion

Miniaturized electrochemical platforms for protein detection were developed through AJP. Electrodes and conductive tracks with a resolution of about $\pm 6 \mu\text{m}$ and controllable thickness with a standard deviation always less than 20% could be realized using this technique, showing proper values of electrical resistivity coherent with what declared by the manufacturers. Furthermore, antibodies have shown good adhesion to the sensors. Beside confirming the significant improvement of AJP nanostructures compared to AJP bulk material in term of LOD (from 2.1 to 0.3 ng/mL), the obtained results allowed to improve the repeatability, if compared with commercially available screen-printed electrodes, thanks to the better liquid confinement and the lower operator dependency achieved in the functionalization phase. In detail, the RSD could be reduced from 60 to 15%, comparing drop-casted nanostructures to AJP nanostructures, and from 40% to 20%, comparing SP to

AJP carbon. The improved repeatability will allow in future studies to deepen the investigation of further metrological characteristics (e.g., resolution) and the possibility to directly AJ print biomolecules (e.g., enzymes, antibodies) to realize ready to use electrochemical sensors. In addition, the validation of NOA as UV-curable printable polymer represents an important starting point to address future works integrating not only a polymer well but a proper microfluidic. Overall, the results obtained suggest this technique as a really promising one to combine reliability and repeatability with the wide possibilities offered by these printed devices for several biotechnological applications.

8.2 Glucose sensing and microfluidics

The research work reported in this section was published in the MDPI journal *Sensors* with the title *Support-Material-Free Microfluidics on an Electrochemical Sensors Platform by Aerosol Jet Printing* [72]. Results and pictures are reported with permission of the editor.

8.2.1 Introduction

The sensitive quantification of specific biomolecules and analytes in biological fluids, drinkable water or food has a key role in medical, biotechnological and environmental research [128], [129]. The presence of specific biomolecules or ions above their normal levels in human fluids affects biochemical cycles and causes adverse health effects [132]. Similarly, the possibility to detect contaminants, specific ions or metals in drinkable water, beverages or food, when still in low concentration, might bring a significant improvement in term of food waste and of effects on human wealth [117], [133]. Several highly specific and sensitive analytical techniques have been used to detect target analytes in biological or environmental samples such as Enzyme-Linked Immunosorbent Assay (ELISA) [134], [135], Surface Plasmon Resonance (SPR) [136], Surface Enhanced Raman Scattering (SERS) [137] and high-performance liquid chromatography (HPLC) [138]. The disadvantages are the analysis high costs, the need of expensive equipment and trained personnel [132].

In recent years, the demand for disposable biosensors with high sensitivity, low limit of detection (LOD), repeatability, miniaturization, and cost efficiency received increasing attention for early diagnosis and health monitoring [139]. Electrochemical Biosensors (EB) are good candidates for scalable production of point-of-care (PoC) disposable devices [132], [140], [141]. They are a feasible solution for analyzing the content of a biological fluid sample by directly converting a biological event into an electrical signal [142]. Despite planar three-electrodes electrochemical configuration is the most commonly adopted for EB, it shows some practical problems: (i) the functionalization and sample droplets are commonly deposited by hand using a micropipette. In presence of small electrodes (e.g. lower than 1 mm) and low amount of fluid (few μl), the deposition is difficult and strongly depends on the operator, introducing errors and high variability. (ii) The lack of an effective physical barrier that separate working (WE) and counter (CE) electrodes can cause an improper functionalization of the CE and distort the analysis. (iii) Furthermore, in specific methods of analysis, the sample has to be splitted, transported and collected on functionalized

electrodes. In these cases, the fluid could be not properly splitted or transported or collected and the sensors can overestimate or underestimate the real analyte concentration.

Focusing on the requirements of precise control of fluids, low reagent consumption and parallel multi-analysis, an easy-to-use electrochemical sensors platform with microfluidics was developed. It is the first example of AJ microfluidics printing directly on electronics without any support material by photopolymer jetting and UV-curing, minimizing the structural material amount, and it could also be printed on non-planar surfaces opening to new possibilities of integration with miniaturized electronics. In details, a platform composed by six EB in a hexagonal shape integrated with a customized photopolymer structure was realized, with six microchannels that branch off from a central inlet to each working electrode (WE) chamber. The validation has been performed quantifying glucose using a standard enzyme-mediated procedure, directly printing both mediator and enzyme using AJP. The microfluidic platform allows to improve and control sample deposition on WEs, lowering operator-dependency and ensuring a proper deposition of reduced sample volumes. The miniaturization of the electrochemical sensors ensures to reduce electrochemical noise, voltage drop and to maximize analyte detection [309]. Finally, the direct AJP of mediator and enzyme makes the device standardized and ready for use.

8.2.2 Materials and Methods

a) Platform design and material choice

The schematic representation of the designed microfluidic sensor platform is reported in Fig. 87, each layer and material used in the development of the platform is indicated. Alumina is the selected substrate material due to its mechanical properties, good adhesion because of its porosity and ease of handling. We purchased the substrates in 22 x 22 mm squares. The platform is composed of six electrochemical cells with a diameter of 3.5 mm, each of them characterized by three electrodes; Working Electrode (WE) is designed in AutoCAD with 0.85 mm diameter; the nominal distance between Working Electrode (WE) and Counter Electrode (CE) is 0.55 mm. A UV-cured material to manage liquid samples surrounds the whole structure. The yellow central structure in Fig. 87 permits to deliver the sample on WEs by introducing a micropipette in the inlet and injecting. The six bigger chambers serve to contain the buffer solution. We design microfluidics in order to contain 20 μ l of sample fluid including the amount that remains in channels and inlet. WE chambers have a diameter of 1.5 mm and the channel length is of 2.8 mm. The CAD geometry of the channel is an

isosceles triangle with base angle of 50° and base length equal to $300\ \mu\text{m}$. The central inlet nominal diameter is about $1.1\ \text{mm}$ and it is dimensioned with interference on a $1.1\ \text{mm}$ tip micropipette.

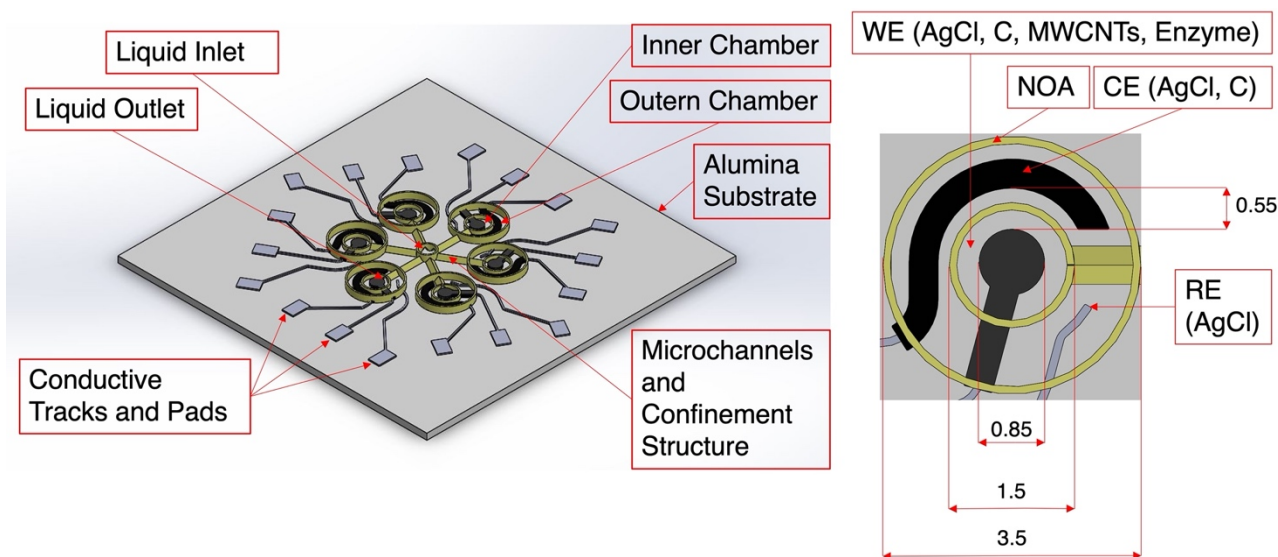


Fig. 87 Schematic representation of the final prototype [72].

The materials employed for EB are silver chloride (AgCl) for conductive tracks, pads and Reference Electrode (RE), carbon (C) ink for WE and CE. Furthermore, multi-wall carbon nanotubes (MWCNTs) ink was selected and printed over WE to enhance both electrical performances and the surface to volume ratio for biofunctionalization. Silver chloride ink (XA-3773) was purchased by Fujikura Kasei. Co. Ltd. (Shibakouen Minato-ku, Tokyo, Japan) together with its own thinner. The ink was chosen with Ag/AgCl weight proportion ratio of 8/2. A dilution of the ink, with its specific thinner, was mandatory to obtain a proper viscosity for the printing stage (ink starting viscosity was 300 ± 50 dPas), following the equations reported in the literature regarding a two-component blend [164]. Rotational viscosity measurements were performed using Viscotech VR 3000 MYR Viscometers modelV2-L (C/ Lleida, 17-23 · Pol. Ind. L'empalme, 43712 Llorenç del Penedès, Tarragona, España) to measure the viscosity after dilution. The tests were performed in a common range of ambient temperatures, from $19\ ^\circ\text{C}$ to $25\ ^\circ\text{C}$, evaluating the behavior of the ink for each $0.5\ ^\circ\text{C}$ in the abovementioned range. Different rotating speeds were selected: 5, 6, 10, 12 and 20 rpm. Fig. 88a shows the linear behavior of AgCl ink for different testing temperatures, demonstrating it can be considered as a Newtonian fluid in our range. Temperature has an important role in the printability of the material, as it is clearly visible in Fig. 88b: the higher the temperature, the lower the viscosity. Concluding, the ink was deposited at $23\ ^\circ\text{C}$ with a viscosity of about 19.5 mPas.

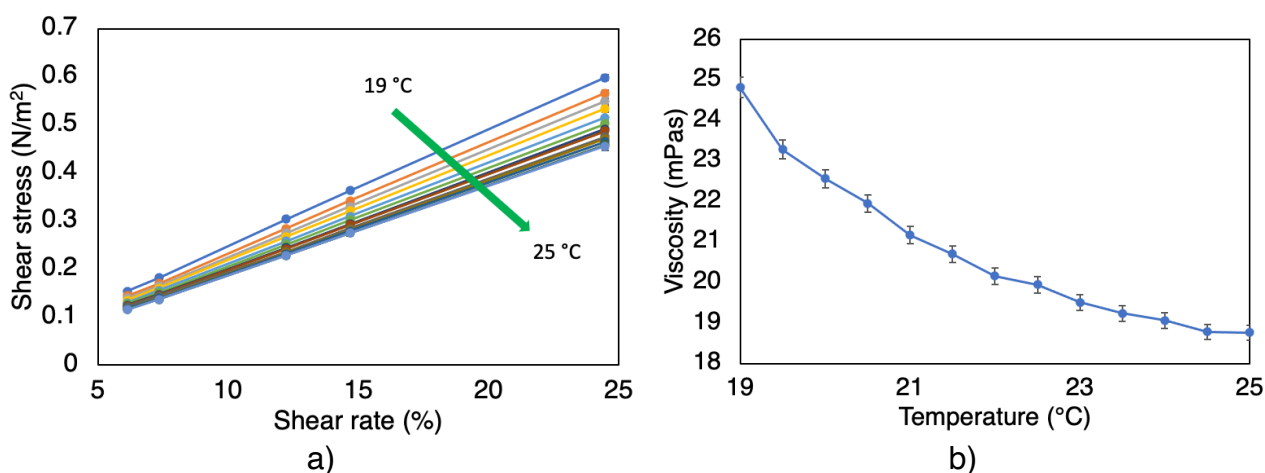


Fig. 88 A) Shear stress vs Shear rate, showing a complete linear behavior for temperature in the range 19-25 °C for AgCl ink; B) Viscosity as a function of temperature for AgCl ink [72].

Carbon ink (EXP 2652-28) was acquired from Creative Materials Inc. (Ayer, MA, United States of America), characterized by a starting viscosity of 250 mPas. Nink 1000, commercialized by NANOLAB (Waltham, MA, United States of America), is the abovementioned MWCNTs ink, it has a viscosity about 3 mPas and it contains carboxyl (COOH) functionalized carbon nanotubes in an aqueous suspension (the viscosity is proximal to the one of water) with the minimum concentration of additives to impart long-term stability and printability to the ink. UV-curable polymer NOA 81 was purchased by Norland Products (Cranbury, NJ, United States of America). We selected NOA 81 for several reasons: fast curing with a 365 nm light, high viscosity (300 mPas at 25 °C) that limits the polymer spread before curing [310], transparency, natural hydrophilicity [311] to permit a spontaneous capillary flow inside channels, low shrinkage during curing because it is a crosslinking process without evaporation, biocompatibility with biomolecules and cells [312], [313], good mechanical properties to have a robust structure with minimum material employed, excellent adhesion on a wide range of material and chemical resistance [314].

b) Fabrication process

AJ300 system was used to manufacture and functionalize the electrochemical sensors platform with microfluidics; Table 16 resumes the process parameters for each ink, while Fig. 89 shows the process scheme.

Table 16 Printing process parameters.

Process parameters	AgCl	C	NOA 81	Nink 1000	Mediator/ Enzyme (UA)
Sheath gas flow (SCCM)	55	40	40	50	60
Atomizer flow (SCCM)	750	805	1395	670	40
Exhaust flow (SCCM)	720	770	1365	580	/
Process speed (mms ⁻¹)	2	4	1.5	2	2
Plate temperature (°C)	65	70	/	40	/
Current (mA)	/	/	/	/	500

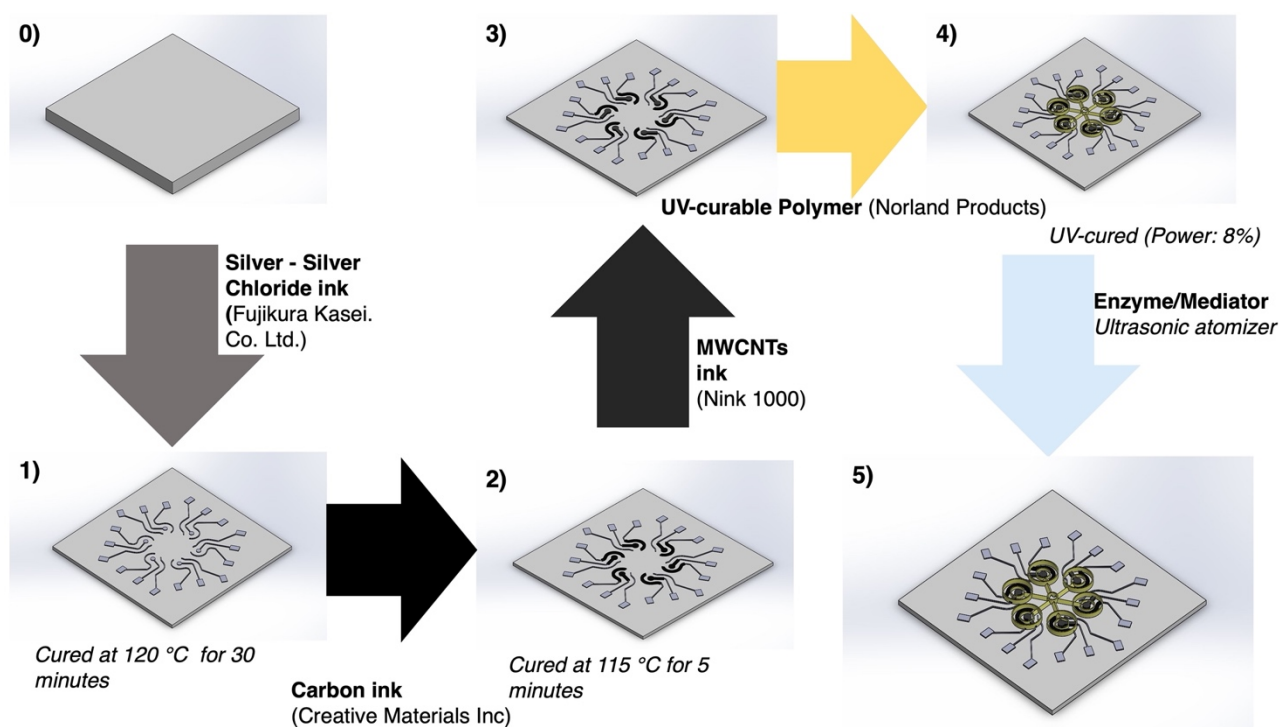


Fig. 89 AJP process for microfluidic sensors platform fabrication [72].

AgCl, C and MWCNTs inks were printed with two consecutive depositions, followed by its own specific heat treatment, using a 200 μm nozzle tip. Pneumatic atomization was selected. NOA 81 printing was performed in a single deposition step and UV curing is performed during printing process. The UV Curing System is the LED Spot type Panasonic ANUJ6180 series, model 6423 (Panasonic, Kadoma, Osaka, Japan) characterized by a spot diameter of 3 mm, wavelength of 365 nm in correspondence of the peak and a peak intensity of 17200 mWcm^{-2} at the distance of 8 mm. The selected power was 8% of the peak intensity.

NOA 81 printability requires a particular attention. The AJP pneumatic atomizer produces a mist of micro-droplets dispersed inside nitrogen (atomizer flow). The virtual impactor permits to reduce and filter the mist removing the smaller droplets by controlling a negative pressure (exhaust flow). The remaining flow (aerosol flow) is accelerated and collimated in the nozzle through a coaxial nitrogen flow (sheath flow). The ratio between sheath and aerosol flows (χ) requires a fine tuning in order to reduce overspray. Indeed, as precisely explained in [315], bigger droplets deviate to the center of the flow more than the smaller ones due to Saffman forces. Thus, the droplets size distribution along the jet section changes. In the center of the jet, the presence of larger particles that, after impact, form the core of the printed line increases, whereas on the sides there are smaller droplets that form overspray. As discussed in [316], higher values of χ reduces this effect but implies also less material deposition and can cause nozzle clogging. In printing NOA 81, the printed line requirements are: thickness in the order of tens of microns to lower the printing time, no porosity and less overspray as possible. NOA 81 overspray increases with temperature, and it is probably related to atomizer droplets size distribution change due to viscosity and surface tension lowering. With optimized printing parameters (see Table 16), NOA droplets coalesce during the collimation and it is possible to generate a dense NOA jet with a low amount of overspray. The UV laser quickly solidifies the jet as it hits the substrate and before it can spread and flow (Fig. 90a). Stacked cantilevered solid lines can be printed to create an overhang wall without any sacrificial material (Fig. 90b).

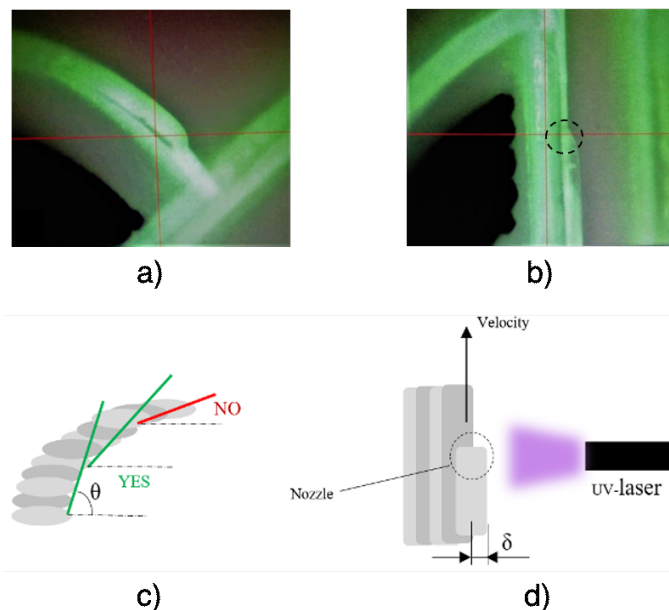


Fig. 90 Process camera photo during printing of A) a chamber wall and B) a microchannel cantilevered line; representation of the critical angle (C); printing scheme and line off-set δ (D) [72].

Therefore, microchannels can be fabricated without any support material. The idea is to generate and print 2D drawings obtained by longitudinal slicing of the CAD channel at different heights. There is not yet a software dedicated to AJP that allows to make slices from a virtual 3D object and to convert them directly into machine files. We used Solidworks for 3D modeling, Netfabb to create slices of the desired thickness and Autocad VMTTools provided by Optomec to generate machine files. The layer thickness (h) is chosen in accordance with the NOA line thickness. Therefore, a preliminary geometrical analysis was performed with Filmetrics Profilm 3D optical profilometer (Filmetrics Inc., 10655 Roselle St., San Diego, CA United States of America). With the parameter reported in Table 16, the measured thickness for one single line was about 25 μm and about 10-20% less for cantilevered or stacked lines. The analysis showed a slight lowering of thickness for cantilevered or stacked lines because the new line adapts to the real geometry of the previous one. Therefore, we chose h equal to 20 μm . The channel transversal section geometry that minimizes the layers number necessary to close the channel is the triangular one with the lower angle possible (θ) between the wall and the substrate. Reasonably, θ has a minimum value θ_{cr} below which collapse can occur before solidification (Fig. 90c). Indeed, fixed the thickness of the layers, if the angle decreases, the offset δ between the cantilevered lines increases. Higher offset means minor support area for the new line (Fig. 90d). We have found that θ_{cr} is approximately 45 ° for our printing parameters. However, fixing the jet flow rate and increasing the printing velocity, the line thickness decreases, thinner CAD slices can be generated and therefore is possible to have a smaller offset between lines also for $\theta < \theta_{cr}$. Thus, also quasi-circular channels could be investigated. Considering these geometrical constraints, it is possible to model and print microfluidics in one-step with a great variety of shapes including inlets, outlets and chambers.

The final platform with microchannel and chamber details is shown in Fig. 91. In this figure, the prototype is shown with its specific geometrical and production features (Fig. 91a), together with magnification regarding a single chamber (Fig. 91b) and the profile of the triangular channel (Fig. 91c). It is also possible to observe the inlet and the outlet of the microfluidic system developed and a channel filled with pen ink to test its correct usage (respectively Fig. 91a, Fig. 91c, Fig. 91d).

After completing the overall platform, both in term of sensors and of microfluidic channels, AJP has been finally adopted to functionalize WEs with specific chemicals required to

perform glucose sensing. In detail, first of all a ferro/ferri-cyanide ($\text{Fe}^{2+}/\text{Fe}^{3+}$) 5 mM solution have been printed only on the WEs, in order to act as a mediator during chemical reaction for glucose sensing. Further, a solution of 300 U/ml of Glucose Oxidase (GOx) in Acetate Buffer (pH 5) has been printed in order to provide ready-to-use sensors. Both the solution of mediator and enzyme have been printed via Ultrasonic atomization (UA). Despite we focused on glucose sensing, the proposed approach can be used with different measurement methods and applications with other enzymes or chemicals.

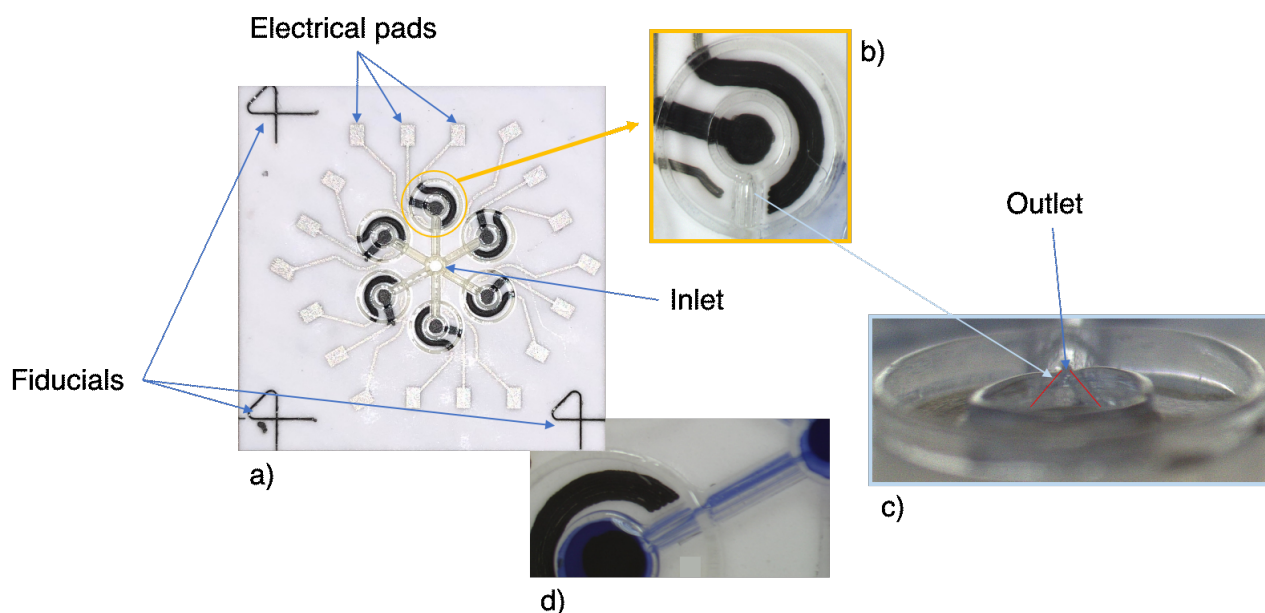


Fig. 91 Final platform produced by means of AJP (a), with specific details of the two concentric limiting circles (b) and a frontal view of the triangular channel (c); a channel filled with pen ink (d) [72].

c) Geometrical analysis and electrical resistances

Geometrical and electrical tests were performed on printed lines. Filmetrics Profilum 3D optical profilometer (Filmetrics Inc., 10655 Roselle St., San Diego, CA United States of America) was used to evaluate the thickness of the printed lines. It is based on state-of-the-art white light interferometry (WLI), a non-contact optical method for surface height measurement on 3-D structures, to measure surface profiles and roughness down to $0.05 \mu\text{m}$. The instrument works in the range of 50 nm – 10 mm with substrates and materials characterized by a reflectance between 0.05 – 100 %. The system implements a 5MP camera, the Nikon CF IC Epi Plan 20x model (field-of-view: 1.0 x 0.85 mm).

In order to measure the width of the microfluidic structure in which the liquid sample would be inflated during glucose sensing, an optical microscope by Orma Scientific NB50T (trinocular zoom 0.8x – 5x – LED), with its devoted software and HDMI MDH5 camera

model, was used to acquire the images and to evaluate the features of the printed elements (Orma Scientific, Italy).

Electrical resistance was evaluated using the digital bench-top multimeter Hewlett-Packard 34401a (HP, Palo Alto, CA, United States of America), applying testing probes to the extremities of each path, in standardized and repeatable points, thus measuring the resistance offered by all its length. Each measure has been repeated ten times, in order to ensure the proper calculation of the mean values and of the standard deviations. Resistivity was then calculated from the classical equation $R=\rho lS^{-1}$ where R is resistance, ρ is resistivity, l is the length of the considered path and S its section.

d) *Electrochemical analysis*

The electro-active surface area (A_{real}) was evaluated for every electrode-type from Randles-Sevcik equation (41) for reversible reaction, as well described in [300], by performing Cyclic Voltammetry (CV) at 0.1 V/s scan-rate (ν) in a phosphate buffer saline (50 mM, pH 7.0) containing a 5 mM concentration (C) of ferro/ferri-cyanide ($[Fe(CN)_6]^{3-/4-}$). Indeed, the electrochemical couple Fe^{2+}/Fe^{3+} redox process has a very well-known diffusion coefficient ($D = 6.20 \times 10^{-6} \text{ cm}^2$).

$$I_{rev} = \pm 0.446 \cdot nFA_{real}C \sqrt{\frac{nFD\nu}{RT}} \quad (41)$$

Further, an electrochemical characterization was performed in order to investigate the effect of scan rate on oxidation and reduction currents and potentials. In detail, multiple CVs in presence of 5mM $[Fe(CN)_6]^{3-/4-}$ were performed at different scan rates (25, 50, 100, 150, and 200 mV/s) in the potential range -0.2 to 0.4 V using the commercially available portable potentiostat Palmsens3 EIS (Palmsens, Compact Electrochemical Interfaces, Houten, Utrecht, The Netherlands).

e) *Glucose Sensing*

Standard solutions of D-Glucose in Deionized (DI) water have been prepared with the following concentration: 0 mM, 5 mM, 10 mM, 25 mM, 50 mM, 100 mM. For each test, the platforms have been directly used after printing. 20 μ l of D-Glucose solution was injected using a micropipette from the central inlet, thus to provide the solution only to the enzymed-coated WEs, in order to allow the following chemical reactions in presence of GOx,

producing an amount of electrons proportional to the concentration of glucose, then transported to the electrodes thanks to the mediator (Fig. 92):

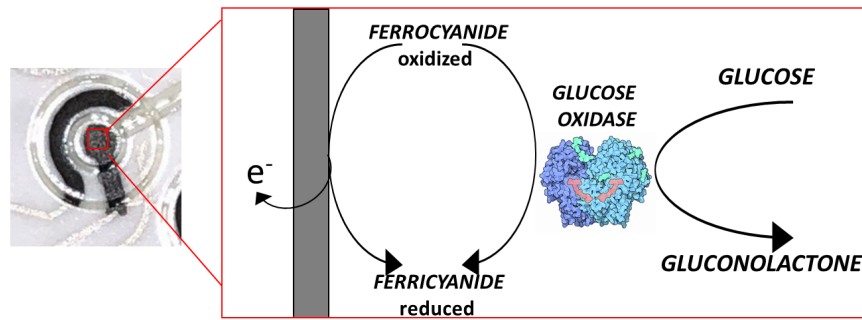
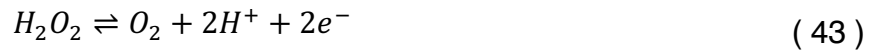


Fig. 92 Mechanism of enzymed mediated glucose sensing [72].

Five seconds after loading the sample, 10 μl of buffer solution was dropped on each electrochemical cell and a potential of +500 mV vs. Ag/AgCl was applied. Chronoamperometric measurements were recorded for 60 seconds with the abovementioned potentiostat. Current value at 60 seconds was taken as output to compare the different concentrations. Three microfluidic platforms have been tested for each concentration.

8.2.3 Results and discussion

a) Geometrical features measurements

The measured values of thicknesses, widths and sections are reported in Table 17. The geometrical data obtained are in agreement with our previous work [71], presenting a better relative standard deviation, denoting an improvement thanks to dedicated process parameters. Fig. 93 presents the profiles measured with the optical profilometer. NOA 81 channels' width presents an average value of 211 μm (relative standard deviation is about 7.8%).

Results from electrical tests show resistivity data in agreement with the nominal values of the manufacturers, considering the specific process parameters for each ink. The use of the thinner in order to achieve the proper final viscosity has affected AgCl experimental resistivity value ($89.5 \times 10^{-8} \Omega\text{m}$) that is higher compared with the nominal one reported by Fujikura Kasei. Co. Ltd. ($56 \times 10^{-8} \Omega\text{m}$). Finally, C experimental resistivity ($7.7 \times 10^{-4} \Omega\text{m}$)

was slightly decreased compared to the one given by Creative Materials ($25 \times 10^{-4} \Omega\text{m}$), due to the choice performed during the heat treatment in term of duration and temperature and to multiple material deposition.

Table 17 Thickness and sections of deposited inks.

Material	Thickness (μm)	Relative Standard Deviation (%)	Width (μm)	Relative Standard Deviation (%)	Section (μm^2)
AgCl	2.71	3	51.8	3.5	136.3
C + MWCNTs	1.97	5	127.8	9	262.74
NOA 81	26.06	1	96.75	4	1580.31

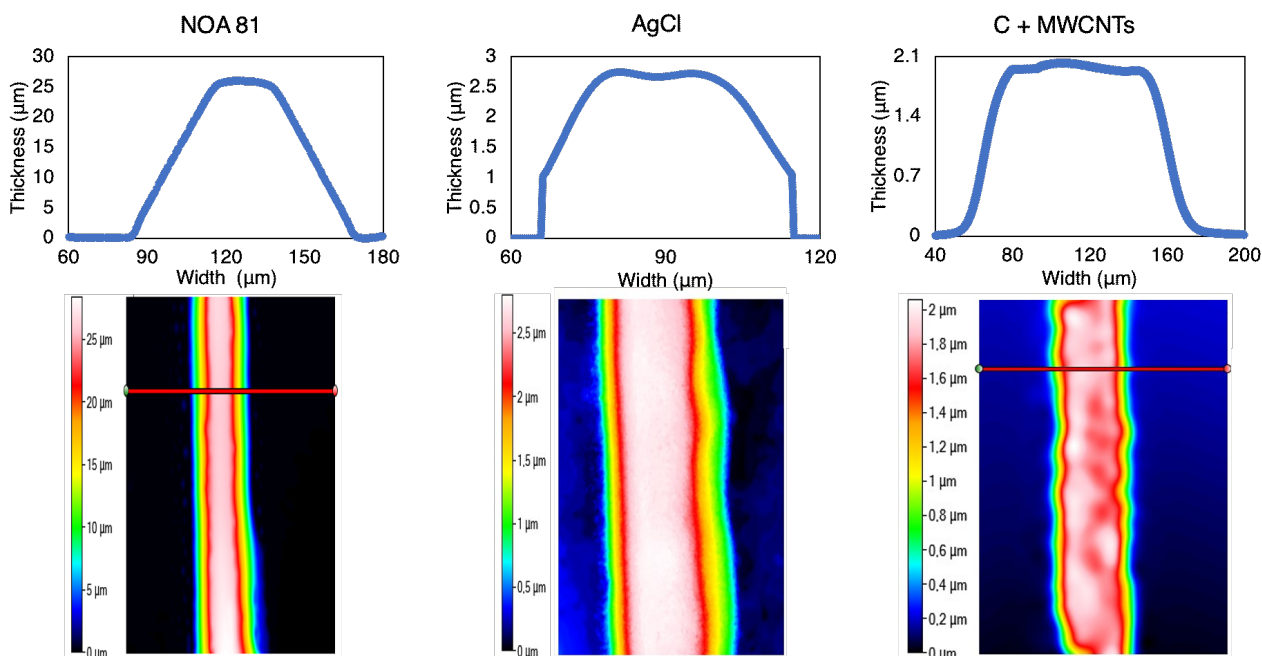


Fig. 93 Profiles obtained thanks to Filmetrics 3D optical profilometer for NOA 81, carbon with MWCNTs and AgCl [72].

b) Electrochemical analysis

The electrochemical analysis performed using at 100 mV/s allowed to calculate, from the Randles-Sevcik equation described in the method section, the average active area of each platform as $18.92 \pm 1.05 \text{ cm}^2$, confirming a high reproducibility of the electrochemical cells geometry and of the active area available for experiments. These is in agreement with what demonstrated in previous works [71], where AJP was shown to ensure a lower variability when compared to screen printing.

Fig. 94 show CV plots for a single electrochemical AJP cell in presence of 5 mM $[\text{Fe}(\text{CN})_6]^{3-/4-}$ with increasing scan rates of 25, 50, 100, 150, and 200 mV/s. Both the

oxidation and reduction peak currents linearly increased with the square root of scan rate, which indicates that the redox reaction is diffusion controlled [317], [318]. Furthermore, the ratio between the anodic and cathodic peak current is near to the unity for each scan rate. Regarding the cathodic and anodic potential (E_{pc} and E_{pa}), they both appear almost perfectly independent from the scan rate. Both the previous findings suggest a reversible behavior of the overall known reversible redox systems such as the ferri/ferrocyanide ones [319].

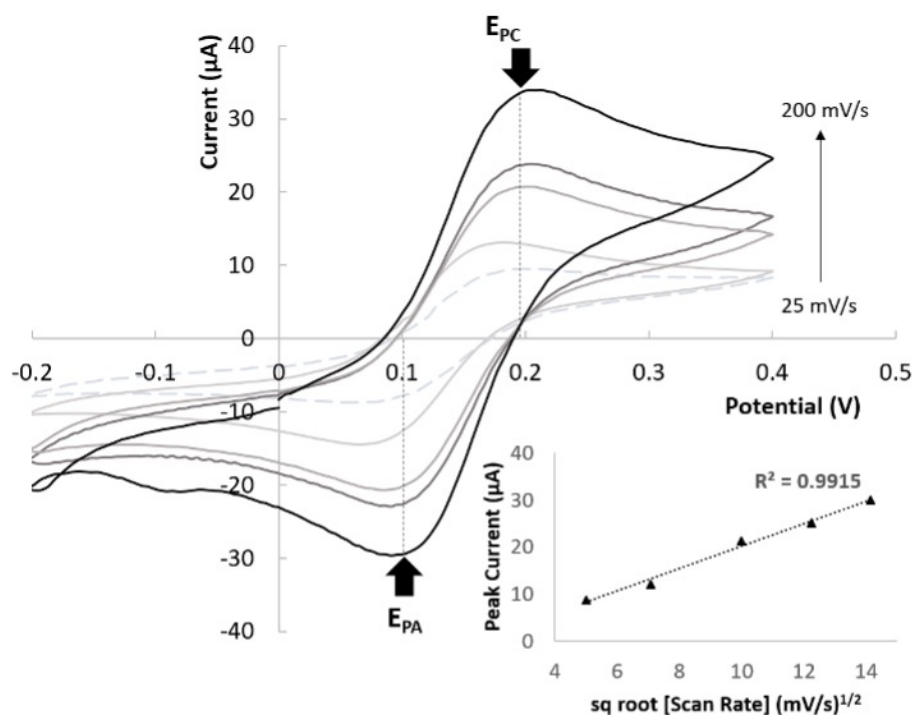


Fig. 94 Electrochemical characterization of AJP sensors in presence of 5mM Ferri-ferrocyanide solution. Cyclic voltammeteries at increasing scan rates (25, 50, 100, 150 and 200 mV/s) and linear relation between peak current height and the square root of the scan rate confirming the diffusion control of the reaction [72].

c) Glucose Sensing

Chronoamperograms obtained with different glucose concentrations suggested the possibility to correlate the increase in the steady state current at 60 seconds with the increase of glucose concentration (Fig. 95). The trend of glucose calibration plot appears to be logarithmic over the full range of concentration (0-100 mM). This suggests a higher sensibility of the overall system for lower concentrations and a saturation for higher glucose concentrations.

The platform output that estimates glucose concentration of a 20 µl sample is the currents sum. Fig. 96 shows the average of the three-platform output values obtained as sum of the six sensors currents of each platform for each concentration, blank corrected. The sum values are compared to the values of the average currents inside each platform for each

concentration. Outputs of proposed platform permits to correctly discriminate between every level of concentration, also at the lowest values. The limit of detection (LOD), calculated using the 3-sigma rule, taking as reference the blank standard deviation, is 2.4 mM. This value appears to be suitable for monitoring glucose concentrations typical of human blood, usually included in the range between 3 mM and 10 mM [320]. Furthermore, due to the versatility of the AJP procedure, and the possibility to easily improve the number of layers, these results could be optimized by varying the amount of mediator and enzyme on WEs.

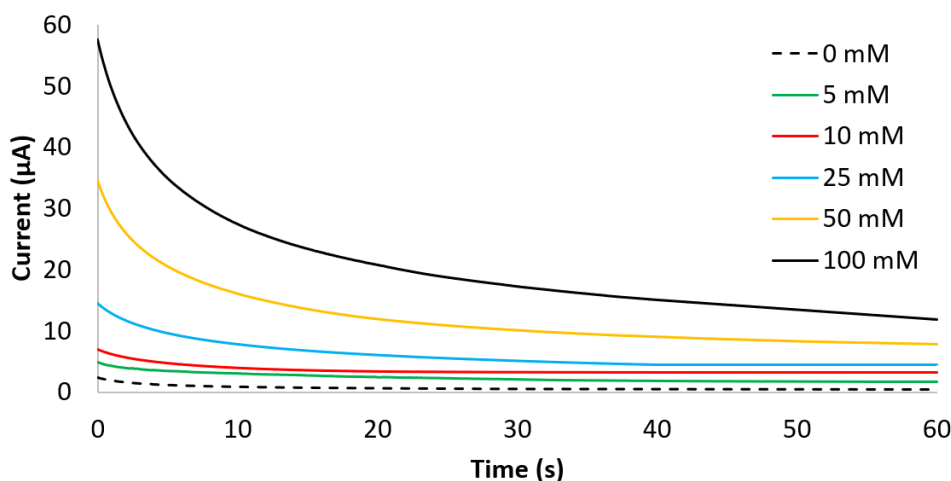


Fig. 95 Chronoamperograms at +500 mV recorded at different glucose concentration [72].

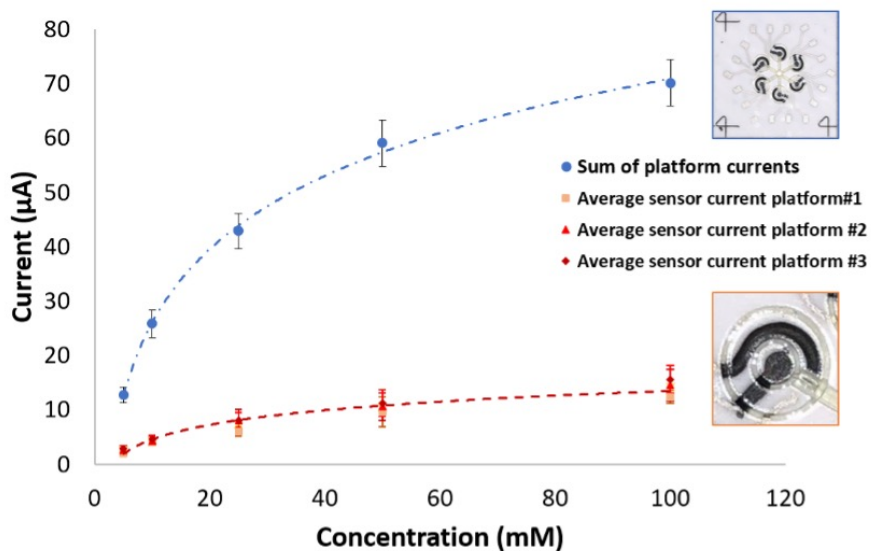


Fig. 96 Current values at 60 seconds (blank corrected) at different glucose concentrations: comparison between single sensor's average value on each repetition and average of the values obtained from the sum of the currents in a single platform [72].

Looking at the relative standard deviations of the measurements summarized in Table 18, an average variability of 16% can be observed when averaging the currents from six sensors of the same platform. The average variability intra-platform (16%) suggests a proper functioning of the microfluidics in homogeneously distributing the sample among the six

different measurements points. The inter-platform average variability (10%) suggests a high reliability of the overall printing strategy with a proper control of all the different steps involved for the final production of the platform. The values obtained for the relative standard deviation appear in agreement with previous works performed fabricating AJP sensors for protein detection [71]. Furthermore, despite the meaning of our paper was not the optimization of the LOD performances in term of glucose sensing, used as a mere validation of the AJP platform, our results appear in line in term on sensitivity with the results of optimized screen-printed sensors using the very same enzymatic mechanism for glucose detection [321]. In detail the sensitivity obtained with our platform in the range 0-10 mM was equal to $2.2 \pm 0.08 \mu\text{A}/\text{mM}$, in agreement with the one obtained in [321] of $2.13 \pm 0.06 \mu\text{A}/\text{mM}$.

Table 18 Current values and standard deviation for each platform and different concentrations.

Concent. (mM)	Platform (#)	Average (μA)	St.Dev. (μA)	Relative Dev %	St. Average sum (μA)	St.Dev. (μA)	sum Relative St. Dev %
	1	12.38	1.13	9.13			
100.00	2	14.60	2.87	19.66	70.15	4.25	6.06
	3	15.60	2.52	16.15			
	4	10.64	1.40	13.16			
50.00	5	9.65	0.40	4.15	59.09	4.26	7.21
	6	11.26	2.02	17.94			
	7	8.13	1.42	17.47			
25.00	8	8.03	1.87	23.29	42.93	3.24	7.54
	9	6.01	0.86	14.31			
	10	4.60	0.70	15.22			
10.00	11	4.32	0.83	19.21	25.86	2.52	9.70
	12	4.02	0.60	14.93			
	5.00	13	2.89	0.60	20.76	12.81	1.42

14	2.61	0.44	16.86
15	2.08	0.29	13.94

8.2.4 Conclusion

A fully Aerosol Jet Printed electrochemical microfluidic sensing platform has been designed, fabricated and tested. The variability observed when printing both conductive and UV-curable polymer inks was evaluated from the values of relative standard deviation lower than 5% for thickness and 9% for line width. This geometrical deviation suggests the potential of AJP technique for realizing sensors for accurate and repeatable environmental and clinical sample analysis. The electrochemical microfluidic sensing platform has been validated performing a standard enzyme-mediated procedure for glucose sensing. The average relative standard deviations observed from the current average evaluation intra platform (16%) and inter platform (10%) suggested the possibility to guide the positioning of the sample on miniaturized electrodes, to replicate the same analysis on separate platforms and, in future developments, to perform multiple analysis. This provides an improvement in term of lower operator dependency, reduction of sample waste and of analysis variability. Results from glucose sensing (LOD = 2.4 mM and sensitivity = $2.2 \pm 0.08 \mu\text{A}/\text{mM}$) confirmed the effectiveness of mediator and enzyme direct printing to provide sensing in a clinically relevant range (3 – 10 mM). This suggests the usefulness of this technique for providing a ready-to-use device, that do not need further processing after fabrication, but is promptly available for the electrochemical sample analysis.

9. General conclusions

The present dissertation discussed innovative methodologies and approaches to embed electronics and sensors in objects, thus realizing smart sensors and objects. Printed electronics technologies employed in this work have allowed pursuing this aim thanks to their flexibility in terms of employable materials. The versatility of the technologies used has allowed to exploit different types of substrates, such as different paper materials, glass, ceramics, plastics of various types and shapes, Kapton sheets, ranging then between planar and 3-D substrates. The functional inks, of different nature, have allowed the realization of sensors and circuits aimed at measuring different quantities. Conductors like silver inks, polymeric insulators, semiconductors like Ag/AgCl, carbon-based materials and carbon nanotubes were printed; exploiting the printing technology properties, also biological materials were selectively printed. For each combination of substrate and ink used, compatibility studies have been carried out with the aim to determine the best process parameters to achieve the required design performance. Compatibility studies covered not only the printing phase, but also the sintering process. This is because in the presence of some substrates such as paper and plastics, it was not possible to use a conventional heat treatment in an oven. In turn, the photonic sintering has required a work of optimization of the parameters in order to obtain the best compromise between obtaining the required electrical resistance and the least possible damage to the materials involved. In some cases, the possibility provided by the employed technologies to selectively combine different materials has been exploited, both considering planar and 3-D configurations, even micro-structured surfaces.

To assess the applicability of the methodologies proposed in this work, smart sensors and objects have been manufactured to be tested in different application fields, starting from the most popular wearable devices, passing through food industry packaging, to smart sensors for wet laboratory applications. The various application examples reported have underlined the versatility of such kind of manufacturing approach, starting from the capability to differentiate the shape of the printed pattern. The ease of customization permits to print any kind of geometrical feature required. This aspect, combined with dedicated studies on employable materials, allows the design of an entire device in all its parts, physical and electronic. For such a purpose, dedicated tests have been carried out considering in each case the specific materials used to understand their stability during time. From the

metrological viewpoint, an appreciable repeatability in the range of 10% was achieved considering the applicative examples. The innovative approach proposed allowed to tailor sensors, circuits and the overall device for a specific application, defining a unique manufacturing procedure. Customized features are all one with the substrate, introducing the concept of functionalizing already existing surfaces and objects. Applying sensors and measuring systems on every kind of object and surface, it is possible to measure quantities in application contexts that were impossible to reach with conventional methods. This aspect opens up new possibilities by being able to expand the knowledge on phenomena that previously was not possible to study.

At the same time, this sector still needs research to achieve the greatest possible diffusion and fully exploit the possibilities offered by these new methodologies. The design phase of the patterns to be printed requires attention in the placement of certain geometric elements according to the type of substrate in use. In addition, the determination of the process parameters for printing is a delicate and laborious phase since it is necessary to realize custom processes dedicated to a specific combination of materials. The result of this step influences not only the final electrical and geometrical properties of the printed element, but also the printing process itself. In fact, once properly defined, the process parameters thus determined allow the printing of several elements consecutively without interruptions for cleaning and avoiding process drifts and overspray. The latter phenomena are defects of the printing process that lead to an inevitable downtime for cleaning. A similar reasoning can be done for the parameters of photonic sintering. In case of too long exposure times or too intense light flashes, it is possible to burn the traces, deform the traces and/or the substrate to the point of detachment, thus destroying the printed elements. For this reason, the determination of these parameters can be even more difficult than the previous ones and requires the use of sacrificial samples specially designed for this purpose.

With a view to a future increased deployment of these innovative methods for making sensors and smart objects, more attention should also be directed to the design and study of complex 3D patterns. This fact can lead to the evaluation of the fabrication limits of the proposed methods, suggesting new solutions to implement such approach in other application fields moving ever more decisively into the era of smart objects.

Courses, Seminars, Conferences, Conference Proceedings, Journal Publications, Awards

a. Attended Courses/Schools

II year:

- 2020 Instrumentation and Measurement Ph.D. School "Italo Gorini" (streaming, 4th-9th September 2020)

III year:

- Ph.D. course on "High Resolution Electronic Measurements in Nano-Bio Science", 7/18 June 2021

b. Attended Seminars

II year:

- Navigating disruptive crises through digital servitization: the impact of covid-19 on Italian firms and supply chain (streaming, Università Degli Studi di Brescia, Laboratorio RISE, 19th May 2020)
- Wearable Devices (streaming, 8th June 2020)
- Sala Metrologica, Luogo di Collaudo, Ambiente d'Innovazione (webinar, 20th October 2020)
- Industrial Workshop on Printable Electronics (webinar, 22nd October 2020)

III year:

- From Plant Health to Community Health (webinar, Università Degli Studi di Brescia, 7th November 2020)
- Corso Soci-LA CALL GREEN DEAL DI H2020, CENNI DI PROGETTAZIONE E ANTICIPAZIONI SU HORIZON EUROPE (streaming, 9th December 2020)
- Survival in the Working World: Navigating the Transition from College to Cubicle, 25 February 2021
- IEEE Authorship and Open Access Symposium: Best Practices to Get Published to Increase the Exposure and Impact of Your Research, 21/04/2021
- A&T Automation and Testing Additive Manufacturing (9-10th June 2021)
- ETICA E DEONTOLOGIA PER L'INGEGNERE_SEMINARIO_1 (7th July 2021)
- ETICA E DEONTOLOGIA PER L'INGEGNERE_SEMINARIO_2 (7th July 2021)
- DIGITAL SMART FLUIDICS - Fluidica Digitale per le Scienze della Vita (21st July 2021)
- Corso Intensivo HP 3D Printing (5-7th, 12-14th October 2021)

c. Attended Congresses/Conferences

II year:

- BIODEVICES 2020, 13th International Conference on Biomedical Electronics and Devices (Malta, La Valletta, 24th-26th February 2020)
- GMEE, IV Forum Nazionale Delle Misure, XXXVII Congresso Nazionale di Misure Elettriche ed Elettroniche (streaming, 10th-12th September 2020)

III year:

- DOTTORANDI IN ATENEO 2020, PRESENTAZIONE DEI PROGETTI DOTTORALI, Ateneo di Brescia, Accademia di Scienze, Lettere ed Arti (streaming, 16th December 2020)
- I2MTC 2021 IEEE International Instrumentation & Measurement Technology Conference (streaming, 17-20th May 2021)
- 2021 IEEE International Workshop on Metrology for Industry 4.0 and IoT (MetroInd4.0&IoT) (streaming, 7-9th June 2021)
- IEEE RTSI 2021 6th online Forum on Research and Technologies for Society and Industry Innovation for a smart world (streaming, 6-9th September 2021)

d. Conference Proceedings

I year:

- [1] A. Bodini, E. Cantu, M. Serpelloni, E. Sardini, and S. Tonello, "Design and implementation of a microsensor platform for protein detection realized via 3-D printing," in *2018 IEEE Sensors Applications Symposium, SAS 2018 - Proceedings*, 2018, vol. 2018-January.
- [2] M. Borghetti and E. Cantu, "Preliminary Study on a Strain Sensor Printed on 3D-plastic Surfaces for Smart Devices," in *2019 IEEE International Workshop on Metrology for Industry 4.0 and IoT, MetroInd 4.0 and IoT 2019 - Proceedings*, 2019.
- [3] E. Cantù, S. Tonello, M. Serpelloni, and E. Sardini, *Aerosol jet printed sensors for protein detection: A preliminary study*, vol. 539. 2019.

II year:

- [4] E. Cantù, M. Soprani, A. Ponzoni, E. Sardini, and M. Serpelloni, "Preliminary Analysis on Cellulose-based Gas Sensor by Means of Aerosol Jet Printing and Photonic Sintering," 2020.

III year:

- [5] S. Tonello *et al.*, "Preliminary Study of a Flexible Printed Multi-Sensing Platform for Electromyography and Lactate Measuring during Rehabilitation," in *2021 IEEE International Symposium on Medical Measurements and Applications (MeMeA)*, 2021, pp. 1–6.
- [6] M. Borghetti, E. Cantù, E. Sardini, and M. Serpelloni, "PVDF Piezoelectric Sensors on 3D low-Melting Point Substrates: a Preliminary Study on Paper," in *2021 IEEE International Instrumentation and Measurement Technology Conference (I2MTC)*, 2021, pp. 1–5.
- [7] M. Borghetti, E. Cantù, E. Sardini, M. Serpelloni, and A. Ponzoni, "Preliminary Analysis on a Paper-based Ammonia Sensor for Future Food Smart Packaging," in *2021 IEEE International Workshop on Metrology for Industry 4.0 & IoT (MetroInd4.0&IoT)*, 2021, pp. 140–144.
- [8] M. Borghetti, E. Cantù, E. Sardini, and M. Serpelloni, "Preliminary Study on Wireless Passive Resistive Sensor Applied for Smart Objects," in *2021 IEEE International Workshop on Metrology for Industry 4.0 & IoT (MetroInd4.0&IoT)*, 2021, pp. 150–155.
- [9] M. Borghetti, M. Serpelloni, and E. Sardini, "Printed Sensors for Smart Objects in Industry 4.0," *IEEE RTSI 2021 6th online Forum Res. Technol. Soc. Ind. Innov. a smart world*, 2021.
→ IN PRESS

e. Publications in Journals

I year:

- [10] M. Marziano *et al.*, "Monitoring Caco-2 to enterocyte-like cells differentiation by means of electric impedance analysis on printed sensors," *Biochim. Biophys. Acta - Gen. Subj.*, vol. 1863, no. 5, 2019.
- [11] E. Cantù, S. Tonello, G. Abate, D. Uberti, E. Sardini, and M. Serpelloni, "Aerosol jet printed 3D electrochemical sensors for protein detection," *Sensors (Switzerland)*, vol. 18, no. 11, 2018.
- [12] M. A. Khan, E. Cantù, S. Tonello, M. Serpelloni, N. F. Lopomo, and E. Sardini, "A review on biomaterials for 3D conductive scaffolds for stimulating and monitoring cellular activities," *Appl. Sci.*, vol. 9, no. 5, 2019.

- [13] N. G. Di Novo, E. Cantù, S. Tonello, E. Sardini, and M. Serpelloni, “Support-material-free microfluidics on an electrochemical sensors platform by aerosol jet printing,” *Sensors (Switzerland)*, vol. 19, no. 8, 2019.

II year:

- [14] S. Tonello *et al.*, “Impedance-Based Monitoring of Mesenchymal Stromal Cell Three-Dimensional Proliferation Using Aerosol Jet Printed Sensors: A Tissue Engineering Application,” *Materials (Basel)*., vol. 13, no. 10, p. 2231, May 2020.
- [15] M. Serpelloni, E. Cantù, M. Borghetti, and E. Sardini, “Printed Smart Devices on Cellulose-Based Materials by means of Aerosol-Jet Printing and Photonic Curing,” *Sensors*, vol. 20, no. 3, p. 841, Feb. 2020.

III year:

- [16] E. Cantù *et al.*, “Printed Multi-EMG Electrodes on the 3D Surface of an Orthosis for Rehabilitation: a Feasibility Study,” *IEEE Sens. J.*, 2021.
- [17] M. Borghetti, E. Cantù, E. Sardini, and M. Serpelloni, “Future sensors for smart objects by printing technologies in Industry 4.0 scenario,” *Energies*, vol. 13, no. 22, Nov. 2020.
- [18] P. Bellitti, E. Cantù, E. Sardini, and M. Serpelloni, “Resistive Sensors for Smart Objects: Analysis on Printing Techniques,” *IEEE Transactions on Instrumentation and Measurement*, Ott. 2021. → IN PRESS
- [19] M. Borghetti, E. Cantù, A. Ponzoni, E. Sardini, and M. Serpelloni, “Aerosol Jet Printed and Photonic Cured Paper-based Ammonia Sensor for Food Smart Packaging,” *IEEE Transactions on Instrumentation and Measurement*, Ott. 2021. → IN PRESS

f. Awards

- Best Paper on Sensors for Metrology and Industry 4.0 - 1st classified, in *2021 IEEE International Workshop on Metrology for Industry 4.0 & IoT (MetroInd4.0&IoT)*, 2021
- Best Presentation Award on CNS 2018, Convegno Nazionale Sensori – 2nd classified, in *CNS 2018, Convegno Nazionale Sensori*, 2018

References

- [1] E. Traini, G. Bruno, G. D'Antonio, and F. Lombardi, "Machine learning framework for predictive maintenance in milling," *IFAC-PapersOnLine*, vol. 52, no. 13, pp. 177–182, Sep. 2019.
- [2] M. I. Bin Iqbal, M. Mohsin, and F. Gula, "Smart-Genie: An IoT-enabled predictive health monitoring system for power generators," in *15th International Conference on Emerging Technologies, ICET 2019*, 2019.
- [3] G. Kortuem, F. Kawsar, V. Sundramoorthy, and D. Fitton, "Smart objects as building blocks for the internet of things," *IEEE Internet Comput.*, vol. 14, no. 1, pp. 44–51, Jan. 2010.
- [4] S. Munirathinam, "Industry 4.0: Industrial Internet of Things (IIOT)," in *Advances in Computers*, vol. 117, no. 1, Academic Press Inc., 2020, pp. 129–164.
- [5] M. O. Gokalp, K. Kayabay, M. A. Akyol, P. E. Eren, and A. Koçyiğit, "Big Data for Industry 4.0: A Conceptual Framework," in *2016 International Conference on Computational Science and Computational Intelligence (CSCI)*, 2016, pp. 431–434.
- [6] T. Ruppert, S. Jaskó, T. Holczinger, and J. Abonyi, "Enabling Technologies for Operator 4.0: A Survey," *Appl. Sci.*, vol. 8, no. 9, 2018.
- [7] O. Özbek and H. Saruhan, "The effect of vibration and cutting zonetemperature on surface roughness and tool wear ineco-friendly MQL turning of AISI D2," *J. Mater. Res. Technol.*, no. x x, pp. 1–11, 2020.
- [8] Y. Cohen, M. Faccio, F. Pilati, and X. Yao, "Design and management of digital manufacturing and assembly systems in the Industry 4.0 era."
- [9] T. Eldemerdash et al., "Iot Based Smart Helmet for Mining Industry Application," *Int. J. Adv. Sci. Technol.*, vol. 29, no. 1 SE-Articles, pp. 373–387, Jan. 2020.
- [10] M. Silverio-Fernández, S. Renukappa, and S. Suresh, "What is a smart device? - a conceptualisation within the paradigm of the internet of things," *Vis. Eng.*, vol. 6, no. 1, pp. 1–10, May 2018.
- [11] M. Saqlain, M. Piao, Y. Shim, and J. Y. Lee, "Framework of an IoT-based Industrial Data Management for Smart Manufacturing," *Journal of Sensor and Actuator Networks*, vol. 8, no. 2, 2019.
- [12] X. Xu and Q. Hua, "Industrial Big Data Analysis in Smart Factory: Current Status and Research Strategies," *IEEE Access*, vol. 5, pp. 17543–17551, 2017.
- [13] A. Pop-Vadean, P. P. Pop, T. Latinovic, C. Barz, and C. Lung, "Harvesting energy an sustainable power source, replace batteries for powering WSN and devices on the IoT," *IOP Conf. Ser. Mater. Sci. Eng.*, vol. 200, p. 012043, May 2017.
- [14] N. Soin, "Chapter 10 - Magnetic Nanoparticles—Piezoelectric Polymer Nanocomposites for Energy Harvesting," in *Micro and Nano Technologies*, A. A. El-Gendy, J. M. Barandiarán, and R. L. B. T.-M. N. M. Hadimani, Eds. Elsevier, 2018, pp. 295–322.
- [15] A. Deroussi, A. A. Madi, A. Addaim, and A. Erraoui, "New scalable smart telemetry for industrial systems: IoT solutions," in *2018 International Conference on Electronics, Control, Optimization and Computer Science, ICECOCS 2018*, 2019.
- [16] R. Lou, K. P. Hallinan, K. Huang, and T. Reissman, "Smart wifi thermostat-enabled thermal comfort control in residences," *Sustain.*, vol. 12, no. 5, pp. 1–15, 2020.
- [17] P. Bellitti *et al.*, "A compact low-power wireless system for in vivo evaluation of heat and moisture exchanger performance," *Meas. Sci. Technol.*, vol. 30, no. 2, 2019.
- [18] C. Del-Valle-Soto, L. J. Valdivia, R. Velázquez, L. Rizo-Dominguez, and J. C. López-Pimentel, "Smart

campus: An experimental performance comparison of collaborative and cooperative schemes for wireless sensor network,” *Energies*, vol. 12, no. 16, 2019.

- [19] M. Bona, M. Borghetti, E. Sardini, and M. Serpelloni, “Telemetric Technique for Passive Resistive Sensors Based on Impedance Real Part Measurement at Fixed Frequency,” *IEEE Trans. Instrum. Meas.*, vol. 67, no. 9, pp. 2160–2168, 2018.
- [20] Y. Fan, Y. Liu, Q. Xiao, X. Ma, X. Ji, and P. Sun, “A passive wireless surface acoustic wave sensor for pillar load measurement,” *AIP Adv.*, vol. 9, no. 10, p. 105305, Oct. 2019.
- [21] A. S. Almuslem, S. F. Shaikh, and M. M. Hussain, “Flexible and Stretchable Electronics for Harsh-Environmental Applications,” *Adv. Mater. Technol.*, vol. 4, no. 9, p. 1900145, Sep. 2019.
- [22] Y. Gu, D. Park, S. Gonya, J. Jendrisak, S. Das, and D. R. Hines, “Direct-write printed broadband inductors,” *Addit. Manuf.*, vol. 30, p. 100843, Dec. 2019.
- [23] J. Stringer *et al.*, “Integration of additive manufacturing and inkjet printed electronics: a potential route to parts with embedded multifunctionality,” *Manuf. Rev.*, vol. 3, p. 12, 2016.
- [24] D. Horst, C. Duvoisin, and R. Vieira, “Additive Manufacturing at Industry 4.0: a Review,” *Int. J. Eng. Tech. Res.*, vol. 8, pp. 3–8, Sep. 2018.
- [25] “Apparatus for production of three dimensional objects by stereolithography - Patent US-6027324-A - PubChem.” [Online]. Available: <https://pubchem.ncbi.nlm.nih.gov/patent/US-6027324-A>. [Accessed: 16-Oct-2021].
- [26] A. Rindfleisch, M. O’Hern, and V. Sachdev, “The Digital Revolution, 3D Printing, and Innovation as Data,” *J. Prod. Innov. Manag.*, vol. 34, no. 5, pp. 681–690, Sep. 2017.
- [27] F. Momeni, S. M. Mehdi Hassani, X. Liu, and J. Ni, “A review of 4D printing,” *Mater. Des.*, vol. 122, pp. 42–79, May 2017.
- [28] S. Cruz, D. Dias, J. C. Viana, and L. A. Rocha, “Inkjet Printed Pressure Sensing Platform for Postural Imbalance Monitoring,” *IEEE Trans. Instrum. Meas.*, vol. 64, no. 10, pp. 2813–2820, Oct. 2015.
- [29] K. S. Kwon, M. K. Rahman, T. H. Phung, S. D. Hoath, S. Jeong, and J. S. Kim, “Review of digital printing technologies for electronic materials,” *Flexible and Printed Electronics*, vol. 5, no. 4. IOP Publishing Ltd, p. 43003, 15-Dec-2020.
- [30] M. Borghetti, E. Cantù, E. Sardini, and M. Serpelloni, “Future Sensors for Smart Objects by Printing Technologies in Industry 4.0 Scenario,” *Energies*, vol. 13, no. 22, p. 5916, Nov. 2020.
- [31] W. D. Niles and P. J. Coassin, “Piezo- and solenoid valve-based liquid dispensing for miniaturized assays,” *Assay Drug Dev. Technol.*, vol. 3, no. 2, pp. 189–202, Apr. 2005.
- [32] S. B. Bammesberger *et al.*, “A Low-Cost, Normally Closed, Solenoid Valve for Non-Contact Dispensing in the Sub- μ L Range,” *Micromachines 2013, Vol. 4, Pages 9-21*, vol. 4, no. 1, pp. 9–21, Feb. 2013.
- [33] J. Friend and L. Yeo, “Piezoelectric Microdispenser,” *Encycl. Microfluid. Nanofluidics*, pp. 1662–1672, Aug. 2008.
- [34] E. A. Rojas-Nastrucci, A. D. Snider, and T. M. Weller, “Propagation Characteristics and Modeling of Meshed Ground Coplanar Waveguide,” *IEEE Trans. Microw. Theory Tech.*, vol. 64, no. 11, pp. 3460–3468, Nov. 2016.
- [35] U. R. Dominguez, “3D printed impedance elements by micro-dispensing,” *ETD Collect. Univ. Texas, El Paso*, Jan. 2013.
- [36] J. Sohn and S.-B. Choi, “Identification of Operating Parameters Most Strongly Influencing the Jetting

Performance in a Piezoelectric Actuator-Driven Dispenser,” *Appl. Sci.*, vol. 8, no. 2, p. 243, Feb. 2018.

- [37] M. Mueller and J. Franke, “Feasibility study of piezo jet printed silver ink structures for interconnection and condition monitoring of power electronics components,” in *2017 IEEE 19th Electronics Packaging Technology Conference, EPTC 2017*, 2018, vol. 2018-February, pp. 1–5.
- [38] M. Ankenbrand, Y. Eiche, and J. Franke, “Programming and Evaluation of a Multi-Axis/Multi-Process Manufacturing System for Mechatronic Integrated Devices,” 2019.
- [39] Lu, Chen, Zheng, Zhao, and Long, “Simulation and Experiment on Droplet Volume for the Needle-Type Piezoelectric Jetting Dispenser,” *Micromachines*, vol. 10, no. 9, p. 623, Sep. 2019.
- [40] Q. H. Nguyen, J. C. Jeon, and S.-B. Choi, “Optimal design of a jetting dispenser actuated by a dual piezoactuator,” in *Active and Passive Smart Structures and Integrated Systems 2014*, 2014, vol. 9057, no. 9, p. 90572U.
- [41] R. Zhang, V. Kolbin, M. Süttenbach, M. Hedges, and O. Amft, “Evaluation of 3D-printed conductive lines and EMG electrodes on smart eyeglasses frames,” in *Proceedings - International Symposium on Wearable Computers, ISWC*, 2018, pp. 234–235.
- [42] J. W. Sohn, J. Jeon, M. Choi, and S.-B. Choi, “Critical operating factors of a jetting dispenser driven by piezostack actuators: statistical analysis of experimental results,” *J. Adhes. Sci. Technol.*, vol. 32, no. 4, pp. 359–374, Feb. 2018.
- [43] A.-H. Alaaldeen, Q. Hala, A. Abdallah, and A.-K. Jumana, “Inkjet printing for the fabrication of flexible/stretchable wearable electronic devices and sensors,” *Sens. Rev.*, vol. 38, no. 4, pp. 438–452, Jan. 2018.
- [44] Y. Guo, H. S. Patanwala, B. Bognet, and A. W. K. Ma, “Inkjet and inkjet-based 3D printing: Connecting fluid properties and printing performance,” *Rapid Prototyp. J.*, vol. 23, no. 3, pp. 562–576, 2017.
- [45] H. Gudapati, M. Dey, and I. Ozbolat, “A comprehensive review on droplet-based bioprinting: Past, present and future,” *Biomaterials*, vol. 102, pp. 20–42, Sep. 2016.
- [46] P. Koltay, R. Steger, G. Birkle, H.-C. Huang, H. Sandmaier, and R. Zengerle, “Microdispenser array for highly parallel and accurate liquid handling,” <https://doi.org/10.1117/12.454604>, vol. 4590, pp. 195–203, Nov. 2001.
- [47] Y. Liu, Y. Yao, L. Chen, and L. Sun, “A closed-loop intelligent control strategy for precise non-contact liquid dispensing,” *2010 IEEE Int. Conf. Mechatronics Autom. ICMA 2010*, pp. 957–962, 2010.
- [48] D. A. Dunn and I. Feygin, “Challenges and solutions to ultra-high-throughput screening assay miniaturization: Submicroliter fluid handling,” *Drug Discov. Today*, vol. 5, pp. S84–S91, Jan. 2000.
- [49] H. C. B. M, and van der S. B, “Precise nanoliter fluid handling system with integrated high-speed flow sensor,” *Assay Drug Dev. Technol.*, vol. 3, no. 2, pp. 203–212, Apr. 2005.
- [50] R. Schramm and J. Franke, “Electrical functionalization of thermoplastic materials by cold active atmospheric plasma technology,” in *Proceedings of the 2013 IEEE 15th Electronics Packaging Technology Conference, EPTC 2013*, 2013, pp. 108–113.
- [51] “MesoScribe™ | MesoPlasma™ Printed Electronics.” [Online]. Available: <https://www.mesoscribe.com/>. [Accessed: 16-Oct-2021].
- [52] D. Tejero-Martin, M. Rezvani Rad, A. McDonald, and T. Hussain, “Beyond Traditional Coatings: A Review on Thermal-Sprayed Functional and Smart Coatings,” *Journal of Thermal Spray Technology*, vol. 28, no. 4. Springer New York LLC, pp. 598–644, 17-Apr-2019.
- [53] G. Hennig *et al.*, “Lasersonic® LIFT Process for Large Area Digital Printing,” *JLMN-Journal of Laser*

Micro/Nanoengineering, vol. 7, no. 3, 2012.

- [54] P. Serra and A. Piqué, "Laser-Induced Forward Transfer: Fundamentals and Applications," *Adv. Mater. Technol.*, vol. 4, no. 1, pp. 1–33, 2019.
- [55] T. Mattle, A. Hintennach, T. Lippert, and A. Wokaun, "Laser induced forward transfer of SnO₂ for sensing applications using different precursors systems," *Appl. Phys. A Mater. Sci. Process.*, vol. 110, no. 2, pp. 309–316, Feb. 2013.
- [56] P. Sopeña, J. M. Fernández-Pradas, and P. Serra, "Laser-induced forward transfer of conductive screen-printing inks," *Appl. Surf. Sci.*, vol. 507, p. 145047, Mar. 2020.
- [57] S. Cohen, O. Ermak, I. Peled, and Z. Kotler, "High throughput LIFT printing of electric circuitry," in *Laser 3D Manufacturing VII, 2020*, p. 11.
- [58] D. Tsakona, I. Theodorakos, A. Kalaitzis, and I. Zergioti, "Investigation on high speed laser printing of silver nanoparticle inks on flexible substrates," *Appl. Surf. Sci.*, vol. 513, p. 145912, May 2020.
- [59] M. Jalaal, M. Klein Schaarsberg, C. W. Visser, and D. Lohse, "Laser-induced forward transfer of viscoplastic fluids," *J. Fluid Mech.*, vol. 880, pp. 497–513, Dec. 2019.
- [60] J. M. Hoey, A. Lutfurakhmanov, D. L. Schulz, and I. S. Akhatov, "A review on aerosol-based direct-write and its applications for microelectronics," *J. Nanotechnol.*, vol. 2012, 2012.
- [61] S. Binder, M. Glatthaar, and E. Rädlein, "Analytical investigation of aerosol jet printing," *Aerosol Sci. Technol.*, vol. 48, no. 9, pp. 924–929, 2014.
- [62] H. W. Tan, T. Tran, and C. K. Chua, "A review of printed passive electronic components through fully additive manufacturing methods," *Virtual and Physical Prototyping*, vol. 11, no. 4. Taylor and Francis Ltd., pp. 271–288, 01-Oct-2016.
- [63] N. J. Wilkinson, M. A. A. Smith, R. W. Kay, and R. A. Harris, "A review of aerosol jet printing—a non-traditional hybrid process for micro-manufacturing," *Int. J. Adv. Manuf. Technol.*, vol. 105, no. 11, pp. 4599–4619, Dec. 2019.
- [64] Optomec, "AEROSOL JET ® PRINTED ELECTRONICS OVERVIEW," pp. 1–6, 2014.
- [65] A. A. Gupta, S. Arunachalam, S. G. Cloutier, and R. Izquierdo, "Fully Aerosol-Jet Printed, High-Performance Nanoporous ZnO Ultraviolet Photodetectors," *ACS Photonics*, vol. 5, no. 10, pp. 3923–3929, Oct. 2018.
- [66] E. Cantù *et al.*, "Printed Multi-EMG Electrodes on the 3D Surface of an Orthosis for Rehabilitation: a Feasibility Study," *IEEE Sens. J.*, 2021.
- [67] S. Agarwala *et al.*, "Wearable Bandage-Based Strain Sensor for Home Healthcare: Combining 3D Aerosol Jet Printing and Laser Sintering," *ACS Sensors*, vol. 4, no. 1, pp. 218–226, Jan. 2019.
- [68] C. Wang, G. Y. Hong, K. M. Li, and H. T. Young, "A miniaturized nickel oxide thermistor via aerosol jet technology," *Sensors (Switzerland)*, vol. 17, no. 11, Nov. 2017.
- [69] H. Yang, M. T. Rahman, D. Du, R. Panat, and Y. Lin, "3-D printed adjustable microelectrode arrays for electrochemical sensing and biosensing," *Sensors Actuators, B Chem.*, vol. 230, pp. 600–606, Jul. 2016.
- [70] A. Habermehl *et al.*, "Lab-on-chip, surface-enhanced Raman analysis by aerosol jet printing and roll-to-roll hot embossing," *Sensors (Switzerland)*, vol. 17, no. 10, Oct. 2017.
- [71] E. Cantù, S. Tonello, G. Abate, D. Uberti, E. Sardini, and M. Serpelloni, "Aerosol Jet Printed 3D Electrochemical Sensors for Protein Detection," *Sensors (Switzerland)*, vol. 18, no. 11, 2018.

- [72] N. G. Di Novo, E. Cantù, S. Tonello, E. Sardini, and M. Serpelloni, "Support-Material-Free Microfluidics on an Electrochemical Sensors Platform by Aerosol Jet Printing," *Sensors (Switzerland)*, vol. 19, no. 8, Apr. 2019.
- [73] R. Salary, J. P. Lombardi, M. S. Tootooni, R. Donovan, P. K. Rao, and M. D. Poliks, "In situ sensor-based monitoring and Computational Fluid Dynamics (CFD) modeling of Aerosol Jet Printing (AJP) process," in *ASME 2016 11th International Manufacturing Science and Engineering Conference, MSEC 2016*, 2016, vol. 2.
- [74] N. Ischdonat, C. Dreyer, D. Gräf, J. Franke, J. Hörber, and M. Hedges, "Influences of Manufacturing Sequences for the Application of Printed Electronics on Aircraft Interior Components," 2018.
- [75] K. Lomakin *et al.*, "Evaluation and characterization of 3-D printed pyramid horn antennas utilizing different deposition techniques for conductive material," *IEEE Trans. Components, Packag. Manuf. Technol.*, vol. 8, no. 11, pp. 1998–2006, Nov. 2018.
- [76] P. Lall, K. Goya, B. LEEVE, and S. Milled, "Factors influencing the line consistency of commonly used geometries for additively printed electronics," in *InterSociety Conference on Thermal and Thermomechanical Phenomena in Electronic Systems, IThERM*, 2019, vol. 2019-May, pp. 863–869.
- [77] P. Lall, A. Abrol, N. Kothari, B. LEEVER, and S. Miller, "Effect of print parameters on print consistency of aerosol jet printed electronics," in *InterSociety Conference on Thermal and Thermomechanical Phenomena in Electronic Systems, IThERM*, 2019, vol. 2019-May, pp. 633–642.
- [78] P. Lall, N. Kothari, K. Goyal, B. LEEVER, and S. Miller, "Extended-Time Process Consistency and Process-Property Relationships for Flexible Additive-Printed Electronics," in *2020 Pan Pacific Microelectronics Symposium, Pan Pacific 2020*, 2020.
- [79] M. Smith, Y. S. Choi, C. Boughey, and S. Kar-Narayan, "Controlling and assessing the quality of aerosol jet printed features for large area and flexible electronics," *Flex. Print. Electron.*, vol. 2, no. 1, p. 015004, Feb. 2017.
- [80] E. B. Secor, "Principles of aerosol jet printing," *Flex. Print. Electron.*, vol. 3, no. 3, Jul. 2018.
- [81] G. Chen, Y. Gu, H. Tsang, D. R. Hines, and S. Das, "The Effect of Droplet Sizes on Overspray in Aerosol-Jet Printing," *Adv. Eng. Mater.*, vol. 20, no. 8, p. 1701084, Aug. 2018.
- [82] H. W. Tan, J. An, C. K. Chua, and T. Tran, "Metallic Nanoparticle Inks for 3D Printing of Electronics," *Adv. Electron. Mater.*, vol. 5, no. 5, p. 1800831, May 2019.
- [83] N. Saengchairat, T. Tran, and C. K. Chua, "A review: additive manufacturing for active electronic components," *Virtual Phys. Prototyp.*, vol. 12, no. 1, pp. 31–46, 2017.
- [84] M. Serpelloni, E. Cantù, M. Borghetti, and E. Sardini, "Printed Smart Devices on Cellulose-Based Materials by means of Aerosol-Jet Printing and Photonic Curing," *Sensors*, vol. 20, no. 3, p. 841, Feb. 2020.
- [85] K. H. Jung, J. Kim, B. G. Park, C. J. Lee, H. J. Sung, and S. B. Jung, "Fabrication of Ag circuit embedded in PDMS substrate and its mechanical and electrical property with variations of photonic energy," *J. Alloys Compd.*, vol. 748, pp. 898–904, Jun. 2018.
- [86] B.-G. Park, C.-J. Lee, and S.-B. Jung, "Enhancing adhesion strength of photonic sintered screen-printed Ag circuit by atmospheric pressure plasma," *Microelectron. Eng.*, vol. 202, no. May, pp. 37–41, Dec. 2018.
- [87] Z. Zhong *et al.*, "Control of thermal deformation with photonic sintering of ultrathin nanowire transparent electrodes †," vol. 12, p. 2366, 2020.
- [88] J. West, M. Carter, S. Smith, and J. Sears, "Photonic Curing of Silver Nanoparticle Based Inks,"

TechConnect Briefs, vol. 2, pp. 210–213, 2010.

- [89] L. Rebohle, S. Prucnal, and W. Skorupa, “A review of thermal processing in the subsecond range: semiconductors and beyond,” *Semicond. Sci. Technol.*, vol. 31, no. 10, p. 103001, Sep. 2016.
- [90] S. Das, D. Cormier, and S. Williams, “Potential for Multi-functional Additive Manufacturing Using Pulsed Photonic Sintering,” in *Procedia Manufacturing*, 2015, vol. 1, pp. 366–377.
- [91] K. A. Schroder, *Mechanisms of Photonic Curing™: Processing High Temperature Films on Low Temperature Substrates*. Nano Science and Technology Institute, 2011.
- [92] L. Rebohle, M. Neubert, T. Schumann, and W. Skorupa, “Determination of the thermal cycle during flash lamp annealing without a direct temperature measurement,” *Int. J. Heat Mass Transf.*, vol. 126, pp. 1–8, Nov. 2018.
- [93] J. Ouyang, D. Cormier, S. A. Williams, and D. A. Borkholder, “Photonic Sintering of Aerosol Jet Printed Lead Zirconate Titanate (PZT) Thick Films,” *J. Am. Ceram. Soc.*, vol. 99, no. 8, pp. 2569–2577, 2016.
- [94] M. Bobinger *et al.*, “On the sintering of solution-based silver nanoparticle thin-films for sprayed and flexible antennas,” *Nanotechnology*, vol. 29, no. 48, Sep. 2018.
- [95] H. M. Cronin, Z. Stoeva, M. Brown, M. Shkunov, and S. R. P. Silva, “Photonic Curing of Low-Cost Aqueous Silver Flake Inks for Printed Conductors with Increased Yield,” *ACS Appl. Mater. Interfaces*, vol. 10, no. 25, pp. 21398–21410, Jun. 2018.
- [96] M. Rizwan *et al.*, “Possibilities of Fabricating Copper-Based RFID Tags with Photonic-Sintered Inkjet Printing and Thermal Transfer Printing,” *IEEE Antennas Wirel. Propag. Lett.*, vol. 16, pp. 1828–1831, 2017.
- [97] M. Borghetti and E. Cantu, “Preliminary Study on a Strain Sensor Printed on 3D-plastic Surfaces for Smart Devices,” in *2019 IEEE International Workshop on Metrology for Industry 4.0 and IoT, MetroInd 4.0 and IoT 2019 - Proceedings*, 2019.
- [98] B. K. Mahajan, X. Yu, W. Shou, H. Pan, and X. Huang, “Mechanically Milled Irregular Zinc Nanoparticles for Printable Bioresorbable Electronics,” *Small*, vol. 13, no. 17, May 2017.
- [99] M. Akbari, H. He, J. Juuti, M. M. Tentzeris, J. Virkki, and L. Ukkonen, “3D Printed and Photonicallly Cured Graphene UHF RFID Tags on Textile, Wood, and Cardboard Substrates,” *Int. J. Antennas Propag.*, vol. 2017, Jun. 2017.
- [100] B. K. Mahajan *et al.*, “Aerosol printing and photonic sintering of bioresorbable zinc nanoparticle ink for transient electronics manufacturing,” *Sci. China Inf. Sci.*, vol. 61, no. 6, Jul. 2018.
- [101] H. Ota *et al.*, “Application of 3D Printing for Smart Objects with Embedded Electronic Sensors and Systems,” *Adv. Mater. Technol.*, vol. 1, no. 1, p. 1600013, 2016.
- [102] F. Mekki, M. Borghetti, E. Sardini, and M. Serpelloni, “Wireless instrumented cane for walking monitoring in Parkinson patients,” in *2017 IEEE International Symposium on Medical Measurements and Applications, MeMeA 2017 - Proceedings*, 2017, pp. 414–419.
- [103] S. K. Mahadeva, K. Walus, and B. Stoeber, “Paper as a Platform for Sensing Applications and Other Devices: A Review,” 2015.
- [104] S. Kim *et al.*, “Inkjet-printed sensors on paper substrate for agricultural applications,” in *2013 European Microwave Conference*, 2013, pp. 866–869.
- [105] A. Kumar, S. K. Pahuja, and A. Singh, “Real time monitoring of muscle fatigue and muscle disorder of biceps brachii using Surface Electromyography (sEMG),” in *2018 First International Conference on Secure Cyber Computing and Communication (ICSCCC)*, 2018, pp. 401–405.

- [106] J. Wan, Z. Qin, P. Wang, Y. Sun, and X. Liu, "Muscle fatigue: general understanding and treatment," *Exp. Mol. Med.*, vol. 49, no. 10, pp. e384–e384, 2017.
- [107] G. Tartarisco, L. Billeci, G. Ricci, L. Volpi, G. Pioggia, and G. Siciliano, "A personal monitoring architecture to detect muscular fatigue in elderly.," *Neuromuscul. Disord.*, vol. 22 Suppl 3, pp. S192-7, Dec. 2012.
- [108] G. Gugliandolo *et al.*, "A Movement-Tremors Recorder for Patients of Neurodegenerative Diseases," *IEEE Trans. Instrum. Meas.*, vol. 68, no. 5, pp. 1451–1457, 2019.
- [109] J. Liu *et al.*, "Future paper based printed circuit boards for green electronics: Fabrication and life cycle assessment," *Energy Environ. Sci.*, vol. 7, no. 11, pp. 3674–3682, Nov. 2014.
- [110] H. Chang *et al.*, "Direct Writing and Repairable Paper Flexible Electronics Using Nickel–Liquid Metal Ink," *Adv. Mater. Interfaces*, vol. 5, no. 20, Oct. 2018.
- [111] X. Zou *et al.*, "Paper-Based Resistive Networks for Scalable Skin-Like Sensing," *Adv. Electron. Mater.*, vol. 4, no. 8, Aug. 2018.
- [112] Z. Wang *et al.*, "Paper-based metasurface: Turning waste-paper into a solution for electromagnetic pollution," *J. Clean. Prod.*, vol. 234, pp. 588–596, Oct. 2019.
- [113] P. Bezuidenhout, S. Smith, K. Land, and T. H. Joubert, "Inkjet-printed interconnects for unpackaged dies in printed electronics," *Electron. Lett.*, vol. 55, no. 5, pp. 252–254, Mar. 2019.
- [114] Z. H. Guo *et al.*, "Self-Powered Electrowetting Valve for Instantaneous and Simultaneous Actuation of Paper-Based Microfluidic Assays," *Adv. Funct. Mater.*, vol. 29, no. 15, Apr. 2019.
- [115] J. Hu *et al.*, "Advances in paper-based point-of-care diagnostics," *Biosensors and Bioelectronics*, vol. 54. Elsevier Ltd, pp. 585–597, 15-Apr-2014.
- [116] X. Sun *et al.*, "Ultrasensitive microfluidic paper-based electrochemical/visual biosensor based on spherical-like cerium dioxide catalyst for miR-21 detection," *Biosens. Bioelectron.*, vol. 105, pp. 218–225, May 2018.
- [117] A. Hayat and J. L. Marty, "Disposable screen printed electrochemical sensors: Tools for environmental monitoring," *Sensors (Switzerland)*, vol. 14, no. 6. MDPI AG, pp. 10432–10453, 13-Jun-2014.
- [118] P. Tee-Ngam, N. Nunant, P. Rattanarat, W. Siangproh, and O. Chailapakul, "Simple and rapid determination of ferulic acid levels in food and cosmetic samples using paper-based platforms," *Sensors (Switzerland)*, vol. 13, no. 10, pp. 13039–13053, Sep. 2013.
- [119] A. Ferraretto *et al.*, "New methodological approach to induce a differentiation phenotype in Caco-2 cells prior to post-confluence stage.," *Anticancer Res.*, vol. 27, no. 6B, pp. 3919–3925, 2007.
- [120] A. Garcia-Lorenzo *et al.*, "Cytotoxicity of selected imidazolium-derived ionic liquids in the human Caco-2 cell line. Sub-structural toxicological interpretation through a QSAR study," *Green Chem.*, vol. 10, no. 5, pp. 508–516, 2008.
- [121] T. Langerholc, P. A. Maragkoudakis, J. Wollgast, L. Gradisnik, and A. Cencic, "Novel and established intestinal cell line models - An indispensable tool in food science and nutrition," *Trends Food Sci. Technol.*, vol. 22, no. SUPPL. 1, 2011.
- [122] R. B. van Breemen and Y. Li, "Caco-2 cell permeability assays to measure drug absorption.," *Expert Opin. Drug Metab. Toxicol.*, vol. 1, no. 2, pp. 175–185, Aug. 2005.
- [123] J. Wegener, C. R. Keese, and I. Giaever, "Electric cell-substrate impedance sensing (ECIS) as a noninvasive means to monitor the kinetics of cell spreading to artificial surfaces.," *Exp. Cell Res.*, vol. 259, pp. 158–166, 2000.

- [124] D. Dziong, P. O. Bagnaninchi, R. E. Kearney, and M. Tabrizian, "Nondestructive online in vitro monitoring of pre-osteoblast cell proliferation within microporous polymer scaffolds," *IEEE Trans. Nanobioscience*, vol. 6, no. 3, pp. 249–258, Sep. 2007.
- [125] K. F. Lei, Z.-M. Wu, and C.-H. Huang, "Impedimetric quantification of the formation process and the chemosensitivity of cancer cell colonies suspended in 3D environment," *Biosens. Bioelectron.*, vol. 74, pp. 878–885, Dec. 2015.
- [126] K. F. Lei, C.-H. Huang, and N.-M. Tsang, "Impedimetric quantification of cells encapsulated in hydrogel cultured in a paper-based microchamber," *Talanta*, vol. 147, pp. 628–633, Jan. 2016.
- [127] C. Justice, J. Leber, D. Freimark, P. Pino Grace, M. Kraume, and P. Czermak, "Online- and offline-monitoring of stem cell expansion on microcarrier," *Cytotechnology*, vol. 63, no. 4, pp. 325–335, Aug. 2011.
- [128] S. Saem, Y. Zhu, H. Luu, and J. Moran-Mirabal, "Bench-top fabrication of an all-PDMS microfluidic electrochemical cell sensor integrating micro/nanostructured electrodes," *Sensors (Switzerland)*, vol. 17, no. 4, 2017.
- [129] J. Hart, K. Honeychurch, K. Westmacott, A. Crew, G. Hughes, and R. Pemberton, "Recent Advances in the Fabrication and Application of Screen-Printed Electrochemical (Bio)Sensors Based on Carbon Materials for Biomedical, Agri-Food and Environmental Analyses," *Biosensors*, vol. 6, no. 4, p. 50, 2016.
- [130] Y. T. So *et al.*, "Classification and prediction of clinical Alzheimer's diagnosis based on plasma signaling proteins," *Nat. Med.*, vol. 13, no. 11, pp. 1359–1362, 2007.
- [131] H. J. Kim, H. Li, J. J. Collins, and D. E. Ingber, "Contributions of microbiome and mechanical deformation to intestinal bacterial overgrowth and inflammation in a human gut-on-a-chip," *Proc. Natl. Acad. Sci.*, vol. 113, no. 1, pp. E7–E15, 2015.
- [132] N. Nesakumar, S. Kesavan, C.-Z. Li, and S. Alwarappan, "Microfluidic Electrochemical Devices for Biosensing," *J. Anal. Test.*, no. 0123456789, 2019.
- [133] D. Meadows, "Recent developments with biosensing technology and applications in the pharmaceutical industry," *Adv. Drug Deliv. Rev.*, vol. 21, no. 3, pp. 179–189, 1996.
- [134] S. Tonello *et al.*, "Enhanced sensing of interleukin 8 by stripping voltammetry: Carbon nanotubes versus fullerene," *IFMBE Proc.*, vol. 65, pp. 213–216, 2017.
- [135] R. M. Lequin, "Enzyme immunoassay (EIA)/enzyme-linked immunosorbent assay (ELISA)," *Clin. Chem.*, vol. 51, no. 12, pp. 2415–2418, 2005.
- [136] P. Singh, "SPR Biosensors: Historical Perspectives and Current Challenges," *Sensors Actuators, B Chem.*, vol. 229, pp. 110–130, 2016.
- [137] W. E. Doering, M. E. Piotti, M. J. Natan, and R. G. Freeman, "SERS as a foundation for nanoscale, optically detected biological labels," *Adv. Mater.*, vol. 19, no. 20, pp. 3100–3108, 2007.
- [138] C. Ma, Z. Sun, C. Chen, L. Zhang, and S. Zhu, "Simultaneous separation and determination of fructose, sorbitol, glucose and sucrose in fruits by HPLC-ELSD," *Food Chem.*, vol. 145, pp. 784–788, 2014.
- [139] J. Wu, Y. Liu, F. Lin, C. Rigatto, and M. Dong, "Lab-on-chip technology for chronic disease diagnosis," *npj Digit. Med.*, vol. 1, no. 1, pp. 1–11, 2018.
- [140] G. H. Lee *et al.*, "Single Microfluidic Electrochemical Sensor System for Simultaneous Multi-Pulmonary Hypertension Biomarker Analyses," *Sci. Rep.*, vol. 7, no. 1, pp. 1–8, 2017.
- [141] R. Riahi *et al.*, "Automated microfluidic platform of bead-based electrochemical immunosensor

integrated with bioreactor for continual monitoring of cell secreted biomarkers,” *Sci. Rep.*, vol. 6, no. April, pp. 1–14, 2016.

- [142] J. Wang, *ANALYTICAL ELECTROCHEMISTRY*, Third edit. Hoboken, New Jersey: John Wiley & Sons, Inc., 2006.
- [143] S. Tonello, N. F. Lopomo, M. Serpelloni, M. Serzanti, P. Dell’Era, and E. Sardini, “Preliminary Study of Inkjet Printed Sensors for Monitoring Cell Cultures,” in *Procedia Engineering*, 2016, vol. 168, pp. 578–581.
- [144] S. Tonello *et al.*, “Preliminary Study of a Flexible Printed Multi-Sensing Platform for Electromyography and Lactate Measuring during Rehabilitation,” in *2021 IEEE International Symposium on Medical Measurements and Applications (MeMeA)*, 2021, pp. 1–6.
- [145] Z. Abass, W. Meng, S. Q. Xie, and Z. Zhang, “A Robust, Practical Upper Limb Electromyography Interface Using Dry 3D Printed Electrodes*,” in *2019 IEEE/ASME International Conference on Advanced Intelligent Mechatronics (AIM)*, 2019, pp. 453–458.
- [146] Y. Hu *et al.*, “Stretchable and Printable Medical Dry Electrode Arrays on Textile for Electrophysiological Monitoring,” in *2019 IEEE 69th Electronic Components and Technology Conference (ECTC)*, 2019, pp. 243–248.
- [147] D. De Venuto, S. Carrara, J. Rabaey, and J. Ohta, “Guest Editorial Special Issue on Sensors and Interfaces for Mobile Healthcare,” *IEEE Sens. J.*, vol. 16, no. 23, p. 8185, 2016.
- [148] S. Shustak *et al.*, “Home monitoring of sleep with a temporary-tattoo EEG, EOG and EMG electrode array: a feasibility study.,” *J. Neural Eng.*, vol. 16, no. 2, p. 26024, Apr. 2019.
- [149] L. Inzelberg and Y. Hanein, “Electrophysiology Meets Printed Electronics: The Beginning of a Beautiful Friendship.,” *Front. Neurosci.*, vol. 12, p. 992, 2018.
- [150] M. B. I. Reaz, M. S. Hussain, and F. Mohd-Yasin, “Techniques of EMG signal analysis: Detection, processing, classification and applications,” *Biol. Proced. Online*, vol. 8, no. 1, pp. 11–35, Mar. 2006.
- [151] M. Hakonen, H. Piitulainen, and A. Visala, “Current state of digital signal processing in myoelectric interfaces and related applications,” *Biomed. Signal Process. Control*, vol. 18, pp. 334–359, 2015.
- [152] B. Tapia, I. Soto, D. Marinez, and N. Candolfi, “Myoelectric interfaces and related applications: Current state of EMG signal processing- A Systematic Review,” *IEEE Access*, vol. PP, p. 1, Jan. 2020.
- [153] N. Rabin, M. Kahlon, S. Malayev, and A. Ratnovsky, “Classification of human hand movements based on EMG signals using nonlinear dimensionality reduction and data fusion techniques,” *Expert Syst. Appl.*, vol. 149, 2020.
- [154] T. Tuncer, S. Dogan, and A. Subasi, “Surface EMG signal classification using ternary pattern and discrete wavelet transform based feature extraction for hand movement recognition,” *Biomed. Signal Process. Control*, vol. 58, 2020.
- [155] A. Subasi and E. Yaman, “Emg signal classification using discrete wavelet transform and rotation forest,” in *IFMBE Proceedings*, 2020, vol. 73, pp. 29–35.
- [156] C. J. Baby, K. J. Das, and P. Venugopal, “Design of an Above Knee Low-Cost Powered Prosthetic Leg Using Electromyography and Machine Learning,” *Advances in Intelligent Systems and Computing*, vol. 1057, pp. 339–348, 2020.
- [157] M. A. Lobo, M. L. Hall, B. Greenspan, P. Rohloff, L. A. Prosser, and B. A. Smith, “Wearables for Pediatric Rehabilitation: How to Optimally Design and Use Products to Meet the Needs of Users,” *Phys. Ther.*, vol. 99, no. 6, pp. 647–657, Jun. 2019.

- [158] V. Musalimov *et al.*, “Modelling of the human knee joint supported by active orthosis,” *Int. J. Appl. Mech. Eng.*, vol. 23, no. 1, pp. 107–120, Feb. 2018.
- [159] V. T. Minh, M. Tamre, A. Safonov, V. Musalimov, P. Kovalenko, and I. Monakhov, “DESIGN AND IMPLEMENTATION OF A MECHATRONIC ELBOW ORTHOSIS,” *Mechatron. Syst. Control 2020*, vol. 48, no. 1, pp. 231–238, Jan. 2020.
- [160] F. A. Ferdiansyah, P. Prajitno, and S. K. Wijaya, “EEG-EMG based bio-robotics elbow orthotics control,” *J. Phys. Conf. Ser.*, vol. 1528, no. 1, p. 012033, Apr. 2020.
- [161] S. Gao, Y. Wang, C. Fang, and L. Xu, “A Smart Terrain Identification Technique Based on Electromyography, Ground Reaction Force, and Machine Learning for Lower Limb Rehabilitation,” *Appl. Sci. 2020, Vol. 10, Page 2638*, vol. 10, no. 8, p. 2638, Apr. 2020.
- [162] I. Kang, P. Kunapuli, H. Hsu, and A. J. Young, “Electromyography (EMG) signal contributions in speed and slope estimation using robotic exoskeletons,” *IEEE Int. Conf. Rehabil. Robot.*, vol. 2019-June, pp. 548–553, Jun. 2019.
- [163] A. Péter *et al.*, “Comparing Surface and Fine-Wire Electromyography Activity of Lower Leg Muscles at Different Walking Speeds,” *Front. Physiol.*, vol. 10, p. 1283, Oct. 2019.
- [164] B. Zhmud, D. Ph, and A. Prof, “Lube-Tech093-ViscosityBlendingEquations,” *Lube Mag.*, no. 121, pp. 2–5, 2014.
- [165] K. Kaneda, “The features of muscle activity during chair standing and sitting motion in submerged condition,” *PLoS One*, vol. 14, no. 8, p. e0220602, Aug. 2019.
- [166] S. Hellmers *et al.*, “Measurement of the Chair Rise Performance of Older People Based on Force Plates and IMUs,” *Sensors (Basel)*, vol. 19, no. 6, p. 1370, Mar. 2019.
- [167] G. Li, Y. Li, L. Yu, and Y. Geng, “Conditioning and sampling issues of EMG signals in motion recognition of multifunctional myoelectric prostheses,” *Ann. Biomed. Eng.*, vol. 39, no. 6, pp. 1779–1787, Jun. 2011.
- [168] S. A. Go, K. Coleman-Wood, and K. R. Kaufman, “Frequency analysis of lower extremity electromyography signals for the quantitative diagnosis of dystonia,” *J. Electromyogr. Kinesiol.*, vol. 24, no. 1, pp. 31–36, Feb. 2014.
- [169] T. Roland, S. Amsuess, M. F. Russold, and W. Baumgartner, “Ultra-Low-Power Digital Filtering for Insulated EMG Sensing,” *Sensors 2019, Vol. 19, Page 959*, vol. 19, no. 4, p. 959, Feb. 2019.
- [170] P. Regier, H. Briceño, and J. N. Boyer, “Analyzing and comparing complex environmental time series using a cumulative sums approach,” *MethodsX*, vol. 6, pp. 779–787, 2019.
- [171] W. El Falou, J. Duchêne, D. Hewson, M. Khalil, M. Grabisch, and F. Lino, “A segmentation approach to long duration surface EMG recordings,” *J. Electromyogr. Kinesiol. Off. J. Int. Soc. Electrophysiol. Kinesiol.*, vol. 15, no. 1, pp. 111–119, Feb. 2005.
- [172] W. El Falou, M. Khalil, and J. Duchêne, *Adaptive approach for change detection in EMG recordings*, vol. 2. 2001.
- [173] R. S. A. Brinkworth and K. S. Türker, “A method for quantifying reflex responses from intra-muscular and surface electromyogram,” *J. Neurosci. Methods*, vol. 122, no. 2, pp. 179–193, 2003.
- [174] N. Tam, “A theoretical analysis of an alternative CUSUM statistic called CUSUM-slope for detecting signals from background noise in a low signal-to-noise environment,” *BMC Neurosci.*, vol. 10, Jul. 2009.
- [175] A. Strazza, F. Verdini, L. Burattini, S. Fioretti, and F. Di Nardo, *Time-frequency analysis of surface EMG signals for maximum energy localization during walking*. 2018.

- [176] A. Phinyomark, S. Thongpanja, H. Hu, P. Phukpattaranont, and C. Limsakul, "The Usefulness of Mean and Median Frequencies in Electromyography Analysis," in *Computational Intelligence in Electromyography Analysis - A Perspective on Current Applications and Future Challenges*, 2012, pp. 195–220.
- [177] R. N. Khushaba, "Correlation analysis of electromyogram signals for multiuser myoelectric interfaces," *IEEE Trans. Neural Syst. Rehabil. Eng.*, vol. 22, no. 4, pp. 745–755, 2014.
- [178] K. Watanabe, M. Kouzaki, M. Ogawa, H. Akima, and T. Moritani, "Relationships between muscle strength and multi-channel surface EMG parameters in eighty-eight elderly," *Eur. Rev. Aging Phys. Act. 2018 151*, vol. 15, no. 1, pp. 1–10, Apr. 2018.
- [179] N. Malesevic *et al.*, "A database of multi-channel intramuscular electromyogram signals during isometric hand muscles contractions," *Sci. Data 2020 71*, vol. 7, no. 1, pp. 1–12, Jan. 2020.
- [180] P. J. Millington, B. M. Myklebust, and G. M. Shambes, "Biomechanical Analysis of the Sit-to-Stand Motion in Elderly Persons."
- [181] A. I. Cuesta-Vargas and M. González-Sánchez, "Differences in muscle activation patterns during sit to stand task among subjects with and without intellectual disability," *Biomed Res. Int.*, vol. 2013, 2013.
- [182] C. T. Candotti, J. F. Loss, M. La Torre, M. O. Melo, L. D. Araçá, and V. V. Marcks, "Use of electromyography to assess pain in the upper trapezius and lower back muscles within a fatigue protocol," *Brazilian J. Phys. Ther.*, vol. 13, pp. 144–151, 2009.
- [183] L. Syedmoradi, M. Daneshpour, M. Alvandipour, F. a. Gomez, H. Hajghassem, and K. Omidfar, "Point of care testing: The impact of nanotechnology," *Biosens. Bioelectron.*, vol. 87, pp. 373–387, 2017.
- [184] K. Rathee, V. Dhull, R. Dhull, and S. Singh, "Biosensors based on electrochemical lactate detection: A comprehensive review," *Biochem. Biophys. Reports*, vol. 5, pp. 35–54, 2016.
- [185] M. E. Payne, A. Zamarayeva, V. I. Pister, N. A. D. Yamamoto, and A. C. Arias, "Printed, Flexible Lactate Sensors: Design Considerations Before Performing On-Body Measurements," *Sci. Rep.*, vol. 9, no. 1, p. 13720, 2019.
- [186] L. J. Currano, F. C. Sage, M. Hagedon, L. Hamilton, J. Patrone, and K. Gerasopoulos, "Wearable Sensor System for Detection of Lactate in Sweat," *Sci. Rep.*, vol. 8, no. 1, p. 15890, 2018.
- [187] G. Yang *et al.*, "A Health-IoT platform based on the integration of intelligent packaging, unobtrusive biosensor, and intelligent medicine box," *IEEE Trans. Ind. Informatics*, vol. 10, no. 4, pp. 2180–2191, Nov. 2014.
- [188] Y. Khan, A. E. Ostfeld, C. M. Lochner, A. Pierre, and A. C. Arias, "Monitoring of Vital Signs with Flexible and Wearable Medical Devices," *Adv. Mater.*, vol. 28, no. 22, pp. 4373–4395, Jun. 2016.
- [189] K. Fukuda and T. Someya, "Recent Progress in the Development of Printed Thin-Film Transistors and Circuits with High-Resolution Printing Technology," *Adv. Mater.*, vol. 29, no. 25, p. 1602736, Jul. 2017.
- [190] S. Tonello *et al.*, "Wireless Point-of-Care Platform with Screen-Printed Sensors for Biomarkers Detection," *IEEE Trans. Instrum. Meas.*, vol. 66, no. 9, pp. 2448–2455, Sep. 2017.
- [191] M. Borghetti, M. Ghittorelli, E. Sardini, M. Serpelloni, and F. Torricelli, "Electrical characterization of PEDOT: PSS strips deposited by inkjet printing on plastic foil for sensor manufacturing," *IEEE Trans. Instrum. Meas.*, vol. 65, no. 9, pp. 2137–2144, Sep. 2016.
- [192] F. Povolo, C. Schwartz, and E. B. Hermida, "Stress Relaxation of PVC Below the Yield Point."
- [193] H. Enser *et al.*, "Printed Strain Gauges Embedded in Organic Coatings," *Procedia Eng.*, vol. 168, pp. 822–825, Jan. 2016.

- [194] H. Enser *et al.*, "Printed strain gauges embedded in organic coatings - Analysis of gauge factor and temperature dependence," *Sensors Actuators A Phys.*, vol. 276, pp. 137–143, Jun. 2018.
- [195] H. Enser, J. K. Sell, M. Schatzl-Linder, B. Strauß, W. Hilber, and B. Jakoby, "Hysteresis and Material Effects of Printed Strain Gauges Embedded in Organic Coatings," *Proc. 2017, Vol. 1, Page 624*, vol. 1, no. 4, p. 624, Aug. 2017.
- [196] P. Bezuidenhout, S. Smith, and T. H. Joubert, "A low-cost inkjet-printed paper-based potentiostat," *Appl. Sci.*, vol. 8, no. 6, Jun. 2018.
- [197] Y. Wang *et al.*, "Paper-Based Inkjet-Printed Flexible Electronic Circuits," *ACS Appl. Mater. Interfaces*, vol. 8, no. 39, pp. 26112–26118, Oct. 2016.
- [198] C.-J. Lee, Y.-C. Chang, L.-W. Wang, and Y.-H. Wang, "Biodegradable Materials for Organic Field-Effect Transistors on a Paper Substrate," *IEEE Electron Device Lett.*, vol. 40, no. 2, pp. 236–239, Feb. 2019.
- [199] M.-Z. Xie, L.-F. Wang, and L. Dong, "Low Cost Paper-Based LC Wireless Humidity Sensors and Distance-Insensitive Readout System," *IEEE Sens. J.*, vol. 19, no. 12, pp. 4717–4725, Jun. 2019.
- [200] Y. Jo, D. W. Jeong, J. O. Lee, Y. Choi, and S. Jeong, "3D-printed origami electronics using percolative conductors," *RSC Adv.*, vol. 8, no. 40, pp. 22755–22762, 2018.
- [201] L. Ren'Ai *et al.*, "Green polymerizable deep eutectic solvent (PDES) type conductive paper for origami 3D circuits," *Chem. Commun.*, vol. 54, no. 18, pp. 2304–2307, Mar. 2018.
- [202] C. Linghu, S. Zhang, C. Wang, and J. Song, "Transfer printing techniques for flexible and stretchable inorganic electronics," *npj Flex. Electron.*, vol. 2, no. 1, Dec. 2018.
- [203] J. Bian, L. Zhou, X. Wan, C. Zhu, B. Yang, and Y. Huang, "Laser Transfer, Printing, and Assembly Techniques for Flexible Electronics," *Adv. Electron. Mater.*, vol. 5, no. 7, p. 1800900, Jul. 2019.
- [204] H. Luo, C. Wang, C. Linghu, K. Yu, C. Wang, and J. Song, "Laser-Driven Programmable Non-Contact Transfer Printing of Objects onto Arbitrary Receivers via an Active Elastomeric Micro-Structured Stamp," *Natl. Sci. Rev.*, Aug. 2019.
- [205] M. Borghetti, E. Cantu, E. Sardini, and M. Serpelloni, "Preliminary Study on Wireless Passive Resistive Sensor Applied for Smart Objects," in *2021 IEEE International Workshop on Metrology for Industry 4.0 & IoT (MetroInd4.0&IoT)*, 2021, pp. 150–155.
- [206] J. Jansen and A. van der Merwe, "A Framework for Industrial Internet of Things," in *Responsible Design, Implementation and Use of Information and Communication Technology*, 2020, pp. 138–150.
- [207] S. Selvaraj and S. Sundaravaradhan, "Challenges and opportunities in IoT healthcare systems: a systematic review," *SN Appl. Sci.*, vol. 2, no. 1, pp. 1–8, 2020.
- [208] T. A. Khoa *et al.*, "Designing Efficient Smart Home Management with IoT Smart Lighting: A Case Study," *Wirel. Commun. Mob. Comput.*, vol. 2020, 2020.
- [209] G. Fuertes, I. Soto, R. Carrasco, M. Vargas, J. Sabattin, and C. Lagos, "Intelligent Packaging Systems: Sensors and Nanosensors to Monitor Food Quality and Safety," *J. Sensors*, vol. 2016, 2016.
- [210] Y. Ji, Q. Tan, H. Wang, W. Lv, H. Dong, and J. Xiong, "A Novel Surface LC Wireless Passive Temperature Sensor Applied in Ultra-High Temperature Measurement," *IEEE Sens. J.*, vol. 19, no. 1, pp. 102–112, 2019.
- [211] U. M. Jow and M. Ghovanloo, "Design and optimization of printed spiral coils for efficient transcutaneous inductive power transmission," *IEEE Trans. Biomed. Circuits Syst.*, vol. 1, no. 3, pp. 193–202, 2007.

- [212] S. S. Mohan, M. D. M. Hershenson, S. P. Boyd, and T. H. Lee, "Simple accurate expressions for planar spiral inductances," *IEEE J. Solid-State Circuits*, vol. 34, no. 10, pp. 1419–1420, 1999.
- [213] E. Cantù, M. Soprani, A. Ponzoni, E. Sardini, and M. Serpelloni, "Preliminary Analysis on Cellulose-based Gas Sensor by Means of Aerosol Jet Printing and Photonic Sintering," SCITEPRESS - Science and Technology Publications, 2020.
- [214] M. Borghetti, E. Cantu, E. Sardini, M. Serpelloni, and A. Ponzoni, "Preliminary Analysis on a Paper-based Ammonia Sensor for Future Food Smart Packaging," in *2021 IEEE International Workshop on Metrology for Industry 4.0 & IoT (MetroInd4.0&IoT)*, 2021, pp. 140–144.
- [215] V. Selamneni, S. K. Ganeshan, N. Nerurkar, T. Akshaya, and P. Sahatiya, "Facile Fabrication of MoSe₂ on Paper as an Electromechanical Piezoresistive Pressure-Strain Sensor," *IEEE Trans. Instrum. Meas.*, vol. 70, 2021.
- [216] G. Di Pasquale, S. Graziani, A. Pollicino, and C. Trigona, "Performance Characterization of a Biodegradable Deformation Sensor Based on Bacterial Cellulose," *IEEE Trans. Instrum. Meas.*, vol. 69, no. 5, pp. 2561–2569, May 2020.
- [217] M. Springmann *et al.*, "Options for keeping the food system within environmental limits," *Nature*, vol. 562, no. 7728, pp. 519–525, Oct. 2018.
- [218] S. Chen, S. Brahma, J. Mackay, C. Cao, and B. Aliakbarian, "The role of smart packaging system in food supply chain," *J. Food Sci.*, vol. 85, no. 3, pp. 517–525, Mar. 2020.
- [219] A. H. Ismail, N. A. Mohd Yahya, M. H. Yaacob, M. A. Mahdi, and Y. Sulaiman, "Optical ammonia gas sensor of poly(3,4-polyethylenedioxythiophene), polyaniline and polypyrrole: A comparative study," *Synth. Met.*, vol. 260, p. 116294, Feb. 2020.
- [220] A. Pasha, S. Khasim, F. A. Khan, and N. Dhananjaya, "Fabrication of gas sensor device using poly (3, 4-ethylenedioxythiophene)-poly (styrenesulfonate)-doped reduced graphene oxide organic thin films for detection of ammonia gas at room temperature," *Iran. Polym. J. (English Ed.)*, vol. 28, no. 3, pp. 183–192, Mar. 2019.
- [221] R. Ghosh, J. W. Gardner, and P. K. Guha, "Air Pollution Monitoring Using Near Room Temperature Resistive Gas Sensors: A Review," *IEEE Trans. Electron Devices*, vol. 66, no. 8, pp. 3254–3264, Aug. 2019.
- [222] R. Ghosh, A. K. Nayak, S. Santra, D. Pradhan, and P. K. Guha, "Enhanced ammonia sensing at room temperature with reduced graphene oxide/tin oxide hybrid films," *RSC Adv.*, vol. 5, no. 62, pp. 50165–50173, Jun. 2015.
- [223] A. Maity, A. K. Raychaudhuri, and B. Ghosh, "High sensitivity NH₃ gas sensor with electrical readout made on paper with perovskite halide as sensor material," *Sci. Rep.*, vol. 9, no. 1, pp. 1–10, Dec. 2019.
- [224] G. Barandun *et al.*, "Cellulose Fibers Enable Near-Zero-Cost Electrical Sensing of Water-Soluble Gases," *ACS Sensors*, vol. 4, no. 6, pp. 1662–1669, Jun. 2019.
- [225] Y. Nagata, "Measurement of Odor Threshold by Triangle Odor Bag Method," 2003.
- [226] "FIGARO TGS 826-for the detection of ammonia datasheet."
- [227] "<https://webbook.nist.gov/chemistry/>." [Online]. Available: <https://webbook.nist.gov/chemistry/>.
- [228] M. Nilsson, "Conductance phenomena in microcrystalline cellulose," *Phys. status solidi c*, vol. 3, no. 2, pp. 251–254, Feb. 2006.
- [229] A. D. Fernandopulle, L. Karunanayake, D. A. S. Amarasinghe, A. M. P. B. Samarasekara, and D. Attygalle, "HUMIDITY SENSING POTENTIAL OF A MICROCRYSTALLINE CELLULOSE SHEET,"

Cellul. Chem. Technol. Cellul. Chem. Technol., vol. 55, no. 6, pp. 469–475, 2021.

- [230] S. Sapiuha, M. Inoue, and P. Lepoutre, “Conductivity and water sorption in paper,” *J. Appl. Polym. Sci.*, vol. 30, no. 3, pp. 1257–1266, Mar. 1985.
- [231] N. T. Phan, K. H. Kim, E. C. Jeon, U. H. Kim, J. R. Sohn, and S. K. Pandey, “Analysis of volatile organic compounds released during food decaying processes,” *Environ. Monit. Assess.*, vol. 184, no. 3, pp. 1683–1692, Mar. 2012.
- [232] W. Y. Chung, G. T. Le, T. V. Tran, and N. H. Nguyen, “Novel proximal fish freshness monitoring using batteryless smart sensor tag,” *Sensors Actuators B Chem.*, vol. 248, pp. 910–916, Sep. 2017.
- [233] M. Marziano *et al.*, “Monitoring Caco-2 to enterocyte-like cells differentiation by means of electric impedance analysis on printed sensors,” *Biochim. Biophys. Acta - Gen. Subj.*, vol. 1863, no. 5, 2019.
- [234] T. Lea, “Caco-2 Cell Line,” in *The Impact of Food Bioactives on Health: in vitro and ex vivo models*, K. Verhoeckx, P. Cotter, I. López-Expósito, C. Kleiveland, T. Lea, A. Mackie, T. Requena, D. Swiatecka, and H. Wichers, Eds. Cham: Springer International Publishing, 2015, pp. 103–111.
- [235] Y. Sambuy, I. De Angelis, G. Ranaldi, M. L. Scarino, A. Stamatii, and F. Zucco, “The Caco-2 cell line as a model of the intestinal barrier: influence of cell and culture-related factors on Caco-2 cell functional characteristics,” *Cell Biol. Toxicol.*, vol. 21, no. 1, pp. 1–26, 2005.
- [236] I. J. Hidalgo, T. J. Raub, and R. T. Borchardt, “Characterization of the human colon carcinoma cell line (Caco-2) as a model system for intestinal epithelial permeability,” *Gastroenterology*, vol. 96, no. 3, pp. 736–749, Mar. 2018.
- [237] M. J. Engle, G. S. Goetz, and D. H. Alpers, “Caco-2 cells express a combination of colonocyte and enterocyte phenotypes,” *J. Cell. Physiol.*, vol. 174, no. 3, pp. 362–369, Mar. 1998.
- [238] A. Kourtidis *et al.*, “Distinct E-cadherin-based complexes regulate cell behaviour through miRNA processing or Src and p120 catenin activity,” *Nat. Cell Biol.*, vol. 17, no. 9, pp. 1145–1157, Sep. 2015.
- [239] T. N. MacKenzie *et al.*, “Triptolide induces the expression of miR-142-3p: a negative regulator of heat shock protein 70 and pancreatic cancer cell proliferation,” *Mol. Cancer Ther.*, vol. 12, no. 7, pp. 1266–1275, Jul. 2013.
- [240] J. I. Alvarez *et al.*, “The Hedgehog pathway promotes blood-brain barrier integrity and CNS immune quiescence,” *Science*, vol. 334, no. 6063, pp. 1727–1731, Dec. 2011.
- [241] I. Giaever and C. R. Keese, “Use of electric fields to monitor the dynamical aspect of cell behavior in tissue culture,” *IEEE Trans. Biomed. Eng.*, vol. 33, no. 2, pp. 242–247, Feb. 1986.
- [242] D. Seidel *et al.*, “Impedimetric real-time monitoring of neural pluripotent stem cell differentiation process on microelectrode arrays,” *Biosens. Bioelectron.*, vol. 86, pp. 277–286, Dec. 2016.
- [243] R. Szulcek, H. J. Bogaard, and G. P. V. N. Amerongen, “Electric Cell-substrate Impedance Sensing for the Quantification of Endothelial Proliferation, Barrier Function, and Motility,” no. March, pp. 1–12, 2014.
- [244] I. O. K’Owino and O. A. Sadik, “Impedance Spectroscopy: A Powerful Tool for Rapid Biomolecular Screening and Cell Culture Monitoring,” *Electroanalysis*, vol. 17, no. 23, pp. 2101–2113.
- [245] E. Van Rymenant *et al.*, “Chronic exposure to short-chain fatty acids modulates transport and metabolism of microbiome-derived phenolics in human intestinal cells,” *J. Nutr. Biochem.*, vol. 39, pp. 156–168, Jan. 2017.
- [246] M. Natoli, B. D. Leoni, I. D’Agnano, F. Zucco, and A. Felsani, “Good Caco-2 cell culture practices,” *Toxicol. Vitr.*, vol. 26, no. 8, pp. 1243–1246, 2012.

- [247] J. Fantini *et al.*, "Spontaneous and induced dome formation by two clonal cell populations derived from a human adenocarcinoma cell line, HT29.," *J. Cell Sci.*, vol. 83, pp. 235–249, Jul. 1986.
- [248] M. Natoli *et al.*, "Cell growing density affects the structural and functional properties of Caco-2 differentiated monolayer.," *J. Cell. Physiol.*, vol. 226, no. 6, pp. 1531–1543, Jun. 2011.
- [249] S. Ferruzza, C. Rossi, M. L. Scarino, and Y. Sambuy, "A protocol for in situ enzyme assays to assess the differentiation of human intestinal Caco-2 cells.," *Toxicol. In Vitro*, vol. 26, no. 8, pp. 1247–1251, Dec. 2012.
- [250] O. J. Myers, M. Anjanappa, and C. Freidhoff, "Designing Piezoelectric Interdigitated Microactuators Using Finite Element Analysis," *J. Mech. Des.*, vol. 132, no. 6, pp. 61004–61011, May 2010.
- [251] M. Eichler *et al.*, "A novel 96-well multielectrode array based impedimetric monitoring platform for comparative drug efficacy analysis on 2D and 3D brain tumor cultures," *Biosens. Bioelectron.*, vol. 67, 2015.
- [252] H.-G. Jahnke, A. Braesigk, T. G. A. Mack, S. Ponick, F. Striggow, and A. A. Robitzki, "Impedance spectroscopy based measurement system for quantitative and label-free real-time monitoring of tauopathy in hippocampal slice cultures.," *Biosens. Bioelectron.*, vol. 32, no. 1, pp. 250–258, Feb. 2012.
- [253] J. E. Jackson, "A user's guide to principal components, J. Edward Jackson," 1991.
- [254] J. M. Bland and D. G. Altman, "Statistical methods for assessing agreement between two methods of clinical measurement.," *Lancet (London, England)*, vol. 1, no. 8476, pp. 307–310, Feb. 1986.
- [255] P. F. Watson and A. Petrie, "Method agreement analysis: a review of correct methodology.," *Theriogenology*, vol. 73, no. 9, pp. 1167–1179, Jun. 2010.
- [256] P. Schmiedlin-Ren, K. E. Thummel, J. M. Fisher, M. F. Paine, K. S. Lown, and P. B. Watkins, "Expression of enzymatically active CYP3A4 by Caco-2 cells grown on extracellular matrix-coated permeable supports in the presence of 1 α ,25-dihydroxyvitamin D3.," *Mol. Pharmacol.*, vol. 51, no. 5, pp. 741–754, May 1997.
- [257] S. Ferruzza, C. Rossi, M. L. Scarino, and Y. Sambuy, "A protocol for differentiation of human intestinal Caco-2 cells in asymmetric serum-containing medium," *Toxicol. Vitr.*, vol. 26, no. 8, pp. 1252–1255, 2012.
- [258] K. A. Lentz, J. Hayashi, L. J. Lucisano, and J. E. Polli, "Development of a more rapid, reduced serum culture system for Caco-2 monolayers and application to the biopharmaceutics classification system," *Int. J. Pharm.*, vol. 200, no. 1, pp. 41–51, 2000.
- [259] R. Ehret, W. Baumann, M. Brischwein, a. Schwinde, K. Stegbauer, and B. Wolf, "Monitoring of cellular behaviour by impedance measurements on interdigitated electrode structures," *Biosens. Bioelectron.*, vol. 12, pp. 29–41, 1997.
- [260] B.-W. Chang, C.-H. Chen, S.-J. Ding, D. C.-H. Chen, and H.-C. Chang, "Impedimetric monitoring of cell attachment on interdigitated microelectrodes," *Sensors Actuators B Chem.*, vol. 105, no. 2, pp. 159–163, 2005.
- [261] R. Igreja and C. J. Dias, "Dielectric response of interdigital chemocapacitors: The role of the sensitive layer thickness," *Sensors Actuators B Chem.*, vol. 115, no. 1, pp. 69–78, 2006.
- [262] M. Vakilian and B. Y. Majlis, "Study of interdigitated electrode sensor for lab-on-chip applications," in *2014 IEEE International Conference on Semiconductor Electronics (ICSE2014)*, 2014, pp. 201–204.
- [263] E. Jabari and E. Toyserkani, "Aerosol-Jet printing of highly flexible and conductive graphene/silver patterns," *Mater. Lett.*, vol. 174, pp. 40–43, 2016.

- [264] K. Benson, S. Cramer, and H.-J. Galla, "Impedance-based cell monitoring: barrier properties and beyond," *Fluids Barriers CNS*, vol. 10, p. 5, Jan. 2013.
- [265] D. Das, F. A. Kamil, K. Biswas, and S. Das, "Evaluation of single cell electrical parameters from bioimpedance of a cell suspension," *RSC Adv.*, vol. 4, no. 35, pp. 18178–18185, 2014.
- [266] C. M. Lo, C. R. Keese, and I. Giaever, "Impedance analysis of MDCK cells measured by electric cell-substrate impedance sensing.," *Biophys. J.*, vol. 69, no. 6, p. 2800, 1995.
- [267] U. E. B. M, and B. FJ, "Impedance analysis of cultured cells: a mean-field electrical response model for electric cell-substrate impedance sensing technique," *Phys. Rev. E. Stat. Nonlin. Soft Matter Phys.*, vol. 74, no. 4 Pt 1, 2006.
- [268] C. Xiao, B. Lachance, G. Sunahara, and J. H. T. Luong, "An in-depth analysis of electric cell-substrate impedance sensing to study the attachment and spreading of mammalian cells," *Anal. Chem.*, vol. 74, no. 6, pp. 1333–1339, Mar. 2002.
- [269] B. Srinivasan, A. R. Kolli, M. B. Esch, H. E. Abaci, M. L. Shuler, and J. J. Hickman, "TEER measurement techniques for in vitro barrier model systems.," *J. Lab. Autom.*, vol. 20, no. 2, pp. 107–126, Apr. 2015.
- [270] M. Amin, P. P. Dey, and H. Badkoobehi, "A Complete Electrical Equivalent Circuit Model for Biological Cell," in *Proceedings of the 7th WSEAS International Conference on Applied Computer and Applied Computational Science*, 2008, pp. 343–348.
- [271] J. Hickman, "Transepithelial/endothelial Electrical Resistance (TEER) theory and applications for microfluidic body-on-a-chip devices," *J. Rare Dis. Res. Treat.*, vol. 1, pp. 46–52, 2016.
- [272] E. Latorre *et al.*, "Active superelasticity in three-dimensional epithelia of controlled shape," *Nature*, vol. 563, no. 7730, pp. 203–208, 2018.
- [273] S. Tonello *et al.*, "Impedance-Based Monitoring of Mesenchymal Stromal Cell Three-Dimensional Proliferation Using Aerosol Jet Printed Sensors: A Tissue Engineering Application," *Materials (Basel)*, vol. 13, no. 10, p. 2231, May 2020.
- [274] N. Chaicharoenaudomrung, P. Kunhorm, and P. Noisa, "Three-dimensional cell culture systems as an in vitro platform for cancer and stem cell modeling," *World Journal of Stem Cells*, vol. 11, no. 12, Baishideng Publishing Group Co, pp. 1065–1083, 01-Dec-2019.
- [275] K. Dzobo *et al.*, "Advances in regenerative medicine and tissue engineering: Innovation and transformation of medicine," *Stem Cells Int.*, vol. 2018, 2018.
- [276] M. Dominici *et al.*, "Minimal criteria for defining multipotent mesenchymal stromal cells. The International Society for Cellular Therapy position statement," *Cytotherapy*, vol. 8, no. 4, pp. 315–317, Aug. 2006.
- [277] A. Andrzejewska, B. Lukomska, and M. Janowski, "Concise Review: Mesenchymal Stem Cells: From Roots to Boost," *Stem Cells*, vol. 37, no. 7, Wiley-Blackwell, pp. 855–864, 01-Jul-2019.
- [278] Y. H. Tsou, J. Khoneisser, P. C. Huang, and X. Xu, "Hydrogel as a bioactive material to regulate stem cell fate," *Bioactive Materials*, vol. 1, no. 1, KeAi Communications Co., pp. 39–55, 01-Sep-2016.
- [279] M. Nikbakht, B. Pakbin, and G. Nikbakht Brujeni, "Evaluation of a new lymphocyte proliferation assay based on cyclic voltammetry; an alternative method," *Sci. Rep.*, vol. 9, no. 1, Dec. 2019.
- [280] P. M. Mendes, "Cellular nanotechnology: Making biological interfaces smarter," *Chemical Society Reviews*, vol. 42, no. 24, Royal Society of Chemistry, pp. 9207–9218, 21-Dec-2013.
- [281] K. Chawla *et al.*, "Integrating impedance-based growth-rate monitoring into a microfluidic cell culture platform for live-cell microscopy," *Microsystems Nanoeng.*, vol. 4, no. 1, Dec. 2018.

- [282] B. Brazey, J. Cottet, A. Bolopion, H. Van Lintel, P. Renaud, and M. Gauthier, "Impedance-based real-time position sensor for lab-on-a-chip devices," *Lab Chip*, vol. 18, no. 5, pp. 818–831, Mar. 2018.
- [283] W. Gamal, H. Wu, I. Underwood, J. Jia, S. Smith, and P. O. Bagnaninchi, "Impedance-based cellular assays for regenerative medicine," *Philosophical Transactions of the Royal Society B: Biological Sciences*, vol. 373, no. 1750. Royal Society Publishing, 05-Jul-2018.
- [284] M. A. Khan, E. Cantù, S. Tonello, M. Serpelloni, N. F. Lopomo, and E. Sardini, "A review on biomaterials for 3D conductive scaffolds for stimulating and monitoring cellular activities," *Appl. Sci.*, vol. 9, no. 5, 2019.
- [285] K. Dey *et al.*, "Rational Design and Development of Anisotropic and Mechanically Strong Gelatin-Based Stress Relaxing Hydrogels for Osteogenic/Chondrogenic Differentiation," *Macromol. Biosci.*, vol. 19, no. 8, Aug. 2019.
- [286] S. E. De León, A. Pupovac, and S. L. McArthur, "Three-Dimensional (3D) cell culture monitoring: Opportunities and challenges for impedance spectroscopy," *Biotechnol. Bioeng.*, vol. 117, no. 4, pp. 1230–1240, Apr. 2020.
- [287] A. De Luca *et al.*, "Comparative Analysis of Mesenchymal Stromal Cells Biological Properties," *ISRN Stem Cells*, vol. 2013, pp. 1–9, Mar. 2013.
- [288] N. G. Mehr, X. Li, G. Chen, B. D. Favis, and C. D. Hoemann, "Pore size and LbL chitosan coating influence mesenchymal stem cell in vitro fibrosis and biomineralization in 3D porous poly(epsilon-caprolactone) scaffolds," *J. Biomed. Mater. Res. Part A*, vol. 103, no. 7, pp. 2449–2459, Jul. 2015.
- [289] Q. Meng *et al.*, "A composite scaffold of MSC affinity peptide-modified demineralized bone matrix particles and chitosan hydrogel for cartilage regeneration," *Sci. Rep.*, vol. 5, Dec. 2015.
- [290] J. H. Song, S. M. Lee, and K. H. Yoo, "Label-free and real-time monitoring of human mesenchymal stem cell differentiation in 2D and 3D cell culture systems using impedance cell sensors," *RSC Adv.*, vol. 8, no. 54, pp. 31246–31254, 2018.
- [291] D. Gupta *et al.*, "Bioelectrical impedance phase angle in clinical practice: Implications for prognosis in stage IIIB and IV non-small cell lung cancer," *BMC Cancer*, vol. 9, Jan. 2009.
- [292] T. Gerasimenko *et al.*, "Impedance Spectroscopy as a Tool for Monitoring Performance in 3D Models of Epithelial Tissues," *Frontiers in Bioengineering and Biotechnology*, vol. 7. Frontiers Media S.A., 24-Jan-2020.
- [293] K. Dey *et al.*, "Preparation and properties of high performance gelatin-based hydrogels with chitosan or hydroxyethyl cellulose for tissue engineering applications," *Int. J. Polym. Mater. Polym. Biomater.*, vol. 68, no. 4, pp. 183–192, Mar. 2019.
- [294] C. Jensen and Y. Teng, "Is It Time to Start Transitioning From 2D to 3D Cell Culture?," *Frontiers in Molecular Biosciences*, vol. 7. Frontiers Media S.A., 06-Mar-2020.
- [295] N. Carragher, F. Piccinini, A. Tesei, O. J. Trask, M. Bickle, and P. Horvath, "Concerns, challenges and promises of high-content analysis of 3D cellular models," *Nature Reviews Drug Discovery*, vol. 17, no. 8. Nature Publishing Group, 2018.
- [296] A. Bodini, E. Cantu, M. Serpelloni, E. Sardini, and S. Tonello, "Design and implementation of a microsensor platform for protein detection realized via 3-D printing," in *2018 IEEE Sensors Applications Symposium, SAS 2018 - Proceedings*, 2018, vol. 2018-Janua.
- [297] E. Cantù, S. Tonello, M. Serpelloni, and E. Sardini, *Aerosol jet printed sensors for protein detection: A preliminary study*, vol. 539. 2019.
- [298] A. Spanu, S. Lai, P. Cosseddu, M. Tedesco, S. Martinoia, and A. Bonfiglio, "An organic transistor-based

system for reference-less electrophysiological monitoring of excitable cells,” *Sci. Rep.*, vol. 5, p. 8807, Mar. 2015.

- [299] P. Fanjul-Bolado, D. Hernández-Santos, P. J. Lamas-Ardisana, A. Martín-Pernía, and A. Costa-García, “Electrochemical characterization of screen-printed and conventional carbon paste electrodes,” *Electrochim. Acta*, vol. 53, no. 10, pp. 3635–3642, 2008.
- [300] R. A. S. Couto, J. L. F. C. Lima, and M. B. Quinaz, “Recent developments, characteristics and potential applications of screen-printed electrodes in pharmaceutical and biological analysis,” *Talanta*, vol. 146. Elsevier B.V., pp. 801–814, 01-Jan-2016.
- [301] J. Li, F. Rossignol, and J. Macdonald, “Inkjet printing for biosensor fabrication: combining chemistry and technology for advanced manufacturing,” *Lab Chip*, vol. 15, no. 12, pp. 2538–2558, 2015.
- [302] M. M. da Silva Neves, M. B. González-García, D. Hernández-Santos, and P. Fanjul-Bolado, “Future trends in the market for electrochemical biosensing,” *Curr. Opin. Electrochem.*, vol. 10, pp. 107–111, 2018.
- [303] K. Agarwal, S. Hwang, A. Bartnik, N. Buchele, A. Mishra, and J.-H. Cho, “Small-Scale Biological and Artificial Multidimensional Sensors for 3D Sensing,” *Small*, vol. 14, no. 35, p. 1801145.
- [304] C. S. Alex Gong, W. J. Syu, K. F. Lei, and Y. S. Hwang, “Development of a flexible non-metal electrode for cell stimulation and recording,” *Sensors (Switzerland)*, vol. 16, no. 10, 2016.
- [305] Z. P. Chen, Z. F. Peng, J. H. Jiang, X. B. Zhang, G. L. Shen, and R. Q. Yu, “An electrochemical amplification immunoassay using biocatalytic metal deposition coupled with anodic stripping voltammetric detection,” *Sensors Actuators, B Chem.*, vol. 129, pp. 146–151, 2008.
- [306] A. Shrivastava and V. Gupta, “Methods for the determination of limit of detection and limit of quantitation of the analytical methods,” *Chronicles Young Sci.*, vol. 2, no. 1, pp. 21–25, Jan. 2011.
- [307] D. A. Armbruster and T. Pry, “Limit of blank, limit of detection and limit of quantitation.,” *Clin. Biochem. Rev.*, vol. 29 Suppl 1, no. Suppl 1, pp. S49-52, Aug. 2008.
- [308] D. U. Sarah Tonello, Mariagrazia Marziano, Giulia Abate, Tugba Kilic, Maurizio Memo and and E. S. Sandro Carrara, Nicola F. Lopomo, Mauro Serpelloni, “Enhanced Sensing of Interleukin 8 by Stripping Voltammetry: Carbon Nanotubes versus Fullerene,” *EMBEC NBC 2017-Joint Conf. Eur. Med. Biol. Eng. Conf. Nord. Conf. Biomed. Eng. MedicalPhysics*, pp. 213–218, 2018.
- [309] W. Oelßner, F. Berthold, and U. Guth, “The iR drop - Well-known but often underestimated in electrochemical polarization measurements and corrosion testing,” *Mater. Corros.*, vol. 57, no. 6, pp. 455–466, 2006.
- [310] “<https://www.norlandprod.com/adhesives/NOA%2081.html>.”
- [311] P. Wägli, A. Homsy, and N. F. De Rooij, “Norland optical adhesive (NOA81) microchannels with adjustable wetting behavior and high chemical resistance against a range of mid-infrared- transparent organic solvents,” *Sensors Actuators, B Chem.*, vol. 156, no. 2, pp. 994–1001, 2011.
- [312] D. Bartolo, G. Degré, P. Nghe, and V. Studer, “Microfluidic stickers,” *Lab Chip*, vol. 8, no. 2, pp. 274–279, 2008.
- [313] M. Morel, D. Bartolo, J. C. Galas, M. Dahan, and V. Studer, “Microfluidic stickers for cell- and tissue-based assays in microchannels,” *Lab Chip*, vol. 9, no. 7, pp. 1011–1013, 2009.
- [314] E. Sollier, C. Murray, P. Maoddi, and D. Di Carlo, “Rapid prototyping polymers for microfluidic devices and high pressure injections,” *Lab Chip*, vol. 11, no. 22, pp. 3752–3765, 2011.
- [315] I. S. Akhatov, J. M. Hoey, O. F. Swenson, and D. L. Schulz, “Aerosol focusing in micro-capillaries:

Theory and experiment,” *J. Aerosol Sci.*, vol. 39, no. 8, pp. 691–709, 2008.

- [316] S. Binder, M. Glatthaar, E. Rädlein, S. Binder, M. Glatthaar, and R. Edda, “Analytical Investigation of Aerosol Jet Printing Analytical Investigation of Aerosol Jet Printing,” vol. 6826, no. November, 2017.
- [317] M. M. Radhi, E. A. Jaffar Al-Mulla, and W. T. Tan, “Electrochemical characterization of the redox couple of Fe(III)/Fe(II) mediated by grafted polymer electrode,” *Res. Chem. Intermed.*, vol. 40, no. 1, pp. 179–192, Jan. 2014.
- [318] J. I. Gowda and S. T. Nandibewoor, “Electrochemical behavior of paclitaxel and its determination at glassy carbon electrode,” *Asian J. Pharm. Sci.*, vol. 9, no. 1, pp. 42–49, 2014.
- [319] D. A. C. Brownson and C. E. Banks, “Interpreting Electrochemistry,” *Handb. Graphene Electrochem.*, pp. 23–77, 2014.
- [320] M. Güemes, S. A. Rahman, and K. Hussain, “What is a normal blood glucose?,” *Arch. Dis. Child.*, vol. 101, no. 6, pp. 569–574, Jun. 2016.
- [321] J. Biscay, E. C. Rama, M. B. G. García, J. M. P. Carrazón, and A. C. García, “Enzymatic Sensor Using Mediator-Screen-Printed Carbon Electrodes,” *Electroanalysis*, vol. 23, no. 1, pp. 209–214, Jan. 2011.